YIELDING AND PARTICLE REARRANGEMENTS IN HARD SPHERE GLASSES

A Dissertation

submitted by

ALAN RANJIT JACOB

in partial fulfillment of the requirements
for the award of the degree

of

DOCTOR OF PHILOSOPHY

DEPARTMENT OF MATERIALS SCIENCE AND TECHNOLOGY
UNIVERSITY OF CRETE
24 NOVEMBER 2016

THESIS CERTIFICATE

This is to certify that the thesis titled **Yielding and particle rearrangements in hard sphere glasses**, submitted by **Alan Ranjit Jacob**, to the University of Crete, Greece, for the award of the degree of **Doctor of Philosophy**, is a bona fide record of the research work done by him under our supervision. The contents of this thesis, in full or in parts, have not been submitted to any other Institute or University for the award of any degree or diploma.

George Petekidis
Supervisor
Professor
Dept. of Material Sci. and Tech.
University of Crete, Greece, 70013

Place: Heraklion

Date: 24th November 2016

ACKNOWLEDGEMENTS

I enjoyed immense support from many dear friends and loved ones through the good and bad times during my last four years, which has finally culminated in this thesis. The inception, facilities and funding for this work I owe a big thank you to my supervisor Prof. George Petekidis. I enjoyed the freedom he gave to pursue my work. The final months was very difficult and he supported me through those hard times which helped me immensely. I acknowledge Thales Covisco, ARISTEA,ESMI and SMART PRO for the funding that helped me survive more than four years in Greece and the travel for collaborative work and conferences. Prof. Dimtris Vlassopoulos has been an amazing pillar of support and inspiration throughout my whole stay in Greece. I enjoyed the discussions with Benoit about all things under the sun from science to politics. I thank Prof. Jan Vermant for the amazing collaboration opportunity as well as hospitality he provided during the whole collaboration. Other collaborators who have provided invaluable support during this work are Dr. Andreas Poulos, Dr. Sunhyung Kim and Dr. Nick Koumakis. I have to thank High Performance Computing Facility in University of Crete for availing me the resources to run my BD simulations which have also wreaked havoc at times due to my lack of experience. I thank Dr. Andrew Schofield for providing the hard sphere samples and Prof. John Brady for the Brownian Dynamics simulation codes. I have to specifically thank Esmaeel as an amazing collaborator and a good friend who stood by me through the good and specifically bad times. Special thanks to Salvatore and Angela have been so helpful, kind and warm to me. I specially remember them and their family who took care of me when I was physically unwell traveling during my trip to Italy. The calmness and support Salvatore, as a friend and a collaborator, emoted has helped me through a lot of tight spots. 'The Bogris' have been of immense support in helping me get around the Greek problems as well as many other problems. Antje and Aygris are a family away

i

ABSTRACT

KEYWORDS: Colloidal Glass, Size Asymmetric Binary Glass, Rheology, Brownian Dynamics simulations, Orthogonal Superposition Rheometry, Aging, Large Amplitude Oscillatory Shear, Creep, Start-up shear, Shear thickening

A very high concentration or volume fraction of colloidal hard spheres ($\phi > 0.58$) dispersed in a continuous medium, characterized by the long lived entropic caging of colloidal particles by its neighbours, is termed a colloidal glass. This is a metastable state where the inherent relaxation time of the system deviates to infinity and the study of such systems under flow has garnered immense attention. In this work, we employ rheology and BD simulations to probe the linear and non-linear viscoelastic properties at rest and under shear. We also perform rheological experiments to probe aging as well as non-linear transient behaviour of colloidal glasses. Orthogonal superposition rheometery is utilized to understand the effect of inter particle potential on steady shear of hard sphere and soft colloidal glasses. Furthermore, we verify the presence and investigate different types of glasses existing in asymmetric binary mixtures with the help of BD simulations.

TABLE OF CONTENTS

ABBREVIATIONS

MSD	Mean Square Displacement
BD	Brownian Dynamics
LAOS	Large Amplitude Oscillatory Shear
MCT	Mode Coupling Theory
SGM	Soft Glassy Materials

NOTATION

ϕ	Volume fraction
R	Radius of colloidal particle, nm
γ	Strain
$\dot{\gamma}$	Shear Rate, s^{-1}
ω	Frequency of oscillation, $rad\ s^{-1}$
σ	Stress, Pa
η	Viscosity, Pas
G'	Storage modulus, Pa
G''	Viscous modulus, Pa
$tan\delta$	Ratio of viscous moduli to storage moduli G''/G'
k_B	Boltzmann constant, $1.3 \times 10^{-23} JK^{-1}$
T	Temperature, K
t_B	Brownian time, s
Pe	Peclet, $\dot{\gamma}t_B$
χ_s	Mixing ratio (volume of small particles to total volume fraction)
δ_{sb}	Ratio of radius of small particles to radius of big particles R_s/R_b

CHAPTER 1

INTRODUCTION

Atoms form different states of matter which flow at different timescales, in order to study these states of matter colloidal particles are employed. Furthermore colloidal particles are omnipresent, generally being lesser than fewer microns length they might be invisible to the naked eye but they have grown to be an essential part of day to day activities for example in paints, ink, shampoo, milk, blood. The omnipresence of colloidal systems in nature shows the relevance of exploring and understanding already existing states in soft condensed matter. Due to the size range of colloidal particles the quantum mechanical effects(present in atoms) can be ignored but they are small enough to sense the thermal fluctuations in the suspending environment. Colloidal particles tend to retain their rigidity when transfered or heated which makes them ideal candidates for processing of optics and semiconductors. Hence, colloidal particles are preferred to study different states of matter because of their size range and time scales, very simple techniques like microscopy can be utilized to study these systems in detail. One of the most challenging phases in condensed matter physics is the topology of glass and super cooled liquid and the vitrification or glass transition process (Angell, 1995; Debenedetti and Stillinger, 2001; Gotze and Sjogren, 1992; Pusey, 1991; Stillinger, 1995).

Vitrification is a process in which a liquid is quenched or compressed into a solid amorphous state. This process has a lot of relevance in ceramics, nuclear waste disposal (Wang *et al.*, 2010), and extensive research has recently been undertaken to understand vitrification of embryos, organs for long term storage (Fahy *et al.*, 2009, 2004). Vitrification can also be termed as glass transition when a liquid at temperature T is cooled below the glass transition temperature T_g. Then liquid will become a disordered, amorphous, non-equilibrium solid termed as glass. This is a kinetically arrested metastable state which always moves towards an equilibrated state or towards lowest free energy. Hence,

timescale is extremely important in order to define glass as a solid or liquid. An interesting example for glassy behaviour and timescales is the "Pitch Drop Experiment". Pitch does not flow at short timescales but when transferred into a funnel, it has dripping rate of approximately 1 drop every 110 months. This experiment is currently underway since 1927 in Queensland,Australia (Edgeworth *et al.*, 1984). Also the fundamental understanding of these amorphous states of matter can be extended to application level problems like traffic jams (de Wijn *et al.*, 2012), neural networks in computers (Mézard *et al.*, 2007) and in biological systems (Angelini *et al.*, 2011; Ellis and Minton, 2003; Gravish *et al.*, 2015).

1.1   Hard Sphere Colloids

An ideal colloidal hard sphere interaction between two particles can be defined as follows:

$$V(r) = \begin{cases} \infty & \text{if } r \leq 2R \\ 0 & \text{if } r > 2R \end{cases} \tag{1.1}$$

where r is defined as the center to center distance between two spheres and $2R$ is the sum of the two sphere radii of radius R. This equation denotes a sharp transition to repulsive potential when two spheres come into contact. For all possible configurations in such a system the potential energy is zero. This also indicates that the spheres are impenetrable which would have lead to a softer potential. Thermodynamically,

$$F = U - TS = (3/2)N_A k_B T - TS = (const - S)T \tag{1.2}$$

F is the free energy of the system, U is Internal Energy of the system, S is the Entropy, T is Temperature, k_B is the Boltzmann constant and N_A is Avogadro's number. Therefore, the colloidal hard sphere systems are governed by

entropy for a constant temperature. In a monodisperse colloidal hard sphere suspension volume fraction ϕ is the only parameter that controls the entropy of the system.

A characteristic of a colloidal particle in a suspending medium is "Brownian motion" which occurs due to the 'random kicks' exerted by solvent molecules on the colloidal particle with thermal energy $k_B T$ (Einstein, 1905) and Brownian motion tends to homogenize regions of different concentrations. The Brownian force or the stress tensor acting in all direction can be defined as

$$\mathbf{F}_B(r) = -k_B T \frac{d \ln g(\mathbf{r}; \phi)}{d\mathbf{r}} \qquad (1.3)$$

where $g(r; \phi)$ is the radial distribution function (Batchelor, 1976, 1977).

Since the kicks/collisions are random in magnitude and orientation the average displacement of the particle, $\langle x \rangle$ should be equal to zero. Thus a new variable known as mean square displacement (MSD), $\langle \Delta x^2 \rangle$ in one dimension, is defined as

$$\langle \Delta x^2 \rangle = \langle [x(t + \Delta t) - x(t)]^2 \rangle = 2D\Delta t \qquad (1.4)$$

where $\langle \rangle$ indicates the average over all particles and time t and lag time Δt and D is the diffusion coefficient. In three dimension Eq. 1.4 becomes

$$\langle \Delta r^2 \rangle = 6D\Delta t \qquad (1.5)$$

This indicates that in the dilute regime MSD is directly proportional to the time while at high volume fraction, ϕ, this deviates from the simple linear relationship of the colloidal suspension. Stokes-Einstein-Sutherland equation defines diffusion coefficient of a single particle of radius R as

$$D = \frac{k_B T}{6\pi\eta R} \qquad (1.6)$$

where η is the viscosity of the suspending medium. Finally, the diffusive time scale of particle is the time taken to diffuse a distance comparable to its own radius and can be derived as

$$\tau_B = \frac{R^2}{D} = \frac{6\pi\eta R^3}{k_B T} \tag{1.7}$$

Thus the time scale of diffusion is affected by the the viscosity of the suspending medium, η and the radius of the particle, R.

1.2 Phase Diagram
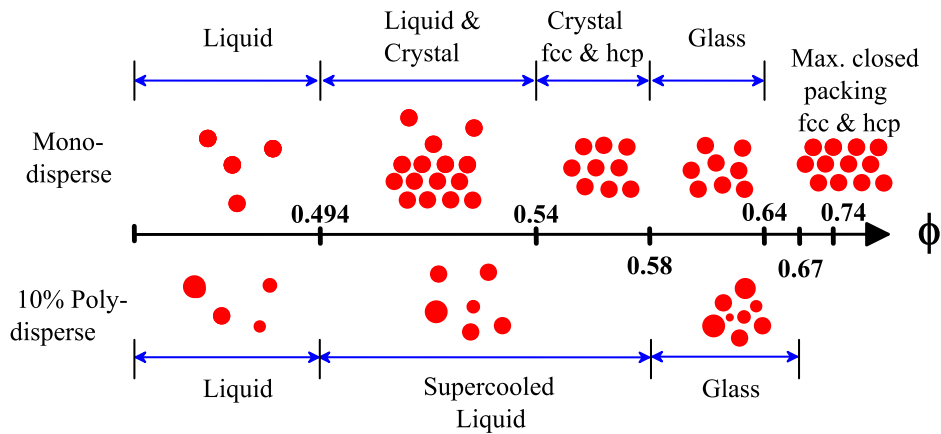
Figure 1.1: Phase Diagram of hard sphere colloidal suspensions for monodisperse and polydisperse colloids as a function of volume fraction.

An athermal colloidal hard sphere suspension phase diagram is shown in Fig. 1.1 as function of ϕ (Pusey and Van Megen, 1986). The suspending medium contributes via hydrodynamic interactions which slow down the timescales of the system. Colloidal suspensions exhibit liquid-like behaviour at very dilute concentrations of colloidal particles. Monodisperse colloidal particles at $\phi > 0.494$, the suspension is pushed into a crystal-liquid coexistence regime where the fluid phase coexist with the crystal phase. Colloidal particles are kinetically trapped for $\phi > 0.58$ and this phase is called glass. The thermodynamically

equilibrium state is a fcc crystal at $\phi_{fcc} = 0.74$ where the particles have maximum closed packed. On the other hand polydispersity in the colloidal particles modifies the phase diagram (Pusey *et al.*, 2009; Zaccarelli *et al.*, 2009). In fact experiments, theory and simulations suggest that colloidal suspensions below glass transition, with particle size polydispersity $\sigma > 12\%$, does not crystallize (Phan *et al.*, 1998; Pusey *et al.*, 2009) but hard sphere glasses was observed to crystallize in microgravity (Zhu *et al.*, 1997). Fig. 1.1 also indicates the phase diagram for 10% polydisperse system. When $\phi > 0.494$, particles form loose cages indicating a supercooled liquid regime. Further increasing ϕ the system reaches a disordered and amorphous phase called glass where caging of the particle by entropic constraints becomes dominant feature. The upper limit after this phase is the random closed packing ϕ_{rcp}. ϕ_{rcp} also depends on the polydispersity of the colloidal particles (Hermes and Dijkstra, 2010; Schaertl and Sillescu, 1994).

Solvent affects the suspension by modifying the interparticle interaction between colloidal particles. For example a refractive index mismatch between the colloidal particles and solvent can induce van der Waals attraction. Undesirable development of interaction potential can be avoided by mixing two solvents of different refractive indices which enables matching of the refractive index with the colloidal particle. Additionally, this kind of index matched suspensions are ideal candidates for performing single scattering light scattering experiments in very high ϕ. Furthermore, density mismatch between the colloidal particle and solvent changes effect of gravity on the colloidal suspension, sedimentation of the colloidal particles occur if the suspension is left undisturbed for long time periods. This leads to the conclusion that solvent choice should not be overlooked.

1.3   Hard Sphere Colloidal Glass

The sterically stabilized samples were utilized to develop a phase diagram with Light Scattering techniques as early as 1980's (Pusey and Van Megen, 1986;

Pusey and van Megen, 1987).
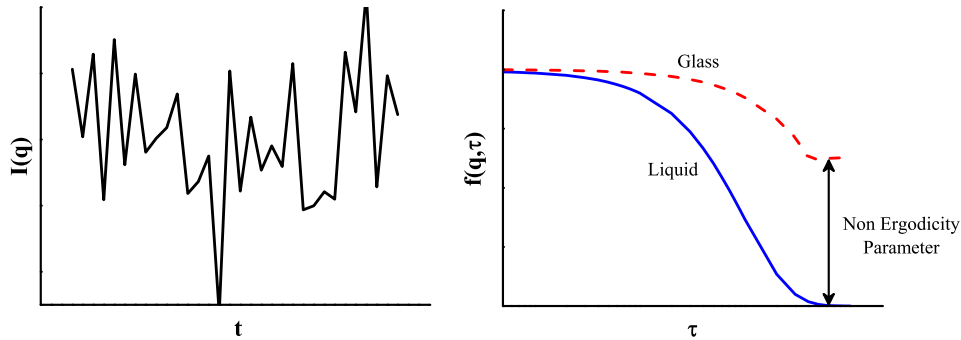
Figure 1.2: (a) Density fluctuations captured by intensity variations with time during light scattering (b) the auto correlation function compared for a liquid and glass.

In Fig. 1.2 Intermediate Scattering Functions (ISF) $f(q, \tau)$ are shown from Dynamic Light Scattering experiments (Berne and Pecora, 1976) which indicate the decay of random density fluctuations with time for hard sphere colloidal suspensions. (Brambilla *et al.*, 2009; Masri *et al.*, 2009; van Megen and Underwood, 1994). The length scale measured is defined as $2\pi/q$. At low volume fractions the density fluctuations decay completely to zero, $f(q, \infty) = 0$, this is thermodynamically called an ergodic state. When the colloidal suspension are dilute, the ISF can be fitted with a single exponential decay function. As ϕ is increased such that the system approaches a liquid crystalline or super-cooled liquid the ISF exhibits two separate exponential decays functions. The first relaxation is the β relaxation which corresponds to the rattling of the particle within the cage. The second longer relaxation time corresponds to the α relaxation which corresponds to the particle escaping the cage and particles need to cooperate with its neighbours to rearrange themselves. Hence particles exhibit cooperative motion in the glass phase. Both the α and β relaxation are found to be functions of ϕ (Brambilla *et al.*, 2009; Lu *et al.*, 2016; van Megen *et al.*, 1998). In a non-ergodic state, colloidal glass, the ISF parameter does not decay fully for the experimental time scale due to 'structural-arrest' observed and corroborated with theory and simulations(Pusey and van Megen, 1987). It has been

found that ISF always has a finite value $f(q, \infty) > 0$. This finite value is termed the 'non-ergodicity parameter' which increases with ϕ as shown in Fig. 1.2. In this regime β relaxation still exists while the α relaxation moves into extremely long timescales a signature of almost frozen cages. Light scattering experiments were probed for eight decades in time to extract non-ergodicity parameter (van Megen and Underwood, 1994; van Megen *et al.*, 1991). Above glass transition, the effects on α relaxation time during aging, thermal variations and settling has been studied (Masri *et al.*, 2009). There still exists debate over the exact glass transition ϕ (Brambilla *et al.*, 2010*a*,*b*, 2009; Reinhardt *et al.*, 2010; van Megen *et al.*, 1998; van Megen and Williams, 2010). But the consensus is that beyond $\phi \equiv 0.59$ the system exhibits solid like response due to frozen cage although dynamic heterogeneities related with rare events and cooperative particle motion exist.

In colloidal glasses, where the particles are trapped by their neighbours, it was observed that a fraction of the particles exhibit non Gaussian behaviour (Kasper *et al.*, 1998; Marcus *et al.*, 1999) leading to the advent of temporal and spatial heterogeneities in these systems. Here particles rattle within the cages formed by its neighbours for certain amount of time. After some time cage hopping is observed forcing the particles diffuse and undergo cage rearrangements in the region around the particle that hopped its cage. This is a process by which the particles can diffuse in a cooperative motion. It was later confirmed that these non-Gaussian distribution or string like motion was directly related to spatial heterogeneities existing in colloidal glass like sample (Kegel and van Blaaderen, 2000) which was also suggested by simulations (Donati *et al.*, 1998; Kob *et al.*, 1997; Perera and Harrowell, 1999). Furthermore in confoca; experiments, two kinds of particles motions were observed slow and fast below the glass transition. The fast moving particles were correlated spatially (Weeks *et al.*, 2000). On approaching glass transition these domains of slow and fast moving particles grew in size but spatial correlation decreased (Weeks and Weitz, 2002*a*,*b*). Moreover the "caging" was also quantified by confocal microscopy experiments (Weeks and Weitz, 2002*b*). Surprisingly, spatially heterogeneous dynamics was found to be independent of the waiting time (Weeks

and Weitz, 2002*a,b*). The slow moving particles were found to contribute toward bulk elasticity (Conrad *et al.*, 2006) and the the dynamic heterogeneities were found to be a universal phenomenon in glassy materials (Chaudhuri *et al.*, 2007). Fast confocal microscopy was utilized to understand supercooled colloidal suspensions under shear. Spatial heterogeneous dynamics was observed with particles rearranging in localized regions and these regions was isotropically present in the sample under shear (Chen *et al.*, 2010). Molecular dynamics simulations also confirmed the existence of spatial correlations in mobility of particles in a glass former Lennard-Jones liquid (Donati *et al.*, 1998, 1999; Kob *et al.*, 1997).

On the other hand, light scattering techniques did find a universal dependence of slow dynamics with aging time (Cipelletti *et al.*, 2003*b*). Clever modification of light scattering techniques enabled to identify dynamic heterogeneities with parameter like multipoint susceptibility, χ_4, and four point correlation function, G_4, (Berthier *et al.*, 2005; Cipelletti *et al.*, 2003*a*; Duri *et al.*, 2009). Employing BD simulations, a four point correlation density function was defined and studied for binary mixture of Lennard-Jones fluid in order to investigate dynamical heterogeneities (Glotzer *et al.*, 2000; Lačević *et al.*, 2003). Recently a linear correlation between dynamical and spatial heterogeneities was established for colloidal glasses (Golde *et al.*, 2016). Free volume of hard sphere colloidal suspensions near glass transition was calculated using Monte Carlo simulations and the excess chemical potential was derived (Sastry *et al.*, 1998). Furthermore, thermodynamic parameters like free energy in colloidal suspensions below and above glass transition have also been obtained from confocal microscopy. A decrease in free energy with waiting time was observed in a colloidal glass (Dullens *et al.*, 2006; Zargar *et al.*, 2013).

Detailed reviews of hard sphere colloidal suspensions specifically on amorphous glass phase are available (Brader, 2010; Cipelletti and Ramos, 2005; Cipelletti and Weeks, 2011; Hunter and Weeks, 2012; Joshi, 2014). Such a large interest in these very systems is driven mainly by the simplicity and well defined nature of nearly hard sphere interaction (Bryant *et al.*, 2002) in between

the particles which helps in performing intense simulations. Furthermore, the availability, size range and time scales of the colloidal particles make them appropriate candidates for investigating phase behaviour with optical microscopy, light scattering and rheometry.

A lot of open questions remain in the fundamental aspects of flow in colloidal glasses which is addressed in this thesis. We try to explore the yielding properties of colloidal glass under flow with the aid of rheology and simulations. The bulk response of the system under flow and the microscopic dynamics of particles in the glass under shear are extracted. Additionally, microscopic insights are provided for different types of glasses present in bidisperse colloidal systems.

CHAPTER 2

SYSTEMS AND TECHNIQUES

2.1   Sterically Stabilized PMMA spheres

Poly(methyl methacrylate)(PMMA) colloidal spheres steric stabilized with poly-(12 hydroxystearic acid)(PHSA) hairs of $\approx 10 \ nm$ (Antl *et al.*, 1986; Barrett, 1973, 1975; Napper, 1983) are found to be model systems that behave like hard spheres (Bryant *et al.*, 2002; Ottewill and Williams, 1987; Poon *et al.*, 2012; Royall *et al.*, 2013; Underwood *et al.*, 1994). Refractive index mismatch between the solvent and colloidal particle can induce van der Waals interaction or there could be a presence of inherent electrostatic potential due to the dielectric constant of the solvent which can be generally ignored for organic solvents (Royall *et al.*, 2013). The side effect of mixing two solvents is that PMMA spheres tend to swell in the presence of certain solvents like Cyclohexyl Bromide and Bromonapthalene which modifies the inter particle from hard sphere to soft sphere (Poon *et al.*, 2012). In this thesis two distinct solvents have been used refractive index matched Octadecene and Bromonapthalene mixture and Squalene. Both these solvents have been selected because they have minimal van der Waals force. But there exists a density mismatch($\rho_{colloid} > \rho_{solvent}$) in between the solvent and colloidal particles. The density mismatch is manipulated to bring the colloidal suspension to random closed packing, ϕ_{rcp}, by employing centrifugation. This helps in solvent exchange and cleaning of the colloidal suspensions. Two distinct phases are obtained after centrifugation of the colloidal suspension : random closed packed colloids and supernatant solvent ,which is discarded. The random closed packed colloids are assumed have a specific value for ϕ_{rcp} based on the polydispersity of the colloids (Schaertl and Sillescu, 1994). The random closed packed sample is diluted to the required colloidal glass concentration. Although it has been estimated that determination of ϕ_{rcp} is always bound to have 3% error that is unavoidable (Poon *et al.*, 2012).

Volume fraction for the colloidal glasses for dilution and concentration was based on the following equation

$$\phi = \phi_o \left[1 + \frac{m_s}{m_c} \left(1 + \frac{\phi_o(\chi - 1)}{1 + \alpha\chi} \right) \right]^{-1} \tag{2.1}$$

where ϕ is the volume fraction to be calculated, ϕ_o is the present volume fraction, m_s is the mass of the solvent to be added to go from ϕ_o to ϕ, m_c is the mass of the colloidal suspension, $\chi = \rho_c/\rho_s$ is the ratio of density of the colloid to the density of the solvent, α is the parameter that is introduced because the PHSA stabilizing layer will have solvent in between them. The parameters used in this thesis are $\rho_{colloid} = 1.188 \, g/cm^3$, $\rho_{octadecene} = 0.789 \, g/cm^3$, $\rho_{bromonapthalene} = 1.47 \, g/cm^3$, $\rho_{squalene} = 0.858 \, g/cm^3$ and $\alpha = 0.12$ (Koumakis, 2011) .

2.2 Rheology Fundamentals

2.2.1 Simple Shear

Consider a simple flow condition as seen in Fig . 2.1 where an ideal fluid exists in between two infinite long plates. The top plate is moving with a velocity V_x and the bottom plate is stationary. The velocity at the top layer is such that $v_x = V_x$ and the bottom plate has 0 velocity. This is called the "no-slip" condition. The two plates are separated by a distance d. The velocity gradient along the y-axis is constant in this condition and is given by

$$\frac{dv_x}{dy} = V/d = \dot{\gamma} = \frac{d\gamma}{dt} = constant \tag{2.2}$$

where $\dot{\gamma}$ is the shear rate and γ is the strain.

In order to move the top plate a force F_x needs to be applied on it. The force required to move the plates with velocity V will be proportional to the surface area of the plates. Hence we can define shear stress σ_{xy} which is the
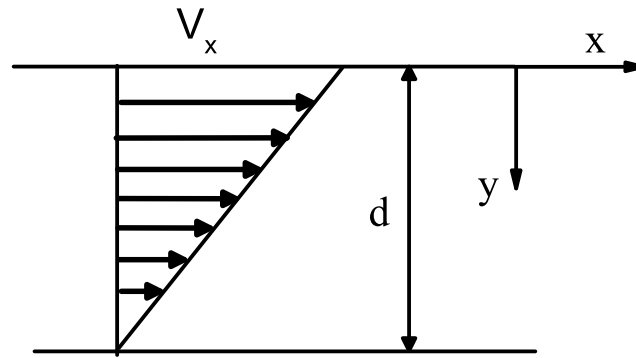
Figure 2.1: An ideal velocity profile for an ideal fluid flow in between two infinitely long plates. The top plate moving with velocity V_x and the bottom plate is stationary. The two plates are separated by a distance d

force applied per unit area with x denoting the direction of shear stress and y denoting the plane normal to which the force is acting. In an ideal liquid the velocity gradient or shear rate determines the internal stresses. According to Newton's constitutive equation for fluids the stress is proportional to the shear rate and the proportionality constant determines the viscosity of the fluid.

$$\sigma_{xy} = \eta \frac{dv_x}{dy} \tag{2.3}$$

If the ideal liquid is replaced by an ideal elastic solid Hooke's law is applicable. The shear stress is proportional to the strain or the deformation and the proportionality constant is the shear modulus of the solid.

$$\sigma_{xy} = G \frac{dx}{dy} \tag{2.4}$$

Eqs. 2.3 and 2.4 are valid for one dimensional case. The real world problem is a three dimensional vector field where the velocity $v(\mathbf{r})$ is defined for each position $\mathbf{r}(x, y, z)$ with velocity components (v_x, v_y, v_z). Here x is the flow direction, y is the velocity gradient direction and z is the vorticity direction.

The velocity gradient in three dimensions is thus defined as

$$\nabla v = \begin{pmatrix} \frac{\delta v_x}{\delta x} & \frac{\delta v_x}{\delta y} & \frac{\delta v_x}{\delta z} \\ \frac{\delta v_y}{\delta x} & \frac{\delta v_y}{\delta y} & \frac{\delta v_y}{\delta z} \\ \frac{\delta v_z}{\delta x} & \frac{\delta v_z}{\delta y} & \frac{\delta v_z}{\delta z} \end{pmatrix} \tag{2.5}$$

Then, the rate of strain tensor $\mathbf{D}$ is defined as

$$\mathbf{D} = (\nabla v + \nabla v')/2 \tag{2.6}$$

$$\mathbf{D} = \begin{pmatrix} \frac{\delta v_x}{\delta x} & \frac{1}{2}\left(\frac{\delta v_x}{\delta y} + \frac{\delta v_y}{\delta x}\right) & \frac{1}{2}\left(\frac{\delta v_x}{\delta z} + \frac{\delta v_z}{\delta x}\right) \\ \frac{1}{2}\left(\frac{\delta v_y}{\delta x} + \frac{\delta v_x}{\delta y}\right) & \frac{\delta v_y}{\delta y} & \frac{1}{2}\left(\frac{\delta v_y}{\delta z} + \frac{\delta v_z}{\delta y}\right) \\ \frac{1}{2}\left(\frac{\delta v_z}{\delta x} + \frac{\delta v_x}{\delta z}\right) & \frac{1}{2}\left(\frac{\delta v_z}{\delta y} + \frac{\delta v_y}{\delta z}\right) & \frac{\delta v_z}{\delta z} \end{pmatrix} \tag{2.7}$$

From Eq. 2.3 the stress is modified to

$$\sigma_{xy} = \eta \dot{\gamma}_{xy} \ where \ \dot{\gamma}_{xy} = 2D_{xy} \tag{2.8}$$
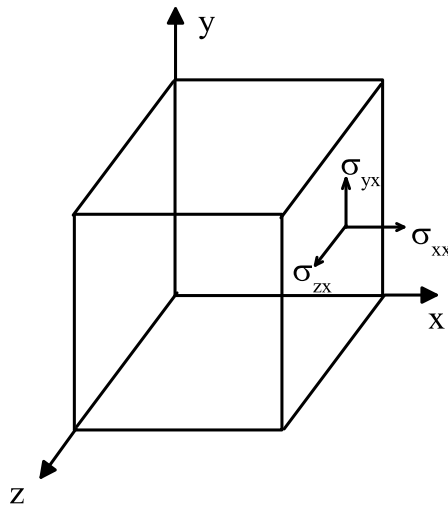
Figure 2.2: The stress components in three dimensional space

Expanding the stress tensor we obtain

$$\sigma_{ij} = \begin{pmatrix} \sigma_{xx} & \sigma_{xy} & \sigma_{xz} \\ \sigma_{yx} & \sigma_{yy} & \sigma_{yz} \\ \sigma_{zx} & \sigma_{zy} & \sigma_{zz} \end{pmatrix} \tag{2.9}$$

As observed in Fig. 2.2 the first index indicates the direction of stress and the second index depicts the normal to the plane on which the stress acts. The diagonal stress components σ_{ij} are the normal stresses and the off diagonal elements which are oriented in the plane that is considered is called shear stresses. Generally for ordinary fluids the stress matrix is symmetric around its diagonal elements such that $\sigma_{ij} = \sigma_{ji}$.

Finally the Newton's constitutive equation for fluids (Eq. 2.3) in tensorial notation can be written as

$$\boldsymbol{\sigma} = -P\mathbf{I} + 2\eta\mathbf{D} \tag{2.10}$$

where $\mathbf{I}$ is an identity tensor, P is the pressure with negative sign indicating the notation norm and $\boldsymbol{\sigma} + P\mathbf{I}$ is termed the extra stress or deviatoric stress. The diagonal elements in the extra stress components are zero for Newtonian fluids. In a viscoelastic sample there exist shear stress as well as the normal components which are defined as first and second normal stress an given by the following equation

$$N_1 = \sigma_{xx} - \sigma_{yy}$$
$$N_2 = \sigma_{yy} - \sigma_{zz} \tag{2.11}$$

2.2.2 Oscillatory shear

Fig. 2.1 is an ideal case which is used for deriving the fundamentals of rheology and understanding the basic concepts of rheometry. A different kind of flow profile can be applied to the top moving plate namely oscillatory. In this profile

the strain applied is as seen in Fig .2.3 (a) which is can mathematically expressed as

$$\gamma = \gamma_o \sin(\omega t) \tag{2.12}$$

where ω is the frequency of oscillation, t is time of oscillation and γ_o is the maximum amplitude of strain. The shear rate is defined as derivative of strain

$$\frac{d\gamma}{dt} = \dot{\gamma} = \frac{d(\gamma_o \sin(\omega t))}{dt} = \gamma_o \omega \cos(\omega t) = \dot{\gamma}_o \cos(\omega t) \tag{2.13}$$

where $\dot{\gamma}_o$ is maximum amplitude of shear rate within a cycle as seen in Fig. 2.3 (a).

(a)   (b)
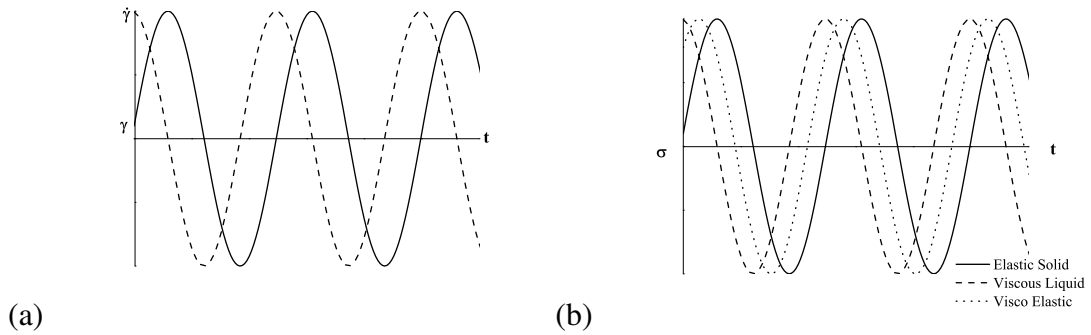
Figure 2.3: (a) Strain and shear rate during oscillatory shear and (b) Stress response for the oscillatory strain for ideal elastic solid, viscous fluid and a visco-elastic material

In the case of an ideal elastic solid which follows Hookes law, $\sigma = G\gamma$ the stress response will be

$$\sigma(t) = G\gamma(t) = G\gamma_o \sin(\omega t) \tag{2.14}$$

On the other hand for a Newtonian fluid as mentioned earlier, $\sigma = \eta\dot{\gamma}$ then oscillatory response will be

$$\sigma(t) = \eta\dot{\gamma}(t) = \eta\dot{\gamma}_o \cos(\omega t) \tag{2.15}$$

which shows that there exists a phase difference of 90° between an ideal elastic solid and Newtonian fluid. All soft material investigated exhibit both elastic and viscous characteristics that can be quantified by probing the system using oscillatory shear. So for a viscoelastic material one can write the stress response as a function of strain as follows

$$\sigma(t) = \sigma_o \sin(\omega t + \delta) \tag{2.16}$$

where δ is the phase angle difference between the stress and the applied oscillating strain. Expanding Eq. 2.16

$$\sigma(t) = \gamma_o \Big(\frac{\sigma_o \cos \delta}{\gamma_o} \sin(\omega t) + \frac{\sigma_o \sin \delta}{\gamma_o} \cos(\omega t) \Big) \tag{2.17}$$

Eq . 2.17 is made a function of the strain and the strain rate which aids in extraction of the storage modulus, G', and loss modulus, G'' which are defined as follows.

$$G' = \frac{\sigma_o \cos \delta}{\gamma_o} \tag{2.18}$$

$$G'' = \frac{\sigma_o \sin \delta}{\gamma_o} \tag{2.19}$$

The loss tangent is defined as the ratio of the loss modulus to the storage modulus and given by the following equation

$$\tan \delta = \frac{G''}{G'} \tag{2.20}$$

Also the storage and loss modulus can be written as real and imaginary parts of the complex moduli, G^*

$$G^*(\omega) = G'(\omega) + iG''(\omega) \tag{2.21}$$

Hence oscillatory shear helps in extracting the elastic viscous components of the viscoelastic samples. It should be noted that all the above equations are valid only if the amplitude of γ_o is small or in the linear regime of shear. In case of large amplitude of γ_o the above definition for storage and loss moduli will not be sufficient and other representation methods are required Ewoldt *et al.* (2008); Hyun *et al.* (2011); Jacob *et al.* (2014); Poulos *et al.* (2013); Rogers *et al.* (2011). More details on fundamentals of rheology can be found in popular and commonly prescribed books (Barnes *et al.*, 1989; Macosko, 1994; Morrison, 2001).

2.3 Rheometry

2.3.1 Cone and Plate

Cone and Plate is one of the most commonly used geometries in rheometry for suspension rheology because the velocity is constant all along the geometry. In Fig . 2.4 (a) When the angle α is small the shear rate depends on the tangential velocity and the local distance between the plates.

$$\dot{\gamma} = \frac{\omega}{\alpha} \quad where \ \alpha <= 0.1 rad \tag{2.22}$$

here ω is the rotational speed in rad/s^{-1} and α is the angle of the cone in rad. The shear stress of a cone and plate arrangement is calculated as

$$\sigma = \frac{3\tau}{2\pi R^3} \tag{2.23}$$

where τ is torque experienced by the geometry and R is the radius of the geometry. The first normal stress difference is calculated as

$$N_1 = \frac{F_N}{\pi R^2} \tag{2.24}$$

where F_N is the normal force acting on the plates.

(a)   (b)
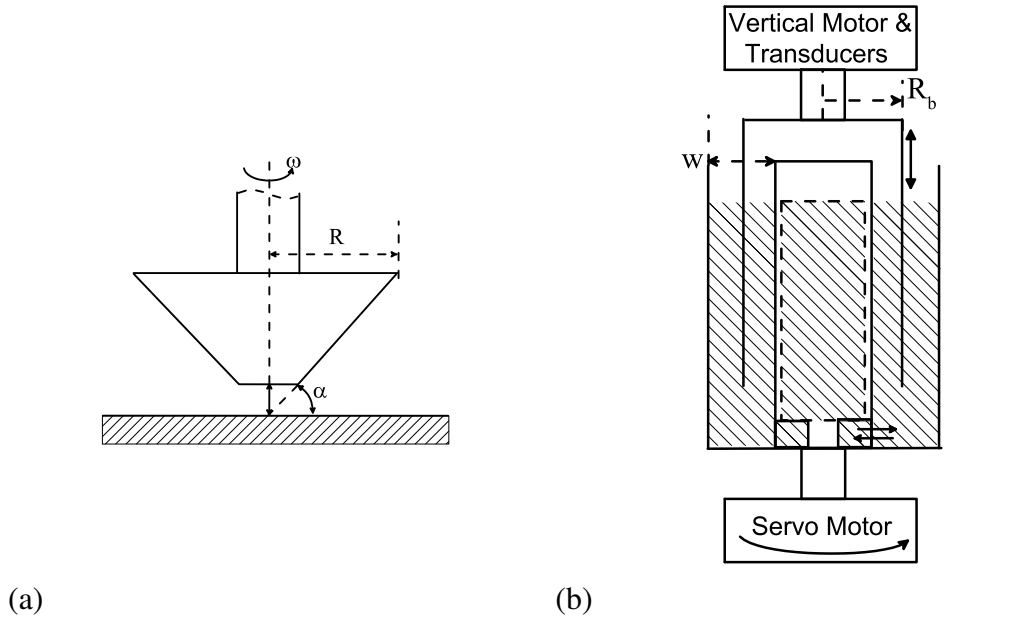
Figure 2.4: (a) Cone and plate geometry (b) Double wall Couette geometry used for orthogonal superposition

2.3.2 Orthogonal Superposition Setup

Fig . 2.4 (b) shows the schematic of a double-wall Couette geometry which was used in the orthogonal superposition measurements in this thesis (Vermant *et al.*, 1997). This geometry has two motors one in the horizontal direction and the second motor in the vertical direction. The horizontal motor performs shear experiments similar to an ordinary Couette geometry. The vertical motor imposes only oscillation in the vertical direction. The horizontal and vertical transducers are separate and housed in the top part of the system. The inner cylinder of the double walled Couette acts as a reservoir for the sample removing all instabilities arising due to the vertical oscillation. The hatched regions in Fig. 2.4 (b) indicates the volume occupied by the sample. The orthogonal storage and loss moduli are calculated by the following equations

$$G' = \frac{1}{A}\left(\frac{F_o}{z_o}\cos\phi - K + (m + \beta A\rho)\omega^2\right) \qquad (2.25)$$

$$G'' = \frac{1}{A}\left(\frac{F_o}{z_o}\sin\phi - \xi\omega)\right) \tag{2.26}$$

The geometric factors A and β are defined as follows:

$$A = \frac{4\pi h}{\ln(\frac{R_b}{R_a})} \tag{2.27}$$

$$\beta = \frac{R_b^2}{2}\left(\frac{(\frac{R_b}{R_a})^2 - 1}{2\ln(\frac{R_b}{R_a})} - \left[1 + \ln\left(\frac{R_b}{R_a}\right)\right]\right) \tag{2.28}$$

where R_b is the average radius of the oscillating cylinder, $R_a = R_b - w$ and w is the width of the gap. F_o/z_o is the force amplitude divided by the height amplitude of the oscillating cylinder and ϕ is the phase difference between the strain input and stress output in the vertical direction. Finally, m,K and ξ are the parameters describing the vertical transducer.

2.4 Brownian Dynamics Simulations

A particle suspended in a fluid medium will exhibit Brownian motion (Einstein, 1905). Other than Brownian motion the particle also experiences viscous drag from the suspended fluid. Additionally, deterministic external forces also acts on the particle when the whole system flows. All these forces acting on the particle are governed by momentum balance equation. Here, the viscous medium is assumed to be a continuum but the particles are larger than the viscous molecules such that there is a clear separation between length scales and timescales.

If the system as N inelastic particles of radius R and mass m a N-body Langevin equation can be written as follows

$$m\frac{d\mathbf{U}}{dt} = \mathbf{F}^B + \mathbf{F}^H + \mathbf{F}^P \tag{2.29}$$

where Eq . 2.29 m indicates the generalized mass of the particles, $\mathbf{F^B}$ is

the stochastic/Brownian force vector, $\mathbf{F^H}$ viscous drag vector and $\mathbf{F}^P$ is the deterministic non hydrodynamic force vector (Russel *et al.*, 1989).

Since inertial forces are assumed to be trivial, $m \to 0$ in colloidal dispersions thus Reynolds number is assumed to be much less than $1(Re << 1)$. Then Left Hand Side $\to 0$ in Eq. 2.29. Thus,

$$0 = \mathbf{F}^B + \mathbf{F}^H + \mathbf{F}^P \tag{2.30}$$

$\mathbf{F}^B$ in Eq. 2.30 is the Brownian force vector that the particle experiences which is a stochastic process. According to fluctuation-dissipation theorem (Kubo, 1966)

$$\langle \mathbf{F}^B(t) \rangle = 0$$
$$\langle \mathbf{F}^B(t)\mathbf{F}^B(\Delta t) \rangle = 2k_B T(6\pi\eta_s R)\mathbf{I}\delta(\Delta t) \tag{2.31}$$

where $\langle \rangle$ denote average over all fluctuations in a fluid with thermal energy $k_B T$, $\delta(t)$ is the Dirac delta function, $\mathbf{I}$ is a unit second order tensor, $6\pi\eta_s R$ is the drag coefficient and Δt is the time step for the simulation. The stochastic process should be random in direction and magnitude as two different particles should have uncorrelated motion. Additionally, the kinetic energy of the particle is equally divided in three directions.

In Eq . 2.30 $\mathbf{F}^H$ is defined as Stokes Drag Force

$$\mathbf{F}^H = -6\pi\eta_s R\mathbf{U} \tag{2.32}$$

where $\mathbf{U}$ is the translational velocity vector on the particle. The negative sign indicates that it acts in opposite direction to the motion of the particle. The Stokes drag force is a very simplified assumption of hydrodynamic interactions. In an actual scenario a particle that moves in a viscous fluid interacts with the viscous drag of other particles due to the wake created by the particles in motion. In BD simulations it is assumed the above case is not valid. In order to

have all the hydrodynamic interactions it is computationally exhaustive. Thus it is preferable to perform Stokesian dynamics simulations (Brady and Bossis, 1988).

In Eq . 2.30 $\mathbf{F}^P$ is defined as

$$\mathbf{F}^P = \mathbf{F}^{HS} + \mathbf{F}^{Pe} \tag{2.33}$$

where $\mathbf{F}^{HS}$ is the inter particle hard sphere potential and $\mathbf{F}^{Pe}$ is the deterministic force vector on particles. In the simulations performed in this thesis a "potential free" algorithm is employed where the overlaps between the particles is considered as a collision (Heyes and Melrose, 1993). This potential free algorithm for BD simulations has been extensively used for colloidal hard sphere suspensions (Foss and Brady, 2000; Koumakis *et al.*, 2013, 2012*a*, 2016*b*) and colloidal crystals (Koumakis *et al.*, 2016*a*). More complex potential can be added into Eq. 2.33 such the Asakura-Oosawa potential (Asakura and Oosawa, 1954, 1958) which has recently been extensively used in BD simulations to simulate model colloidal depletion gels (Koumakis *et al.*, 2015; Moghimi *et al.*, under review; Moghimi and Petekidis, in preparation). Other potential like Derjaguin Landau Verwey Overbeek (DLVO) (Russel *et al.*, 1989) or Lennard Jones potential (Allen and Tildesley, 1989) can also be applied depending on the inter-particle potential to be simulated. $\mathbf{F}^{Pe}$ corresponds to simple shear flow in this thesis.

The particle evolution equation is obtained by integrating Eq. 2.30 twice over a time step Δt as follows

$$\Delta\mathbf{x}(\Delta t) = \Delta\mathbf{x}(t) + \Delta\mathbf{x}^B(\Delta t) + \Delta\mathbf{x}^{Pe}(\Delta t) \tag{2.34}$$

where $\Delta \mathbf{x}^B(\Delta t)$ is defined as

$$\langle \Delta \mathbf{x}^B(t) \rangle = 0$$

$$\langle \Delta \mathbf{x}^B(t) \Delta \mathbf{x}^B(t + \Delta t) \rangle = 2D\mathbf{I}\Delta t \qquad (2.35)$$

$$D = \frac{k_B T}{6\pi \eta_s R}$$

where D is the translational diffusion coefficient, η_s is the viscosity of the suspending medium. The stochastic Brownian motion should give a displacement of $\sqrt{2D\Delta t}$. The random displacements are picked from a random vector $\mathbf{\Psi}$. Each element in $\mathbf{\Psi}$ is selected from a uniform distribution of random numbers ranging from -1 to 1 with a mean value 0. This leads to an equation

$$\Delta \mathbf{x}^B(\Delta t) = \sqrt{2\Delta t} \mathbf{\Psi} \sqrt{3} \qquad (2.36)$$

which produces a Gaussian distribution after a few time steps. In Eq. 2.34 $\Delta \mathbf{x}^{Pe}(\Delta t) = Pe\mathbf{y}\Delta t$ since the shear rate gradient is only in the x-direction alone. $\mathbf{y}$ is the position of the particles in the y-direction. Another assumption to obtain Eq. 2.34 is that rotational and translational motions are decoupled. $\mathbf{X}$ is made non-dimensionless by the radius R and the time in the simulation by the Brownian time $t_B = R^2/D$ and velocity $\mathbf{U}$ by D/R.

Thus the displacements in all three dimensions can be written as follows

$$\Delta \mathbf{x}_x = \sqrt{2\Delta t} \mathbf{\Psi} \sqrt{3} + Pe\mathbf{y}\Delta t$$

$$\Delta \mathbf{x}_y = \sqrt{2\Delta t} \mathbf{\Psi} \sqrt{3} \qquad (2.37)$$

$$\Delta \mathbf{x}_z = \sqrt{2\Delta t} \mathbf{\Psi} \sqrt{3}$$

In case of steady simple shear

$$\Delta \mathbf{x}^{Pe} = \mathbf{y}\Delta t \qquad (2.38)$$

and for oscillatory shear

$$\gamma = \gamma_o \sin(Pe_\omega t)$$

$$\Delta \mathbf{x}^{Pe} = Pe_\omega \gamma_o \cos(Pe_\omega t)\mathbf{y}\Delta t \qquad (2.39)$$

$$Pe_\omega = \frac{\omega R^2}{D} = \frac{2\pi t_B}{T}$$

where γ_o is the peak of the amplitude of shear and ω is the frequency of oscillation. Simple and oscillatory shear are related such that $Pe = \gamma_o Pe_\omega$.

In each time step the algorithm calculates the pairwise inter particle forces that would result in hard sphere displacements. From Eq. 2.30 equating the interparticle force with hard sphere displacement we get in dimensional form

$$\mathbf{F}^P = 6\pi\eta_s R\frac{\Delta \mathbf{x}}{\Delta t} \qquad (2.40)$$

The total stress can be calculated by knowing the interparticle forces from each collision. Thus the bulk stress can be defined as total stress per unit volume for N particles (Foss and Brady, 2000).

$$\langle \boldsymbol{\sigma} \rangle = -\langle p \rangle_f \mathbf{I} + 2\eta_s(1 + \frac{5}{2}\phi)\langle \mathbf{D} \rangle - Nk_BT\mathbf{I} - N\langle \mathbf{x}\mathbf{F}^P \rangle \qquad (2.41)$$

where $\langle p \rangle_f$ is the average fluid pressure, $-Nk_BT\mathbf{I}$ is the isotropic pressure due to Brownian thermal motion, $2\eta_s(1 + \frac{5}{2}\phi)\langle \mathbf{D} \rangle$ is the hydrodynamic contribution to the stress that reduces to the single particle Einstein correction, $\langle D \rangle$ is the rate of strain tensor. The rheological contribution of the stress is obtained from $\langle \mathbf{x}\mathbf{F}^P \rangle$. The contribution for all particles to the stress is calculated as

$$\sigma_{xy} = \sum_{1}^{N} -\frac{r_i^x \Delta y_i^{HS}}{V\Delta t} \qquad (2.42)$$

Additionally these simulations include Periodic Boundary Conditions to mimic an infinitely large system that avoids surface and size effects. The simulation

volume is divided into small cells with length of each cell at least the size of the interaction. The advantage is two fold, one this system is computationally more efficient than that picking each and every particle and checking all its neighbours. The second advantage is that none of the particles will be missed out in the simulation.
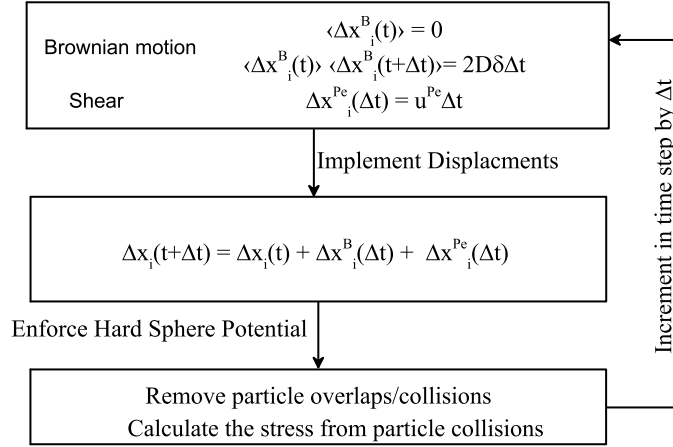
Figure 2.5: Algorithm for the Brownian Dynamics simulations with hard sphere potential employed to simulate colloidal glasses

The BD algorithm used in this thesis is represented as shown in Fig. 2.5. Initially the N particles are placed randomly in a volume V based on the volume fraction ϕ required then the particle overlaps are removed. The cell list is made and each particle is given the address of the cell list. In the first time step increment, displacements for Brownian and shear motion are implemented on all the particles. The each cell is stepped through systematically in order to count the particle overlaps, calculate the stress from Eq. 2.42 and remove the overlaps. The time step is incremented and the whole process is repeated by implementing Brownian and shear displacements on the particles.

The pair distribution function is defined as follows

$$g(r, \mathbf{r}_{ab}) = \frac{V}{4\pi r^2 N_a N_b} \left\langle \sum_{i=1}^{N_a} \sum_{j=1}^{N_b} \delta\big(r - |\mathbf{r}_i(t) - \mathbf{r}_j(t)|\big) \right\rangle_t \qquad (2.43)$$

where N_a and N_b are number of particles, r is the examined pair distance, $\mathbf{r}_i$ and $\mathbf{r}_j(t)$ are the position vectors for the ith and j^{th} particle respectively. The pair distribution function is defined as the probability for finding a particle at a distance r.

The mean square displacement is statistical measure for a particle that has moved a specific distance in a specific time. The MSD in the x-direction is given as follows

$$\left\langle \Delta x^2(\Delta t) \right\rangle = \left\langle \frac{1}{N} \sum_{i=1}^{N} [x_i(t+\Delta t) - x_i(t)]^2 \right\rangle_{\Delta t} \tag{2.44}$$

where x_i is the non affine position calculated by subtracting the affine shear component. Moreover, x_i can be substituted for y_i and z_i for different directions.

Finally the average MSD in the radial direction is calculate as follows

$$\left\langle \Delta r^2(\Delta t) \right\rangle = \left\langle \Delta x^2(\Delta t) \right\rangle + \left\langle \Delta y^2(\Delta t) \right\rangle + \left\langle \Delta z^2(\Delta t) \right\rangle \tag{2.45}$$

The two time particle displacement is calculated is obtained by modifying the above equations as follows

$$\left\langle \Delta z^2(\Delta t, t_w) \right\rangle_N = \frac{1}{N} \sum_{i=1}^{N} \left[\left(y_i(t_w+\Delta t) - y_i(t_w) \right) - \frac{1}{N} \sum_{i=1}^{N} \left[\left(y_i(t_w+\Delta t) - y_i(t_w) \right) \right] \right]^2 \tag{2.46}$$

which gives the average displacement between two specific times during shear where $t_w > 0$, is elapsed time from the beginning of shear and t is the absolute elapsed time and $\Delta t = t - t_w$ being the time frame for the displacement.

An example of simulated colloidal glass with particles having a polydispersity of 10% in this thesis is shown in Fig. 2.6. The colour code represents the radius of the particle.
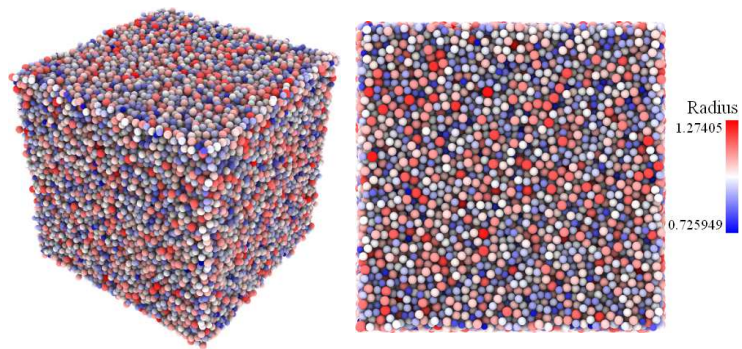
Figure 2.6: Representative image of a colloidal glass obtained from BD simulations in 3D and 2D.

CHAPTER 3

BACKGROUND LITERATURE

3.1 Rheology of Colloidal suspensions

On laboratory scale colloidal suspension have been extensively used to study different phases of matter. Some of the earliest experiments brought out the similarities in colloidal and atomic systems (Hiltner and Krieger, 1969). Mixtures of different sized colloids were found to form 'Wigner Glass' which does not exhibit long range order but shows finite elasticity(Lindsay and Chaikin, 1982). Charged stabilized colloidal suspensions have been utilised as model systems to investigate liquids and crystals (Aastuen *et al.*, 1986; Murray and Van Winkle, 1987; Sirota *et al.*, 1989). One of the model hard sphere system used was silica coated by a stabilizing layer of 1-octadecanol (de Kruif *et al.*, 1985; Helden *et al.*, 1981; Vrij *et al.*, 1983; Wagner and Russel, 1990). Silica sphere suspended in ethylene glycol also interacts like hard sphere (Mason and Weitz, 1995; Shikata and Pearson, 1994). The advent of uncharged sterically stabilized colloidal suspensions as model colloidal systems lead to an enhanced understanding in these systems (Marshall and Zukoski, 1990; Pusey and Van Megen, 1986). Fundamental flow problems in colloidal suspensions and glasses have been addressed with the aid of techniques like confocal microscopy and the easy availability of model hard sphere colloidal systems. Recent advances in this hard sphere model colloidal suspensions are discussed in (Besseling *et al.*, 2009). Detailed information regarding colloidal suspension rheology can be obtained from (Mewis and Wagner, 2012).

Poly-methyl methacrylate particles stabilized with poly-12- hydroxystearic acid have been used as model uncharged colloidal suspensions in rheological measurements as early as 1976. These particles were used to investigate the shear thickening effects in very highly concentrated suspensions (Strivens,

1976). Rheology of high volume fraction dispersions of PMMA spheres were investigated and the effect of hair softness was found to vary with colloidal size. Large particles ($1\mu m$) behaved like hard sphere while small particles ($\approx 100nm$) interacted with a softer potential (Frith *et al.*, 1987; Mewis *et al.*, 1989). Additionally, the expansion coefficient of the spheres where explored with temperature (Frith *et al.*, 1987) and for concentrated hard sphere suspensions the Cox-Merz rule failed (Frith *et al.*, 1990). A scaling equation was proposed such that the plateau moduli, G'_∞, will depend on the inter particle distance in concentrated dispersions and this in turn will help elucidate the inter particle potential that exists in between particles with the help of the following equation.

$$G'_\infty \approx \frac{\phi_{rcp}N_1}{5\pi d_c k_B T}\frac{d^2\Phi}{dr^2}\bigg|_{R_m} \tag{3.1}$$

where ϕ_{rcp} is the random close packing, N_1 is the number of nearest neighbours, d_c is the diameter of the colloid and $\Phi(r)$ is the inter particle potential, R_m is the distance between the nearest neighbours and G'_∞ corresponds to the plateau moduli (Mewis and Haene, 1993). Experimentally, it has been observed that G' near glass transition becomes a power law as function of ϕ and changes slope from 30 to 50 from below to above $\phi = 0.60$ respectively (Koumakis *et al.*, 2012*b*). Furthermore, these sterically stabilized particles were utilised to investigate structures formed under shear during shear thickening using opto-rheological tools (D'Haene *et al.*, 1993) and also to understand the effect of particle size and the solvent effect on shear thickening (Frith *et al.*, 1996). The effect of ionic and non-ionic stabilizing layer on the viscosity and dynamic moduli have also been investigated (Raynaud *et al.*, 1996). Shear induced ordering was found to be more pronounced for oscillatory shear than steady shear in liquids suspensions (Ackerson, 1990; Ackerson and Pusey, 1988). Monodisperse colloidal glass was also observed to crystallize under large amplitude oscillatory shear (Koumakis *et al.*, 2008).

Yield stress is another important characteristic in high volume fraction nearly hard sphere colloidal glass. The yield stress value increases as a function of

ϕ (Koumakis *et al.*, 2012*b*) for hard sphere colloidal glasses. Generally for colloidal glasses the yield stress can be fitted to Herschel-Bulkley model with a power law fit of $\nu = 0.5$. Hard sphere colloidal glasses were classified as thixotropic yield stress material due to the aging of colloidal glasses with help of Brownian motion which was investigated by performing long time creep experiments (Moller *et al.*, 2009).

Smooth surfaces promote slip at low shear rates in colloidal glass (Ballesta *et al.*, 2008, 2012). On the other hand a weak slip was observed for liquid suspensions which lead to the appearance of yield stress plateau. When roughened plates are used at high volume fractions shear banding occurs at very flow rates (Besseling *et al.*, 2010). The stable and unstable region in shear banding was mapped as function of ϕ and $\dot{\gamma}$. Slip and shear bands were also observed in colloidal crystals under oscillatory shear via confocal microscopy (Cohen *et al.*, 2006). Flow profile in square capillary was investigated using confocal microscopy for volume fraction near random closed packing was found to be that close to predicted in granular media(Isa *et al.*, 2007). Velocity profiles of concentrated hard sphere suspensions through microfluidic devices have also been investigated (Isa *et al.*, 2009).

Yielding mechanisms with start-up and oscillatory shear was compared and contrasted with attractive colloidal glasses. In pure repulsive glass, a single yielding process was observed and in attractive process two yielding process was observed (Pham *et al.*, 2008, 2006). the yielding process in pure repulsive glass is related to the distortion of the cages while in attractive process the first yielding occurs due to bond breaking and the second yielding is due to cage breaking. From real time imaging of soft and hard particles and rheology it was elucidated that soft particles show larger length scale cooperative motion than hard spheres. In other words the dynamic susceptibilities for soft spheres is greater than hard spheres for same volume fraction (Rahmani *et al.*, 2012). Below random closed packing it was established that 'cage elasticity' contributes to the viscoelasticity for both hard and soft spheres. Above random close packing for soft spheres the shell elasticity becomes prominent. The yield strain

of hard sphere colloidal glasses obtained from creep and recovery shows a non monotonic response with increase ϕ possibly due to decreasing inter particle potential and increasing effects of the cages (Le Grand and Petekidis, 2008).

The intensity of stress peaks during startup shear was observed to be much stronger for softer particles as a function of ϕ for a specific shear rate (Koumakis *et al.*, 2012*b*). Extensive studies on transient dynamics and yielding of colloidal glasses during start-up shear with rheology, confocal microscopy and simulations provide insights how the cages deform under transient shear and the dependence of microstructure on bulk properties with varying volume fraction, shear rate and aging (Koumakis *et al.*, 2012*a*, 2016*b*; Laurati *et al.*, 2012; Mutch *et al.*, 2013). The short time MSD was found to be smaller during start-up shear than at rest. This was attributed to the cage distortion at short time scales (Koumakis *et al.*, 2012*a*). The effect of aging on the transient start-up shear was also investigated. In general, it was observed that with aging time a colloidal glass system was driven deeper into the solid regime. Aging was found to have a non-trivial dependence for the stress overshoot peak versus ϕ and $\dot{\gamma}$ (Koumakis *et al.*, 2016*b*). The stress overshoot peak and superdiffusive regime became more predominant with $\dot{\gamma}$ (Koumakis *et al.*, 2012*a*; Laurati *et al.*, 2012). A non-monotonic dependence of the stress peak was observed with ϕ (Koumakis *et al.*, 2016*b*). Cessation after steady shear of colloidal glasses lead to the retention of a part of the stresses which was termed as residual stress (Ballauff *et al.*, 2013). The lower shear rates aided in trapping of higher residual stresses than the high shear rates in hard sphere colloidal glass which was corroborated with MCT and simulations.

Strain Rate Frequency Superposition was applied to hard sphere colloidal and it was observed that the relaxation time of the system under shear for a colloidal glass was a linear function of shear rate (Wyss *et al.*, 2007) but this method proven to be wrong. Non-linear oscillatory shear was employed for this superposition which is not the correct approach for superposition to be performed (Erwin *et al.*, 2010*b*). Experiments with confocal microscopy showed that the alpha relaxation time had a sub-linear dependence on the shear rate (Bessel-

ing *et al.*, 2007) while another set of experiments showed a linear dependence (Eisenmann *et al.*, 2010).

Light scattering echo was utilised to understand particle rearrangements in the yielding process under oscillatory shear in polymer stabilized colloidal glass. Low volume fraction glasses were found to exhibit more reversible arrangement than high volume fraction glasses. Additionally, it was was also discerned from creep and recovery experiments that colloidal glasses could store elasticity upto $\gamma = 15\%$ before yielding occurs (Petekidis *et al.*, 2002, 2003). The softness of the cage impacts the yielding of colloidal glasses under oscillatory shear. For hard sphere glasses the yielding happens much earlier than softer glasses because the cage can only be distorted to small values unlike soft systems (Zhou *et al.*, 2014). Large amplitude oscillatory shear (LAOS) has been utilised to understand yielding mechanisms in hard sphere glasses when oscillatory shear is employed. A two-step process yielding was observed where the initial yielding was due to Brownian motion and the second was due to shear-induced collisions depending on the timescale of the system is probed (Koumakis *et al.*, 2013). The $\gamma_{cross}(G' = G'')$ was found to have a non-monotonic dependence on ϕ under oscillatory shear unlike softer systems like PNIPAM microgels and star like micelles (Koumakis *et al.*, 2012*b*). Sequence of Physical Processes(SPP) (Rogers, 2012) was used to understand the yielding process in hard sphere colloidal suspensions and contrast with soft sphere suspensions. The inter particle compliance between the soft spheres was found to be responsible for the delayed yielding and smooth volume fraction dependence with ϕ unlike the hard sphere colloidal suspensions (van der Vaart *et al.*, 2013).

Extensive creep and recovery experiments were performed to characterize colloidal glasses near and above glass transition. Creep is used to study the strain accumulation in colloidal glasses. The presence of high elastic recovery after creep even after flow of samples was attributed to cage elasticity. Additionally, creep below yield stress of hard sphere glasses exhibited very slow accumulation which was speculated to be due to dynamic heterogeneities (Petekidis *et al.*, 2004). Recently the effect of aging hard sphere colloidal glasses

was investigated with creep flow (Ballesta and Petekidis, 2016). The hard sphere colloidal glass was found to exhibit a more solid like response with increasing aging time. Localised events was also found to decrease with increasing aging time. Microscopically creep was observed to activate localized regions in the colloidal glass. These regions grew in size with time of stress application until all the regions merged to start flow. The steady state flow was observed to be similar to that of steady shear rate flow of hard sphere colloidal glasses (Sentjabrskaja *et al.*, 2015). The transient dynamics of highly concentrated hard sphere suspensions under time dependent flow are reviewed in (Brader, 2010; Mutch *et al.*, 2013).

Large size asymmetric binary mixtures of hard sphere are also of interest in order to understand biological systems (Angelini *et al.*, 2011; Ellis and Minton, 2003; Gravish *et al.*, 2015). Sterically stabilized PMMA hard spheres are chosen as model systems to study these binary mixtures. Similar to pure colloidal glasses various techniques like rheology, light scattering and confocal microscopy are utilised to understand the dynamics and mechanical properties of binary colloidal hard spheres at quiescent state and under flow (Sentjabrskaja *et al.*, 2013*a*, 2015, 2014, 2016). Highly anisotropic size mixtures of binary colloidal glass was observed to pass through a liquid phase at intermediate mixing ratios of the binary particles. This was attributed to neither species dominating to form cages in the binary glass mixture. This in turn affected the yielding behaviour of the particles under oscillatory (Sentjabrskaja *et al.*, 2013*a*) and transient shear (Sentjabrskaja *et al.*, 2014). Anomalous diffusion was observed in small particles in colloidal particles based on the matrix that drives caging. If the size ratio between the small to big particles are large the small particles tend to move in localized voids of the big particles (Sentjabrskaja *et al.*, 2016).

The timescale probed in a colloidal suspension can be quantified with the help of Peclet number. Peclet number is a dimensionless number in transport phenomena which is defined as the ratio of advection transport rate to diffusive transport rate. In colloidal suspensions, Peclet number is defined as the product

of rate of shear and the time scale of Brownian diffusion.

$$Pe = \dot{\gamma} t_B \tag{3.2}$$

where t_B is given by

$$t_B = R^2/D = 6\pi\eta_s R^3/k_B T \tag{3.3}$$

where D is the diffusivity and η_s is the viscosity of the solvent. Thus when $Pe < 1$ Brownian diffusion dominates and when $Pe > 1$ shear-induced motion of colloidal particles becomes predominate leading to structural changes. For oscillatory shear Eq. 3.2 is modified as follows

$$Pe_\omega = \omega t_B \tag{3.4}$$

where ω is the frequency of oscillation. The above equation is valid, provided the oscillatory shear is in the linear regime of the material. In a concentrated hard sphere suspension the Brownian time for self diffusion of the particle is much slower than in dilute suspensions due to hydrodynamic effects (Sierou and Brady, 2001). So there exists two definitions for Peclet number. Bare Peclet number which is the Peclet number associated with the corresponding t_B in the dilute suspension regime. Dressed Peclet number which is derived from t_B considering the hydrodynamic interactions. In this thesis we define all Peclet based on bare Peclet number unless otherwise specified. Additionally, in this thesis the volume fraction of colloidal glass ϕ mentioned is obtained by scaling the storage modulus G' at $Pe_\omega = 0.5$ from the already available normalized elastic moduli versus volume fraction master curve for hard sphere colloidal glass (Koumakis *et al.*, 2012*b*).

Theories are essential to predict and design materials that have time dependent response for efficient design of materials and processing parameters. Mode coupling theory (MCT) is extensively used to model hard sphere colloidal sus-

pensions near and above glass transition (Gotze and Sjogren, 1992). It is based on the principle that the colloid is trapped by its neighbours The neighbouring particle does not allow the caged particle to escape which delay the α relaxation which as the neighbouring particles are themselves trapped. For hard sphere particles the glass transition has been found to be at $\phi = 0.525$ for MCT theory while experiments the transition to be around $\phi = 0.58$. A modified model based on MCT was found to capture the rheological behaviour of colloidal suspensions (Mason and Weitz, 1995; Siebenbürger *et al.*, 2009). The Green Kubo based description in theory helped in unified understanding of linear viscoelastic behaviour and diffusion in colloidal glass (Nägele and Bergenholtz, 1998). MCT has also been extended to account for a deformation field (Fuchs and Cates, 2002, 2003*a,b*). A generalised Green Kubo relation was dervied to describe time dependent flow with arbitrary shear history (Brader *et al.*, 2007). MCT was further modified to account for any arbitrary deformation field the Trouton ratio for uniaxial as well as planar extensions were compared to that of simple shear flow (Brader *et al.*, 2008). A schematic MCT with full tensorial structure of the theory was implemented (Brader *et al.*, 2009). The schematic MCT was extensively utilised to predict the response of colloidal glasses under Large Amplitude Oscillatory Shear, it was found to compliment both experiments and BD simulations (Brader *et al.*, 2010). Yield stress of colloidal glass was found to play influence the response during LAOS. Later a full review comparing the theoretical approaches with the experiments of colloidal suspension was conducted to reveal only the partial success of the theories in capturing the behaviour of real world systems (Brader, 2010). MCT was modified not only to include shear thinning but also to account for shear thickening. The modified model was also able to account for jamming transitions (Cates *et al.*, 2003). Residual stresses have been predicted by the MCT and these stresses was found to be dependent on the perturbation history of the colloidal glasses (Ballauff *et al.*, 2013; Fritschi *et al.*, 2014). The existence of these stress was attributed to the non-linear response of the colloidal glass system which deviates from Onsager hypothesis in statistical mechanics which does not predict rate independent response of a material. MCT could also predict the rheological properties

for a liquid and glass which was experimentally verified with core shell particles (Siebenbürger *et al.*, 2009). Creep was studied using MCT which predicted the colloidal glass behaviour based on various parameters like sample age and magnitude of the stress applied (Siebenbürger *et al.*, 2012). Recently the structure factor of colloidal glass during steady shear was found to undergo a transition from quadrupolar to hexadecupolar symmetry which was related to the plastic events occurring during shear (Amann *et al.*, 2015). Here the quadrupolar symmetry in the structure factor is defined as the non vanishing spherical harmonic Y_{22} in the q_x and q_z plane. This also relates to the normal stress coefficient N_1. The next important contributions in the same plane is due to Y_{42} and Y_{44} which leads to hexadecupolar symmetry in the structure factor. In the elastic regime of start-up shear quadrupolar symmetry dominates. When plastic events dominate hexadecupolar symmetry becomes prominent in colloidal glasses. MCT has also predicted the existence of different types of glasses in highly size asymmetric binary hard sphere glasses which has lead a surge in interest to explore and understand these glasses experimentally (Voigtmann, 2011).

Soft Glassy rheology is another mean field theory approach based on a trap model (Bouchaud, 1992). A volume is defined as small mesoscopic domains that evolve independently as a function of time under deformation. Under shear these domains have a possibility to explore new minima in the energy wells in the time domain (Sollich, 1998). Aging has been extensively studied using SGM (Fielding *et al.*, 2000).

Another theory that is a hybrid between MCT and SGR is the activated cage hopping process. Extensive details about this approach and the advantages over MCT can be obtained from (Schweizer, 2007) and its references. More details regarding phenomenological models and their rheological predictions can be obtained from (Mewis and Wagner, 2009, 2012). The current theoretical models that describe a homogeneous liquid to an amorphous solid have been reviewed (Voigtmann, 2014).

Although a lot of investigations have been performed in colloidal glasses there are few fundamental questions that need to be still addressed. Do hard

sphere colloidal glasses shows signatures of aging during rheology? Can we quantify such aging effects? Is the relaxation of hard sphere colloidal glasses similar to that of soft glasses? Does colloidal glasses and colloidal suspensions show different non-linear behaviour during transient oscillatory shear? Can we obtain the alpha relaxation for colloidal glass under shear and is it possible to perform a shear rate superposition of moduli? Does a softer potential glass affect the dependence of alpha relaxation on shear rate? Is it possible to extract the dynamics of different types of colloidal glasses formed by asymmetric binary hard sphere mixtures? In this thesis we try to address the above questions with the help of rheology and BD simulations.

In Chapter 4, we address the thixotropic effects of colloidal glasses after rejuvenation. Linear and non-linear shear test are performed to identify signatures of aging in hard sphere colloidal glasses

In Chapter 5, we investigate the structure and dynamics during relaxation of colloidal glass during shear interruption and after steady shear. Non-linear oscillatory measurements are employed on colloidal glass suspension below and above glass transition to elucidate the different mechanisms existing during LAOS. Edge effects during shear thickening are also visually inspected for colloidal glasses

In Chapter 6, we perform orthogonal superposition measurements to extract the alpha relaxation time of a colloidal glass under shear. We also employ for the first time a shear rate orthogonal superposition for a colloidal glass. Star like micelles are employed to understand the effect of shear on the relaxation time when there is softer potential.

In Chapter 7, BD simulations are employed in order to investigate the dynamics of asymmetric binary glasses at rest and under start-up shear. Different types of glasses are investigated and compared with that already existing in literature

CHAPTER 4

TIME EFFECTS OF NEARLY HARD SPHERE COLLOIDAL GLASSES

Out of equilibrium systems are always driven to a lower free energy state with waiting time (Zargar *et al.*, 2013) and intrinsic properties like relaxation time change with time. This system is said to undergo aging with waiting time, t_w. Aging is generally defined as time elapsed after suddenly quenching an equilibrium liquid to an out of equilibrium state. In terms of the energy landscape, the system immediately after quenching will have a narrow distribution of shallow energy wells which with time changes to a broader distribution with deep energy wells (Joshi, 2014). The concept of physical aging has been investigated for glass formers (Struik, 1978) as well as molecular glasses (Angell *et al.*, 2000) and polymer glasses (McKenna *et al.*, 2009; O'Connell and McKenna, 1997). There has been a surge of interest in aging in colloidal systems with different attractive or repulsive interactions such as laponite gels (Bellour *et al.*, 2003; Kaushal and Joshi, 2014) and glasses(Angelini *et al.*, 2014; Koumakis *et al.*, 2008), colloidal depletion gels (Fluerasu *et al.*, 2007; Koumakis *et al.*, 2015) .

Aging phenomena in purely repulsive hard sphere glasses were reported in light scattering experiments (van Megen *et al.*, 1998). The drawback in these experiments were that the experimental time scales were too short to properly characterize aging, although the data does show that aged sample dynamics slow down . However recently, aging dynamics was studied using intermediate scattering functions (Martinez *et al.*, 2008, 2010). The intermediate scattering functions depicted a crossover from fast decay to the slower decay. The coupling between these two decays was found to decrease algebraically with waiting time. The alpha relaxation time of colloidal hard sphere glasses was accessed using dynamic light scattering experiments and correlation function

was reported for seven decades in time (Brambilla *et al.*, 2009). The alpha relaxation time was found to slow down with waiting time and finally saturate (Masri *et al.*, 2009). Direct visualization of aging using confocal microscopy was performed on hard sphere colloids in order to obtain the particle displacements during aging (Courtland and Weeks, 2003; Simeonova and Kegel, 2004). In general, amorphous glasses exhibit a slowing down of MSD with age of the sample. However, gravity was also believed to affect the aging phenomena in colloidal hard sphere glasses (Simeonova and Kegel, 2004) although gravity might not be the only reason driving aging. If a sample is very polydisperse there exists regions with varying levels of mobility in the system. This leads to dynamic heterogeneities in the system which drives aging in a colloidal glass. There exists a very close association between structural heterogeneities and dynamic heterogeneities during the temporal evolution of the sample (Golde *et al.*, 2016). Moreover, simulations have also shown that subtle changes in the structural rearrangement are the reason behind aging (Kob *et al.*, 2000*a*,*b*; Utz *et al.*, 2000).

An attempt towards identifying the rheological signatures of aging model nearly hard sphere glasses have already been attempted experimentally (Ballesta and Petekidis, 2016; Koumakis *et al.*, 2016*b*) as well as via theory (Joshi, 2015; Siebenbürger *et al.*, 2012). In this work we present rheological experiments with well defined history in order to elucidate some of the rheological signatures of an aging hard sphere colloidal glass system.

We have performed a detailed study of the effects of aging for nearly hard sphere glasses using poly-methy methacrylate (PMMA) sterically stabilized by poly hydroxystearic acid (PHSA). These colloidal particles are dispersed in two different solvents (i) octadecene/bromonapthalene mixture ($\eta = 0.0045 \, Pas$, $n_D = 1.48$) and (ii) squalene ($\eta = 0.015 \, Pas$, $n_D = 1.494$). Both solvents have a high boiling point which hinders evaporation and they are closely refractive index matched to the colloidal particles so that van der Waals attractions are also suppressed. The colloidal particles used for the following set of experiments have a radius $R = 106 \, nm, 137 \, nm, 196 \, nm, 350 \, nm$ with the polydispersity

of the particles greater than 12%. Hence none of these systems crystallize.

Anton Paar MCR 501 rheometer has been used for all the measurements except for the fast step rate measurements which was performed using ARES Rheometrics strain controlled rheometer. Additionally, a DSR Rheometer was also used to perform the long time creep experiments.

4.1 Aging effects of Linear Viscoelastic properties

Different types of shear rejuvenation protocols were employed depending on the volume fraction ϕ in order to avoid complex flow patterns and edge fracture in highly concentrated especially glassy colloidal suspensions. Supercooled liquids ($\phi < 0.58$) was rejuvenated with constant $\dot{\gamma} = 30 \ s^{-1}$ first in the reverse direction and immediately in the forward direction with the total time of the rejuvenation in each direction such that $\gamma > 100\%$. Colloidal glass with $0.58 \leq \phi \leq 0.60$ was rejuvenated with large amplitude oscillatory shear with frequency of $1 rad/s$. Above $\phi = 0.60$ the system was rejuvenated with a frequency of $0.1 \ rad/s$. Empirically we have found that higher the volume fraction lower the shear rate employed for rejuvenation in order to avoid edge fracture. Aging is monitored after rejuvenation either setting zero shear rate or zero stress. This is done in order to allow the sample to relax after the rejuvenation.

In the linear regime the system was initially rejuvenated with 1000% strain and $0.1 \ rad/s$ frequency of oscillatory shear. Then the system was allowed to rest at $0 \ Pa$ stress for $100 \ s$ before the initial dynamic frequency sweep was performed. The system was probed in the linear regime with alternating frequency sweep and time sweep in the linear regime for more than $16 \ hours$ to probe aging.

Fig. 4.1 depicts a typical linear viscoelastic frequency sweep of a colloidal glass. Here two different sizes of colloidal particles are compared at the $\phi = 0.61$. The trivial size effects are removed by scaling the moduli by $k_B T/R^3$ and the frequency is scaled by the Brownian time t_B. Since Brownian forces
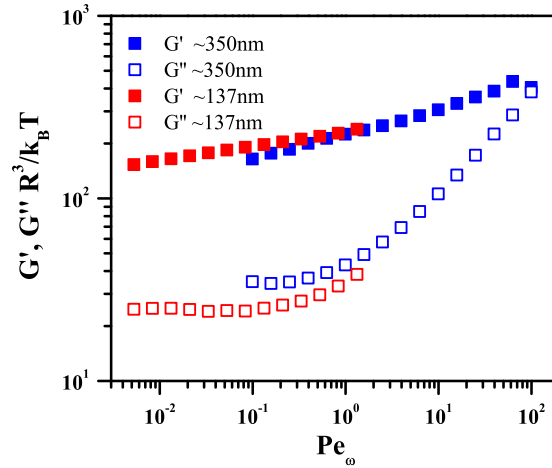
Figure 4.1: The frequency dependence of the storage and loss moduli for a nearly hard sphere colloidal glass with $\phi = 0.61$ for two different size particles scaled by thermal energy and relaxation time respectively in order to remove the trivial size dependence in octadecene/bromonapthalene mixture

are the sole contributor to the elasticity this scaling should be possible. G' data superimposes quite well for both particles while for G'' there seems to be a larger mismatch in the regime near the minimum of G''. The small mismatch between the curves for small and large particles could be due to the difference in the aging time between glass comprising of two different particle sizes, as the aging time after rejuvenation was kept at $\approx 100\ s$ in both cases. In this scenario the small particles age more than the big particles for the same experimental time by a factor of : $t_{B\ small} = R^3_{small}/R^3_{big} \times t_{B\ big}$. The large particles exhibit the high frequency crossover where $G'' > G'$. This indicates the in-cage motion of the particles within the cage. The small particles on the other hand exhibit a very typical minimum in G'' which shows the transition from in-cage to out-of-cage motion in colloidal glasses.

Fig. 4.2 indicates the evolution of the linear viscoelasticity of a hard sphere colloidal glass. As it can be inferred from Fig. 4.2 (a) and (b) the loss moduli (G'') are more affected than the elastic moduli (G'), especially at low frequencies. Although a very clear trend does not seem to emerge, a general feature is the decrease of the low frequency viscous moduli G'' with aging time similar to what has been seen before (Ballesta and Petekidis, 2016). This could also
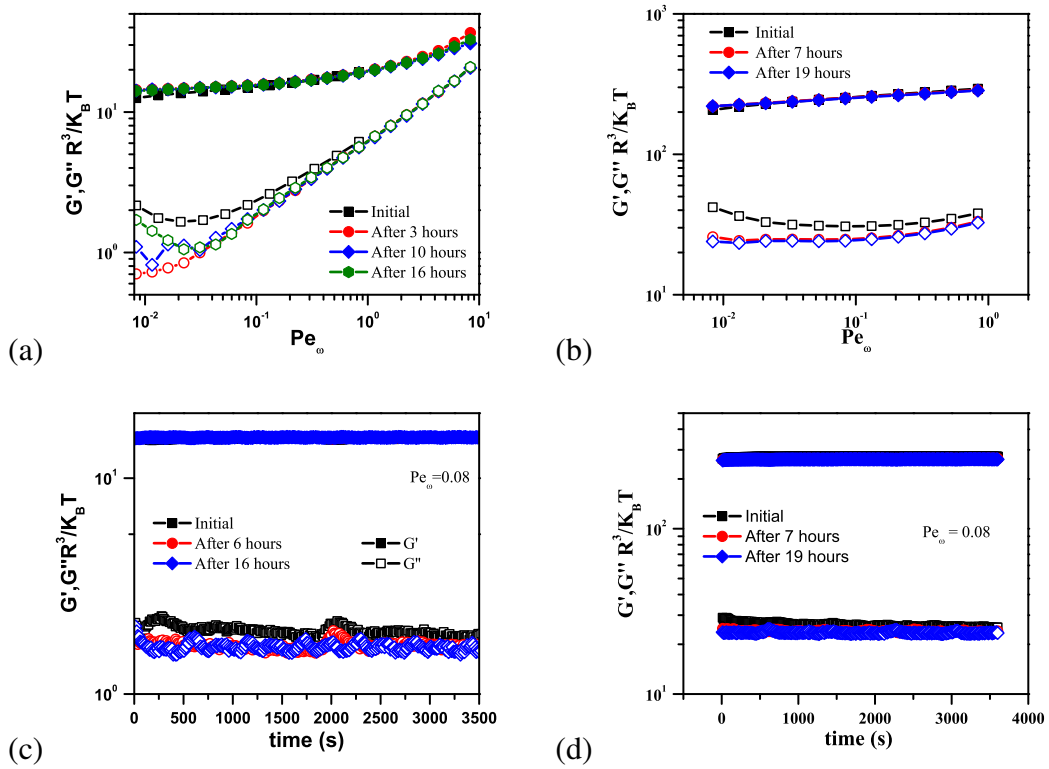
Figure 4.2: Linear viscoelasticity of a glass with (a) $\phi = 0.58$ and (b) $\phi = 0.62$ after various aging time. Time sweep data for a period of one hour for the (c) $\phi = 0.58$ and (d) $\phi = 0.62$ with colloidal particles of $R = 106\ nm$ dispersed in squalene

University of Crete, Greece

mean that the α relaxation time decreases with waiting time. At the same time Dynamic Time Sweep at $Pe_\omega = 0.08$ show no deviations in the storage moduli while fluctuations can be observed in G'' (Fig. 4.2 (c) and (d)). Unlike polymer glasses which are well known to age and have been investigated and can be predicted (McKenna *et al.*, 2009; O'Connell and McKenna, 2002) the mechanism driving aging in colloidal hard spheres is not yet well understood, although drawing similarities with polymer glasses one could speculate that change in free volume available for a colloidal particle affect the structural properties. On the other hand, it is very interesting to contrast such hard sphere systems with repulsive interactions such as glasses and systems having attractive interactions like depletion gels (Koumakis *et al.*, 2015), charged Laponite gels (Joshi, 2015; Joshi and Reddy, 2008; Kaushal and Joshi, 2014) that show extensive aging of their linear viscoelastic properties. Extensive structural reorganization seems to be a necessary condition for a system to exhibit a sensitive linear viscoelasticity during aging. Thus, hard sphere colloidal glasses exhibit very subtle changes in the viscous moduli due to aging in the linear viscoelastic moduli.

4.2   Non-Linear Rheology : Aging effects on Start-up shear

A representative flow curve for a system near and above glass transition is represented in Fig. 4.3. A colloidal system in the glass state generally tends to show a yield stress behaviour at low $Pe(< 10^{-2})$. As expected, the deeper a system is in the glass phase the higher is the yield stress. Slip and shear banding appear at very high volume fraction glasses and at very low Pe. These effects disappear below glass transition $\phi \leq 0.58$ (Ballesta *et al.*, 2008; Besseling *et al.*, 2010).

Typical start-up tests of a hard sphere colloidal glass at $\phi = 0.61$ are shown in Fig. 4.4 with aging time of $100s$. At this ϕ, the system initially deforms elastically and then tends to flow plastically above yield strain (Koumakis *et al.*, 2012*a*, 2016*b*). The elastic regime where the stress increases with strain during start-up flow of colloidal glass is related to the anisotropic deformation of the
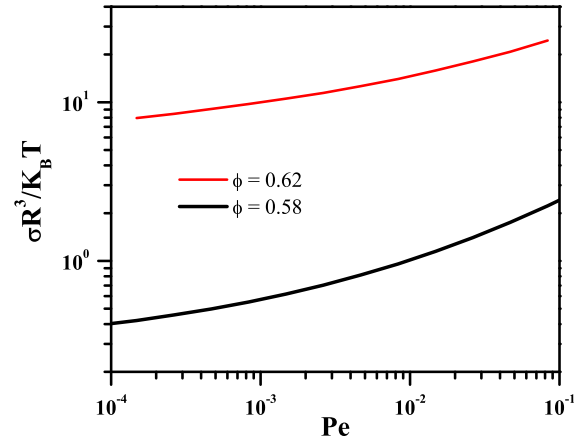
Figure 4.3: Steady state flow curves for colloidal particles $R = 106 \ nm$ in squalene.

(a)

(b)
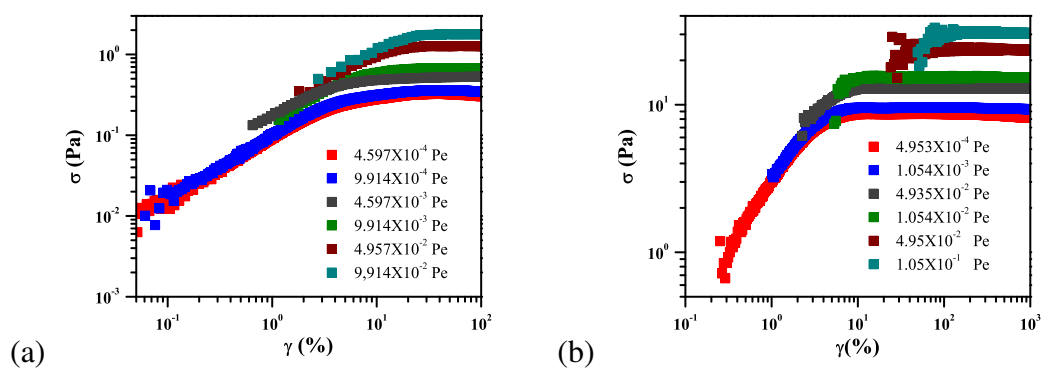
Figure 4.4: Representative startup curves for colloidal glass at various Pe as indicated for (a) $R = 350 \ nm$ and (b) $R = 137 \ nm$ in a solvent mixture of octadecene/bromonapthalene at $\phi = 0.60$ with $t_w = 100 \ s$

cages. After the elastic regime the system yields plastically leading to flow immediately after the deformation of the cages as a consequence the stress reaches a steady state. This kind of plastic deformation was also observed during oscillatory shear (Petekidis *et al.*, 2002). At lower ϕ ($\phi < 0.59$) which is not shown here a larger cage anisotropy is possible due to availability of free volume leading to a peak in stress during start-up shear. The transition from elastic to plastic flow is generally associated with quadrupolar and hexadecupolar structure respectively (Chikkadi, 2011). Here the quadrupolar symmetry in the structure factor is defined as the non vanishing spherical harmonic Y_{22} in the q_x and q_z plane. This also relates to the normal stress coefficient N_1. The next important contributions in the same plane is due to Y_{42} and Y_{44} which leads to hexadecupolar symmetry in the structure factor. In the elastic regime of start-up shear quadrupolar symmetry dominates. When plastic events dominate hexadecupolar symmetry becomes prominent in colloidal glasses. Additionally in Fig. 4.4 (a) γ_{pk} is found to increase with Pe. This is due to the fact that higher Pe can elongate the cage to larger extent before exhibiting cage breaking and flow. γ_{pk} was also found to be nearly independent of ϕ (Koumakis *et al.*, 2016*b*). The extensive dynamics of yielding under start-up flow has been discussed before and will not be repeated here.

Before each measurement, a rejuvenation protocol was followed consisting of a series of tests starting with a high shear rate ($10\ s^{-1}$) for $50\ s$, a small waiting time ($30\ s$), the same shear rate but in the opposite direction for another $50\ s$ and, usually, a waiting time depending on the aging time required.

Fig. 4.4 shows the start-up response for a young colloidal glass. The waiting time dependence of the stress overshoot is shown in Fig. 4.5 which depicts the stress overshoot becoming stronger with waiting time, mainly at low Pe (Fig. 4.5(a)), until it reaches a steady state after long time, often larger than $5000\ s$. At high Pe however, Fig. 4.5 (c), the stress overshoot is independent of the waiting time. In general, Fig. 4.5(d) reveals a non-monotonic dependence of the stress overshoot as function of the Pe. This type of dependence of stress overshoot with waiting time has also been observed in experiments of core shell

PS-PNIPAM particles in the glassy state and subsequently predicted by MCT (Siebenbürger *et al.*, 2012).
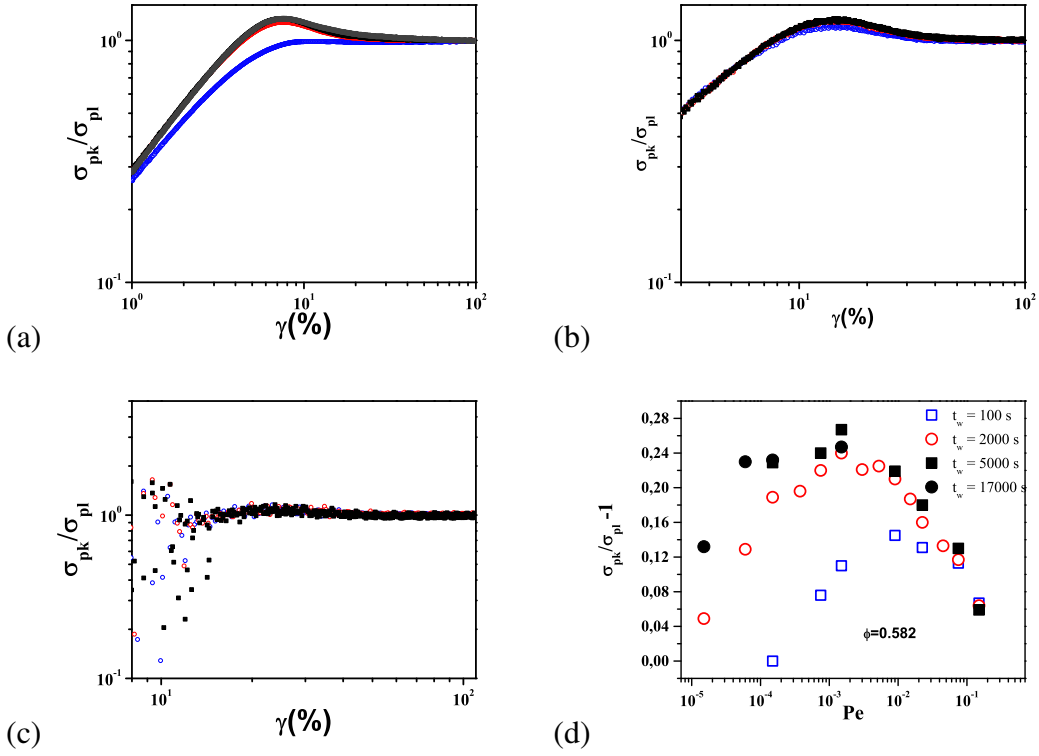
Figure 4.5: Start-up curves for (a) $Pe = 6 \times 10^{-4}$, (b) $Pe = 2 \times 10^{-3}$, (c) $Pe = 0.2$. (d) The intensity of stress overshoot peak with respect to aging time for all Pe. The colloidal glass represented here is at $\phi = 0.582$ with colloidal particles having a radius $R = 196\ nm$ in octadecene bromonapthalene solvent mixture

Hence the magnitude of the stress overshoot exhibits a maximum at some characteristic Pe in Fig. 4.5 (d). This response is more pronounced at shorter waiting times, while at longer ones the increase at low rates tends to level-off. The characteristic Pe beyond which the stress overshoot starts to become weaker is also slightly ϕ-dependent. The same non-monotonic trend of the height of the overshoot as a function of Pe is seen for binary mixtures (Sentjabrskaja *et al.*, 2014). Hence at high Pe rejuvenation seems to be dominating rather than aging (Viasnoff *et al.*, 2003).

Fig. 4.6 shows a colloidal suspension at $\phi = 0.565$, the stress peak overshoot sustains the non-monotonic response. This is expected as in the previous case because there is dominance of aging at low Pe and shear induced rejuvenation
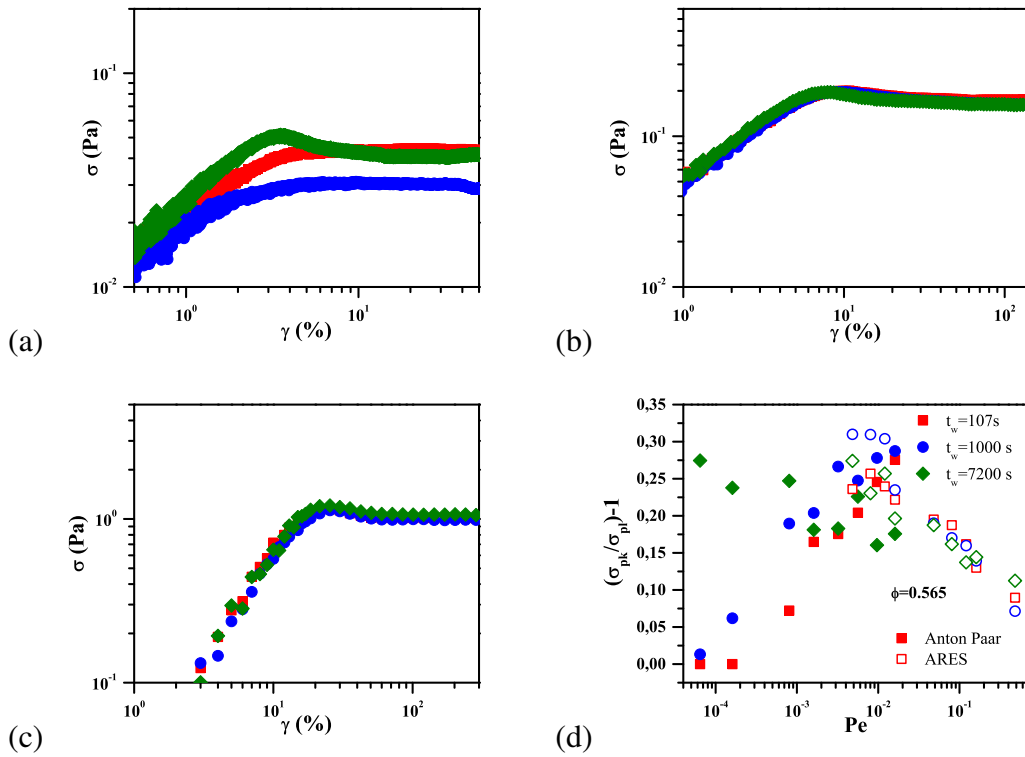
Figure 4.6: Start-up curves for (a) $Pe = 2 \times 10^{-4}$, (b) $Pe = 2 \times 10^{-2}$, (c) $Pe = 0.1$. (d)The intensity of stress overshoot peak with respect to aging time at for all Pe. The colloidal glass represented here is at $\phi = 0.565$ with colloidal particles having a radius $R = 196\ nm$ in octadecene bromonapthalene solvent mixture

that eliminates aging at high Pe. As we increase ϕ, the stress peak decreases which makes it very difficult to extract the stress peaks without considerable error. Ideally we would expect this peak in the non-monotonic transition to occur at $Pe = 1$ which depicts a competition between Brownian motion and advection. Surprisingly, this transition occurs at 100 times lower than $Pe = 1$. This might happen because here we have calculated Pe_{bare} with t_B for a colloidal particle in the dilute regime. It has been clearly established that the actual t_B is much slower (approx 10 to 100 times lower) than estimated due to hydrodynamic interactions (Brady, 2001; Foss and Brady, 2000).

The same set of experiments for the start-up shear versus aging time indicates how the aging time influences the stress overshoot peak. Comparing linear and non-linear responses it is obvious that the non-linear response is more sensitive to aging rather than the linear viscoelastic quantities (G' and G''). Moreover the non-linear start-up also helps to identify a general trend. Upon increasing aging time the stress overshoot in start-up shear increases. Core-shell PS-PNIPAM systems in glass state which exhibits hard sphere interactions show similar response, moreover this was also captured by MCT (Siebenbürger *et al.*, 2012). As we increase Pe the effect of the aging on the stress overshoot peaks decreases until a critical value of Pe where it vanishes as rejuvenation of the microstructure is complete.
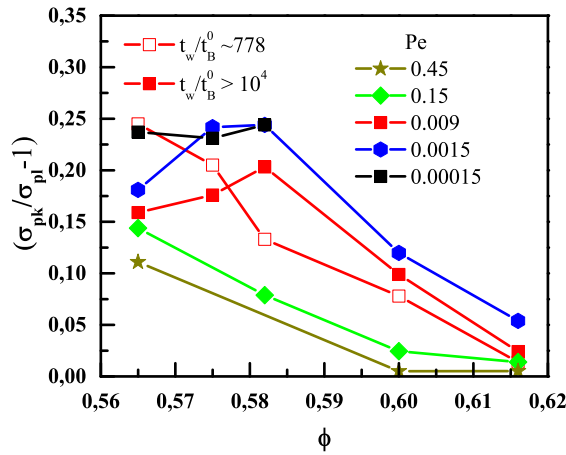
Figure 4.7: Comparison of the stress overshoot peak at different ages with respect to ϕ

In Fig. 4.7 the magnitude of the stress overshoot is shown as a function of volume fraction for different Pe. For an intermediate $Pe(= 0.009)$ data are shown both for short and long waiting times for comparison. Aging causes a change in the response at low rates. At short times ($t_w \approx 100\ s$) the stress overshoot drops continuously with volume fraction both below and above the glass transition volume fraction. At longer times approaching steady state a non-monotonic behavior is detected with a strengthening of the overshoot at low rates and a weakening at higher ones. While this behavior is typically observed at low rates, at high ones (here $Pe > 0.1$) the magnitude of the overshoot decreases monotonically as ϕ is increased at all regimes both in the liquid and glassy state as found earlier and attributed to the decrease in free volume available for a particle as the volume fraction is increased towards close packing (Koumakis *et al.*, 2012*a*, 2016*b*).
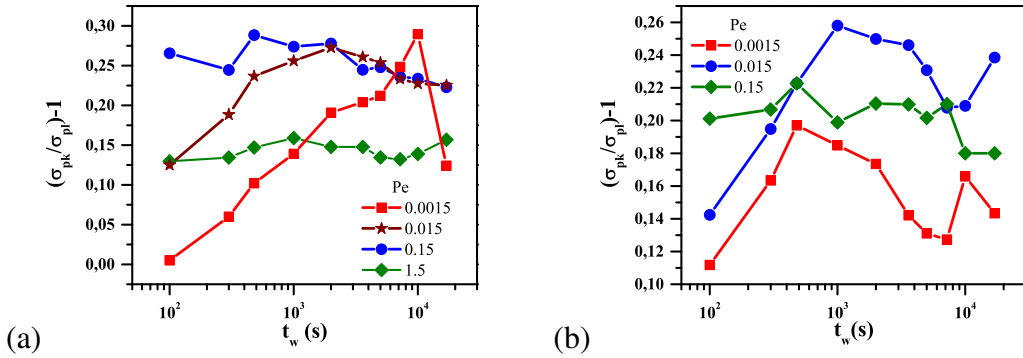
Figure 4.8: The stress overshoot peaks is shown as a function of the waiting time at (a) $\phi = 0.565$ and (b) $\phi = 0.575$ for $R = 196\ nm$ in octadecene/bromonapthalene solvent mixture

Fig. 4.8 shows a non-trivial and complicated response of the colloidal glass with respect to the aging time. Fig. 4.8 (a) suggests that low Pe there is a consistent increase in the stress overshoot peak with aging time. The dip in the overshoot peak (last point) could be due to slip at the top surface where particles detach due to gravity from the geometry after such long waiting time. At higher Pe, the overshoot of the peak appears to be fluctuating around an average value. Similar observations can be deduced from the Fig. 4.8 (b). Thus aging exhibits a very strong dependence at low Pe while at high Pe rejuvenation sets in.

A non-trivial dependence is found for the stress overshoot peaks as a func-

tion of waiting time as well as the volume fraction. Additionally, start-up shear appears to be more sensitive to aging effects in colloidal glass than the linear viscoelastic quantities. Since in the dynamic frequency sweep a very limited amount of frequencies are probed the effects of aging is possibly seen in the linear viscoelastic regime at very low frequencies below the experimental window. The hints of aging in linear viscoelastic regime are seen as subtle variations of loss moduli with time.

4.3 Non-Linear Rheology : Aging effects on Stress Relaxation

Cessation of shear in colloidal systems aids in understanding the relevance and dynamics of internal stresses in hard sphere glasses (Ballauff *et al.*, 2013; Fritschi *et al.*, 2014), anisotropic particle glasses (Negi and Osuji, 2010), soft glasses (Mohan *et al.*, 2013, 2015) and also depletion gels (Chung *et al.*, 2006) also used extensively in studying aging phenomena(Bandyopadhyay *et al.*, 2010; Kaushal and Joshi, 2014).
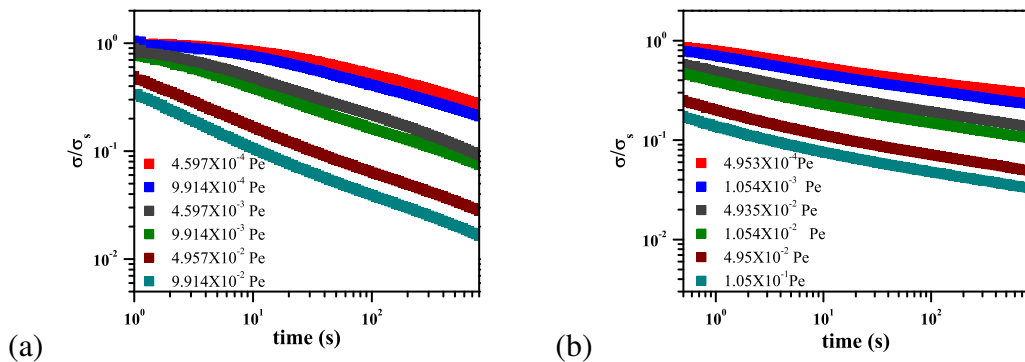
Figure 4.9: Representative stress relaxation for colloidal glass at various Pe for (a) $R = 350 \ nm$ and (b) $R = 137 \ nm$ at $\phi = 0.61$ octadecene/bromonapthalene solvent mixture for $t_w = 100 \ s$

Here we show the typical evolution of the internal stresses after the steady shear cessation in Fig. 4.9 for colloidal glass at $\phi = 0.61$ for two different particle sizes. The stress in the ordinate axis is scaled with the value of steady state stress just before cessation of shear. Irrespective of the particle size it is evident

that lower Pe tends to stores more stress in the material. In general there are two protocols to perform stress relaxation experiments i) Stress relaxation during start-up shear (where the $\dot{\gamma} = 0$ is imposed) and ii) Stress relaxation after the step-strain experiment. Below we present measurements with both the protocols separately below and discuss the effects of aging in these measurements.

4.3.1 Stress Relaxation during start-up shear
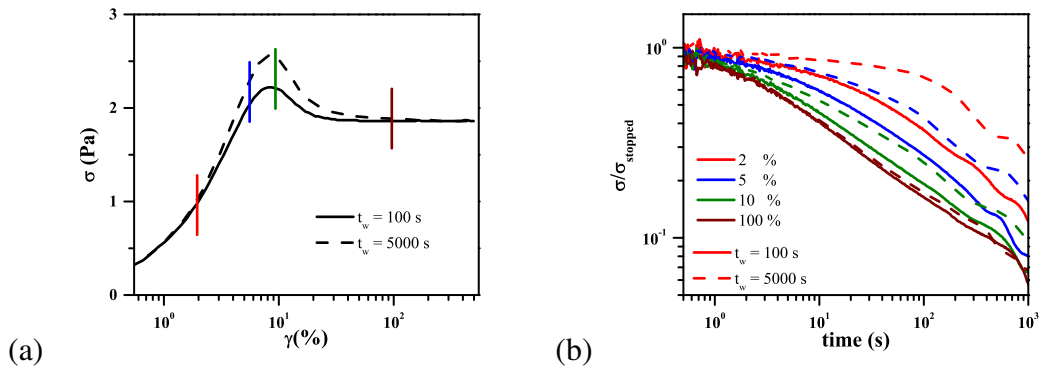
Figure 4.10: (a) Start-up shear and (b) interruption of start-up shear at various strains for $t_w = 100\ s$ and $t_w = 5000\ s$ for $\phi = 0.58$ and for $Pe = 8.33 \times 10^{-4}$. The colloidal systems represented here have $R = 106\ nm$ suspended in squalene. The vertical lines in (a) indicate the strain at which flow is interrupted

In Fig. 4.10 (a), start-up experiment is shown at two different waiting times on $\phi = 0.58$ at $Pe = 8.38 \times 10^{-4}$ and interrupted at different points along the start-up experiment. The stress after cessation of shear is followed with time. From Fig. 4.10 (a) it can be clearly inferred that below $\gamma \leq 100\%$ aging is important in start-up tests. The peak of the stress overshoot, indicating the yield point occurs around 10% (also seen in Fig. 4.5), where one can observe the difference in the stress relaxation due to the age of the sample up to 10%. When stopping the shear above 10%, where the sample starts to flow stress relaxation seems be unaffected by the aging time. Another clear finding is that during start-up shear the difference in the stress values for the two different ages varies non-monotonically along the start-up curve (Fig. 4.10 (a)). Fig. 4.10(b) depicts interrupting the start-up shear at different strains and following the stress scaled by the stress at flow interruption as a function of time for two different sample

ages. During stress relaxation it can be clearly observed that the older samples retains more stress before rejuvenation sets-in, erasing the memory of the age in the sample. With increasing age of a colloidal glass, the availability of free volume for a particle trapped in cage increases. This indicates that the cage expands with waiting time leading to a more anisotropic cage during shear for an older colloidal glass and thus storing more stress during stress relaxation. It should also be noted that some kinks in the stress relaxation can be seen in Fig. 4.10 (b) which will be discussed later.
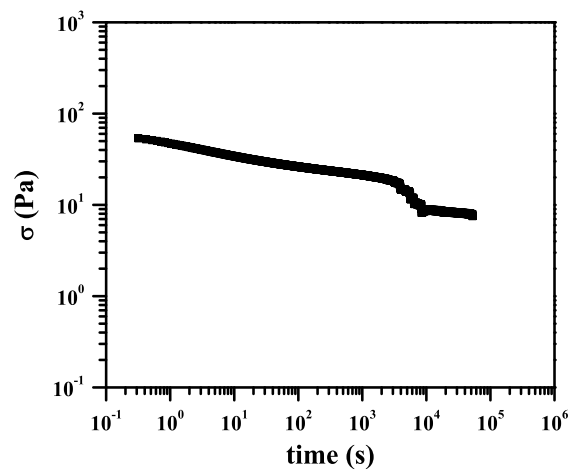
Figure 4.11: Long time stress relaxation of colloidal glass with $\phi = 0.63$, $R = 106$ nm after $Pe = 2.5 \times 10^{-4}$ in octadecene/bromonapthalene mixture.

The long term effects during stress relaxation of colloidal glass at $\phi = 0.63$ is followed for 14 hours continuously. This is done by applying $\dot{\gamma} = 0$ after steady shear stress is attained at $Pe = 2.5 \times 10^{-4}$ as represented in Fig. 4.11. In contrast to soft jammed particles (Mohan *et al.*, 2013, 2015), we do not see a two-step relaxation in colloidal hard spheres glasses. The non-linear rheological tests provide us ample evidence that the relaxation time increase with waiting time. Recently, a SGM model was proposed where the aging was made a decreasing function of free energy and an increase in free energy was associated to rejuvenation (Joshi, 2015). This model predicted the existence of residual stresses when the relaxation time had a stronger than linear dependence with waiting time. Above glass transition a stronger than linear dependence of the

alpha relaxation time on the waiting time has been observed in light scattering experiments for hard sphere glasses (Masri *et al.*, 2009). Hence our rheological experiments combined with light scattering data published earlier seems to support the modfied SGM model predictions. Moreover, the long time stress relaxation at $\phi \geq 0.62$ is filled with sudden drops in the stress as observed in Fig. 4.11. Colloidal glasses are known to exhibit cooperative motion (Zhang *et al.*, 2011) and very recently avalanches in hard sphere colloidal glasses has been predicted by simulation due to the heterogeneous dynamics present in the system (Rosales-Pelaez *et al.*, 2016). This indicates that a particle trapped by its neighbors, during cage escape tends to reorganize a local region in its surroundings leading to avalanches of particles. At this point, it is not clear what drives these phenomenon which we have observed during numerous occasions.

4.3.2 Stress Relaxation after step-strain

The system was rejuvenated with 1000% strain and $1\ rad/s$ frequency of oscillatory shear. Then the system was allowed to rest at $0\ Pa$ stress for the required waiting time before the step-strain is applied.
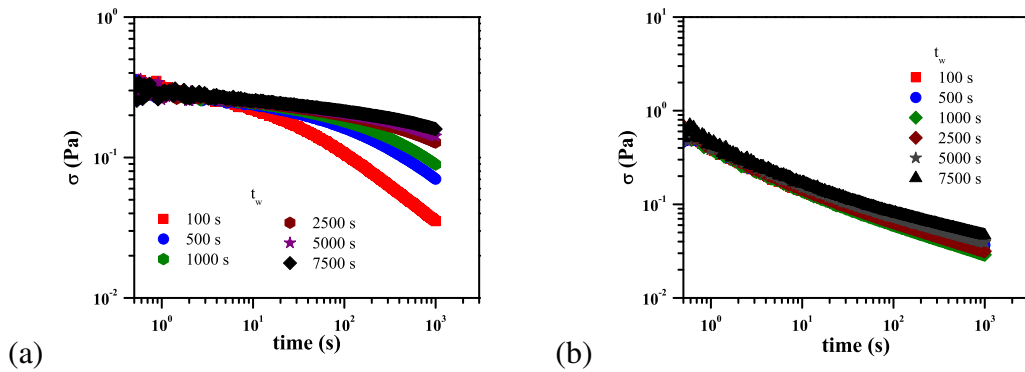
Figure 4.12: Stress relaxation data for colloidal glass ($R = 196\ nm$)in octadecene/bromonapthalene solvent mixture with a volume fraction $\phi = 0.6$ at step-strain of (a) $\gamma = 1\%$ and (b) $\gamma = 50\%$ for different waiting time after rejuvenation

Stress relaxation as function of aging time for linear and non-linear step-strain is shown in Fig. 4.12. Samples immediately after rejuvenation bear the characteristics of a viscoelastic fluid as the system releases the stress quickly.

With increasing age of the sample the stress is retained much more, as clearly observed in Fig. 4.12 (a). For the step-strain in the non-linear regime, the stress relaxation curves become independent of the aging time as seen in Fig. 4.12 (b). This is clear indication that rejuvenation in the colloidal glass sample has occurred. In the linear step-strain experiments, the young samples have a fresh memory of the rejuvenation protocol applied before, hence the colloidal glass releases the stresses in the sample. For aged samples, the system has little memory of the rejuvenation protocol hence show characteristics of viscoelastic solid by retaining the stress.

(a)   (b)
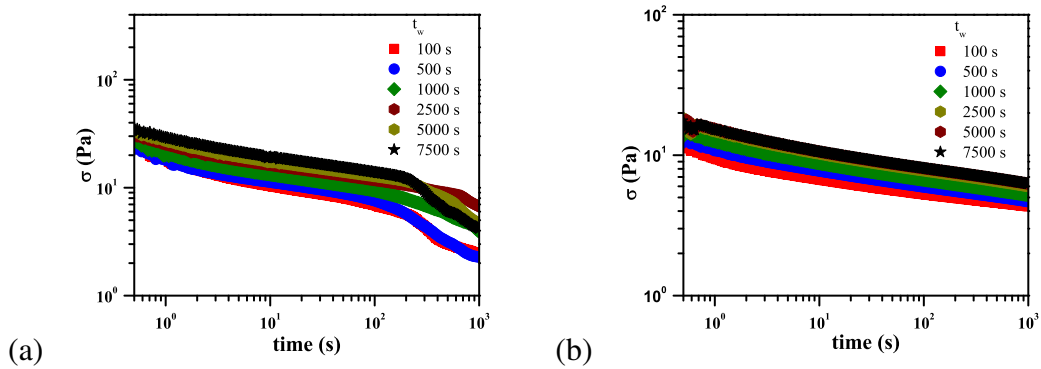
Figure 4.13: Stress relaxation data for colloidal glass ($R = 106\ nm$) in octadecene/bromonapthalene mixture with a volume fraction $\phi = 0.63$ at step-strain of (a) $\gamma = 1\%$ (b) $\gamma = 50\%$ for different waiting time after rejuvenation

The stress relaxation during step-strain of a colloidal glass at $\phi = 0.63$ is shown in Fig. 4.13. At short time we observe that aged samples retain more stress than young samples. The stress relaxation at long time takes place with kinks appearing in the data. These are avalanches occurring during stress relaxation as observed earlier in Fig. 4.11 due to large scale cooperative rearrangements. Simulations have earlier observed that subtle changes in configuration space occurs during aging (Kob *et al.*, 2000*a*,*b*). This phenomenon could lead to sudden drops in the stress for aged samples during stress relaxation. We also observe that these kinks disappear when the step-strain beyond the yield strain is applied Fig. 4.13. In the linear regime, the colloidal particles are pushed into deeper energy wells with sample age. Thus, subtle fluctuations in particle position could lead to drastic local rearrangements of the colloidal particles

leading to sudden drops in stress. On the other hand when step-strain beyond the yield strain is applied, all particles are pushed to shallow wells which aids in rearrangements on larger length scales spanning the whole available space.

In general the aging effects during stress relaxation indicate how much memory of the rejuvenation is retained by colloidal glasses and this determines its viscoelastic behaviour. Moreover, aged samples exhibit very drastic drops in stress during stress relaxation which could be related to local avalanches taking place in a colloidal glass.

4.4   Non-Linear Rheology : Aging effects on Creep

A creep experiment is defined when an instantaneous step-stress is applied on a sample. In yield stress materials like colloidal glass, we can generally observe 3 regimes. When the stress applied is lesser than yield stress ($\sigma < \sigma_y$) the system does not accumulate strain as $\dot{\gamma} = 0$. When the stress applied approximately close to the yield stress ($\sigma \sim \sigma_y$) a delayed yield process takes place in colloidal glass, the strain is accumulated by the glass slowly. After certain amount of strain is accumulated by the system it yields suddenly leading to flow. Above the yield stress ($\sigma > \sigma_y$) the system flows continuously (Siebenbürger *et al.*, 2012). Aging effects have been investigated with creep in colloidal hard sphere glass (Ballesta and Petekidis, 2016). It was clearly established that there is a slowing down of the intrinsic relaxation time of the colloidal glasses after rejuvenation under creep. Using confocal microscopy application of stress below the yield stress was found to have localized domains having non-affine motion and sub-diffusive behaviour (Sentjabrskaja *et al.*, 2015). Above the yield stress localized domains start to swell and connecting to each other leading to the flow of colloidal glasses.

The system was rejuvenated with 1000% strain and 0.1 rad/s frequency of oscillatory shear. Then the system was allowed to rest at 0 Pa stress for the required waiting time before either step-stress or step shear rate is applied.
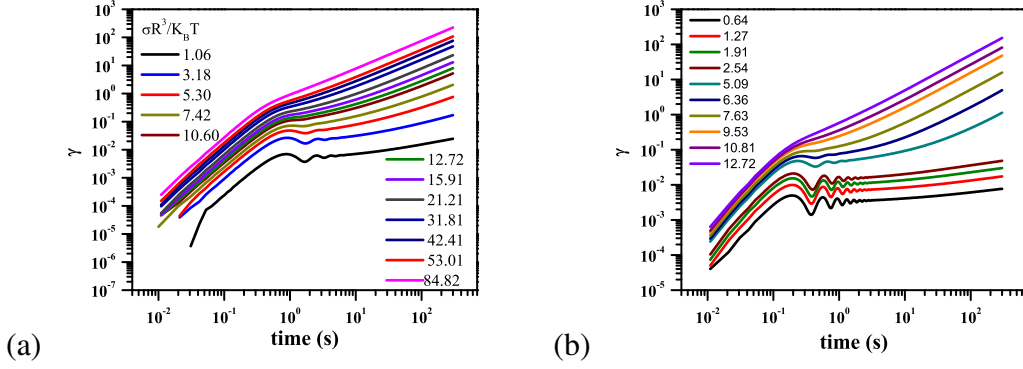
Figure 4.14: Representative creep curves for colloidal glass at various step-stresses for (a) $R = 350\ nm$ with $\sigma_y R^3/k_B T = 1.06$ and (b) $R = 137\ nm$ with $\sigma_y R^3/k_B T = 2.70$ at $\phi = 0.61$ in octadecene/bromonapthalene solvent mixture for $t_w = 100\ s$.

Fig. 4.14 shows representative creep data for colloidal glass of two different sizes of colloidal particles. Creep tests in glass comprising of big particles are always above the σ_y but for the small particle colloidal glass we probe the whole range of stresses from below to above σ_y. An evident feature of the measurements is the ringing that is visible at early times. This happens due to the coupling of the motor inertia with viscoelastic properties of the sample. Irrespective of the particle size, creep ringing appears to be prominent at small stresses in both the glasses. When $\sigma < \sigma_y$ in Fig. 4.14 (b) strain shows a sub-linear dependence with time. Strain is not accumulated by the glass and $\dot{\gamma} << 10^{-5}$. For $\sigma \geq \sigma_y$ the rate of strain accumulation is small at early times which increases drastically at long time which is defined as delayed yielding. This type of yielding is seen for glasses of both sizes but it is more apparent in the glass comprising of small particles as shown in Fig. 4.14 (b). When $\sigma >> \sigma_y$ the strain tends to have a slope of 1 with respect to time independent of particles size in this regime undergoes flow with constant $\dot{\gamma}$ (Ballesta and Petekidis, 2016; Siebenbürger *et al.*, 2012).

Fig. 4.15 indicates creep measurements on colloidal glass of $\phi = 0.58$ after rejuvenation where a constant stress $\sigma \sim \sigma_y$ is applied. It can be clearly observed that the sample creeps more slowly as the t_w is increased. For the longest waiting time the transition from creep to flow is slow as seen in Fig. 4.15 (a). In order to clearly understand the transitions taking place in strain
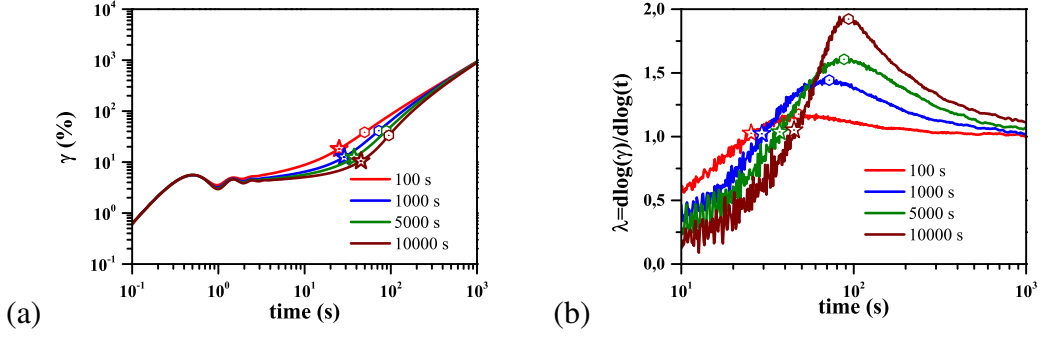
Figure 4.15: (a) The strain data at different sample ages for $\sigma = 1.86\ Pa$ and (b) λ calculated for the creep data. The unfilled star indicate the point t_1 where $\lambda = 1$ and the unfilled diamond indicate where λ has maximum value for t_{max} for aging colloidal hard sphere glass with $\phi = 0.58$ in squalene

with respect to time, a logarithmic derivative of the strain with respect to time is calculated according to the following equation

$$\lambda = \frac{d\log(\gamma)}{d\log(t)} \tag{4.1}$$

For $t \leq 10\ s$ where ringing of the creep is seen in Fig. 4.15 (a) the data appears very scattered and hence we do not show them in Fig. 4.15 (b). However in Fig. 4.15 (a) ringing seem to have very subtle effects due to aging. The young sample shows a smaller overshoot during ringing than the aged samples. Fig. 4.15 (b) depicts an increase in λ with respect to time immediately after ringing. When the sample reaches $\lambda = 1$ (shown by the stars), the sample transitions from the creeping regime and begins to flow. This is followed by a maximum in λ just before dropping and attaining the steady state at $\lambda = 1$. The logarithmic derivative reaches the value of 1 at different times depending on the age of the sample. As the age of the sample increases it takes a longer time to attain $\lambda = 1$. This indicates that the samples creeps for a longer period as the relaxation time of the sample has increased with time. The circle symbols indicate the transition time t_1 where the rate of strain accumulation increases from sub-linear to super-linear regime. The maximum in λ also depends on the age of sample. After the peak in λ it can be seen that the younger sample reaches the yielding point earlier i.e. simple flow with constant η is reached. The diamonds indicate the

time at which the maximum of λ attained above which steady state flow occurs.

4.4.1   Stress versus strain controlled shear

In Fig. 4.16 we show comparative plots of strain controlled flow measurements and stress controlled flow measurements. All applied stress values for stress controlled measurements are greater than σ_y. Stress and strain controlled measurements are performed at different waiting time after rejuvenation. The start-up shear and the creep experiments for each measurement are chosen such that superimposition of these curves under steady state flow is possible. The start-up shear data for all the rates clearly show the peak in stress, as is expected in concentrated colloidal suspensions. The overshoot of the stress peak is seen to be affected by aging which has been already discussed above. After yielding, the systems begin to flow reaching a constant steady state value irrespective of the aging time. It is difficult to discern the time to reach steady state flow in start-up shear. In the case of constant stress the aging effect is clearly evident in the transition of flow unlike the constant shear rate experiment. As the sample age increases the colloidal glass creeps for a longer time than young samples. The time to reach steady state flow in constant stress conditions increases with sample aging time as seen in Fig 4.16. Furthermore, the arrows in Fig. 4.16 indicate where the system reaches steady state flow. The black arrows represent the shear rate controlled experiments where the system tends to yield at a specific time irrespectively of sample age. While in creep tests the colored arrows depict a clear dependence of yielding time, before steady state flow is reached, with age of the sample. In shear rate controlled experiments, activation of cage breakage occurs at once all throughout the sample, while in creep test, activated domains are know to exist in the sample that grows with time until flow sets in. From the above results one can speculate that activating and growing these heterogeneous sites during creep is a function of the waiting time / aging.

In Fig. 4.17 different time scales are defined based on step rate and creep shown above. t_{peak} is the time where the σ reaches the σ_{peak} for strain rate controlled experiments, while t_1 and t_{max} are the time where $\lambda = 1$ and λ
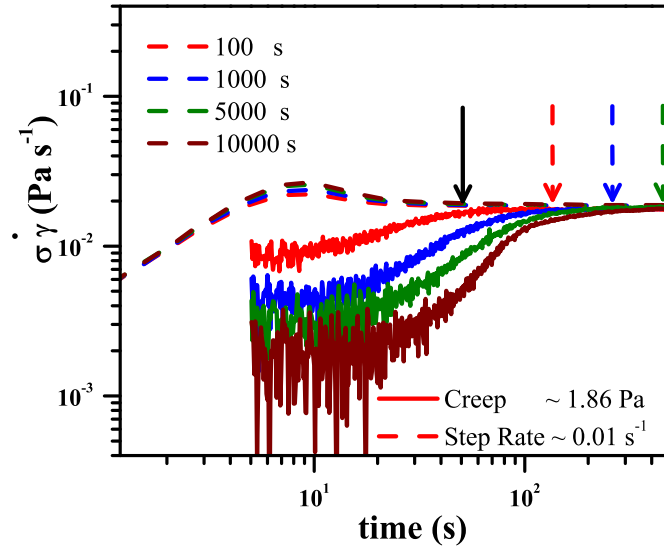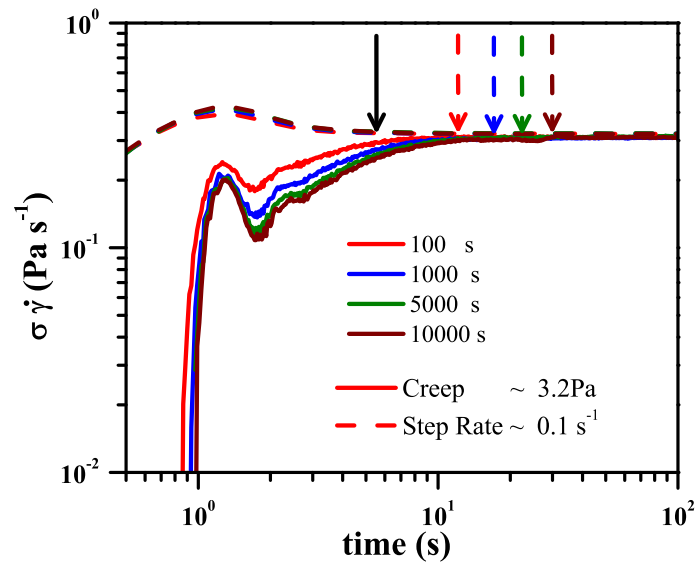
Figure 4.16: Comparison of the creep and shear rate data for $\phi = 0.58$ at (a) $\dot{\gamma} = 0.01 \; s^{-1}$ and $\sigma = 1.86 \; Pa$ and (b) $\dot{\gamma} = 0.1 \; s^{-1}$ and $\sigma = 3.2 \; Pa$. The arrows indicate the time when stress and strain controlled experiments reach steady state flow
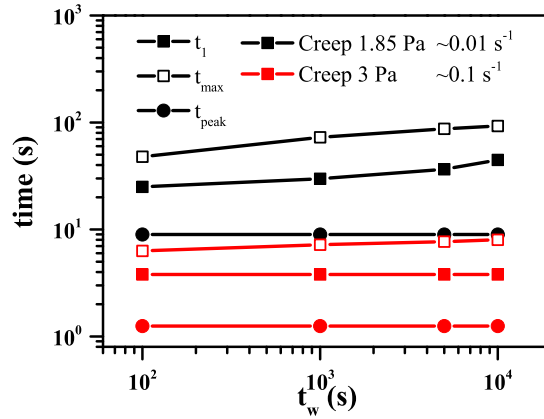
Figure 4.17: t_1 and t_{max} obtained from Fig. 4.15 for step-stress data and t_{peak} obtained from the step rate data for aging colloidal hard sphere glass with $\phi = 0.58$

reaches maximum value for stress controlled experiments. Interestingly, t_{peak} in the strain rate controlled experiment does not seem to change with aging time irrespectively the shear rate applied. Only the strength of the stress overshoot peak is affected by the aging. t_1 and t_{max} increase with aging time for $\sigma = 1.85\ Pa$, although for $\sigma = 3\ Pa$ only t_{max} shows a positive slope while t_1 appears to be constant.
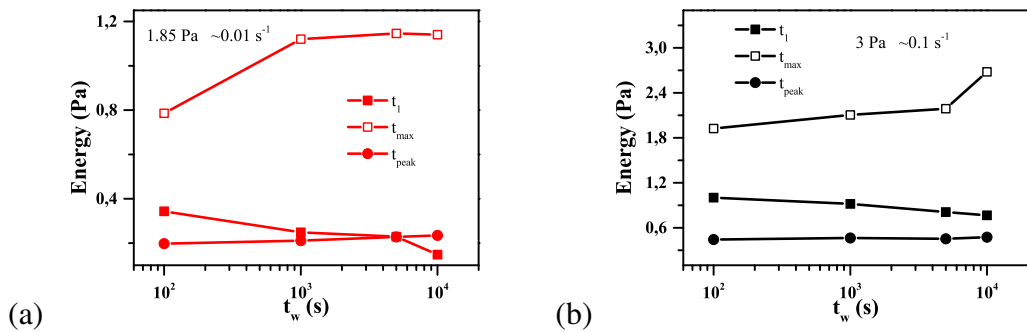
Figure 4.18: The energy per unit volume as a function the waiting time after rejuvenation for colloidal hard sphere glass with $\phi = 0.58$ for two different shear rates

Fig. 4.18 indicates the energy required to induce flow in colloidal glass for $\sigma = 1.85\ Pa$ and $\sigma = 3\ Pa$. This energy per unit volume is calculated by the

following equation

$$Energy/volume = \int_{t_o}^{t_n} \sigma\dot{\gamma}dt \qquad (4.2)$$

t_o is the time for the start of the experiment and t_n indicates the t_1, t_{max} for stress controlled experiments and t_{peak} for the strain controlled experiments. The energy determined in this way is the area under the curve in Fig. 4.16 with limits the time as described above. For start-up experiments the energy seems to slightly increase with aging time. This is obvious because the stress during the start-up test increases with aging time of the sample with the stress overshoot becoming stronger. In the stress controlled experiments the energy per unit volume calculated upto t_1 shows decreasing trend irrespective of the magnitude of the stress. In Fig. 4.16 we can observe that the aged samples creeps for a longer time than the young samples leading to a decreasing energy magnitude with age. This suggests that colloidal glasses seem to require more energy during the first stage of creep rather than a young sample. Interestingly, the energy required for the upper limit t_{max} to be reached is approximately 2 times that required in start-up experiment and creep up to the limit t_1. A positive slope in energy can be observed in Fig. 4.18 for the upper limit of t_{max} which also suggests that more energy is required to make an aged colloidal glass to flow. It is only after the t_{max} that the colloidal glass begins to flow as is evident form Fig. 4.15. Hence, it can be inferred that a strain controlled experiment is more energy efficient in inducing flow in the sample than a stress controlled experiment. Additionally, the energy required in start-up experiments at t_{peak} and creep test at t_{max} have similar values as they represent similar regimes in the shear process. In the case of start-up shear and creep test this is the energy per unit volume required for the transition to steady state flow.

4.4.2   Long creep test

Simulations indicated appearance of dynamic noise in the stress during steady shear. These fluctuations where directly correlated to the cascading quadrap-
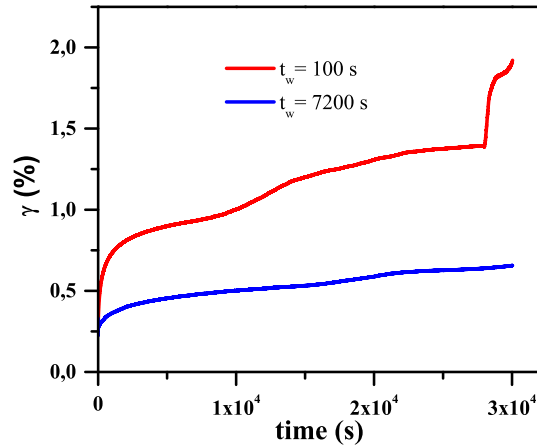
Figure 4.19: Long time creep experiments performed at two different waiting times after rejuvenation for $\sigma = 0.25\ Pa$ for a colloidal glass of $\phi = 0.59$ with $R = 106\ nm$ in squalene and $\sigma_y = 2\ Pa$

olar events or avalanches during steady state flow (Bailey *et al.*, 2007; Barrat and Lemaître, 2011; Chikkadi, 2011; Lemaître and Caroli, 2009; Maloney and Lemaître, 2006). An entire three dimensional mapping of the dislocation avalanches was conducted for a constant load (stress) during plastic flow of ice crystals (Weiss and Marsan, 2003). These dislocation avalanches were related to plastic flow. In yield stress fluid avalanche type of behaviour was also observed during flow (Coussot *et al.*, 2002). An avalanche process in such a fluid was defined as process where the fluid starts flowing abruptly and the flow accelerates. Microstructurally, this kind of process was speculated to be the unjamming of the jammed system.

Here, we study the long time effects on colloidal glasses under constant stress. In Fig. 4.19 the long time effects of a colloidal glass under constant stress are investigated. Initially the sample is rejuvenated and then allowed to wait for two different waiting time 100 and 7200s. A positive $\sigma = 0.25$ is applied which is below the yield stress, σ_y for 3×10^4 s. In Fig. 4.19 we observe the effect of waiting time on the creep test as shown earlier (Ballesta and Petekidis, 2016). An interesting finding is that, we observe sudden jumps in the strain. This could be due to avalanches occurring in the microstructure of colloidal glass leading to strain jumps. The values of strain jumps are quantitatively less

than 1% . Since we have an amorphous colloidal glass under constant stress ($\sigma < \sigma_y$), the strain distribution may be heterogeneous in nature. There will be localized regions were more cages will be strained than others. This could lead to localized avalanches in the colloidal samples very similar to local fracture in metals. These strain jumps can be seen as rheological fingerprints to avalanches occurring in colloidal hard sphere glasses under constant stress.
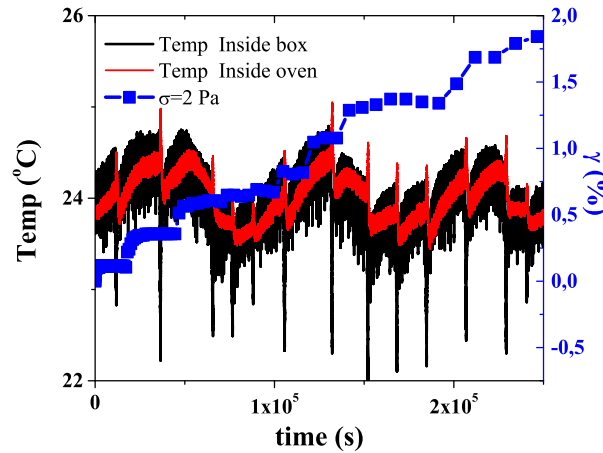
Figure 4.20: Long time creep with $\sigma = 2\,Pa$ for $\phi = 0.62$ and colloidal particle radius $R = 106\,nm$ in squalene performed on a DSR Rheometer. The temperature fluctuations due to the surroundings are also noted.

Finally, we tried to isolate the rheometer by using a homemade isolation box out of thermocol in attempt to understand if external temperature fluctuations activates such avalanches, although such an attempt was not successful as seen in Fig. 4.20. Here the temperature inside the isolation box as well as inside the oven is collected using a Pico log thermocouple. There was large fluctuations in temperature due to the external factors in the room that was not perfectly isolated using the isolation box. This is reflected in the change in temperature about 1^oC in the oven over the time of the experiment. When $\sigma < \sigma_y$ we observe frequent strain jumps in the colloidal glass under constant stress (under such conditions). Although it cannot be directly correlated to the temperature fluctuations/jumps with the strain jumps these temperature fluctuations could be the one of the reasons for strain jumps. From long time stress relaxation seen in Fig. 4.11 and the creep data in Fig. 4.20 it can be speculated that avalanche

mechanisms are the long time effects of colloidal glasses.

In this chapter, we identified the rheological signatures for aging of nearly hard sphere colloidal glass. In the linear viscoelastic regime subtle changes in the viscous modulus were observed. During non-linear shear experiments like start-up, creep and stress relaxation, discernible differences were observed due to aging. In general, a clear transition form the viscoelastic liquid to viscoelastic solid was found when the colloidal glass ages with time. The intensity of the stress overshoot peak shows a non-trivial dependence with waiting time and volume fraction. Colloidal volume fractions close to the glass transition show more aging due to the availability of space to access more configurations, hence move into deeper energy wells while above the glass transition the system is kinetically more trapped. Stress relaxation helps in discerning shear protocols for rejuvenation and aging. Creep and stress relaxation shows extensive hints of avalanche type processes which leads to drastic stress jumps occurring in a colloidal glass. Finally, comparing stress controlled and shear rate controlled experiments the later was found to be energy efficient to make colloidal glasses flow.

CHAPTER 5

TRANSIENT SHEAR EFFECTS IN NEARLY HARD SPHERE COLLOIDAL GLASSES

Out of equilibrium colloidal glasses have been extensively studied under transient shear. These studies are driven by the need to understand the relation of yielding with microstructural changes and dynamics during steady shear flow of colloidal glasses. Start-up shear of colloidal glasses showed the development of cage anisotropy before yielding in a colloidal glass(Koumakis *et al.*, 2012*a*, 2016*b*). The in-cage dynamics was suppressed due to the cage anisotropy inducing constriction of particles. Moreover, aging dynamics was also studied during transient start-up shear as discussed in previous chapter (Koumakis *et al.*, 2016*b*). Shear banding was related to the instabilities due to shear-concentration coupling in colloidal glass which creates stress localisation during low Pe and high ϕ (Besseling *et al.*, 2010). The microscopic dynamics during shear banding was also investigated (Chikkadi *et al.*, 2014), while the micro structure under shear was elucidated with the help of X-ray scattering and MCT, where the structure factor changed from quadrupolar elastic deformation to hexadecupolar distortion during flow (Amann *et al.*, 2015). After shear cessation stresses were retained in colloidal glasses. These residual stresses were found to be a function of shear rate prior to shear cessation (Ballauff *et al.*, 2013; Fritschi *et al.*, 2014). Creep has also been extensively used to understand aging effects in hard sphere colloidal glasses (Ballesta and Petekidis, 2016; Siebenbürger *et al.*, 2012). The creep flow was understood macroscopically and linked with microscopic dynamics. Dynamic heterogeneous regions arising under creep experiments continue to grow in size until the steady flow condition is met where the full system begins to flow (Sentjabrskaja *et al.*, 2016).

Alternatively, large amplitude oscillatory shear is often employed to study the transient dynamics of colloidal glasses as well as the yielding response.

While hard spheres exhibited a non-monotonic dependence of oscillatory yielding point (γ_{cross}) with volume fraction approaching random closed packing (Petekidis *et al.*, 2002), a monotonic response was observed for softer particles when RCP was exceeded as the particles may interpenetrate and deform, thus transition to a jammed state (Koumakis *et al.*, 2012*b*). The non-monotonic response for hard sphere, an increase followed by a decrease in γ_{cross}, in colloidal glasses was attributed to the appearance and caging at low volume fraction. At high volume fractions, the disappearance of the cage distortion just before random closed packing is reached. Two kinds of yielding processes were identified the Brownian assisted yielding and shear induced yielding (Koumakis *et al.*, 2013) : Brownian-assisted yielding was observed to occur at low Pe while shear-induced yielding was observed at high Pe. High speed confocal microscopy was utilized to capture in-situ pair correlation functions of colloidal suspensions under LAOS (Lin *et al.*, 2013). Additionally, transient measurements like shear reversal were employed to identify the role of frictional and hydrodynamic forces(Lin *et al.*, 2015)

In this chapter, we present transient shear effects for nearly hard sphere glasses during steady and oscillatory shear using poly-methymethacrylate (PMMA) with poly-hydroxystearic acid (PHSA) hairs about 10nm to provide steric stabilization. The colloidal particles used for the following set of experiments have a radius $R = 106\,nm, 137\,nm$ with the polydispersity of the particles greater than 12% dispersed in two different solvent squalene and octadecene/bromonapthalene mixture. Anton Paar MCR 501 rheometer has been used for all the stress relaxation, shear reversal and creep measurements. LAOS measurements were performed in a stress-controlled Anton Paar 501 and ARES TA strain-controlled rheometer .

We also conducted stress relaxation employing BD simulations (Foss and Brady, 2000) using 50000 particles with 10% polydispersity and periodic boundary conditions for $\phi = 0.62, 0.60$ and 0.58 for $Pe = 0.01, 0.1$ and 1).

5.1 Stress Relaxation

5.1.1 Stress relaxation after steady state
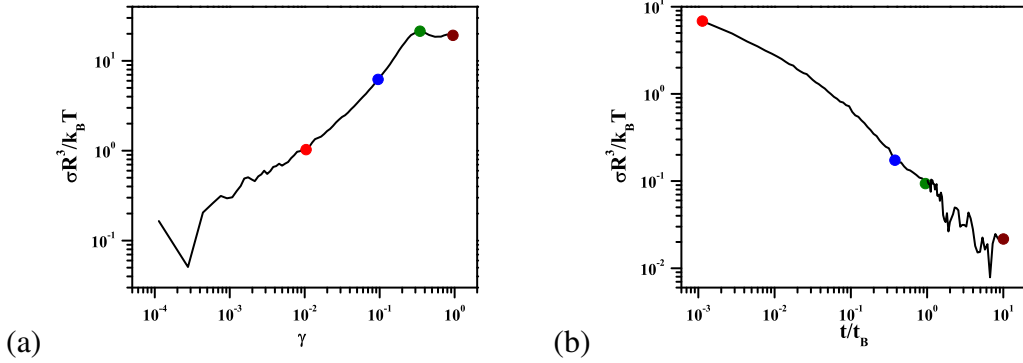
Figure 5.1: (a) Start-up shear at $\phi = 0.60$ and $Pe = 10$ and (b) stress relaxation for $10\ t_B$ after steady state is achieved for BD simulations. The colored points in (a) and (b) indicate the points where g(r) are shown in Figs. 5.2 and 5.3

Fig. 5.1 (a) is a representative start-up shear at $Pe = 10$ for a colloidal glass with $\phi = 0.60$ from BD simulations. Extensive information regarding the dynamics and structure have already been discussed in (Koumakis *et al.*, 2012*a*, 2016*b*). The colored points indicate the time within a start-up shear where the pair distribution function, $g(r)$, was exported as will be shown below. The start-up curve typically constitutes of an elastic regime where the cage distortion dominates. This is considered to be an elastic regime because if the stress on the system is released the cage will come back to its initial isotropic state. This elastic phase is followed by peak in the start-up stress at low volume fractions $0.54 < \phi < 0.60$ while it is generally weakening at high volume fractions as ϕ_{rcp} is approached (Koumakis *et al.*, 2016*b*). The last stage is the steady state flow where the system yields with simultaneous plastic events as well as cage breakage and reformations. Experiments assisted by MCT model suggests that the cages under shear in the elastic phase exhibit a transition from quadrapular symmetry to the hexadecupolar symmetry in the structure factor during steady state shear (Amann *et al.*, 2015).

A representative stress relaxation curve is shown in Fig. 5.1 (b) after ces-

sation of shear. The stress drops off to negligible values after $10t_B$. The dependence of residual stress after cessation of steady shear has already been investigated for hard sphere colloids (Ballauff *et al.*, 2013; Fritschi *et al.*, 2014) and soft jammed systems (Mohan *et al.*, 2013, 2015). In soft jammed systems a two-step relaxation was evident which is not the case in hard sphere colloidal glasses although sudden drops in the stress curve were detected as shown in the previous chapter. The colored points in the stress relaxation are related to the colored frames for which the pair distribution function is extracted during stress relaxation. In hard spheres residual stress was found to be a function of the Pe imposed on the colloidal glass. The higher Pe imposed on the the system, the faster the system releases internal stress (Ballauff *et al.*, 2013), although in absolute values larger residual stresses remain after large Pe shear.
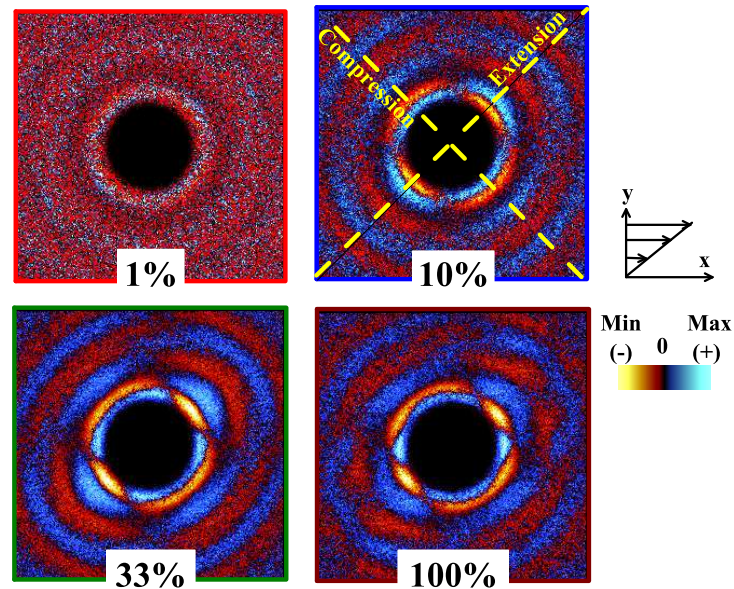
Figure 5.2: $g_{xy}(r)$ under shear subtracted from the $g_{xy}(r)$ rest for start-up shear at the colored points indicated in Fig. 5.1(a)

The pair distribution function in the velocity gradient plane is shown in Fig. 5.2 from the start-up test shown in Fig. 5.1 (a). At 1% strain the system is isotropic but as the strain is increased to 10% a clear deviation of $g(r)$ in extension and compression axis develops. This indicates that there is higher probability in finding the particle in the compression axis than in the extension axis and therefore the cage becomes anisotropic. As the strain is further increased

reaching 33%, at the peak of the shear stress, the $g(r)$ intensity in the extension axis becomes smeared out. Along the compression axis we observe development of clear lobes. As the system reaches steady state 100% the compression lobes becomes intensified along the flow direction as seen in Fig. 5.2 100%. The intensity of $g(r)$ in the extension axis is now lower than 33% because the system starts to yield, i.e., some cages will be breaking with particles escaping under shear and some other cages are being reformed.
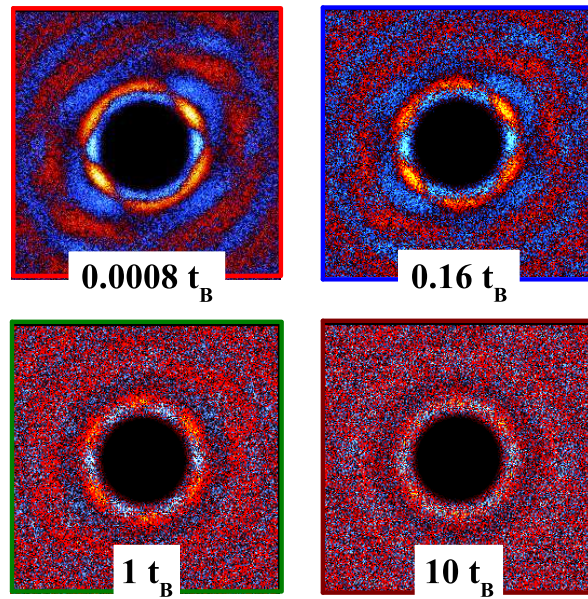
Figure 5.3: $g_{xy}(r)$ subtracted from rest for stress relaxation at the points indicated in Fig. 5.1(b)

The pair distribution function for the stress relaxation subtracted by the pair distribution function at rest shown in Fig. 5.3. In general, a gradual decrease in the intensity of the peaks in the compression and extension direction can be observed with waiting time. Compression and extension axis also disappears within $1\,t_B$. There appears to be a temporary crystallization or ordering appearing during the relaxation at in Fig. 5.3 at $1\,t_B$. At $10\,t_B$ this seems to disappear in $g_{xy}(r)$. The origin behind the appearance of temporary crystallization is not well understood here. Crystallization is not expected to occur in these simulation as 10% polydispersity was introduced to suppress it. Ordering of particles during shear is a possibility for suspensions in Brownian Dynamics simulations into hexagonal shear strings (Heyes and Melrose, 1993).
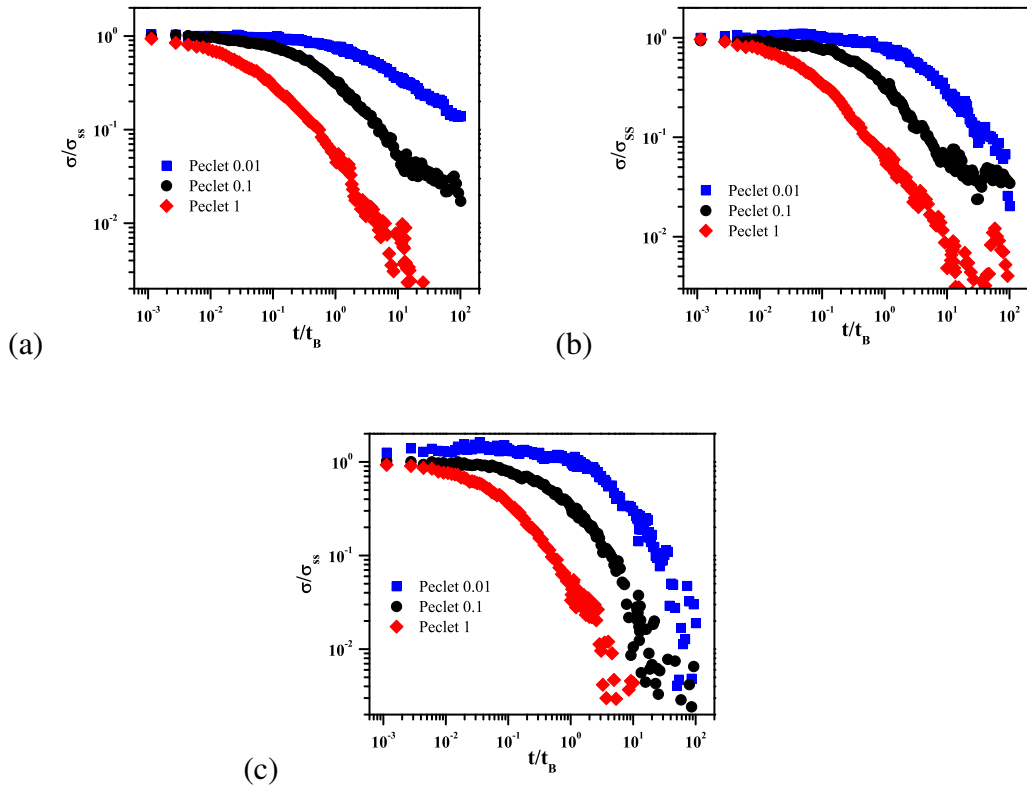
Figure 5.4: Stress Relaxation obtained from BD simulations after steady shear for various Pe at (a) $\phi = 0.62$,(b) $\phi = 0.60$ and (c) $\phi = 0.58$

University of Crete, Greece

Fig. 5.4 show the stress relaxation data versus time for different ϕ and Pe. The stress in the y-axis is scaled with the steady state value before flow cessation at the specific Pe. During steady state shear, the α relaxation of the non-equilibrium colloidal glass becomes accessible by experiments (Besseling *et al.*, 2007). As soon as the shear is stopped the α relaxation time increases with waiting time. If the relaxation time increases faster than the experimental waiting time, the system tends to exhibit residual stresses which has been predicted by a modified SGM model recently (Joshi, 2015). In Fig. 5.4 (a) for the highest ϕ and lowest Pe, BD simulations indicates the existence of 10% residual stress. On the other hand, at the highest Pe the stress relaxes faster than at low Pe. The system is driven further away from equilibrium under high Pe creating large structural deformation which upon shear cessation drives the system to relax faster. This happens for all volume fractions shown in Fig. 5.4. Moreover, there is essentially no evidence of the existence of residual stress for $\phi = 0.58$ in Fig. 5.4 (c). Due to the availability of larger free volume at $\phi = 0.58$ the stresses in the system can relax much faster and fully through local particle rearrangements. On the other hand, cage rearrangements becomes extremely difficult at very high ϕ and stress relaxation is only possible through cooperative motions (Weeks *et al.*, 2000). The number of correlated cooperative zones in the glassy state are however found to be very small compared to that in super cooled liquid (Weeks *et al.*, 2000). This can to lead to avalanche type stress relaxation where a particle hopping the cage leads to displacing a large region of particles for a short time scale as seen in Fig. 4.11. However this kind of behaviour is not captured in the BD simulations, possibly due to absence of hydrodynamic interactions, size of the simulation of box and periodic boundary conditions. Finally, the BD simulations in Fig. 5.4 corroborate the experimental stress relaxation data shown in Fig. 4.9 (Ballauff *et al.*, 2013).

It has already been established during start-up shear that the anisotropic deformation of the cage is responsible for the stress peak over shoot (Koumakis *et al.*, 2012a). In Fig. 5.5 the maximum of g_{xy} in the compression and extension axis are plotted as function of t_B during stress relaxation. The intensity in the extension axis (unfilled symbols) decreases with increasing Pe for all ϕ. The
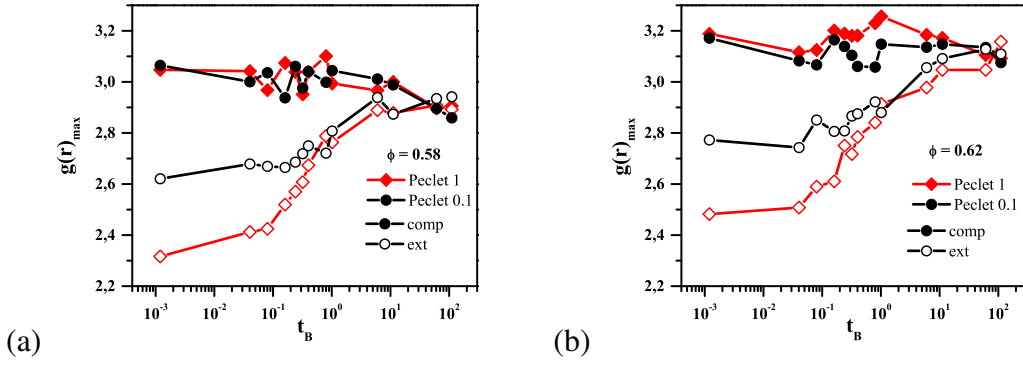
Figure 5.5: The maximum intensity in $g_{xy}(r)$ near the first neighbour peak in the extension and compression axis during stress relaxation of $100\ t_B$ for (a) $\phi = 0.58$ and (b) $\phi = 0.62$ from BD simulations

maximum along the compression axis is independent of Pe. When a comparison for different ϕ is made it can be easily seen that the extension axis is more elongated for lower ϕ. This can be attributed to the availability of more free volume at lower ϕ (Koumakis *et al.*, 2016*b*; Petekidis *et al.*, 2002) which leads to a more anisotropic cage. After shear cessation it can be observed that the g_{xy} maximum at extension axis decreases faster than the g_{xy} maximum along the compression axis. There is only very small observable difference along the compression axis indicating that extension axis plays more dominant role during stress relaxation than the compression axis. Although g_{xy} becomes isotropic by $100\ t_B$ there is evidence of residual stresses in the colloidal glass from Fig. 5.4 (a) at $Pe = 0.1$. A possible explanation is that the colloidal glass is heterogeneous in nature but the $g_{xy}(r)$ is obtained by averaging structure over all particles. Assuming that the contribution to residual stress is due the anisotropic cages in colloidal glass it cannot be captured here due to averaging performed in the simulations.

Fig. 5.6 shows the transient mean square displacement obtained from BD simulation during stress relaxation. MSD is extracted for different waiting times after cessation of shear. Fig. 5.6 (a) depicts the MSD extracted for $\phi = 0.58$ immediately after shear and waiting $1\ t_B$ after shear cessation. From this data it is evident that the system irrespective of the shear rate applied appears to have some microscopic mobility as a long time plateau in the MSD is not present. With increasing waiting time, however the system slows down more. After a
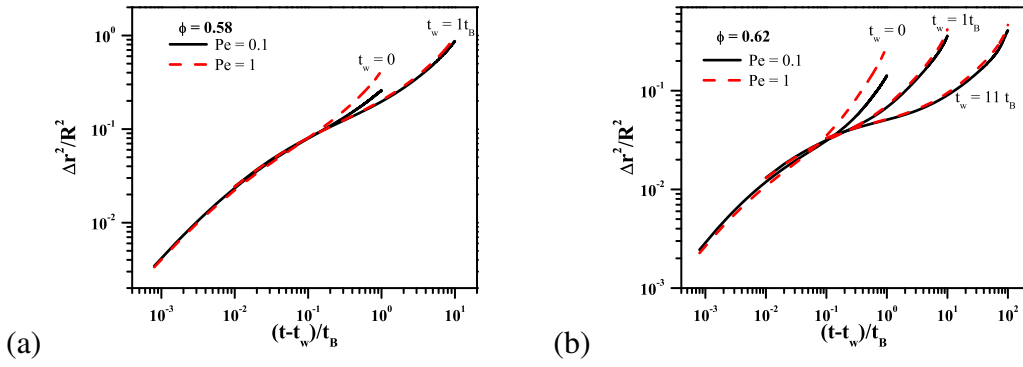
Figure 5.6: Mean Square Displacement for different waiting times after cessation of shear in BD simulations at (a) $\phi = 0.58$ and (b) $\phi = 0.62$

larger Pe shear, particle mobility is larger for all waiting times as seen in Fig. 5.6 (b). This gives a general insight in order to understand why the colloidal glass sheared at a higher Pe relaxes stress faster than at lower Pe. The fluidity arises possibly from the residual plastic deformations taking place in the colloidal glass after shear cessation. This occurs because colloidal particles are so closely packed that an out of equilibrium driving motion in one of the particles and its cages leads to an avalanche type of response in the whole system that dies out slowly with time.

5.1.2 Stress relaxation after interruption of flow

Below, we present experiments where we switch off the shear at different points along the start-up curve and follow the stress relaxation. As there are elastic and plastic regimes during start-up shear, we expect that the stress relaxation will show clear indications to differentiate between these regimes, i.e., relaxation of slightly deformed state yet unyielded cage and fully flowing system. Such a rheological protocol have been also performed in simulations for colloidal glasses (Zausch and Horbach, 2009).

Fig. 5.7 (a) represents an experimental start-up curve for $\phi = 0.63$. As expected the start-up stress overshoot peak is not pronounced at high volume fractions and the colloidal glass yields immediately after the elastic regime (Koumakis *et al.*, 2016*b*; Petekidis *et al.*, 2002). Fig. 5.7 (b) indicates the
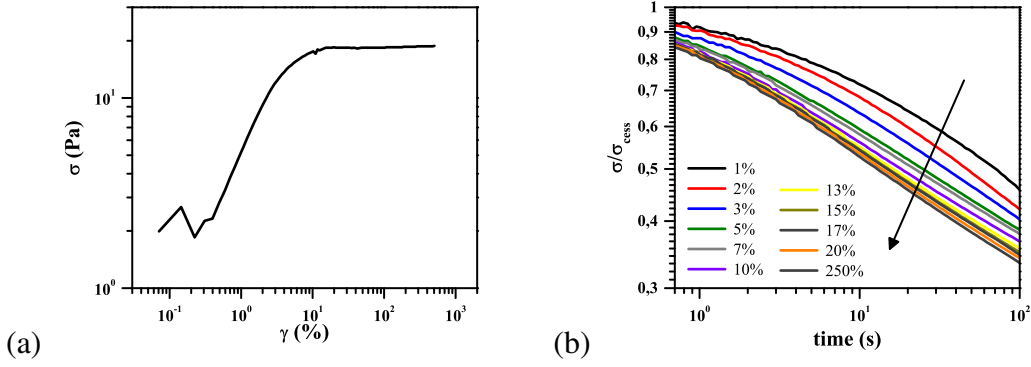
Figure 5.7: Colloidal particles with $R = 137\ nm$ in $\phi = 0.63$ undergoes (a) start-up at $\dot{\gamma} = 0.01$, $Pe = 5.265 \times 10^{-4}$ (b) Stress Relaxation after interruption of the start-up shear at different strains

stress relaxation after stopping start-up at various strains. It is clearly seen that switching of shear in the elastic regime before the steady state flow is reached leads to a weaker stress relaxation, i.e., the system retains more internal stresses. The ordinate axis in Fig. 5.7 (b) is scaled with stress just before cessation of shear. Switching-off shear in the elastic regime which is extending to less than 10% strain, leads to retaining more stress than in switching off the plastic/viscous dominated regime which lies above 10%. In very simple terms, the elastic regime tends to store the stress in the anisotropic cage deformation of the colloidal glass which is only partially released, on the other hand in the plastic dominated regime there is more dissipation of the stress due to the shear convection or the rearrangements of the cages (Amann *et al.*, 2015; Jacob *et al.*, 2015). However, no evidence is seen in BD simulations in Fig. 5.5 for the persistence of the anisotropic cages over long times, $t > 10\ t_B$, possibly due to averaging over all particles in the BD simulations that may remove the heterogeneities in the $g(r)$. Additionally, once the colloidal glass reaches the steady state flow, the relaxation curves lay one on top of each other within error. This indicates that once steady state is reached the magnitude of strain imposed does not influence the system.

Fig. 5.8 (a) depicts another scenario in a start-up curve, where a clear stress overshoot is detected. There exists same values of stress at two different strains related with two different microstructural processes. The red and blue dotted lines in Fig. 5.8 (a) are drawn to guide the eye in order to understand how
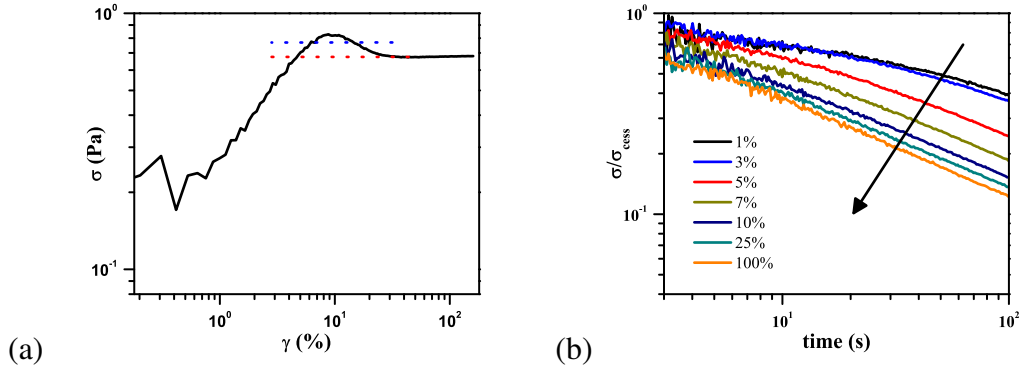
Figure 5.8: Colloidal particles with $R = 137 \ nm$ in $\phi = 0.56$ undergoes (a) start-up at $\dot{\gamma} = 0.01$, $Pe = 5.265 \times 10^{-4}$ (b) Stress Relaxation after interruption of the start-up at different strains

two identical values of stress indicates two different sequential processes taking place during start-up flow. Fig. 5.8 (b) shows the stress relaxation curves after stopping after reaching different strain values. As seen previously in Fig. 5.7, in the elastic regime most of the stress is retained where as in the flow regime, past the stress overshoot, switching off shear, leads to a much stronger, if not full relaxation. Additionally, the lower volume fraction of $\phi = 0.56$ below glass transition regime seen in Fig. 5.8 indicates that irrespectively of the volume fraction, the elastic regime in a start-up curve always holds more stress than plastic regime.
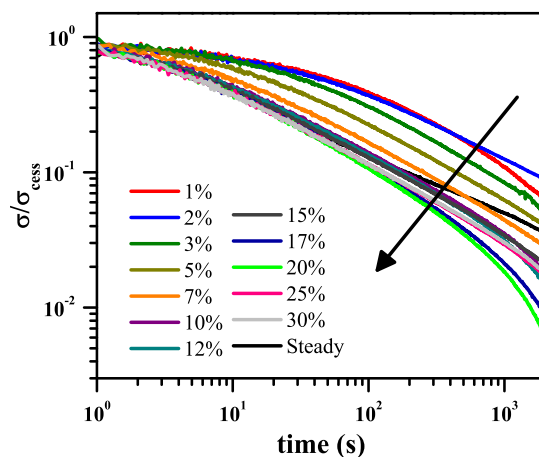
Figure 5.9: Long time stress relaxation after interruption of the start-up at different strains for $R = 137 \ nm$ in $\phi = 0.56$

However in Fig. 5.9, longer time relaxation of the stress is followed, till $2000\ s$. The long time relaxation exhibits a lot of fluctuations that is more difficult to interpret similar to (Mohan *et al.*, 2015). This is reminiscent of the long time relaxation and creep measurements discussed in the previous chapter (Fig. 4.11). Cooperative rearrangements of particles may be the microstructural origin of sudden release of stresses in the glassy regime. However, here a sample with $\phi = 0.56$ is in the super cooled liquid state (no crystallisation is seen due to polydispersity) thus the slow α relaxation is responsible for homogenising structural anisotropy and relaxing of internal stresses.

(a)   (b)
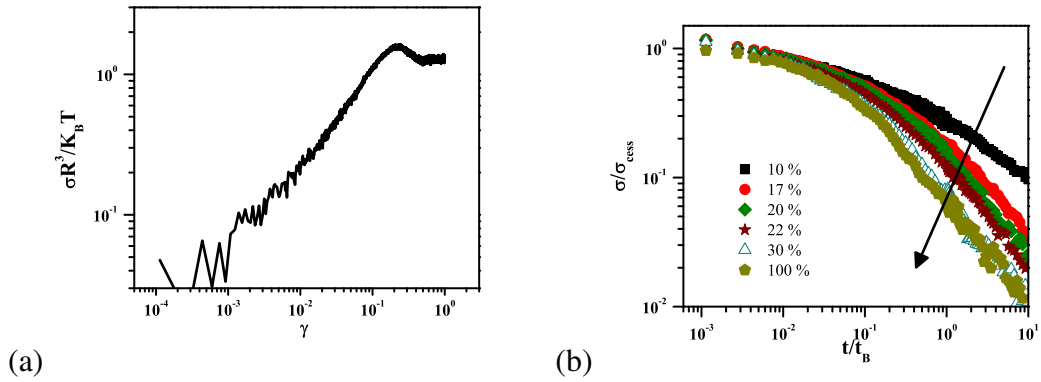
Figure 5.10: BD simulations (a) start-up at $Pe = 1$ (b) Stress Relaxation after interruption of the start-up at different strains for $\phi = 0.60$

In order to understand the microstructural characteristics during interruption of start-up flow, BD simulations were performed as shown in Fig. 5.10. It is evident that stopping within shear for BD simulations corroborates with experimental data shown in Fig. 5.7 and 5.8. In the elastic regime of start-up test, shear cessation leads to retaining more stress during relaxation than in the flow regime, past the stress overshoot. As the colloidal glass reaches steady state, the relaxation curve is independent of the magnitude of deformation similar to that observed in the experiments. Stress relaxation below 10% was not attempted in BD simulations as the noise was too large, not allowing depiction of the stress with good statistics.

In Fig. 5.11 we show structural information, by plotting the velocity - gradient 2D $g(r)$ for all the relaxation tests performed after cessation of shear at different points in the start-up from Fig. 5.10 at $Pe = 1$. 10% strain is in the
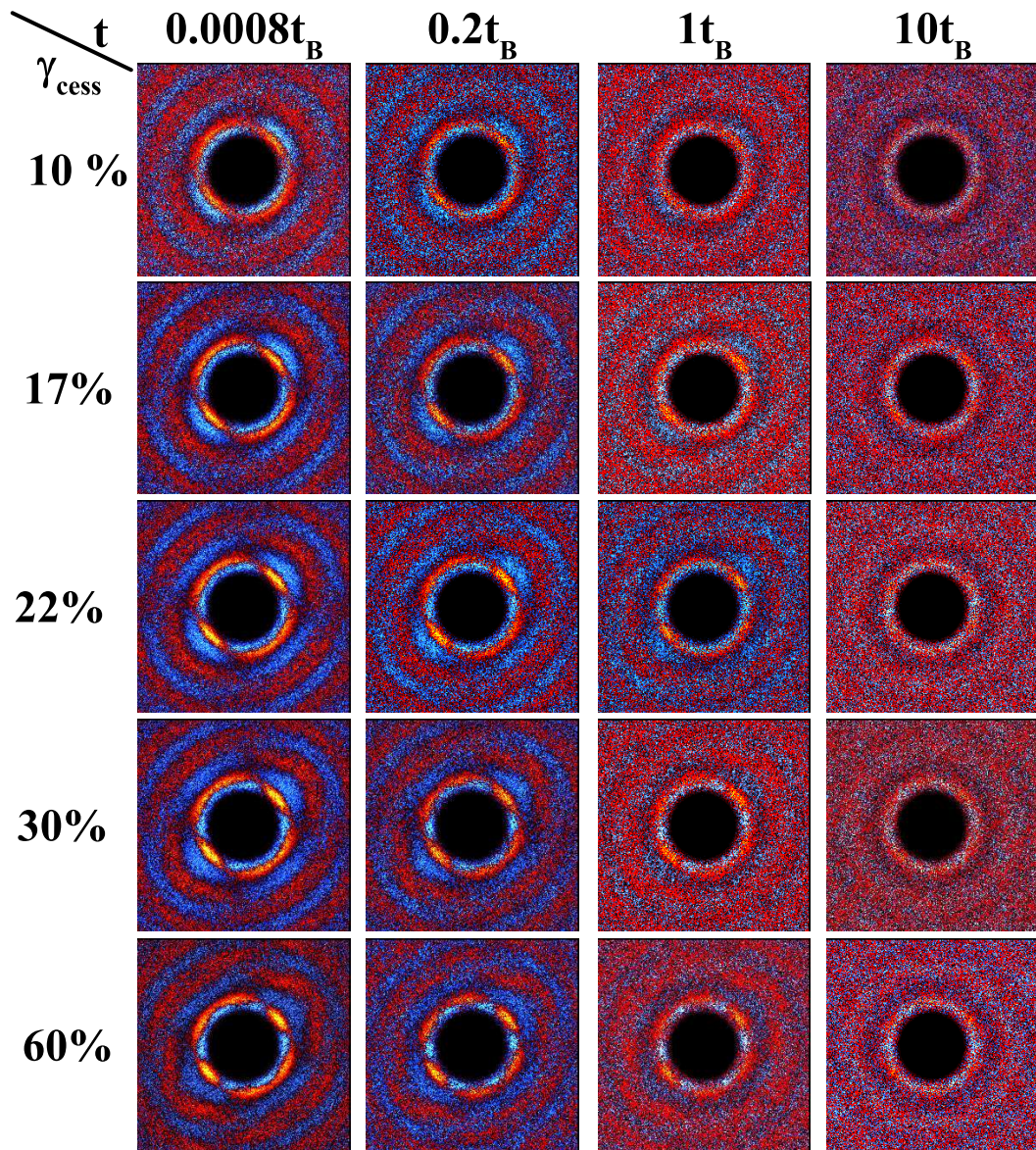
Figure 5.11: $g_{xy}(r)$, subtracted from rest, after cessation of shear at various time after different strain values are achieved during start-up with $Pe = 1$ seen in Fig. 5.10

elastic regime and 22% strain corresponds to the peak of the stress overshoot. After the system yields (30% and 60%) it can be noticed that the $g(r)_{xy}$ shows a temporary crystalline effect. This effect seems to fade away with time. This effect is pronounced for 60% strain. It should be noted that the $g(r)_{xy}$ is obtained after subtracting the $g(r)_{xy}$ at rest. Although the stress retention is higher for cessation at 10% strain the $g(r)_{xy}$ at 60% strain for which the relaxation occurs quicker has more anisotropy in the structure of the cage than 10% at 10 t_B as seen in Fig. 5.10. This leads to the conclusion that the structure of the cage alone does not contribute to the residual stresses unlike jammed soft glasses (Mohan *et al.*, 2013, 2015) where the structural anisotropy was the contributor to the residual stresses. Probably, it is the dynamical heterogeneities assisted with hydrodynamic interactions in colloidal glass that retain the stress and an indirect evidence to such a possibility is seen in Fig. 4.11 where the sudden drops in stress is possible due to avalanches in the colloidal sample.

5.2 Shear Rate and Stress Reversal

Thixotropy is defined as a reversible, time dependent and flow-induced change in the viscosity (Mewis and Wagner, 2012). Complicated rheological protocols were utilized to study thixotropy in different colloidal suspensions such as carbon black suspensions (Dullaert and Mewis, 2005, 2006). This mainly included stress jumps and shear reversal protocols in rheometry, and constitutive models were developed to capture this behaviour. Shear reversal protocols were also recently performed to understand the role of hydrodynamics and friction in shear thickening (Lin *et al.*, 2015). Stress relaxation was also performed within LAOS to identify signatures in the physical processes within large amplitude oscillatory shear (Koumakis, 2011). Another interesting technique is the so called mechanical hole burning spectroscopy performed on polymer solutions to identify the heterogenous effects (Shamim and McKenna, 2014). A large amplitude oscillatory pump is imposed on the sample to burn a mechanical hole in the system which was then probed with a linear step-strain experiment after a specific waiting time. Although, colloidal glasses fall into a very specific category

such that the thixotropic effects are not visible in linear regime, as shown in the previous chapter, these effects can be seen in non-linear experiments. Hence complex rheological protocols such as shear reversal is employed to capture this behavior of colloidal glass under shear.
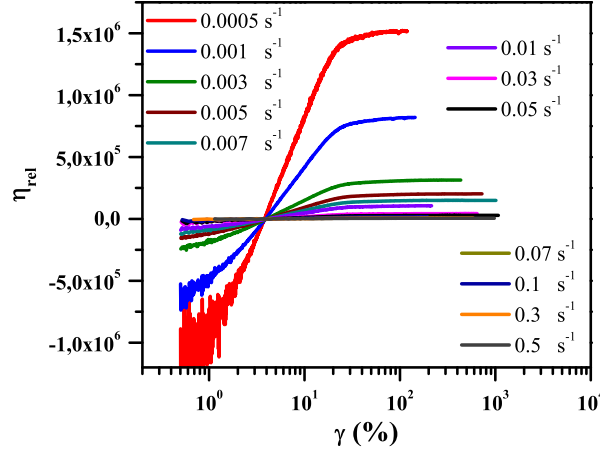
Figure 5.12: Shear Reversal of colloidal glass with $\phi = 0.63, R = 196 \ nm$ for varoius shear rates

Here in Fig. 5.12, we present the relative viscosity versus the strain for shear reversal experiment. Initially, a shear rate of a specific magnitude is applied in the forward direction on the sample until steady state flow is reached after which the flow is immediately reversed by application of same magnitude shear rate in the reverse direction. The relative viscosity is

$$\eta_{rel} = \frac{\eta(t)}{\eta_{sol}} = \frac{\sigma(t)}{\dot{\gamma}(t)\eta_{sol}} \tag{5.1}$$

The strain values in Fig. 5.12 indicates the strain achieved after switching the direction of shear. At low values of strain, or short time, the system has the memory of the the previous flow condition hence the relative viscosity is negative. The sign of the viscosity here indicates the direction of flow. Once the strain is reversed, the viscosity gradually changes from negative values to positive values and finally reaching a steady state as seen in Fig. 5.12. The steady state value of relative viscosity decreases with increasing rate as the relative viscosity is inversely proportional to the rate. All relative viscosity curves seem

to crossover at a particular strain from the negative value of relative viscosity to positive value, this is misleading as the strain axis is plotted in log-scale if plotted in linear scale the differences become evident as seen in Fig. 5.14.
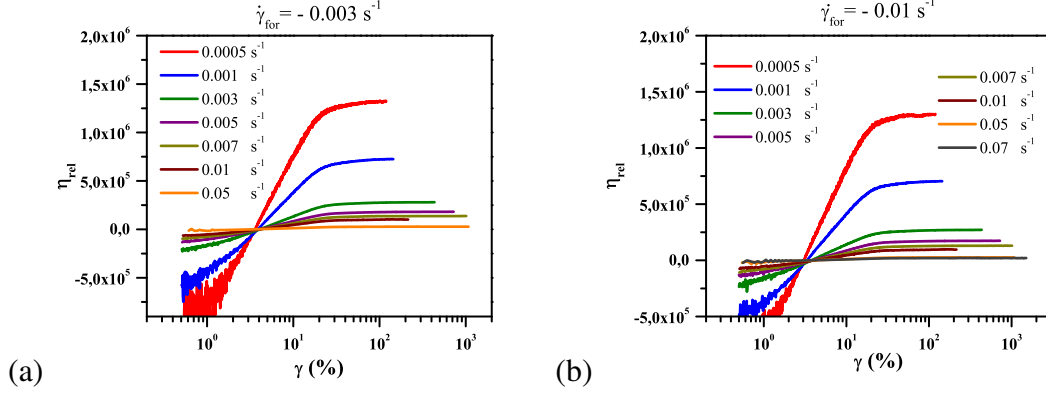
Figure 5.13: Shear reversal performed at forward rate of (a)$\dot{\gamma} = 0.003\ s^{-1}$ (b) $\dot{\gamma} = 0.01\ s^{-1}$ for varying rates in the reverse direction for a colloidal glass $\phi = 0.63$ and $R = 196\ nm$

In Fig. 5.13 (a) we employ a fixed shear rate ($\dot{\gamma}_{for} = 0.003\ s^{-1}$) in the forward direction until steady state flow is reached and immediately the flow is reversed at different rates. The magnitude of rate reversal is chosen such a way that rates slower and faster than the forward rate is achieved. Similar to Fig. 5.13 (a), Fig. 5.13 (b) indicates the different reversal rates for a forward rate of $\dot{\gamma}_{for} = 0.01\ s^{-1}$. This is performed in the same spirit as Fig. 5.12 in order to understand how the dynamics change if shear reversal is introduced from different steady states. Similarly to Fig. 5.12, the steady state viscosity values after shear reversal decrease with increasing rate. Additionally, although the starting steady state viscosity is same, the relative viscosity values are different in Fig. 5.13 at short times because the relative viscosity value is inversely proportional to the shear rate of reversal.

Fig. 5.14 is obtained by extracting the value of the strain, γ_{cross}, at crossover for the relative viscosity from negative to positive values in Figs. 5.12 and 5.13. When the forward and backward rates are the same, $\dot{\gamma}_{for} = \dot{\gamma}_{rev}$, γ_{cross} increases with shear rate. This is reminiscent of the increase of γ_{pk} monotonically during start-up shear with increasing shear rate (Koumakis *et al.*, 2016*b*). The cages under shear become anisotropic in the forward direction and after shear reversal they should change orientation and move in the opposite direction in order to
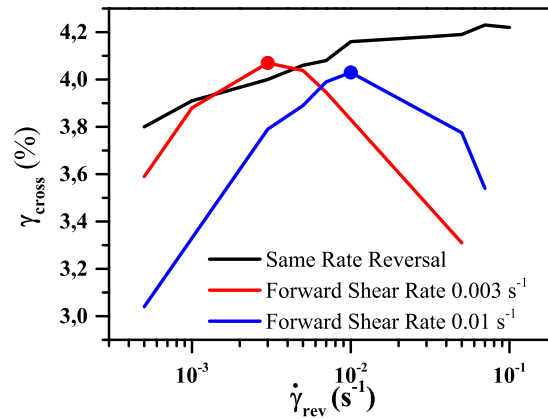
Figure 5.14: The γ_{cross} when the relative viscosity changes from negative to positive value. The dot indicates where $\dot{\gamma}_{for} = \dot{\gamma}_{rev}$

reach steady state flow. This happens because the anisotropic cages are oriented in the opposite direction upon shear reversal the cages become isotropic and then start to deform and flow in the opposite direction. Therefore, γ_{cross} value indicated here should be related to change in orientation of the cage. Additionally, at high rates γ_{cross} seem to reach a plateau (see Fig. 5.14) although there is a bigger error at high rates because data collection is not fast enough to capture γ_{cross} accurately. When $\dot{\gamma}_{for} \neq \dot{\gamma}_{rev}$ a non-monotonic dependence is observed for $\dot{\gamma}_{for}$ measured. This indicates that γ_{cross} depends only on the initial and final metastable states. The larger the difference between the γ_{for} and γ_{rev} the smaller is the value of γ_{cross}.

We now discuss a similar experiment where a step-stress is applied for 1000 s in the forward direction immediately after which the step-stress direction is reversed and applied for 1000 s. Fig. 5.15 (a) is creep reversal performed for a colloidal glass of $\phi = 0.63$ at various step-stresses. The dashed lines indicate the forward direction of step-stress and the solid line indicate the reversed direction. It is observed from Fig. 5.15 (a) that the colloidal glass in the forward direction is always more solid than in the reversal during the transients near the creep ringing. This suggests that the colloidal glass has been pushed into a metastable state in the forward direction which upon stress reversal facilitates easier flow (or creep) although it catches up in the long run. Additionally,

(a)

(b)
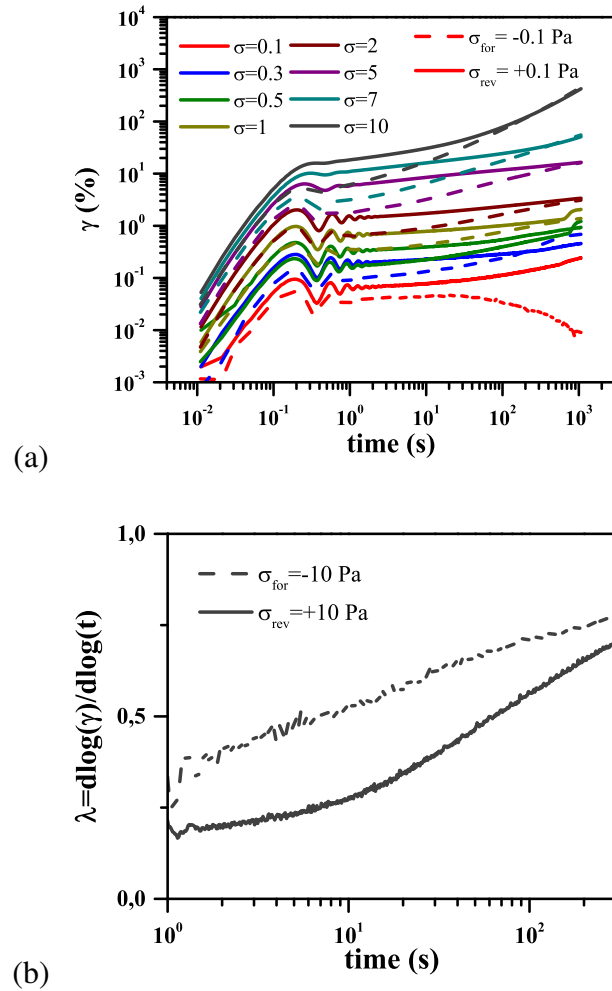
Figure 5.15: (a) Creep Reversal of colloidal glass with $\phi = 0.63$ and $R = 196\ nm$ for varying σ (b) λ for $\sigma = 10\ Pa$ in forward and reverse direction

with the increase in the step-stress values the difference between reversal strain and forward strain for time $t < 1\ s$ becomes larger. For strep stresses the final strain in the forward and reversed creep reach the same values except for the lowest stress $\sigma = 0.1$. A representative of the slope in the creep data shown by $\lambda = dlog(\gamma)/dlog(t)$ in forward and reverse direction for $\sigma = 10\ Pa$ is shown in Fig. 5.15(b). The slope of forward direction is found to be always higher than the reverse direction. This suggests that two different process happens in the forward and reverse direction. The colloidal glass undergoes yielding in the forward direction and then upon reversal the systems attains metastable state at reversal very easily.

Recently, employing confocal microscopy te single particle dynamics under creep of colloidal glasses were investigated (Sentjabrskaja *et al.*, 2016). Heterogeneous domains were observed to appear and then grow in colloidal glasses until these regions merge and the flow under creep occurs. From Fig. 5.15 (a) it can be speculated that such heterogeneous domains developed during creep in the forward direction assist in the glass to creep much more easily during reversal. Thus, more strain is achieved during creep reversal.

5.3 Large Amplitude Oscillatory Shear

5.3.1 Fourier Transform rheology

In this section we show that frequency variation even over a relatively small range of one order of magnitude can profoundly affect the LAOS response. Moreover, we conclusively show that an increase in frequency has opposing effects depending on whether the colloidal dispersion is in a liquid or glassy state; it leads to increasing anharmonic behavior below the glass transition, but decreasing anharmonic response above the glass transition. We explain the observed variation of non-linearity with frequency above and below the glass transition using recent insights that relate the LAOS response with the SAOS response and the flow curve of the material.
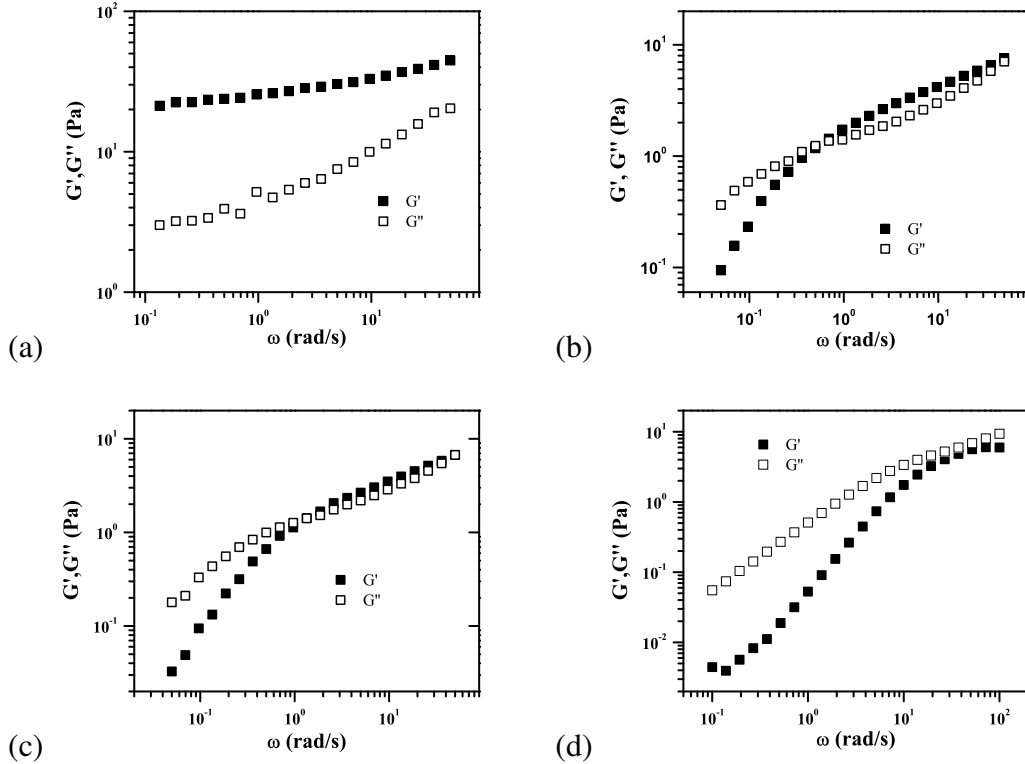
Figure 5.16: Dynamic Frequency Sweep of a colloidal suspension with (a) $\phi = 0.60$, (b) $\phi = 0.54$, (c) $\phi = 0.53$ and (d) $\phi = 0.49$

A universal behavior in colloidal glasses and concentrated suspensions systems during LAOS irrespectively of the interaction potential was validated with the help of PMMA hard spheres and soft star-like diblock copolymer micelles (Poulos *et al.*, 2015). In this case the LAOS frequency dependence of four HS samples at $\phi = 0.49, 0.53, 0.54, 0.60$ is probed. The dynamic frequency sweeps for $\phi = 0.49, 0.53, 0.54, 0.60$ samples can be seen in Fig. 5.16(a-d). It is clear that the $\phi = 0.60$ sample is in the glassy state, the intermediate concentration,($\phi = 0.52, 0.53$) is a viscoelastic liquid and shows a crossover of G' and G'', and the $\phi = 0.49$ sample shows terminal liquid-like behavior (G', G'') in a wide frequency range.

Dynamic strain sweeps are performed at different frequencies on all samples as shown in Fig. 5.17. These show a typical stress response of an either yield stress solid (at $\phi = 0.60$ in Fig. 5.17 (a)) or a shear thinning liquid (at $\phi = 0.49$ Fig. 5.17 (d)). Intermediate volume fractions ($\phi = 0.54, 0.53$) show both sets of behaviour depending on the frequency of strain sweeps since a large
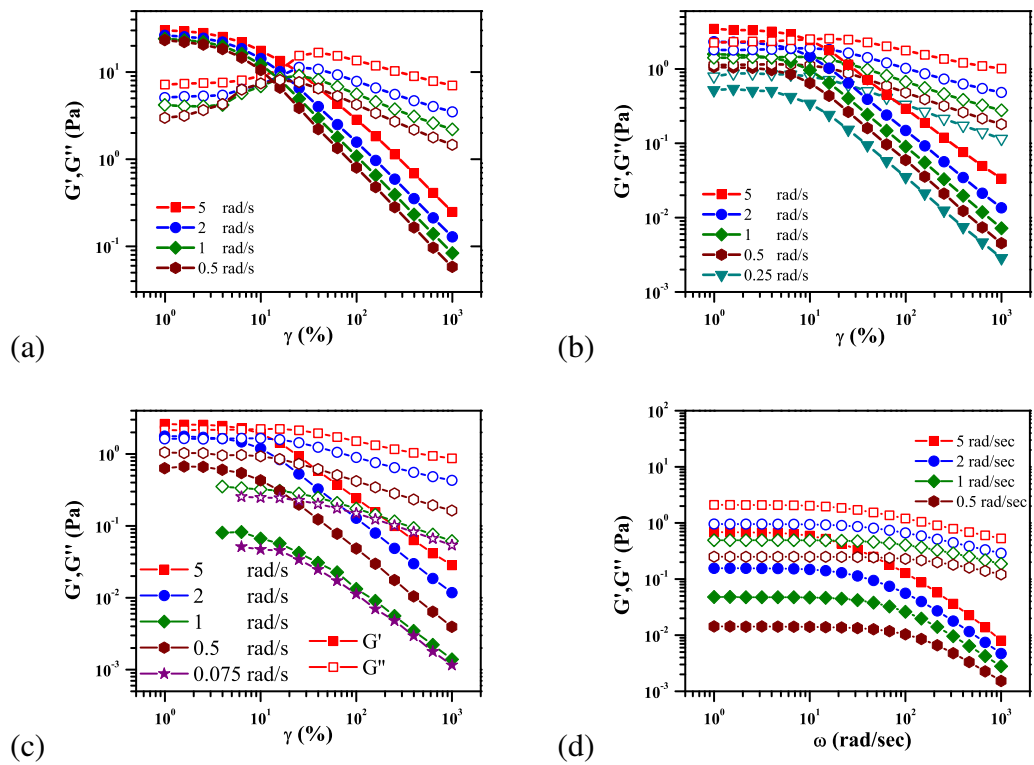
Figure 5.17: Dynamic strain sweep attempted in order to perform LAOS experiments for (a) $\phi = 0.60$ and (b) $\phi = 0.54$, (c) $\phi = 0.53$ and (d) $\phi = 0.49$

dependence of the linear viscoelastic data on frequency is observed. This arises since the linear viscoelasticity moving from a glass to liquid phase starts to exhibit a frequency dependence as seen in Fig. 5.16.

The stress signal was further analyzed at each strain amplitude by FT rheology, and the non-linearity was quantified by the amplitude of the 3rd stress harmonic normalized by the 1st harmonic I_3/I_1 (Wilhelm $et\ al.$, 1998). It should be noted that in general higher harmonics are also important (Poulos $et\ al.$, 2013), and that there are other methods of analysis used to quantify non-linearity (Hyun $et\ al.$, 2011), but for the purposes of this study we follow I_3/I_1 as an indicator of the level of anharmonic stress response in the nonlinear oscillatory shear. In Fig. 5.18, I_3/I_1 is plotted as a function of γ_o for the $\phi = 0.49, 0.53$ and 0.60 samples respectively. It is similar to star-like micelles (Poulos $et\ al.$, 2015), with I_3/I_1 increasing at yielding and developing to a plateau at high γ_o. One major difference is that for the highest concentration glassy sample ($\phi = 0.60$), a peak in I_3/I_1 appears at intermediate amplitudes ($\gamma \approx 10 - 30\%$) for the two highest frequencies Fig.5.18(a); this has been attributed before to a second yielding process and will be discussed below (Koumakis $et\ al.$, 2013).

In Fig. 5.19 I_3/I_1 is plotted as a function of ω at a fixed amplitude of 100% strain, for all volume fractions. Similarly to star-like micelles (Poulos $et\ al.$, 2015), the highest concentration glassy sample ($\phi = 0.60$) shows a decrease of I_3/I_1 with frequency, and the lowest concentration liquid sample ($\phi = 0.49$), shows an increase of I_3/I_1 in the frequency regime measured. Additionally, the intermediate $\phi = 0.53, 0.54$ samples show non-monotonic behavior with I_3/I_1 increasing at low frequencies and decreasing at high frequencies.

For HS glasses a decrease of I_3/I_1 with increasing frequency has been seen before (Koumakis $et\ al.$, 2013). Combining experiments and BD simulations, it was attributed to the transition from a plastic-like response to a simpler liquid-like response, while also a second yielding process emerged at even higher frequencies. Lower frequencies were associated with Brownian activated yielding, while higher frequencies to shear-induced non-Brownian yielding. The peak of I_3/I_1 found for increasing strain at higher frequencies was attributed to the ap-
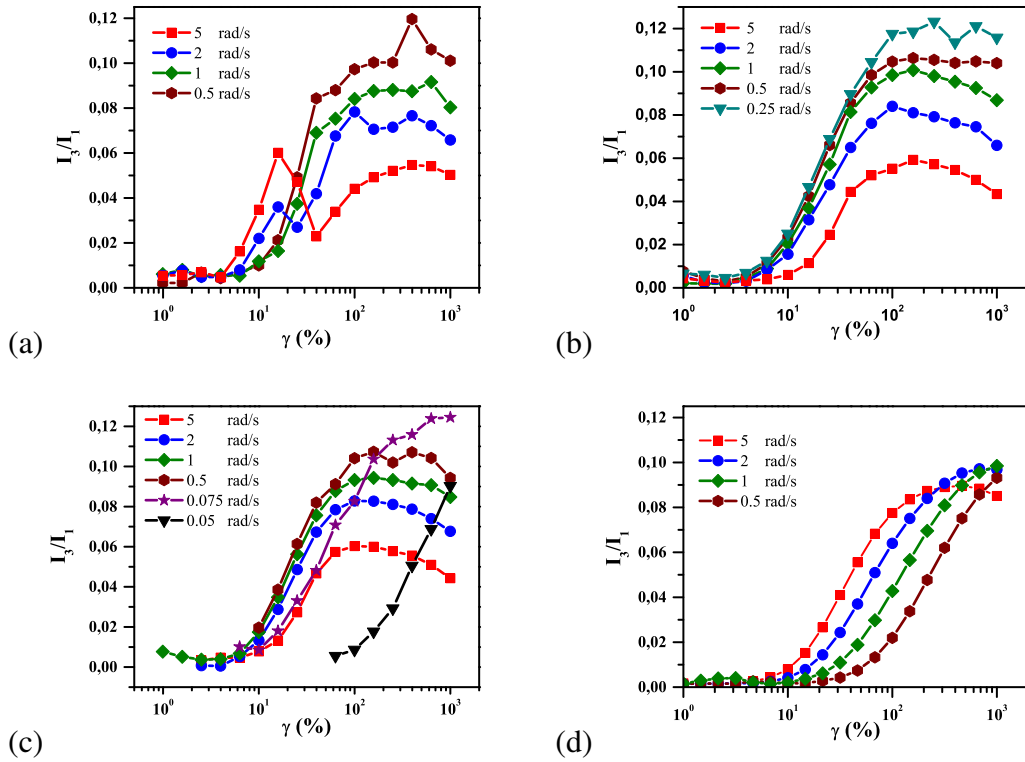
Figure 5.18: 3rd harmonic parameter obtained from Fourier Transform rheology versus γ at (a) $\phi = 0.60$, (b) $\phi = 0.54$, (c) $\phi = 0.53$ and (d) $\phi = 0.49$
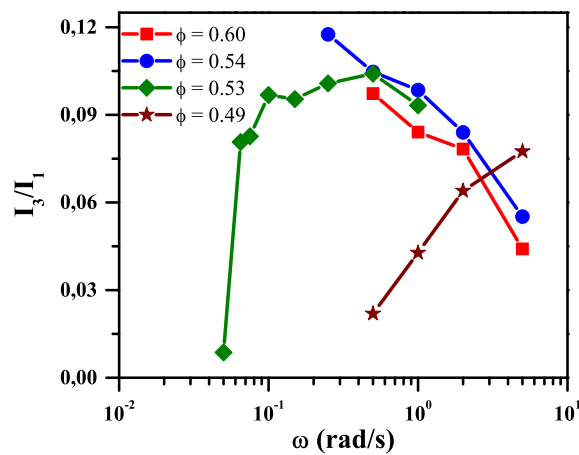
Figure 5.19: 3rd harmonic parameter versus ω for all the volume fraction in Fig. 5.18 at $\gamma_0 = 100\%$

pearance of this second yielding process. For intermediate HS volume fractions, the frequency dependence of I_3/I_1 shows a broad peak in Fig. 5.19. In contrast to the case of star-like micelles, where the chosen frequencies were taken far from the crossover of G' and G'', the hard sphere data show the transitional behavior expected near that point (Poulos *et al.*, 2015). Therefore, it show an increasing I_3/I_1 versus ω, when the linear response is liquid-like and decreasing I_3/I_1 when the linear response becomes solid-like. The similarities in the behavior of I_3/I_1 between hard spheres and star-like micelles suggest a possibility of an independence from specific particle interactions (Poulos *et al.*, 2015). In the case of hard spheres, I_3/I_1 versus ω eventually reached a maximum and then started to decrease at higher ω.

In summary, LAOS experiments were performed at a range of frequencies on four colloidal hard sphere samples above and below the glass transition. It is observed that an increase in frequency from 0.5 rad/s to 5 rad/s leads to an increase of anharmonicity for the liquid-like samples, but to a decrease of anharmonicity for the solid-like samples. This difference can be explained by looking at the contribution to non-linearity at the maximum shear rate inside the period of oscillation. As the frequency is increased, the maximum shear rate is also increased. Thus, for the liquid-like samples, higher shear rates leads to shear thinning over a larger fraction of the period thereby increasing anharmonicity. On the other hand, the solid-like samples at low shear rates are trapped in the yield stress plateau and do not flow but deform plastically. Higher shear rates lead to viscous flow over a larger fraction of the period thereby decreasing anharmonicity. The transition and change in slope of I_3/I_1 from solid- to liquid-like samples is broader at the intermediate volume fraction HS samples where the storage and loss moduli have not reached the terminal regime.

5.3.2   Onset of non-linearity during LAOS

Here we present the onset of non-linearity by evaluating, the anharmonic stress response, of a hard sphere colloidal glass at $\phi = 0.60$ and suspension at $\phi = 0.49$. The anharmonicity in the stress response is expressed as I_3/I_1 the same

quantity as defined in the previous section. Fig. 5.20 indicates the linear vis-coelastic response of colloidal glass and colloidal suspension. In Fig. 5.20 (a) where G' is greater than G'' for all the ω probed which is a representation of a colloidal glass. The minimum in G'' is also seen in Fig. 5.20 (a) which is related to the transition from α to β relaxation in the colloidal glass. Fig. 5.20 (b) shows a colloidal suspension much below the colloidal glass transition. For all frequencies probed $G'' > G'$ which is indicative of a system with a liquid-like response.

(a)   (b)
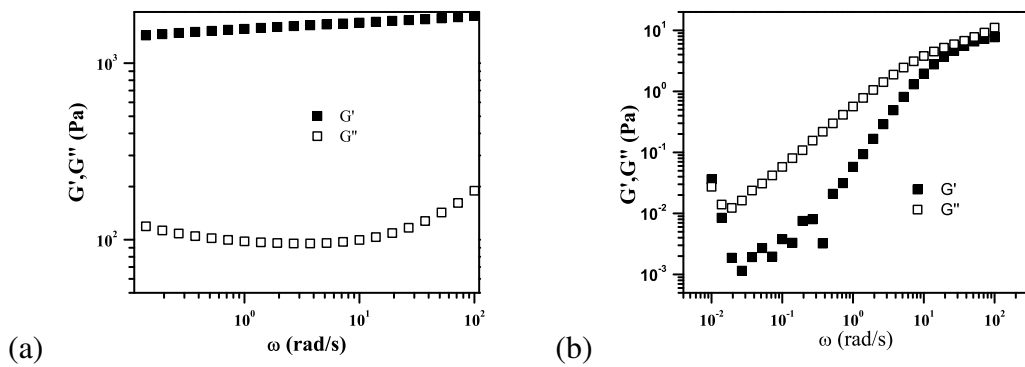
Figure 5.20: Dynamic frequency sweep at (a) $\phi = 0.60$ and (b) $\phi = 0.49$

(a)   (b)
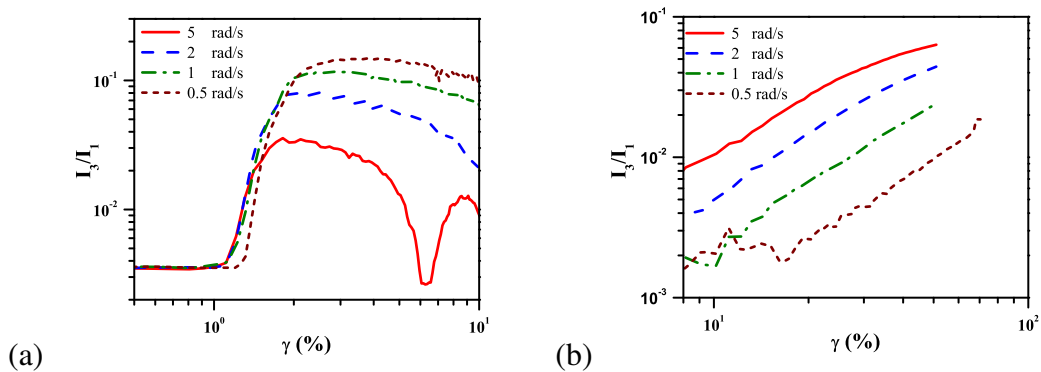
Figure 5.21: The third harmonic parameter for medium amplitude oscillatory measurements in order to capture the onset of non-linearity for (a) $\phi = 0.60$ and (b) $\phi = 0.49$

Data in Fig. 5.21 are produced by sweeping γ_o for a fixed frequency with linear spacing of 0.5% from 0.1% to 10%. This is done in order to capture the transition from linear to non-linear regime by following the amount of non-linearities in the LAOS response. Finally, Fourier transform analysis of the stress oscillation is performed and the non-linearity in the stress for a colloidal

glass and concentrated colloidal suspensions are probed. The data in Fig. 5.21 correspond to the sample shown in Fig. 5.20. Fig. 5.21 (a) shows that the non-linearity in colloidal glass arises always around $\gamma_o \approx 1\%$. Additionally, there is a slight variation at the γ_o at which I_3/I_1 arises with frequency. The non-linearity becomes prominent at lower γ_o with increasing frequency for the colloidal glass shown in Fig. 5.21 (a) and Fig. 5.21 (b) shows the non-linearity in colloidal suspension. For $\phi = 0.49$ the data below $\gamma_o = 8\%$ are extremely noisy. In Fig. 5.21(b) we observe a clear dependence of the onset of non-linearity with the frequency. This kind of frequency dependence in colloidal glass and colloidal suspension is reminiscent of the linear data shown in Fig. 5.20 where the colloidal glass exhibits the expected weak linear dependence whereas the colloidal suspension has a strong dependence on the frequency. The dip in I_3/I_1 seen at $5\ rad/s$ in a colloidal glass has already been observed and reported for colloidal glasses in Fig. 5.21 (Koumakis *et al.*, 2013). This indicates the systems transitioning from linear oscillatory response to plastic flow at large amplitude strains.
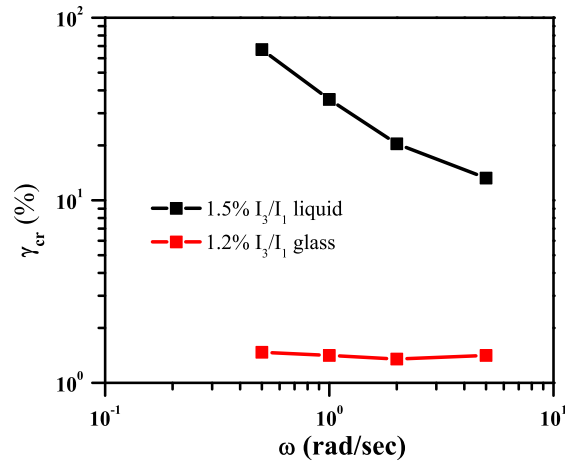
Figure 5.22: Onset of non-linearity, γ_{cr} versus ω for $\phi = 0.60$ and $\phi = 0.49$

In Fig. 5.22 we compare the γ_{cr} at a fixed value for I_3/I_1. As discussed earlier, colloidal glass exhibits a transition to non-linear regime at lower values of γ_o which is also evident from Fig. 5.17. The cages in the colloidal glass providing elasticity in the system can be pushed into a non-linear regime with a small amount of deformation. On the other hand, for concentrated colloidal sus-

pensions a decreasing γ_{cr} is detected with increasing ω. Colloidal suspensions ($\phi = 0.49$) due to their Brownian motion can compete with shear to maintain their equilibrium microstructure even at strains close to 10%. As the frequency of oscillation is increased, the system is pushed out of equilibrium for much lower strain because the Brownian motion cannot compensate for the frequency applied. Recently, the effect of caging in colloidal glass has been investigated with third harmonic elastic and viscous moduli and very similar observations were reported (Kumar *et al.*, 2016).

5.4   Shear thickening colloidal glasses

In this section we present rheological experiments for colloidal suspensions with radius $R = 689\ nm, 405\ nm, 137\ nm$ in dense suspensions and glasses aiming to study some aspects of shear thickening. Rheology experiments were performed on colloidal glass with sterically stabilized PMMA particles in squalene. The largest colloidal particle ($R = 689\ nm$) was investigated in the glass ($\phi = 0.60$) and in supercooled liquid regime ($\phi = 0.56$) while the smaller size particles where investigated only in the glass regime ($\phi = 0.60$). All particles have greater than 6% polydispersity in the radius. The Brownian time t_B are calculated to be $22.87 s, 4.645\ s$ and $0.0179\ s$ for particle radius of $R = 689\ nm, 405\ nm$ and $137\ nm$ respectively.

A glass cone and plate geometry attached to Anton Paar MCR 501 rheometer was utilized for the shear experiments. The specifications of the glass cone are as follows - diameter = $40\ mm$, angle = $1.967\ °$ and gap = $176\ \mu m$. A high speed Basler camera was used to capture the edge effects during shear thickening and images were recorded every $100\ ms$ for a specific amount time depending on the length of the shear experiment. Each transient start-up measurement was performed after a waiting of $200\ s$.

Fig. 5.23 (a) represents the scaled linear viscoelastic rheological data for the colloidal glass systems that were investigated for shear thickening properties. The colloidal glass of large particles in Fig. 5.23 (b) shows discontinuous shear
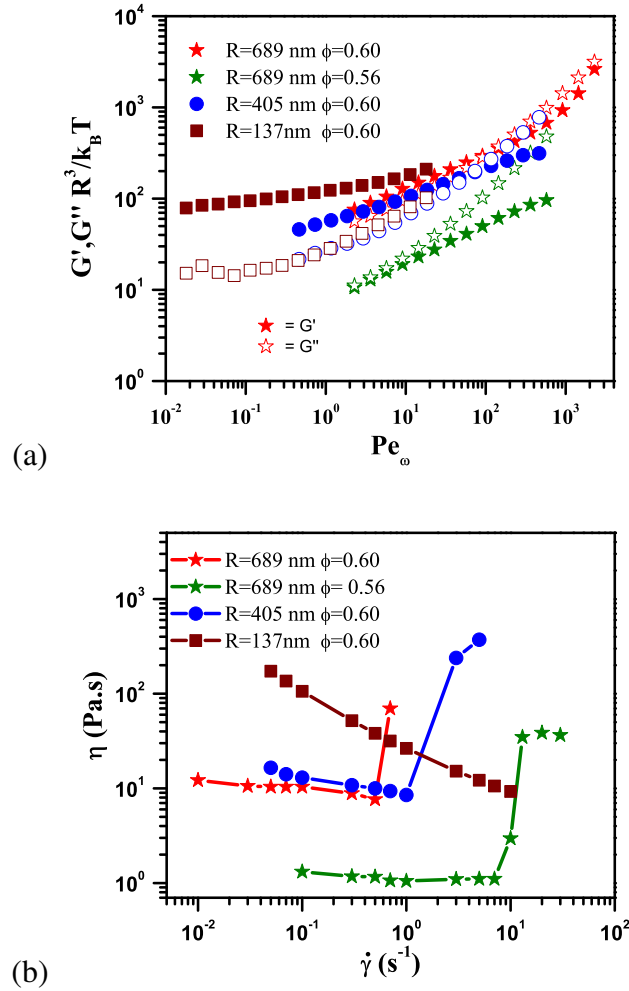
Figure 5.23: (a) Dynamic Frequency Sweep in the linear regime of the samples tested for shear thickening. (b) Flowcurve of the corresponding samples indicating shear thinning and thickening behaviour at high rates.

thickening with a sudden jump in η at a specific $\dot{\gamma}$. The colloidal glass consisting of radius $137\ nm$ only shows the shear thinning behaviour that is prevalent of among colloidal glasses. The critical shear rate above which the shear thickening is seen to be a function of size of the particle as well as the volume fraction. The larger size particles shear thicken at lower $\dot{\gamma}$ as the Pe experienced by the larger particles for the same shear rate is much larger than the small particles. This drives the larger size particles into shear-induced collisions and jamming leading to a shear thickened state. The larger volume fractions shear thicken at lower shear rates because of the reduction in free volume as well as increase in the Brownian time.
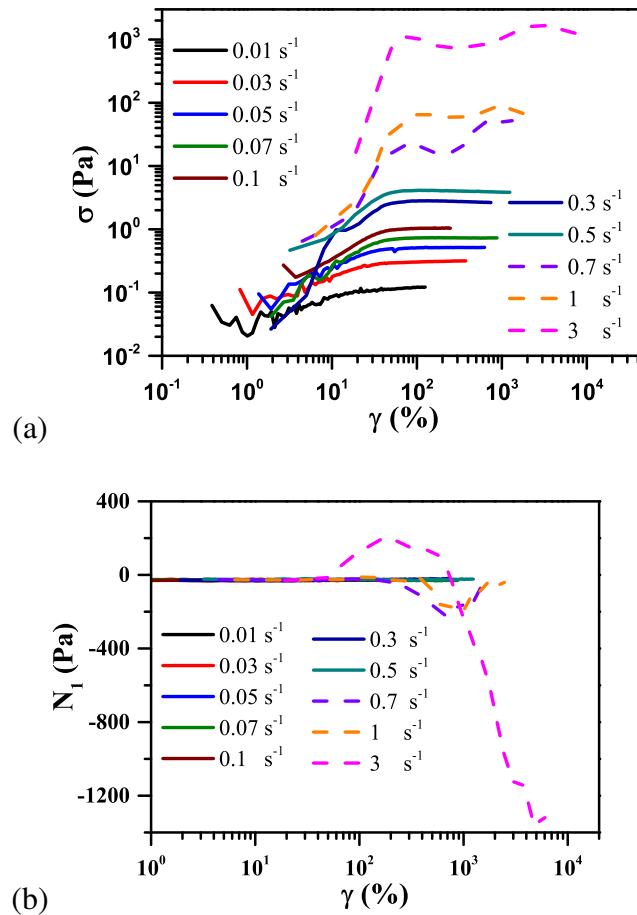
Figure 5.24: Start-up of colloidal glass with particles of $R = 689\ nm$ where the dashed lines indicates the shear thickening response for (a) $\phi = 0.60$. (b) The corresponding N_1 data for the shear rates performed during start-up with $\phi = 0.60$

Fig. 5.24 (a) shows the start-up stress data at rates below and above crit-

ical rate for shear thickening. Below the critical rate, the glass sample shows a typical response to start-up shear consisting of elastic regime and the steady state flow regime. At start-up for rates larger than the critical rates a very sudden increase in the stress as well as oscillations in the stress can be observed which have earlier be identified with the help of dichroism studies (D'Haene *et al.*, 1993). The oscillations during shear thickening are attributed to jamming and unjamming transitions under flow. In this study, since the shear rate is maintained as at a particular value the jammed clusters will be ripped apart or unjammed and then again jammed into other jammed clusters.

N_1 is the first normal stress difference which is defined as explained $\sigma_{xx} - \sigma_{yy}$ as in Chapter 2. N_1 data for the corresponding start-up curves are represented in Fig. 5.24 (b). Below the critical shear rate N_1 values do not show any fluctuations and are slightly negative. But above the critical shear rate the large fluctuations in N_1 are observed. In general, the normal stress data should be taken cautiously because instabilities, granulation and edge fracture are prevalent in these highly concentrated suspensions (Brown and Jaeger, 2014; Cates *et al.*, 2005) as will be discussed. Additionally, the stress fluctuations are correlated to the N_1 fluctuations. At $3\ s^{-1}$ the N_1 rises to positive values which indicates the forces being exerted to separate the plates apart. After a particular time N_1 moves to negative values which indicates the plates are pulled together due to the expelling of the sample through the edges.
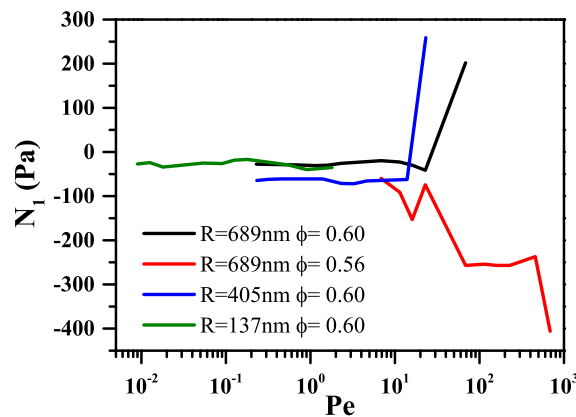
Figure 5.25: N_1 comparison for different particles radius.

Fig. 5.25 compares N_1 for all the colloidal systems investigated in Fig. 5.23 (a). The large particles that show strong shear thickening behaviour in Fig. 5.23 (a) in turn showing large variation in N_1. N_1 values for shear thickening systems here are represented for short times before large fluctuations in N_1 sets in. This is done to avoid any kind of artifacts from edge fracture or slip becoming predominant. Interestingly, colloidal glasses exhibits change of N_1 towards positive values while the samples at lower ϕ that are below the glass transition show predominantly negative N_1. This is in line with the observations for concentrated colloidal suspensions for $\phi \leq 0.52$ that indicated negative values for N_1 (Cwalina and Wagner, 2014). Frictional contacts was discovered to contribute to shear thickening near jamming transitions (Lootens *et al.*, 2003) and discontinuous shear thickening was modeled successfully with the help of friction contacts (Seto *et al.*, 2013). Here, at $\phi = 0.60$ the positive values could be due to the prominence of dilatation effect. At large ϕ, particles have very small free volume hence this leads to much easier contacts between them at large Pe. On the other hand at $\phi = 0.56$ due to larger free volume the system shear thickens due to hydrodynamic effects leading to negative values of N_1 as already predicted (Foss and Brady, 2000). It can also been seen that the glassy state shear thicken at much smaller Pe than the super cooled liquids and for the small particles even for $\dot{\gamma}(Pe < 1)$ is small to induce shear thickening.

In order to capture the edge effects that becomes important during shear thickening, a camera is attached to the side of geometry in Fig. 5.26 the start-up shear stress, σ, and normal stress, N_1, of a colloidal glass at $\phi = 0.60$ with particles of radius $689\ nm$ sheared at $\dot{\gamma} = 3\ s^{-1}$ is shown where edge instabilities are visually observed. In Fig. 5.26 at point C dilation was visually observable, the sample at the edges increased in volume. After point C (corresponding to $\gamma = 280\%$) clear edge instabilities are visible which subsequently continue to grow at the edge of the sample. During dilation, N_1 values remain positive until instabilities become prominent leading to negative N_1 values. Moreover, the sample becomes opaque at the edges indicating that the sample surface becomes rougher due to microscopic instabilities. As shear thickening occurs the opacity and edge instabilities starts increasing thus reflecting more light of the edge.
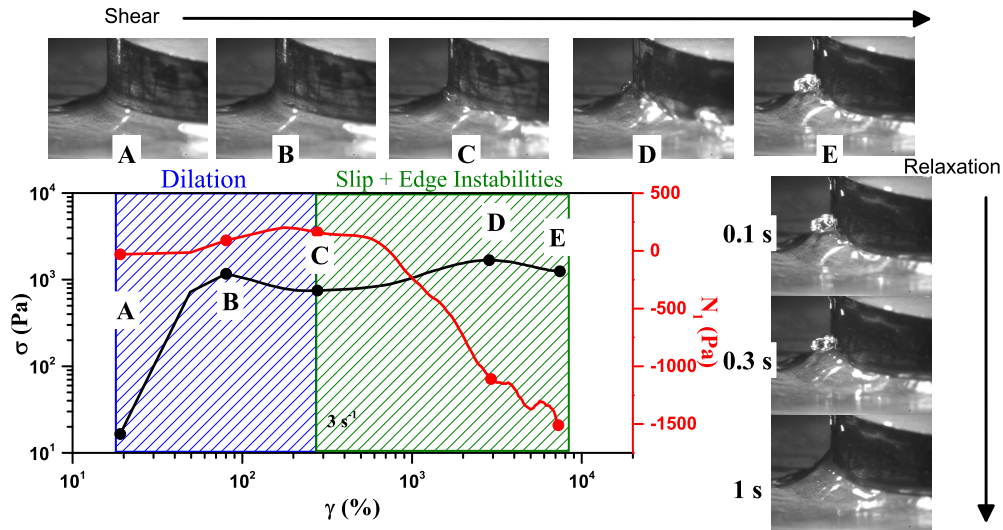
Figure 5.26: start-up of colloidal glass of $\phi = 0.60$, $R = 689\ nm$ and $\dot{\gamma} = 3\ s^{-1}$ shown in Fig. 5.24 (a) with images indicating the edge effects, slip and dilation

This is due to the presence of particle clusters jammed together in the sample as already observed from the dichroism measurements (D'Haene *et al.*, 1993). Microstructurally, the particles form aggregates during shear thickening creating large voids in the sample that drives the suspending medium into the these voids. Additionally, air bubbles were also seen to get trapped in the sample due to the instabilities created in the sample, as observed before (Cates *et al.*, 2005). The edge effects are shown in pictures incorporated in Fig. 5.26. The instability disappears from the edge within one second of flow cessation. The sample is also seen to have uneven sample distribution at the edges after shear thickening.

Fig. 5.27 in comparison shows, a hard sphere glass of smaller particles where no shear thickening is observed at $\dot{\gamma} = 1\ s^{-1}$. In Fig. 5.27 there are no edge effects detectable and the fluctuations of N_1 and σ are much smaller compared to the shear thickening samples. Moreover, N_1 has a negative value through the shear experiment. Since the particles are small in size ($Pe < 1$), the Brownian motion is prominent than shear-induced collisions aiding in shear thinning as observed in Fig. 5.25.

In Fig. 5.28 shows the stress relaxation after steady shear for the samples discussed before, for rates below and above the critical shear rate from the onset
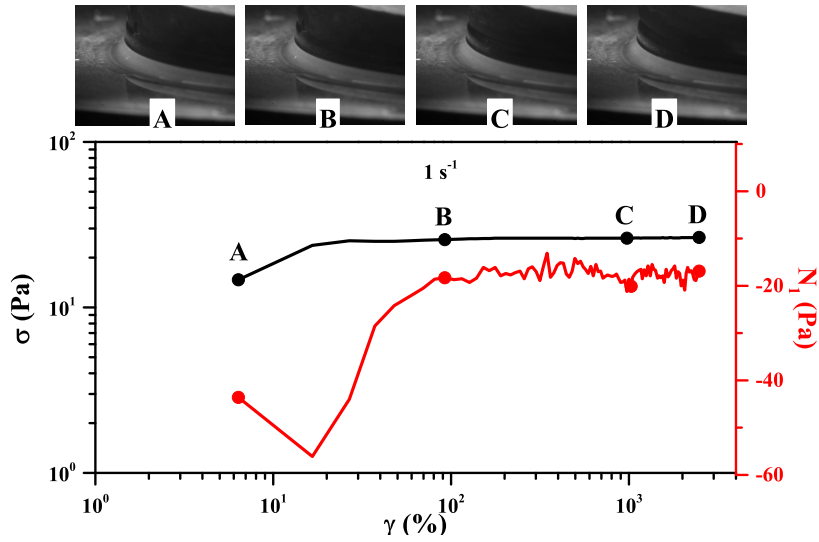
Figure 5.27: start-up of colloidal glass of $\phi = 0.60$, $R = 137\,nm$ and $\dot{\gamma} = 1\,s^{-1}$ with images indicating no edge effects, slip and dilation
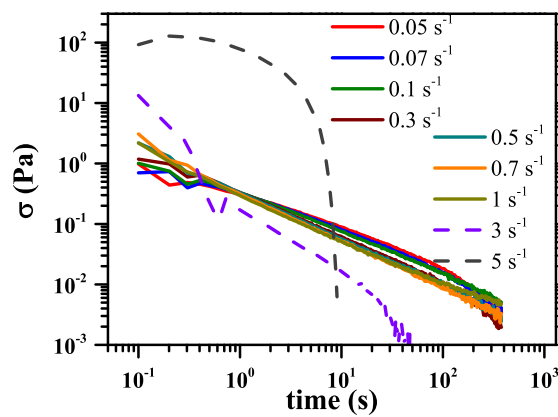
Figure 5.28: Stress relaxation for a shear thickening colloidal glass with $\phi = 0.60$ and $R = 405\,nm$

of shear thickening. Below the critical rate the stress in the sample relaxes completely with time but above the critical shear rate a qualitatively different response is observed. More specifically for $\dot{\gamma} = 5\ s^{-1}$ the system tends to retain the internal stress for much longer time than for rates below critical rate. After a certain amount of time (time = $10\ s$) a sudden release in stress is observed which is reminiscent of a liquid response. This temporary residual stresses was observed earlier (D'Haene *et al.*, 1993) and was attributed to the temporary presence of clusters which then dissipate after short time. The stress in retained for approximately $2\ t_B$ while in the previous chapters the residual stresses was retained for more than $100\ t_B$. It was observed that the edge effects dissipates within $1\ s$ of shear cessation but the residual stresses are maintained much longer. This indicates that the relaxation process starts from the edge and travels inwards until the system is completely relaxed after shear thickening. Non-Brownian concentrated corn starch suspensions could not support a localised static weight for long time and this was attributed to unjamming due to particle migration (von Kann *et al.*, 2011). Recently, it was predicted that if a modest threshold in stress was crossed over the whole sample it would be possible to support a weight for an infinitely long time (Hermes *et al.*, 2016) and possibly retain stress for infinitely long time.

In this chapter we probed the transient shear response of a colloidal glass sample under various shear protocols. BD simulations was employed to identify the cage anisotropy retention and correlate it with the residual stresses. It has been demonstrated that cage anisotropy may not be the only reason for the existence of residual stresses in hard sphere glasses. Flow interruptions performed with experiments and BD simulations helped in extracting rheological signatures for sequence of physical processes occurring during start-up shear. After cessation of shear in the elastic regime, more stress was retained rather than in steady state flow regime. Complex experimental rheological protocols like shear reversal help us understand that initial and final metastable states drive the dynamics of the systems and during creep reversal higher strain is accumulated, this can be attributed to activated heterogeneous domains. Additionally, LAOS was performed with experiments on colloidal glasses and suspensions where

unique non-linear signatures emerged. Anharmonic response increased with frequency for concentrated suspensions and decreased with colloidal glasses. These are related to shear thinning occurring in suspensions and viscous dissipation happening in colloidal glasses. Finally, shear thickening studies were performed and dilation and edge effects were visually inspected. It was observed for the same volume fraction, bigger size particles exhibit shear thickening while small size particles exhibit shear thinning.

CHAPTER 6

ORTHOGONAL SUPERPOSITION RHEOMETRY OF COLLOIDAL GLASSES UNDER FLOW

While the mechanisms of yielding and flow of HS glasses have been extensively investigated, several aspects of steady (Besseling *et al.*, 2010; Chikkadi *et al.*, 2011; Koumakis *et al.*, 2012*a*; Petekidis *et al.*, 2004; Schall *et al.*, 2007; Siebenbürger *et al.*, 2012) and oscillatory shear flow (Brader *et al.*, 2010; Koumakis *et al.*, 2013; Miyazaki *et al.*, 2006; Petekidis *et al.*, 2002) are still unresolved. For example the scaling of shear-induced diffusivity with the applied shear rate has been the subject of controversy (Besseling *et al.*, 2007; Eisenmann *et al.*, 2010).

Orthogonal Superposition Rheometry (OSR) combines two deformation modes, steady shear and small amplitude oscillatory shear applied simultaneously and orthogonally to each other. In this way small amplitude orthogonal frequency sweeps orthogonally interrogates the sample and retrieve its viscoelastic spectra under steady shear (Kim *et al.*, 2013; Mewis and Schoukens, 1978; Simmons, 1966; Tanner, 1968; Vermant *et al.*, 1997, 1998; Zeegers *et al.*, 1995). Our approach is fundamentally different from SRFS (Wyss *et al.*, 2007) as superposition rheometry is based on the linear measurements of a perturbation spectrum characterizing a strongly non-linear state. This technique, that only recently became sensitive enough, enables us to probe model colloidal glasses under steady shear without resorting to non-linear oscillatory measurements with complicated intracycle kinematics such as varying shear rates and higher harmonics in the stress response.

There has been a great inclination to construct database of rheological contour maps for polymers and colloidal suspensions in order to reduce domi-

nant relaxation times into a single plot. In order to achieve this, superposition of rheological curves is performed. Generally, oscillatory rheological measurements are done in the linear regime to achieve superposition curves. Time temperature superposition for polymer solutions (Baumgärtel and Willenbacher, 1996; Ferry, 1980; Fox and Flory, 1948; Rubinstein and Colby, 2003) has been very relevant and of great significance to the polymer processing industry. Time-concentration superposition was also attempted for the polymer suspension where the concentration was varied instead of temperature (Baumgärtel and Willenbacher, 1996; Ferry, 1980; Schausberger and Ahrer, 1995). The advantage of time-concentration superposition is the reduction of both concentration effects on entanglement density and relaxation time onto a master curve. This concept was extended to bulk colloidal suspensions (Trappe and Weitz, 2000; Wen *et al.*, 2015), monolayer colloidal suspensions (Cicuta *et al.*, 2003), polymer-colloid mixtures (Daga and Wagner, 2006) and emulsions (Lorenzo *et al.*, 2011). An extension to these superposition procedures are the time-stress/creep superposition, time-strain superposition and time shear rate superposition. All of these methods utilize dominant relaxation times under flow. The time step-strain superposition method is specifically used to study aging time and in turn predict how the sample ages with time. This method has been applied on amorphous polymers (O'Connell and McKenna, 2002, 1997; Struik, 1978) and recently in aging lapointe suspensions (Gupta *et al.*, 2012; Joshi and Reddy, 2008). Time-stress superposition and their convolution to an arbitrary time domain was extensively studied on Laponite suspensions(Baldewa and Joshi, 2012; Kaushal and Joshi, 2014). Attempts using scaling of non-linear oscillatory frequency sweeps to obtain a strain rate-frequency superposition or time strain rate superposition (SRFS) have been proposed (Wyss *et al.*, 2007), but so far they have been proven problematic (Erwin *et al.*, 2010*b*). Here, we use a more direct approach to explore a wide range of time scales under shear which bears similarities to Time Temperature Superposition (TTS) used in polymeric systems, but with shear used to control the effective temperature in the glass.

6.1 Convective Cage Release in near Hard Sphere Colloidal Glasses

We measure the full viscoelastic spectrum of sheared colloidal glasses through OSR and determine the characteristic crossover frequency, ω_c, which provides a direct measure of the shear-induced structural relaxation. The latter is attributed to the microscopic yielding mechanism of convectively induced cage breaking and is found to scale linearly with shear rate, $\dot{\gamma}$. Moreover, viscoelastic spectra at different $\dot{\gamma}$ can be shifted to produce a strain rate-orthogonal frequency superposition (SROFS). Therefore, in analogy with the convective constraint release (Marrucci, 1996) and time-temperature superposition (TTS) in entangled polymers, *convective cage release* (CCR) in colloidal glasses can be probed by SROFS. In addition to the dominant CCR mechanism, a rich response is detected both at high and low frequencies. Brownian Dynamics (BD) simulations in combination with experiments allow us to attribute the high frequency mismatch of the viscous modulus, G'', to shear-induced in-cage slowing down in agreement with (Koumakis *et al.*, 2012*a*) and the low frequency deviations at high shear rates to hydrodynamic interactions.

We used sterically stabilized poly(methyl methacrylate) (PMMA) nearly hard-sphere particles of $196\ nm$ radius with polydispersity $\sigma \simeq 20\%$, dispersed in an octadecene/ bromonaphthalene solvent $n_D = 1.485$) to minimize residual van der Waal's attractions and evaporation. Volume fractions, initially estimated from random closed packing ($\phi_{rcp} = 0.67$), were precisely determined by matching G' to the master curve provided by (Koumakis *et al.*, 2012*b*). OSR was performed using an ARES-G2 (TA) rheometer with a home modified normal force control loop, equipped with a custom built open bottom double wall Couette geometry (Kim *et al.*, 2013; Vermant *et al.*, 1997). Steady shear flow was imposed in the tangential direction and oscillatory motion vertically. We investigated tangential shear rates, $\dot{\gamma}$, from 10^{-4} to $1\ s^{-1}$ ($\approx 10^{-5}$ to $10^{-1}\ Pe$), reported below by the dimensionless Peclet number, $Pe = \dot{\gamma}t_B$, where $t_B = R^2/D_0$ ($= 0.158\ s$) the free Brownian time and D_0 the bare diffusion coefficient. Or-

thogonal frequency sweeps at a low strain amplitude ($\sim 0.7\%$), in the linear regime Fig. 6.1 (b), were performed once steady state shear with $\dot{\gamma}$ was reached. To prevent slip at low $Pe < 1$ tools were roughened by coating of similar PMMA particles (Ballesta *et al.*, 2008). Moreover, we largely avoided measurements in the shear banding regime (at very low Pe) (Besseling *et al.*, 2007) except for the highest $\phi = 0.64$ and for $Pe < 10^{-4}$. Complementary, we conducted BD simulations (Foss and Brady, 2000) using 50000 particles with 10% polydispersity and periodic boundary conditions for $\phi = 0.62$ at rest, $Pe = 0.01$ and 0.1).

(a)   (b)
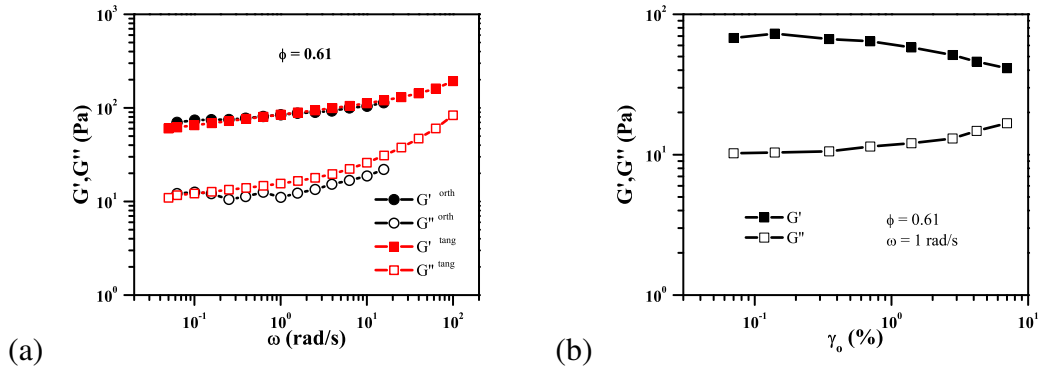
Figure 6.1: (a) Orthogonal frequency sweep and tangential frequency sweep at rest. The frequency sweep is representative of a colloidal glass for all frequencies. Moreover at rest both the orthogonal and tangential frequency sweep matches indicating a homogeneous sample (b) Orthogonal dynamic strain sweep, under no flow conditions, used to determine the linear regime. A strain amplitude well inside this regime ($\sim 0.7\%$) was also used for OSR measurements under steady shear.

OSR experiments were performed at various Pe and three volume fractions, 0.60, 0.61, and 0.64. Fig. 6.2 (a) shows orthogonal frequency sweeps at $\phi = 0.61$, performed at different Pe. At low Pe the OSR reveals a response similar to the quiescent glass Fig. 6.1 with $G' > G''$ for all ω's measured. As Pe is increased flow induces microstructural changes and speeds up internal dynamics as manifested by a crossover frequency, ω_c (at $G' = G''$), entering the experimental window. SROFS was produced through shift of the data in the x- and y-axes by a factor, a, and b, respectively, in a way that ω_c, for all Pe coincide. In the regime where ω_c is not measurable the shift is performed in order to match better the full viscoelastic spectra. Fig. 6.2 (b), (c) and (d) show SROFS

results for HS glasses at $\phi = 0.60$, 0.61, and 0.64. In all measurements two distinct frequency regimes are separated by ω_c. For $\omega > \omega_c$ (short timescales) the elastic moduli G' superimpose for all Pe whereas G'' data exhibit an increase with Pe (see arrow in Fig. 6.2). For $\omega < \omega_c$ (long timescales) the trend varies with volume fraction. In Fig. 6.2 (b), for $\phi = 0.60$, G' and G'' superimpose well with slopes of 1.1 and 0.8, respectively. At $\phi = 0.61$, G' and G'' are closer to each other and exhibit slopes of 0.9 and 0.7 respectively (Fig. 6.2 (c)), while at $\phi = 0.64$ (Fig. 6.2 (d)) G' and G'' are almost identical with a slope of about 0.6.
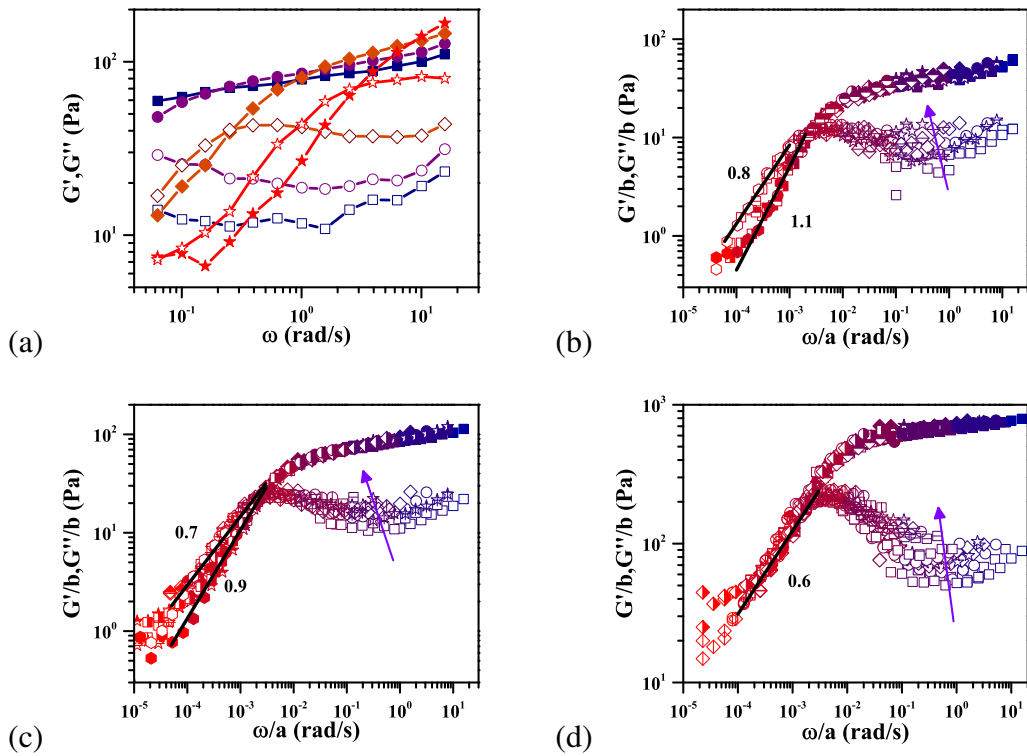
Figure 6.2: (a) The orthogonal frequency sweeps at $\phi = 0.61$ for $Pe = 2 \times 10^{-1}$, 2×10^{-2}, 2×10^{-3} and 2×10^{-4}. SROFS data at $\phi = 0.60$ (b), $\phi = 0.61$ (c) and $\phi = 0.64$ (d). The colormap in (a), (b), (c) and (d) from blue to red indicates steady shear from low to high Pe. Solid black lines indicate G' (filled/half filled symbols) and G'' (open symbols) fits for $G'' > G'$.

In addition, for high Pe and low OSR ω the response is rather rich and unexpected. This is better seen in conjuction with Fig. 6.3 (a) and (b) where we show for $\phi = 0.61$ the orthogonal stress amplitude, σ_o^{orth} as a function of Pe and OSR ω, respectively and indicate liquid (open symbols) and solid-like (filled symbols) regimes. While for low Pe we mainly probe solid-like response, as

the terminal flow regime in OSR is outside of the experimental window, as Pe is increased the relaxation due to convective cage release (or shear-induced out-of cage diffusion) dominates the response, and liquid-like behavior is manifested at low OSR ω. Interestingly, at high steady shear Pe and low OSR ω we detect (beyond experimental error) a reentrant solid-like response and an increase of σ_o^{orth} with Pe (Fig. 6.3 (a), (b)). This response, barely detectable at $\phi = 0.6$ (Fig. 6.2 (b)), is clearly seen at $\phi = 0.61$ (Figs. 6.2 (c) and 6.3 (a), (b)) and becomes more pronounced at the highest $\phi = 0.64$ (Fig. 6.2 (d)).
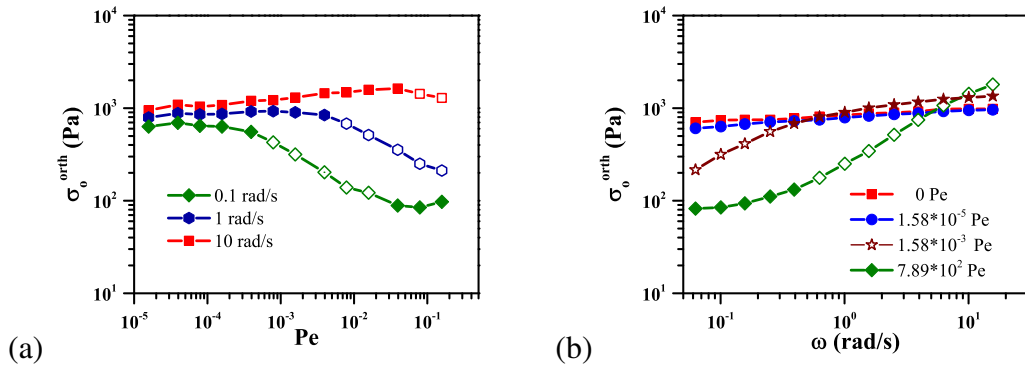
Figure 6.3: (a) σ_o^{orth} vs. Pe at $\omega = 0.1$, 1 and 10 rad/s. (b) σ_o^{orth} vs ω at $Pe = 1$, 0.02, 2×10^{-4} and 0 for $\phi = 0.61$. Filled symbols indicate solid-like response ($G' > G''$) and open liquid-like response ($G' < G''$).

Fig. 6.4 (a) displays the flow curves at different volume fractions (lines) together with the steady state stress reached before the OSR was performed (filled symbols). The crossover frequency, ω_c, is plotted for all ϕ as a function of Pe in Fig. 6.4 (b). As seen here, ω_c exhibits a clear linear dependence with Pe over three decades for all ϕ. Interestingly, the crossover frequency is also ϕ independent suggesting that the in-cage to out-of-cage transition time is not changing within the glassy region ($\phi = 0.6$ to 0.64) and for $Pe < 1$ studied here. The horizontal and vertical scaling factors used in SROFS (Fig. 6.2) are depicted in Fig. 6.4 (c) and (d). In agreement with ω_c, the horizontal shift factor, a, rescaling time, also varies linearly with Pe (Fig. 6.4 (c)). In analogy with TTS in polymers where the horizontal shifting factor relates to the temperature dependent diffusion coefficient (Rubinstein and Colby, 2003), here a reflects the shear rate dependence of the transition from in-cage to out-of cage motion. Our findings are in agreement with the linear scaling predicted by MCT (Fuchs and Cates,

2002, 2003b) for HS glasses, although confocal microscopy experiments with similar PMMA particles under low Pe shear have shown a power-law exponent for the long time diffusion that ranges from 0.8 (Besseling *et al.*, 2007) to 1 (Eisenmann *et al.*, 2010).

Since b is essentially used to shift the plateau modulus it reflects the effect of shear on the in-cage free volume, similarly with the TTS where it represents the temperature dependence of the density (Rubinstein and Colby, 2003). Hence b, which follows the flow curve dependence (Fig. 6.4 (d)), is linked to the maximum limit of in-cage particle displacements prior to yielding and convective cage release. For the highest $\phi(= 0.64)$, $b \simeq 1$ indicating the lower deformability under shear before cage release due to the smaller in-cage free volume. These observations are in line with reports of microscopic particle rearrangements in similar HS glasses by LS-Echo (Petekidis *et al.*, 2002) where, upon increasing ϕ, irreversible rearrangements grow much sharper beyond a critical yield strain, suggesting that cages break more abruptly and the system exhibits at the microscopic level a more brittle yielding.

To further clarify the experimental results, we resorted to BD simulations to examine shear-induced dynamics at $\phi = 0.62$. In Fig. 6.5 (a) we plot the average mean square displacement, $\langle \Delta r^2 \rangle$, from BD simulations at rest and for different Pe as a function of t/t_B. At short times we detect a drop of $\langle \Delta r^2 \rangle$ with increasing Pe (arrow in 6.5 (a)) due to a shear-induced suppression of in-cage diffusivity first reported in (Koumakis *et al.*, 2012a). When converted to viscoelastic moduli, using the Generalized Stokes-Einstein (GSE) relation (Mason, 2000), $|G^*(\omega)| \approx k_B T / \pi a (\Delta r^2(1/\omega)) \Gamma[1 + \alpha(\omega)]$ (where $\alpha(\omega) \equiv d \, ln(\Delta r^2(t))/d \, lnt$ at $\omega = 1/t$), such decrease of short-time in-cage motion is manifested as an increase of G'' with Pe at high OSR ω (arrow in Fig. 6.5 (b)). This is in agreement with SROFS experiments (Fig. 6.2) and hence verify that the high frequency deviations in G'' are linked to such shear-induced slowing down at short-time scales, while Hydrodynamic Interactions (HI) are not important. The phenomenon is microscopically attributed to the build up of structural anisotropy under shear (Koumakis *et al.*, 2012a), as shown in the 2D projection of the
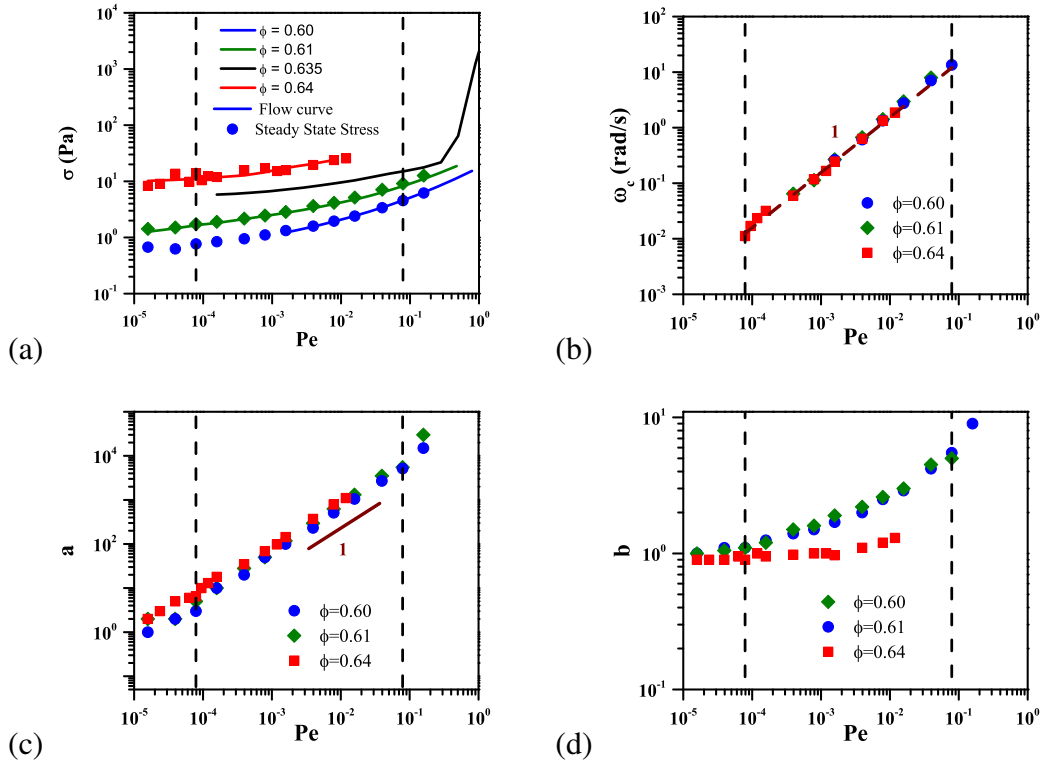
Figure 6.4: (a) Flow curves superimposed with the orthogonal steady state stress at different Pe ($\phi = 0.64$, $\phi = 0.61$, $\phi = 0.60$). The solid line ($-$) indicates the flow curve at $\phi = 0.635$ with the sudden upturn indicative of shear thickening. (b) Crossover frequency ω_c vs. Pe. (c)The horizontal shifting factor, a and (d) the vertical shifting factor, b used in SROFS (Fig. 6.2). The vertical dashed lines indicate the frequency regime where ω_c is accessible. The symbols represent $\phi = 0.64$, $\phi = 0.61$ and $\phi = 0.60$.

difference of the pair correlation function, $g(r)$ under shear from that at rest (Fig. 6.5 (c)) in the velocity-gradient (xy) plane. Similarly, temperature induced structural changes in supramolecular polymers were considered to be the origin of G" deviations at high frequencies in TTS (Seiffert and Sprakel, 2012).
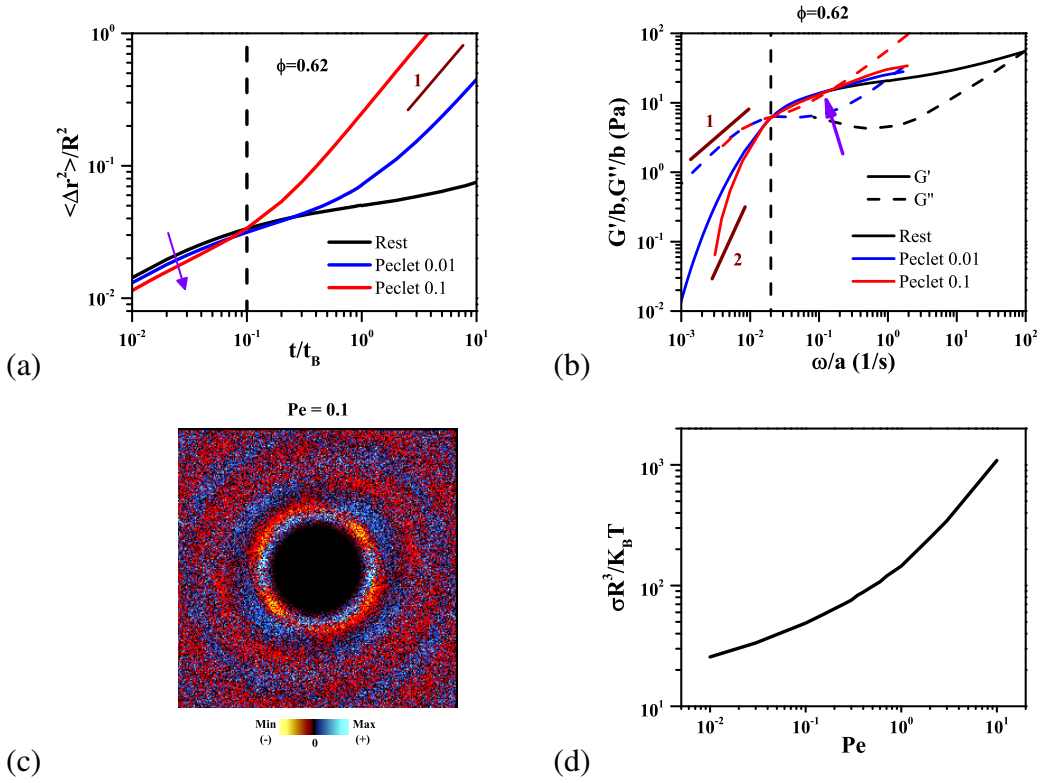
Figure 6.5: (a) Mean Square Displacement from BD simulations for $\phi = 0.62$ when $Pe = 0$, 0.01 and 0.1 during steady flow. (b) Shear rate orthogonal frequency superposition data deduced from BD. G' and G'' obtained by converting MSD data of (a) for $Pe = 0$, 0.01 and 0.1 (Mason, 2000). (c) $g(r)$ in the velocity-gradient plane for $Pe = 0.1$ in steady state flow. (d) flow curve from BD simulations

Whereas BD simulations capture experimental findings at high ω they clearly deviate for $\omega < \omega_c$ and high steady shear Pe (the vertical dash lines in Fig. 6.5 (a) and (b) separate the two regimes). At long times, $\langle \Delta r^2 \rangle$ increases linearly with time, leading to Maxwell type terminal flow with G'' and G' following power-law slopes of 1 and 2 with ω, respectively (Fig. 6.5 (b)). Such simple flow response is markedly different from OSR experiments where G' and G'' never acquire these terminal slopes. The discrepancy is becoming more pronounced at higher ϕ's where the low ω regime with $G'' > G'$ is essentially absent (Fig. 6.2 (d)) and the slopes of G' and G'' merge and decrease towards ~ 0.5. This in-

dicates a power-law dependence of the relaxation spectrum, possibly due to the presence of various sizes of particle clusters not present in BD due to the absence of HI. In experiments however, at high Pe where HI become important, hydroclusters (Mewis and Wagner, 2012) i.e. large length-scale transient structures are formed, increasing the suspension viscoelasticity and eventually leading to shear thickening. Although absent in BD simulations, as seen in the flow curve (Fig. 6.5 (d)), shear thickening was indeed detected in experiments (Fig. 6.4 (a), for $\phi = 0.635$) at Pe, higher but close to those studied in OSR. Hence, it is reasonable to assume that few of these hydroclusters could be present as precursors, giving rise to the unexpected deviation from simple terminal flow and the existence of a reentrant solid-like response at low OSR ω.
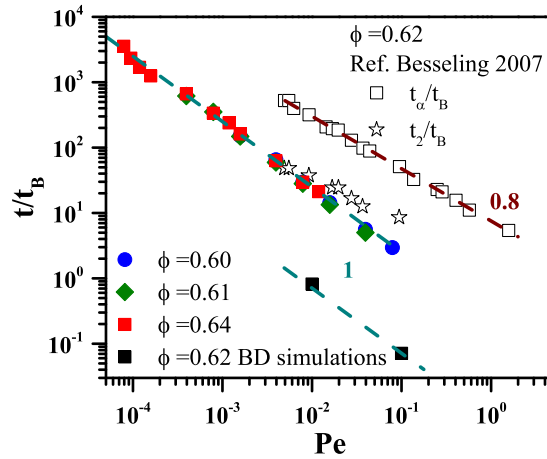
Figure 6.6: t_c/t_B calculated from ω for experiments $\phi = 0.64$, $\phi = 0.61$ and $\phi = 0.60$ is extracted from BD simulations for $\phi = 0.62$. t_α/t_B and t_2/t_B respectively for $\phi = 0.62$ calculated from (Besseling *et al.*, 2007)

In analogy with entangled polymers where convective constraint release modifies the tube relaxation time under shear into $1/\tau = 1/t_o + \beta\dot{\gamma}$ (Ianniruberto and Marrucci, 2014; Marrucci, 1996) (t_o the internal relaxation time at rest and β a constant) similar dependence has been proposed for the structural relaxation in concentrated colloidal suspensions and glasses (Fuchs and Cates, 2003*b*; Miyazaki *et al.*, 2006). For a system with very long (or infinite) alpha relaxation, such as colloidal glasses, shear-induced flow governs the microscopic dynamics as a consequence of convective cage release of particles. Then ω_c

provides a measure of $1/\tau$ corresponding to the transition time from in-cage to out-of-cage motion (as indicated by the GSE conversion), that scales linearly with Pe with $\lim_{Pe \to 0} \omega_c = 0$ congruent with an infinite α relaxation time ($t_o = t_\alpha \to \infty$) in a quiescent glass. Fig. 6.6 shows the relaxation times under shear deduced from ω_c both from OSR experiments and BD simulations; the two having the same linear decrease but different in absolute values due to HI. For comparison Fig. 6.6 includes the data from (Besseling *et al.*, 2007) corresponding to structural relaxation time, t_α and the transition to out-of-cage diffusion, t_2; both however exhibiting clearly a weaker power-law dependences. The relaxation time τ which we obtain here should be smaller than the long time diffusion time and comparable to t_2 from ref (Besseling *et al.*, 2007), hence the proximity of τ to t_2 Fig. 6.6 is reasonable, although it is still unclear why a lower power-law exponent(< 1) was detected in those experiments (Besseling *et al.*, 2007).

In summary, utilizing orthogonal superposition rheometry we are able to measure for the first time the full viscoelastic spectra of a sheared colloidal glass and obtain a scaled map of the dynamics of the system through a Strain Rate Orthogonal Frequency Superposition. Through the scaling of the crossover frequency, ω_c, and the shift factor, b, this method revealed unambiguously a linear dependence of the terminal relaxation time on shear rate due to *a convective cage release*. Moreover, SROFS spectra at high frequencies provided an independent verification of the constriction of short-time in-cage motion under steady shear (Koumakis *et al.*, 2012a) while comparison with BD simulations suggest that deviations from a Maxwell type flow at the low frequency regime of the SROFS spectra, maybe linked to the existence of shear thickening precursors. Our findings provide valuable input to theoretical models and insights for the understanding of other soft matter or even metallic glasses under flow.

6.2   Orthogonal Superposition Rheometry of Star-like micellar systems under steady shear [1]

Here we use orthogonal superposition rheometry (OSR) to study the effect of steady shear on the viscoelastic behaviour of a soft sphere colloidal glass. As discussed above OSR combines two deformation modes, rotational steady shear and orthogonal small amplitude oscillatory shear applied at the same time. In this way, the orthogonal frequency sweeps measure the viscoelastic spectra of the sample under shear (Kim *et al.*, 2013; Mewis and Schoukens, 1978; Simmons, 1966; Tanner, 1968; Vermant *et al.*, 1997, 1998; Zeegers *et al.*, 1995) and recently also to control shear thickening (Lin *et al.*, 2016). We have demonstrated in the previous section the potential of orthogonal superposition rheometry (OSR) in elucidating the mechanism of flow in model hard sphere colloidal glasses (Jacob *et al.*, 2015). More specifically, we have shown that for a range of volume fractions above the glass transition the shear-induced relaxation timescale scales linearly with applied rotational shear rate. We termed this "convective cage release" in analogy with the convective constraint release mechanism put forward for the relaxation of entangled polymer melts under flow (Ianniruberto and Marrucci, 2014; Marrucci, 1996). Here, we expand on the above study by presenting orthogonal superposition rheometry measurements of a colloidal suspension that consists of star-like micelles, a well-characterized system analogous to multi-arm star polymers (Loppinet *et al.*, 2001; Roovers *et al.*, 1993; Willner *et al.*, 1994). The linear and non-linear rheology of star-like micelles has been extensively studied as a function of concentration both above and below the glass transition and hence it can be used as a model system for a colloidal suspension with soft interactions (Koumakis *et al.*, 2012*b*; Poulos *et al.*, 2015, 2013; Renou *et al.*, 2010).

For this study poly(ethylene-alt-propylene)-poly(ethylene oxide) block copolymers were prepared by a two-step anionic polymerization (Allgaier *et al.*, 1997). The number-average molar mass (Mn) was $1300 g/mol$ for the PEP block and

---

[1]This part is in collaboration with Dr. A. S. Poulos who supplied the star-like micelles and helped with the experiments, write-up and discussion in this section

$20300 g/mol$ for the PEO block corresponding to an overall $Mn = 21600 g/mol$ for the block copolymer. PEP-PEO block copolymers with this block ratio form micelles in D_2O with an aggregation number of 120 and a pair interaction potential similar to regular star polymers (Laurati *et al.*, 2005). Previous work has demonstrated that no kinetic exchange of arms between micelles is possible (Lund *et al.*, 2006; Stellbrink *et al.*, 2004). The absence of kinetic exchange ensures that the aggregation number remains constant with varying concentration and temperature. The micelles can thus be considered as stable colloidal entities with star-like pair interactions. Transparent solutions were obtained by dissolving the PEP-PEO polymer in deuterium oxide (D2O 99.8% atom D purchased from Armar Chemicals). The solutions were left to equilibrate at room temperature for at least one week before measurement. The effective volume fraction ϕ_{eff} estimated as the ratio of the concentration, c, to the overlap concentration, $c^*(= 3M/4\pi N_A R_h^3)$, is calculated by using the polymer concentration and the measured by dynamic light scattering hydrodynamic radius of the micelles $R_h = 36 \ nm$ (in dilute solutions). As the micelles can interpenetrate, ϕ_{eff} take the value above one.
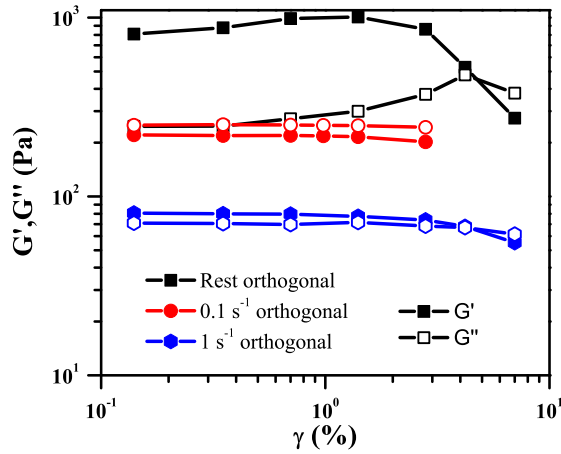
Figure 6.7: Orthogonal Strain Sweep performed at different shear rates to identify the linear regime for $\phi_{eff} = 2.65$.

Orthogonal superposition rheometry (OSR) was performed using an ARES-G2 (TA) rheometer with a modified normal force control loop, equipped with a custom built open bottom double wall Couette geometry (Kim *et al.*, 2013;

Vermant *et al.*, 1997) in Soft matter rheology lab in Leuven. Steady shear flow was imposed in the horizontal direction and a small strain amplitude oscillatory motion was applied in the vertical direction. The range of rotational shear rates that we investigated was from 0.0005 to 10 s^{-1}. For each shear rate, a start-up experiment was run and rotational shear stress was then measured as a function of time. Orthogonal frequency sweeps in the linear regime were performed once the rotational shear stress reached steady state, typically after 300 s for the highest to 800 s for the lowest shear rates. This waiting period corresponds to a total strain of $\gamma > 1$ except at the two lowest shear rates of 0.0005 s^{-1} and 0.001 s^{-1} were the OFDS experiment was started after a total strain $\gamma = 0.4$ and $\gamma = 0.75$ respectively. The linear regime in ODFS was determined at three different rotational shear rates by running orthogonal dynamic strain sweep experiments at a fixed frequency of 1 rad/s (see Fig. 6.7). The linear regime at rest extends to approximately $\gamma_o = 1\%$, while under shear it increases to $\gamma_o = 1\%$ at 0.1 s^{-1} and 2% at 1 s^{-1}. In the actual experiments we chose $\gamma_o = 0.8\%$ for shear rates below 1 s^{-1}. This was increased to $\gamma_o = 1.2\%$ for shear rates of 1 s^{-1} and above to increase the maximum stress and hence the accuracy of the measurement. At each rotational shear rate, orthogonal frequencies sweeps between 0.063 rad/s and 15.7 rad/s were performed covering approximately two-and-a-half orders of magnitude. Orthogonal shear strain sinusoidal oscillations were produced at each specified frequency using a frequency response generator and analyser ($FRA1250$, Solartron Instruments Schlumberger). The amplitude and phase of the stress response were measured by integrating one oscillatory period, and the results transformed to G', G''. At the lowest orthogonal frequencies, we waited at least two full periods before starting the integration; this was progressively increased as the frequency of the experiment was increased. The measurement of a complete ODFS at each shear rate typically took between 20 and 40 min.

The dynamic frequency sweep (DFS) and flow curve of the star-like micelles solution at $\phi_{eff} = 2.65$ are shown in Fig. 6.8. In order to test the orthogonal superposition setup the DFS was obtained both in rotational and orthogonal oscillation. In Fig. 6.8 we show that the orthogonal DFS (triangles) is identical to the rotational DFS (lines) validating the accuracy of the orthogonal
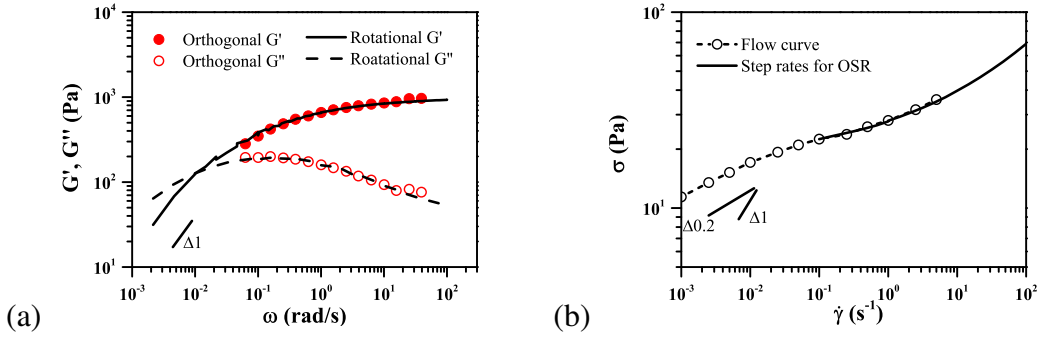
Figure 6.8: (a) DFS of a concentrated star-like micelle solution at $\phi_{eff} = 2.65$. The solid (G') and dashed (G'') lines show the DFS obtained with the small-amplitude oscillation in the horizontal plane while the points (open and solid circles) were obtained with the oscillation in the vertical (orthogonal) direction under the same conditions. (b) Flow curve of the same sample. The line indicates the flow curve obtained by continuously varying the shear rate, while the circles indicate the stress obtained at steady state after a step rate experiment.

measurements. The measured DFS is characteristic of a concentrated colloidal suspension which approaches the glass transition and therefore exhibits a soft glassy response with a crossover at a low frequency, i.e. slowly flowing at long time scales and with elastic behaviour dominating at all frequencies above the crossover frequency which here was $\omega_c = 0.01\ rad/s$. However, below ω_c, G' and G'' present power-law behaviour with exponents 1 and 0.5 respectively rather than the typical exponents of 2 and 1 seen in Maxwell type viscoelastic fluids. This is most likely due to the small frequency range that is accessible to experiment below ω_c. It is conceivable that if we were able to measure up to one order of magnitude lower in frequency we would obtain the expected terminal behaviour. Similarly, the flow curve shows a plateau in stress $\sigma = 20\ Pa$ and shear thinning behaviour at large shear rates in line with previous measurements on the same system (Koumakis *et al.*, 2012*b*). Of course, both the low frequency crossover in the DFS and the reduction in stress at shear rates below $\dot{\gamma} < 0.025\ s^{-1}$ provide evidence of an additional slow relaxation with a timescale of $100\ s$. This has been observed in a variety of soft colloidal glasses especially of ultrasoft polymeric micelles and multi-arm stars (Christopoulou *et al.*, 2009; Erwin *et al.*, 2010*a*; Koumakis *et al.*, 2012*b*; Poulos *et al.*, 2013) and is commonly attributed to out-of-cage activated mechanisms assisted by lo-

University of Crete, Greece

cal polymeric fluctuation at the outer blob level or, in the case of colloids with harder interparticle potential by dynamic heterogeneities (Cipelletti and Ramos, 2005; Helgeson *et al.*, 2007; Pham *et al.*, 2008; Siebenbürger *et al.*, 2009). The slow non-diffusive relaxation might also be related to the unusual power-law exponents of 1 and 0.5 below ω_c, as normal terminal behaviour assumes diffusive exponential type relaxations.

In Fig. 6.9 we show the orthogonal dynamic frequency sweeps (ODFS) for a range of rotational shear rates in the range $0.001 \ s^{-1}$ to $1 \ s^{-1}$. Even at the lowest shear rate shown here ($\dot{\gamma} = 0.001 \ s^{-1}$) the ODFS show a little change from the DFS at rest, with the elastic modulus G' decreasing and the viscous modulus G'' slightly increasing over the whole frequency range. At $\dot{\gamma} = 0.0025 \ s^{-1}$ (Fig. 6.9(c)) the lower crossover frequency ω_c moves inside the experimental frequency window. The crossover frequency can be used to estimate a structural relaxation time-scale $\tau = 1/\omega_c$. As the steady shear rate is further increased, ω_c moves to higher frequencies indicating a decreasing structural relaxation timescale. Above a critical shear rate, $\dot{\gamma}_{cr} = 0.025 \ s^{-1}$, ω_c is still increasing with shear rate, but the whole shape of the ODFS also changes rather markedly as seen in Fig. 6.9 (d). At frequencies below ω_c, G' and G'' become parallel and equal to each other with the same power-law exponent, $\nu \approx 0.5$. We also observe a second crossover frequency. Hence, the overall effect of shear flow on the ODFS is twofold. Firstly, it speeds up continuously the structural relaxation. Secondly, above a critical shear rate of approximately $\dot{\gamma}_{cr} = 0.025 \ s^{-1}$ it changes the power-law behaviour of G' and G'' in the terminal regime.

Since the shape of the ODFS changes at $\dot{\gamma}_{cr}$ we attempt to create two master curves by shifting the curves in the x and y axes for shear rates below and above $\dot{\gamma}_{cr}$. Below this critical shear rate we can superimpose the ODFS by shifting the curves along the frequency and moduli axes. In Fig. 6.10 (a), eight rotational shear rates in the range 0 0.025 s^{-1} are shifted in such a way that the crossover point coincides. In this low shear rate regime the superposition works well. The G' curves are identical to within experimental accuracy. On the other hand, there is a consistent increase in the peak value of G'' as the shear rate is increased, and
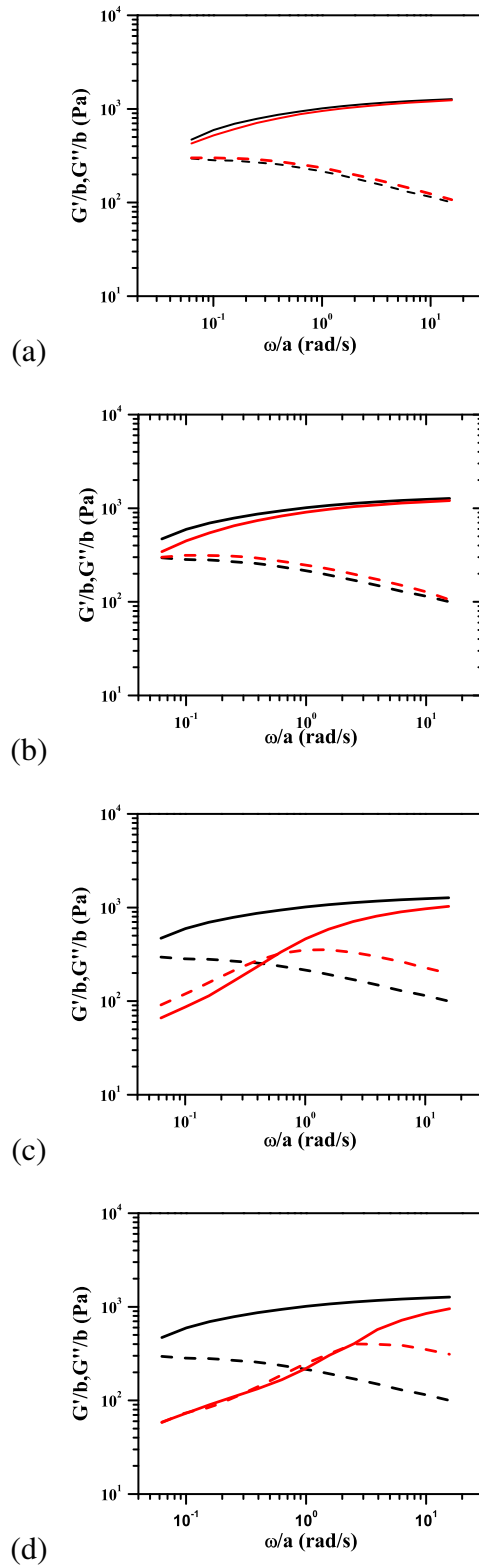
Figure 6.9: Orthogonal Frequency Sweep at performed at different $\dot{\gamma}$ (a) $0.0001\ s^{-1}$ (b) $0.001\ s^{-1}$ (c) $0.025\ s^{-1}$ and (d) $0.1\ s^{-1}$ and compared with Orthogonal DFS at rest (red line). The straight lines indicate G' and the dashed lines indicate G''
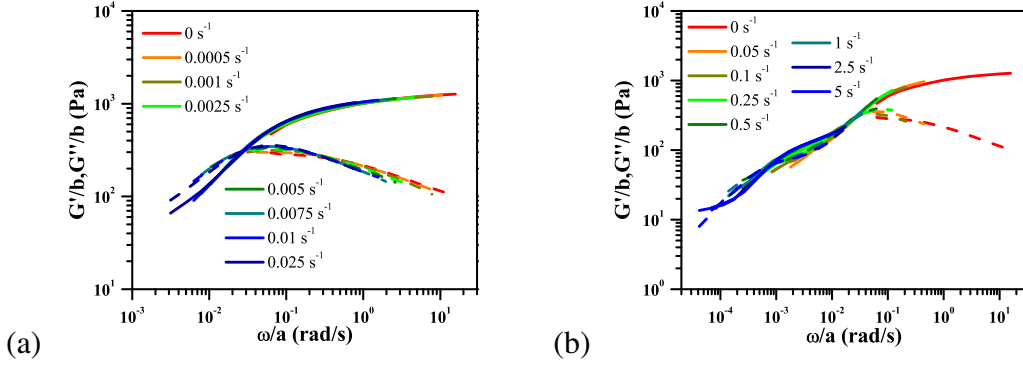
Figure 6.10: Superposition of the orthogonal Storage and Loss modulii obtained for shearates (a) below $0.025 \ s^{-1}$ and (b) above $0.025 \ s^{-1}$

also a slight decrease at higher frequencies. In Fig. 6.10 (b), the same superposition is attempted for shear rates above the critical shear rate $\dot{\gamma}_{cr}$. In this high shear rate regime, the superposition is less satisfactory, especially for frequencies below the crossover frequency. It is clear that G' develops a shoulder as the shear rate is increased. This shoulder leads to the second crossover frequency with G'' that is evident in Fig. 6.9 (d).
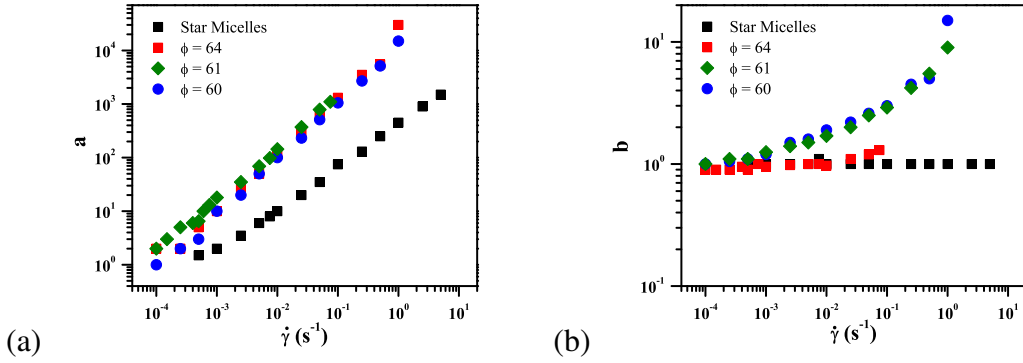
Figure 6.11: (a) The frequency scaling factor, a, and (b) the modulli scaling factor, b, for star-like micelles and nearly hard sphere glasses.

As we have seen before the crossover frequency (or equivalently the frequency shift factors) can be used to estimate the rate or timescale of the structural relaxation under shear. In Fig. 6.11, the horizontal shift factor a is plotted as a function of shear rate and compared to previously obtained data on PMMA hard spheres (Jacob *et al.*, 2015). It can be seen that for the star-like micelles, the shift factor a increases sub-linearly with rotational shear rate. A least squares non-linear fitting of the data suggests that $a \propto \dot{\gamma}^{\nu}$ with $\nu = 0.8 \pm 0.04$. By com-

parison, the horizontal shift factor for hard spheres exhibits a linear increase i.e. it yields $\nu = 1$, which is consistent both with some previous experiments (Eisenmann *et al.*, 2010) and with mode coupling theory (MCT) predictions (Fuchs and Cates, 2002, 2003*b*), although an exponent of 0.8 was also found experimentally in model hard-sphere glasses by confocal microscopy under shear (Besseling *et al.*, 2007).

Hence, the weaker power-law dependence of the crossover frequency (or equivalently the shift factor a) for the soft interpenetrable star-like micelles compared to hard sphere particles indicates that in the former shear is less effective in fluidizing the glassy suspension or speed up the structural relaxation time. Similarly, a sub-linear power-law dependence with an exponent of 0.9 has been found for suspensions of soft hydrogel microspheres by strain-rate frequency superposition (Wyss *et al.*, 2007) although such an approach is questionable as it has been shown not to be applicable for multi-arm star polymers (Erwin *et al.*, 2010*b*). Nevertheless, as hydrogel microspheres are intermediate in softness between PMMA hard spheres and star-like micelles, it is tempting to suggest that the structural relaxation in sheared hard sphere systems exhibit a simple linear dependence on shear rate which then decreases to a weaker power-law dependence for softer particles. Still, the specific details of the soft potential may be important, introducing different effects when chain interpenetration in grafted colloids are present in comparison with the case of microgels where shape deformability is important instead. On the theory side, it should be noted that such potential dependent response is not supported by MCT which predicts a linear dependence irrespective of the form of the potential (Fuchs and Cates, 2002, 2003*b*). Therefore it is possible that the observed behaviour does not stem from the ultra-soft potential but from the polymeric nature of the star-like micelle corona. It is certain that the arms of adjacent micelles are interpenetrated at such high effective volume fractions. It is also possible that the polymeric arms act as an additional constraint on shear-induced cage breaking. Thus qualitatively the effect of interpretation would be to reduce the effectiveness of shear in fluidizing the sample, exactly as we observe. This of course is not taken into account by MCT. On the other hand, the non-linear Langevin equation theory utilized

to model glassy suspensions predicts an exponent of 0.8 both for hard spheres (Saltzman *et al.*, 2008) and multiarm star polymers (Yang and Schweizer, 2011) as shear thinning exponent.

In Fig. 6.11 (b) we show that for star-like micelles the vertical shift factor b does not depend on shear rate and is always close to one. This is also evident from the ODFS in Fig. 6.9. The crossover frequency is always at around $G' = G'' = 300\ Pa$ for all shear rates. For hard spheres, b is volume fraction dependent. At $\phi = 0.6$, b substantially increases with shear rate whereas at a higher volume fraction of $\phi = 0.64$ it is close to one over the whole range (Fig. 6.11 (b). As b shifts the plateau modulus it reflects the effect of shear on the free volume inside the cage. We previously argued that for hard spheres, a loosely packed cage at lower ϕ will deform more under shear before breaking with a much greater effect on the in-cage free volume compared to tightly packed cage at higher ϕ. A similar effect might be true for the star-like micelles. The strong interpenetration of adjacent micelles creates a tightly packed cage which cannot deform much before breaking and hence the effect on the free volume is minimal. Alternatively, one can argue that for star-like micelles (and similarly multiarm star polymers) deformation of the cage due to shear flow will not affect the high frequency part of the viscoelastic spectrum which is related to the polymeric nature of the particles and more specifically the local blob fluctuations. This is congruent with the much weaker concentration dependence of the plateau modulus above the glass transition seen in a variety of ultrasoft colloidal particles such as multiarm star polymers (Erwin *et al.*, 2010*a*; Koumakis *et al.*, 2012*b*; Yang and Schweizer, 2010), and in contrast with the nearly hard sphere PMMA particles or the core-shell microgels (Koumakis *et al.*, 2012*b*; Siebenbürger *et al.*, 2009)

The viscoelasticity of the glassy suspension at low shear rates $\dot{\gamma} = 0.025\ s^{-1}$ is relatively straightforward to comprehend. An ODFS that does not change shape but is shifted only along the frequency axis implies that the physical mechanism of the relaxation remains the same. The major effect of shear is to speed up the internal relaxation by introducing an additional timescale $\tau_{shear} \propto 1/\dot{\gamma}^{0.8}$.
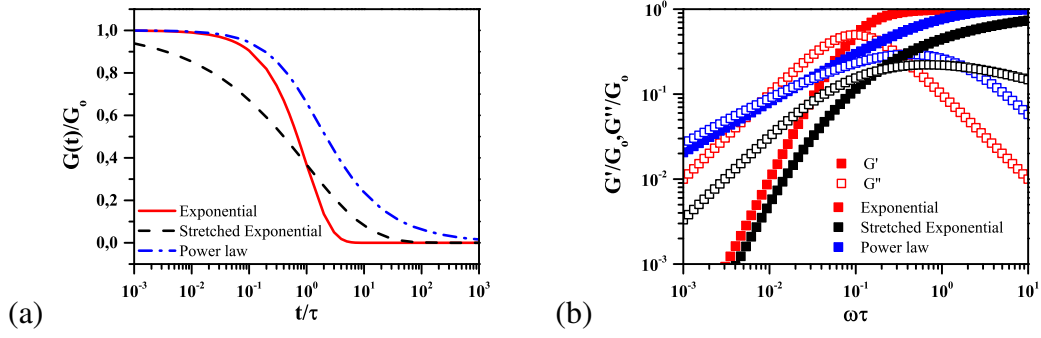
Figure 6.12: (a) The frequency scaling factor, a, and (b) the modulli scaling factor, b, for star like micelles and nearly hard sphere glasses.

However, above $\dot{\gamma} = 0.025 \ s^{-1}$, the terminal behaviour of G' and G'' changes substantially. Both G' and G'' present power-law exponents of 0.5 and they become progressively of equal value over an extended frequency range of approximately one-and-a-half orders of magnitude. It is clear that in this high shear rate regime the physical mechanism of the relaxation has also been modified and it is not anymore the same as in the quiescent glass with just a change of timescales. The specific shape of the viscoelastic spectrum suggests that the relaxation modulus G(t) has a power-law decay instead of an exponential decay. To clarify this statement, we show in Fig. 6.12 (a) numerical simulation of two functional dependences of the relaxation modulus, a stretched exponential with stretching exponent β and a power-law with exponent μ :

$$G(t) = G_o exp(-t/\tau)^{\beta} \quad \beta = 0.4 \tag{6.1}$$

$$G(t) = G_o/(1 + (t\tau))^{\mu} \quad \mu = 0.6 \tag{6.2}$$

In Fig. 6.12 (a) the above relaxation moduli are plotted and compared to a single exponential relaxation which corresponds to the Maxwell model. As expected both the stretched exponential form (especially with such a small exponent $\beta = 0.4$) and the power-law form produce relaxations that are much broader than the Maxwell model. In Fig. 6.12 (b) the relaxation moduli are transformed by numerical integration to G' and G'' (Brader *et al.*, 2010; Ferry,

1980). The difference in the terminal behaviour between the two models is clear. The stretched exponential model shows normal terminal behaviour whereas for the power-law model $G' \approx G'' \propto \omega^{0.5}$. The similarity of the terminal behaviour of these toy models with the measured ODFS strongly suggests that as the shear rate is increased the relaxation takes the form of a power-law. The observation of a second crossover frequency above $\dot{\gamma} = 0.3 \ s^{-1}$ suggests that the power-law behaviour eventually ends and the structure fully relaxes. power-law relaxations are normally associated with critical gels (Winter and Chambon 1986) and have been monitored accordingly in order to determine the gelation point in a variety of soft matter systems. Moreover, multi-step relaxations, such as the ones observed here with alternating exponential and power-law time dependence, have been reported in computational studies of colloidal glasses with the addition of attractive interactions and are associated with sub-diffusive behaviour of single particle displacements (Chaudhuri *et al.*, 2010; Khalil *et al.*, 2014). However, in our system there are strictly no attractions between micelles so a connection is not immediately obvious. Another possibility is that shear produces transient structures of particles with highly correlated dynamics, called shear transformation zones (Chikkadi *et al.*, 2011; Falk and Langer, 1998). These structures have a range of different sizes and hence will relax with a range of different timescales giving rise to power-law relaxations. It is also noteworthy that the critical shear rate $\dot{\gamma} = 0.025 \ s^{-1}$ where the relaxation changes from multi-exponential to power-law corresponds to the inflexion point in the flow curve (Fig. 6.9 (c)). Below this critical shear rate the flow curve shows increasing stress with rate, whereas at higher rates the stress is almost independent of shear rate exhibiting a pseudo-yield stress plateau. It is conceivable that the power-law relaxation of the ODFS above $\dot{\gamma}_{cr}$ is related to the stress plateau where flow is thought to occur through local plastic rearrangements of the particles (Bocquet *et al.*, 2009). On the other hand, below $\dot{\gamma}_{cr}$ the slow relaxation of the soft colloidal glass which is also present at rest, is fast enough to homogenize the flowing colloidal glass, dominating over the externally shear imposed structural relaxation

In summary, we have used orthogonal superposition rheometry (OSR) to directly measure the viscoelastic properties under shear of a concentrated solution

of star-like micelles above the colloidal glass transition, and hence elucidate its mechanism of flow. The star-like micelle solution at rest has all the characteristics of a weak colloidal glass, with a crossover frequency $\omega_c \sim 0.01 \; rad/s$ and elastic behaviour ($G' > G''$) in a wide frequency range above ω_c, as well as an apparent yield stress. In OSR a small-amplitude oscillatory shear deformation is simultaneously applied to a sample under steady shear but in an orthogonal direction. OSR is sensitive enough to obtain orthogonal dynamic frequency sweeps (ODFS) in a wide rotational shear rate range between $5 \times 10^{-4} \; s^{-1}$ to $10 \; s^{-1}$. As expected, the progressive increase of shear rate fluidized the colloidal glass and has a twofold effect on the ODFS obtained at steady state after the initial transient behaviour. Firstly, G' decreases and G'' increases over the whole range of frequencies measured. Secondly, the crossover frequency ω_c steadily moves to higher values reflecting a reduced structural relaxation timescale. We show that the dependence of ω_c on the shear rate is sub-linear and follows a power-law with exponent 0.8 by comparison for hard spheres ω_c varies linearly with shear rate as we have shown in the previous chapter(Jacob *et al.*, 2015). The shape of the ODFS changes at a critical shear rate of approximately $\dot{\gamma}_{cr} = 0.025 \; s^{-1}$ which corresponds to the inflexion point in the flow curve. At low shear rates the ODFS shape is nearly identical to the one at rest but shifted along the frequency axis. On the other hand, above $\dot{\gamma}_{cr}$ the ODFS terminal behaviour changes, with G' and G'' becoming equal and both proportional to $\omega^{0.5}$. ODFS at different shear rates can be superimposed by shifting along the frequency and moduli axes producing two ODFS master curves above and below $\dot{\gamma}_{cr}$. The changing shape of the ODFS at $\dot{\gamma}_{cr}$ is indicative of a structural relaxation that changes from multi-exponential to power-law. This is discussed in terms of localized plastic rearrangements or shear transformation zones that are thought to govern the flow of colloidal glasses.

6.3 Orthogonal Superposition Rheometry of colloidal glasses during transient shear

6.3.1 Orthogonal superposition during start-up shear

In this section the transient start-up shear and oscillatory shear response is investigated by orthogonal superposition shear. A specific $\dot{\gamma}$ is applied in the horizontal direction and then a small amplitude perturbation is superimposed in the orthogonal direction in order to extract an orthogonal elastic and viscous moduli during start-up shear. The horizontal transient start-up measurements were performed with varying rates from $0.0001 \ s^{-1}$ to $0.5 \ s^{-1}$. For all measurements with orthogonal probing, oscillatory shear is performed at $\gamma_o = 1\%$ and $\omega = 10 \ rad/s$. The colloidal glasses investigated have a particle radius $R = 196 \ nm$ dispersed in a mixture of Octadecene and Bromonapthalene ($n_D = 1.48$). The solvent mixture was chosen to closely match the refractive index of the colloidal particles and minimise van der Waal forces. Two volume fractions $\phi = 0.60, 0.61$ are probed during transient flows with orthogonal superposition.

An oscillatory signal is generated by high-accuracy multifunction data acquisition board, interfaced with LabVIEW (NI PCI-6281 and LabVIEW 8.5, National Instruments) for orthogonal superposition of LAOS in hard sphere colloidal glasses and the orthogonal superposition of transient shear for colloidal glasses. The input signal and the output stress signal is collected and analyzed externally using a homemade MATLAB code to extract G'_{orth} and G''_{orth}.

Fig. 6.13 depicts the start-up transients for a hard sphere glass with $\phi = 0.61$ for all $Pe < 1$. At low Pe, in Fig. 6.13 (a), (b) and (c) one can observe that there is very small increase in the orthogonal moduli. This is congruent to the findings at high frequency data and low horizontal Pe in Fig. 6.2 (a) where the G'' on orthogonal superposition of steady shear was found to deviate to higher values with increasing the shear rate. But as the Pe is increased as seen in Fig. 6.13 (d) G'_{orth} and G''_{orth} change with time during transient test. Additionally,
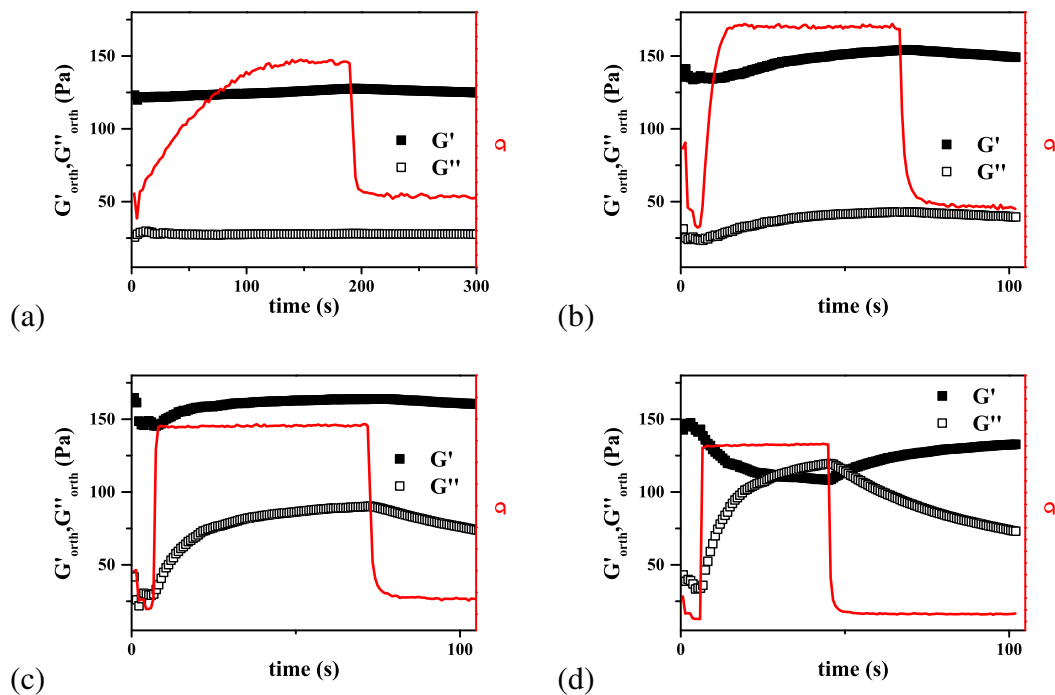
Figure 6.13: Orthogonal time sweep performed during start-up shear tests with (a) $\dot{\gamma} = 7.9 \times 10^{-5} \, Pe$ (b) $\dot{\gamma} = 1.6 \times 10^{-3} \, Pe$ (c) $\dot{\gamma} = 1.6 \times 10^{-2} \, Pe$ and (d) $\dot{\gamma} = 7.9 \times 10^{-2} \, Pe$ for hard sphere particle $R = 196 \, nm$ at $\phi = 0.61$. The red lines indicate the horizontal steady state stress and the filled symbols indicate G' while unfilled symbol G''. The orthogonal frequency was set at $10 \, rad/s$

we also observe the relaxation after steady shear flow, however with quite slow relaxation. The G'_{orth} and G''_{orth} tend to go back to its initial values after the flow cessations.

As the horizontal shear rate is extended towards $Pe = 1$ to approaches the scenario of a liquid-like response with $G''_{orth} > G'_{orth}$ captured in Fig. 6.13 (d). The transient relaxation of stress is observed in all cases after shear cessation. During this relaxation, as expected the the G'_{orth} and G''_{orth} tend to go back to its initial values at rest. The most interesting aspect here is that it seems to take more than $\sim 350\, t_B$ for a system to reach equilibrium values in the orthogonal moduli. This indicates that orthogonal moduli could be sensitive to bulk flow transitions during start-up shear.

6.3.2 Orthogonal superposition during LAOS

In this section, we probe the transients during large amplitude oscillatory shear by superimposing a small amplitude perturbation in the orthogonal direction. This was done in order to extract the instantaneous viscoelastic moduli during oscillatory shear. The horizontal oscillatory shear was kept at a constant frequency of $0.1\, rad/s$ and the strain amplitudes where changed such that it reaches non-linear regime of the colloidal glass. It was empirically observed that instantaneous G'_{orth} and G''_{orth} can be achieved only if the orthogonal frequency is 100 times the frequency of the horizontal oscillation hence frequency was fixed at $\omega = 10\, rad/s$ and the strain at $\gamma_o = 1\%$. In Fig. 6.14, the left axis is plotted with the orthogonal viscoelastic moduli and the right axis is the horizontal stress with respect to time. During SAOS, the orthognal viscoelastic moduli does not show any fluctuations as seen in Fig. 6.14 (a). As the strain amplitude ($\gamma_o = 500\%$) of the horizontal oscillation progress into the non-linear regime the instantaneous G'_{orth} and G''_{orth} start revealing damped oscillatory behaviour (see Fig. 6.14 (b)).

In an attempt to relate the instantaneous horizontal strain, strain rate and stress with respect to the orthogonal viscoelastic moduli we present them in
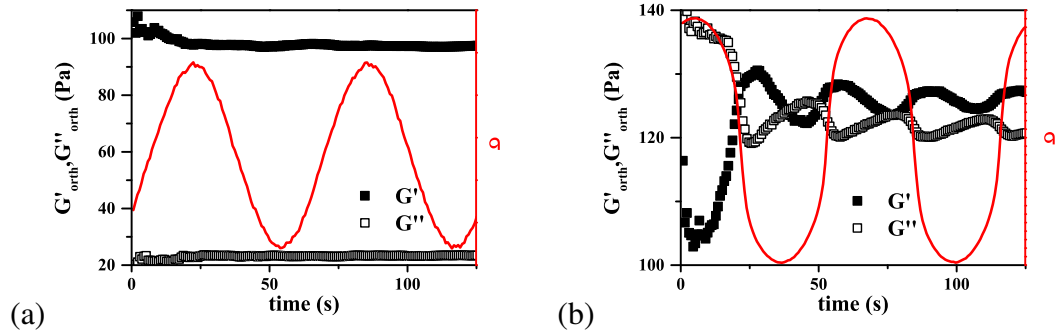
Figure 6.14: Orthogonal time sweep performed at different γ_o (a) 5% (b) 500% for $R = 196\ nm$ and $\phi = 0.61$
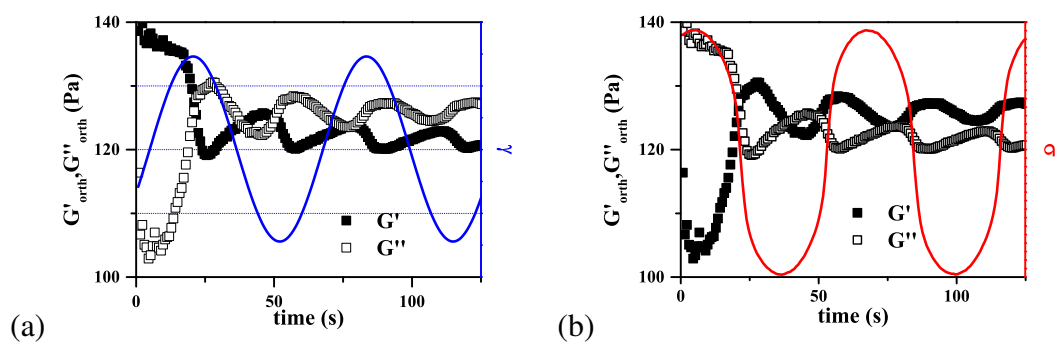
Figure 6.15: Orthogonal time sweep performed at $\gamma_o = 500\%$ shown as a function of (a) horizontal strain and (b) horizontal stress for $R = 196\ nm$ and $\phi = 0.61$

Fig. 6.15. From Fig. 6.15 (a) it can be seen that soon after $\gamma_{hor} \rightarrow \gamma_o$ and $\dot{\gamma}_{hor} \rightarrow 0$ there seems to be a maximum separation between G'_{orth} and G''_{orth} such that $G'_{orth} > G''_{orth}$. Immediately after $\gamma_{hor} \rightarrow 0$ and $\dot{\gamma}_{hor} \rightarrow \dot{\gamma}_o$ it can be seen that $G' \sim G''$. In order to attempt a quantitative comparison we define a phenomenological non-dimensionless parameter relative elasticity, R, which has found to be robust quantity to follow state transitions (McKenzie and Vlassopoulos, 2016).

(a)   (b)
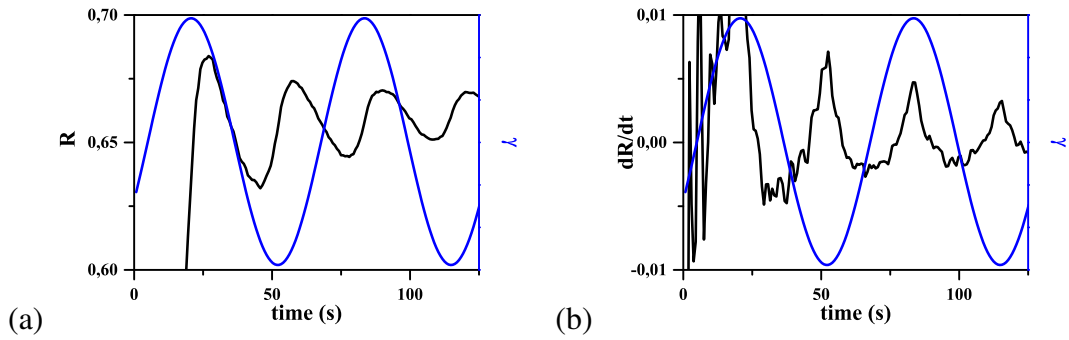
Figure 6.16: Orthogonal time sweep at performed at $500\%\gamma_o$ with (a) Relative Elasticity, R (b) rate of relative elasticity, dR/dt for $R = 196nm$ and $\phi = 0.61$

The Relative Elasticity is defined as

$$R = \frac{1}{(\tan^2 \delta + 1)} \tag{6.3}$$

where

$$\tan \delta = \frac{G''}{G'} \tag{6.4}$$

In Fig. 6.16 (a) Relative elasticity, R, displays a dampened oscillating behaviour. As observed in Fig. 6.15 one can see changing of slope at $\gamma \rightarrow 0$ and $\gamma \rightarrow \gamma_{max}$. In order to display the change of slope the derivative of relative elasticity is represented with respect to time. It can be clearly observed that the transitions during change in direction of horizontal strain in LAOS is very abrupt. On the other hand, transition at maximum shear rate is much smoother. Although, as noted before the intensity of these transitions seem to be decreasing

with time for the experimental window observed long time measurements are essential to identify the equilibrium state of orthogonal moduli during LAOS. Thus different state transitions, abrupt and smooth transitions, can be observed within a cycle of large amplitude oscillatory shear.

In this chapter we investigated the viscoelastic behaviour of colloidal glasses with the aid of orthogonal superposition rheometry. Colloidal glasses were sheared in the horizontal direction and the a linear oscillatory perturbation was superimposed in the orthogonal direction . Hard sphere colloidal glasses exhibited a crossover transition from liquid to solid-like repose at high rates. The crossover frequency was found to be a linear function of the shear rate. Orthogonal frequency superposition was performed from the linear viscoelastic spectra obtained. Deviations were observed at short and long times. The short time deviations were attributed to cage anisotropy corroborated with BD simulations. On the other hand long time deviations were speculated arise from the presence of hydrodynamics. Soft star-like micelles were also investigated using this technique to understand the effect of interparticle interaction in steady shear flow and the crossover frequency was found have a sub linear dependence to the shear rate. This is speculated to be due the interpenetrable soft nature of the star-like micelles. Finally, linear viscoelasticity under transient start-up shear and large amplitude oscillatory shear is also extracted. Abrupt state transition at maximum of horizontal strain amplitude and smooth state transition at zero strain was observed during a large amplitude oscillatory shear.

CHAPTER 7

BROWNIAN DYNAMICS SIMULATIONS OF BINARY COLLOIDAL GLASSES

Glass formation by a single species has been studied extensively. This has led to exploration of different types of glasses formed. Binary mixtures are much less explored although there are relevant applications like transport through disordered media like cells and glass ion conductors (Angelini *et al.*, 2011; Ellis and Minton, 2003; Höfling *et al.*, 2006; Horbach *et al.*, 2002; Sentjabrskaja *et al.*, 2016). In highly asymmetric size hard sphere mixtures, new types of glass were found to exist (Imhof and Dhont, 1995). Additionally, in these highly asymmetric size ratios attractive potential developed between the big particles due to depletion effects induced by the small particles (Crocker *et al.*, 1999). Another type of glass that emerged was formed by the small soft particles that developed asymmetric cages to trap the big soft particles (Mayer *et al.*, 2008). Recently, new phases in glass was observed to emerge when small nearly hard sphere colloids were mixed with large multiarm stars (Truzzolillo *et al.*, 2013). MCT predicts the existence four types of glasses for highly size anisotropic binary mixtures of hard spheres; glass partially frozen by caging, glass partially frozen by depletion, torroncino glass driven by small particle caging and double glass (Voigtmann, 2011).

Such glasses predicted by MCT have started to recently be explored by experiments employing rheology and optical microscopy. The quiescent state dynamics of these asymmetric hard sphere mixtures was probed using confocal microscopy (Sentjabrskaja *et al.*, 2013*b*) while their mechanical properties and yielding behaviour by rheology (linear and non-linear) (Sentjabrskaja *et al.*, 2013*b*) and the transient dynamics (Sentjabrskaja *et al.*, 2014) during start-up shear were probed using confocal microscopy and rheology. The addition of a

second species to an already caged system was found to increase the free volume of the system hence softening the cages (Sentjabrskaja *et al.*, 2013a). Hints of double step yielding were also found too exist. The super-diffusive dynamics and the strength of the overshoot during transient start-up shear was linked to the cage compression effects while the yield strain was also found to depend on the caging species (Sentjabrskaja *et al.*, 2014).

Calculation of the mixing ratio by volume for small particles, χ_s, was based on the following equation

$$\chi_s = \frac{N_s R_s^3}{N_s R_s^3 + N_b R_b^3} \tag{7.1}$$

where the N is the number of particles and R is the radius of the particles and the subscripts s and b indicates the small and big particles respectively. This indicates the ratio of volume of small particles to the total volume of the binary mixture. Another parameter that is used in this chapter is the size ratio, δ, which is defined as the ratio of the small particle radius to the big particle radius. Furthermore, the Peclet for shear is defined based on the small particles as $Pe_s = \dot{\gamma} t_{Bs}$. This means that the big particles for a size ratio of 0.2 flow (Pe_b) at 125 times higher Pe_s since $t_{Bb} = 125 t_{Bs}$ The total volume fraction of the binary mixture is always kept constant although the mixing ratios varied.

Here, we employ BD simulations (Foss and Brady, 2000) with periodic boundary conditions for a fixed size ratio of $\delta = 0.2$ for hard sphere particles. 50000 particle simulation where performed for $\chi_s = 0.1$ to $\chi_s = 0.9$ for a total $\phi = 0.58$ and 0.61. Moreover, smaller sizes with 15000 particle simulations where performed for the $\chi_s = 0.01$ and 0.05 and the pure species for both volume fractions in order to reduce the physical simulation time. The determining species in the simulations are the small particles as the time steps and shear were performed based on the small particle time step.
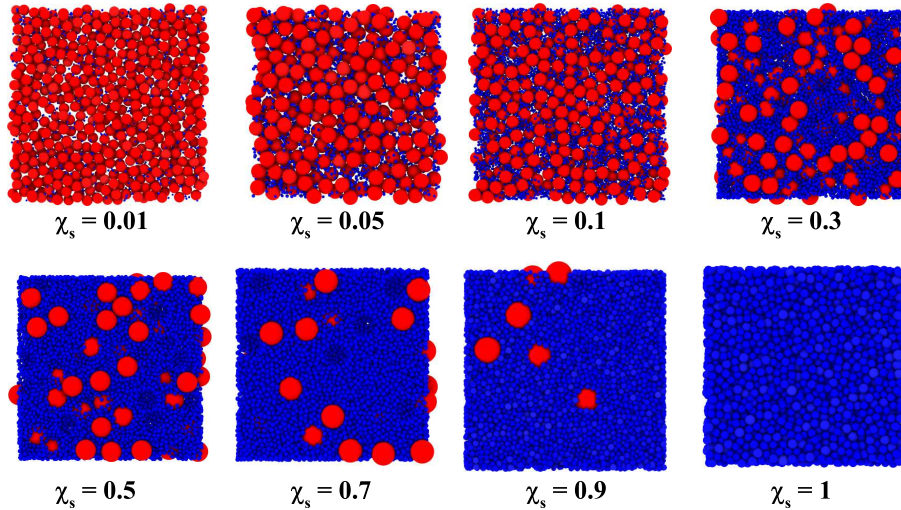
Figure 7.1: Configurations of the Binary glasses obtained by varying χ_s, at $\phi = 0.58$ and $\delta = 0.2$

7.1 Binary mixture at rest

In Fig. 7.1 the structure at rest for the binary mixture glasses at $\phi = 0.58$ are shown. The red colour indicates big particles and small particles are indicated by the blue colour. The size anisotropy can be easily visualized from the Fig. 7.1 and is fixed at a value $\delta = 0.2$ throughout this chapter. From the box defined for the simulation, a slice of thickness $3\ R_b$ is selected for all the χ_s is chosen for visual inspection in Fig. 7.1. The big and small species are represented by red and blue colour, respectively. Visually one can observe that at $\chi_s = 0.01$ the cages are formed by the big particles. There are also some hints of depletion induced structure for the big species at $\chi_s = 0.01$ compared to other χ_s. The white space observed at $\chi_s = 0.01$ is not due to the absence of particles but the due to big particles present in front and behind the observation slice. At $\chi_s = 0.3$, we observed that the neither small nor big particles are prominent and it is very difficult to discern which of the two species are forming the cages. For $\chi_s > 0.7$, it is easily observed that the small particles start predominately to form cages. Thus, it can be discerned that the small particles contribute to the overall dynamics of the system. At $\chi_s = 0.9$ the small particles dominate the cage formation and in turn trapping the big particles which is evident from the Fig. 7.1. Based on the different types of glass predicted by MCT (Voigtmann,

2011), we visually observe partially frozen glass and torroncino glass driven by small particles.
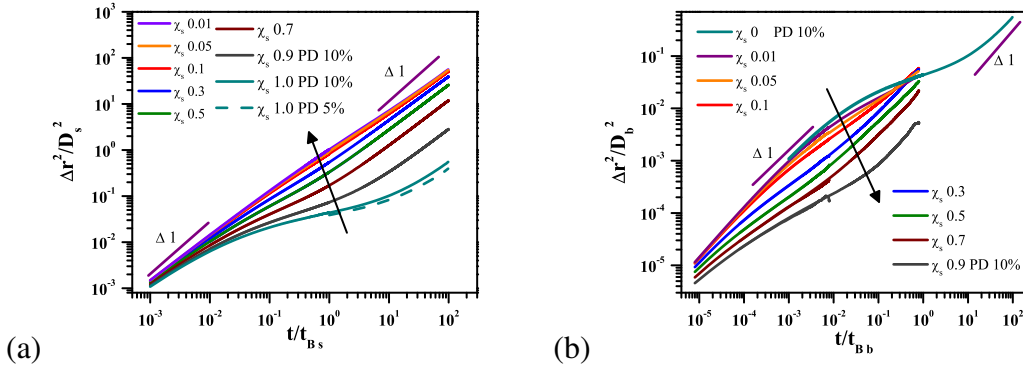
Figure 7.2: Mean Square Displacement of (a) small particles and (b) big particles for different mixing ratios of small particles with total $\phi = 0.58$

In Fig. 7.2 (a) we observe the MSD of the small particles at rest by varying the χ_s for the configurations seen at $\phi = 0.58$ in Fig. 7.2. For $\chi_s = 0.01$ where the big particles predominantly form the cages, the small particles are seen to be extremely mobile. The small particles at this χ_s can be visualized as intruders in a matrix of large particles (Sentjabrskaja *et al.*, 2016). The short time MSD exhibits the slope of 1 due to diffusion of the small particles while at long time a sub-diffusive behaviour is observed. This is because the small particles sense the crowded matrix of the big particles. Small particles being extremely mobile access the space formed by the voids of the big particles. Moreover for the same $\chi_s = 0.01$, the MSD of big particles suggests caging at long times following the MSD of the pure system in Fig. 7.2 (b). As the amount of small particles are increased at $0.05 \leq \chi_s \leq 0.5$ the big particles (Fig. 7.2 (b)) become more mobile than the pure species at long time. $\chi_s = 0.9$ indicates an extensive slowing down of the big particles from Fig. 7.2 (b). In the mean time, a plateau in the MSD of the small particles is observed which is a characteristic of caging effect of the neighbouring particles as seen in Fig. 7.2 (a). Here, the big particles are trapped by the cages of small particles making it literally immobile. The long time behaviour of the big particles in Fig. 7.2(b) are misleading as the statistics is extremely poor owing to the small number of big particles. The absolute MSD values for both big particles and small particles decrease with increasing χ_s which indicates a slowing down of both particles in

131   University of Crete, Greece

general.

In order to understand the effect of polydispersity on the system, a pure system with 5% dispersity is evaluated. It is observed that the MSD for 5% polydispersity is smaller than 10% polydisperse system. This is happens because the more the polydispersity the larger the amount of mobile particles leading to a higher MSD values. Polydispersity was added to binary systems which were found to crystallize under equilibrium conditions. The MSD in general corroborates the idea that the caging at low χ_s is dominated by the big particles which then moves to a transition liquid phase and finally an arrested phase where the system is caged by the small particles (Sentjabrskaja *et al.*, 2013*a*, 2014).
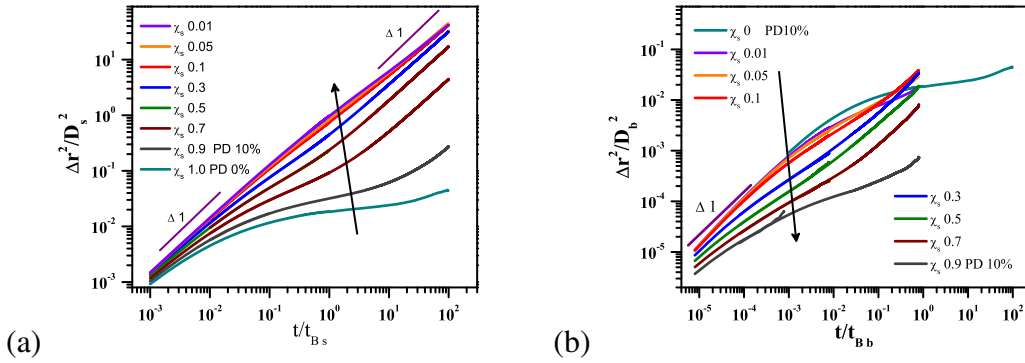
Figure 7.3: Mean Square Displacement of (a) small particles and (b) big particles at for different mixing ratios of small particles with total $\phi = 0.61$

Fig. 7.3 shows the MSD of both small and big particles at $\phi = 0.61$ and is similar to that shown in Fig. 7.2 but a more prominent effect of caging is observed due to increase in the overall ϕ. The fluid regime is more clearly observed in Fig. 7.3 (b) to occur at $0.05 \leq \chi_s \leq 0.5$. The MSD gives a clear indication of the existence of three phases in our investigation regime of size ratio $\delta = 0.2$. The partially frozen glass driven by caging of big particles and extremely mobile small particles at small mixing ratio of small particles. The existence of a liquid regime at intermediate mixing ratio is due to the transitioning of the caging from big species to small species. Finally, at large mixing ratio the existence of "torroncino" glass where the big particles are localised to specific regions due to the caging of the small particles. These simulations corroborates some of the phases predicted by MCT (Voigtmann, 2011).
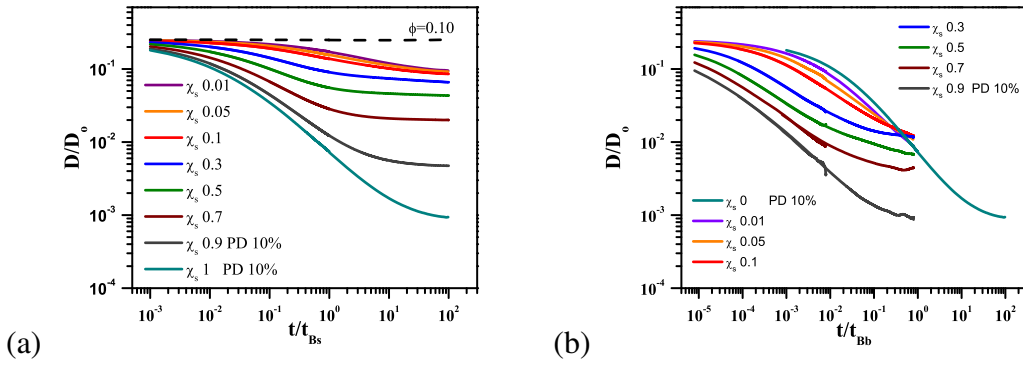
Figure 7.4: Diffusivities of (a) small particles and (b) big particles at for different mixing ratios of small particles with total $\phi = 0.58$

Fig. 7.4 depicts the diffusivity of the particles as function of the mixing ratio, χ_s. In Fig. 7.4 (a), small particles diffusivity for long times ($> 1t_{Bs}$) at $\chi_s = 0.01$ is smaller than the diffusivity of the pure species at $\phi = 0.1$. This shows that the mobility of the small particles are hindered by the matrix of the big particles at long time and hence shows a decrease in the diffusivity. It can be inferred from MSD and the diffusivity that the small particles are mobile and travel through the interstitial voids formed by the cages of big particles. On the other hand, a big particle is caged by neighboring big particles. The big particles at mixing ratio $\chi_s = 0.3$ become extremely mobile at long time as seen from MSD and diffusivities of big particles in Figs. 7.2 (b), 7.3 (b) and 7.4(b). At large mixing ratios the diffusivities of big and small species drop even further suggesting a large hindrance to mobility for both species.
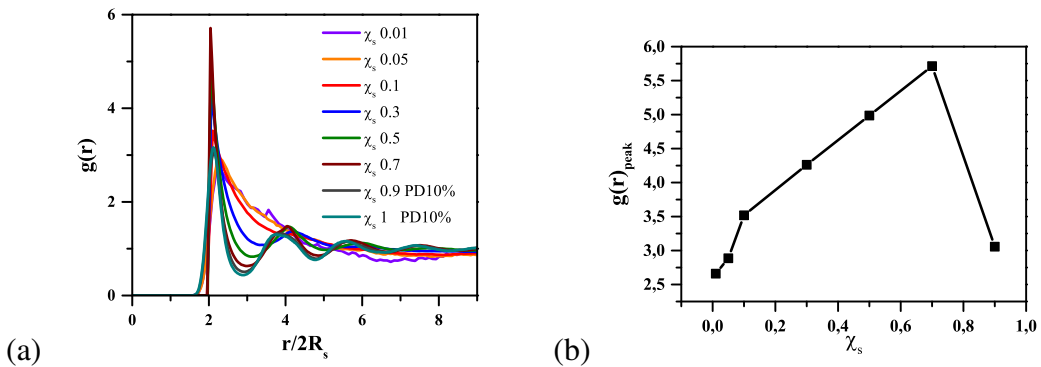
Figure 7.5: (a) $g(r)$ for small particles for different mixing ratios of small particles (b) $g(r)_{peak}$ for small particles as a function for mixing ratio of small particles with total $\phi = 0.58$

In Fig. 7.5 (a), the probability of finding a neighbour for the small particles is shown for different mixing ratios at $\phi = 0.58$. For some ϕ the $g(r)$ rises much before $2R_s$ is reached, due to polydispersity induced in the binary systems. While for others the $g(r)$ rises exactly at $2R_s$ as no polydispersity was incorporated in these system. As the mixing ratio, χ_s, is increased the appearance of a second shell becomes prominent at $4R_s$. Also the peak position of the second neighbour shell moves to smaller r. The intensity of the first $g(r)_{peak}$ is plotted as a function of the mixing ratio χ_s (Fig. 7.5 (b)). A non-monotonic behaviour is observed with the $g(r)_{peak}$ initially increasing with mixing ratio χ_s and steeply dropping at $\chi_s = 0.9$. In experiments, it was observed that the $g(r)_{peak}$ for big particles continuously decreases $g(r)_{peak}$ with increasing χ_s (Sentjabrskaja *et al.*, 2013*b*). This non-monotonic drop in intensity in BD simulations can be attributed to the polydispersity introduced in the sample. Polydispersity cannot be avoided for $\chi_s = 0.9$ as crystallization during equilibration procedure was observed. The $g(r)$ for big particles are not shown here due to the poor statistics of the data. In general, this suggests that caging of the small becomes prominent at $\chi_s > 0.3$
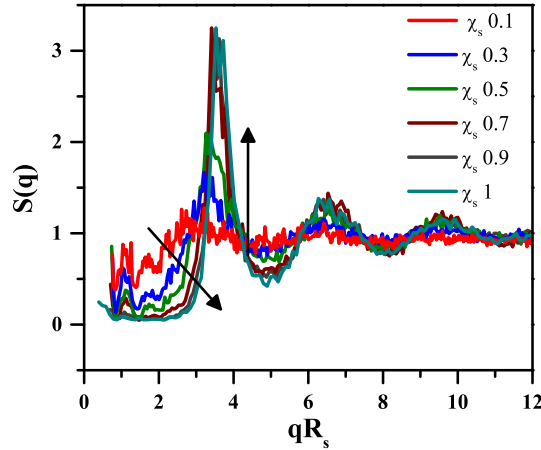
Figure 7.6: $S(q)$ for small particles for different mixing ratios with total $\phi = 0.58$

Fig. 7.6 represents $S(q)$ for small particles in a binary mixture for varying χ_s and the data for $\chi_s < 0.1$ is not presented due to poor statistics. For $\chi_s = 0.1$, it is clear that the system does not have any long range order similar

to a liquid. As the mixing ratio for the small particles increases the the position of the initial peak moves to higher values of q and a long range order becomes prominent. The appearance of second and third peaks indicates that caging becomes prominent at mixing ratios, $\chi_s > 0.3$, by small particles which is also observed in Fig. 7.1. Figs. 7.5 and 7.6 depict the small species to small species structure information, thus it does not reveal any kind of cage transition from the big species to small species.
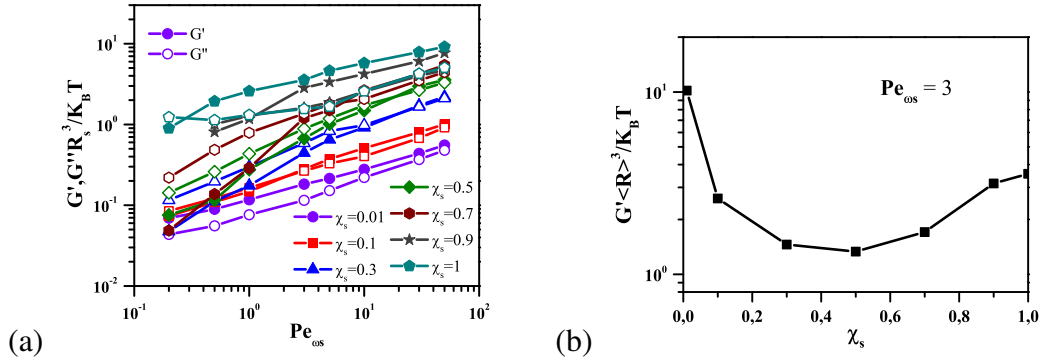
Figure 7.7: (a) Linear viscoelastic response of a binary colloidal mixture with a total $\phi = 0.58$ (b) G' scaled with average radius, $\langle R \rangle$, plotted as a function of mixing ratio of small particles, χ_s

Linear viscoelastic response of the binary colloidal mixtures at $\phi = 0.58$ for different mixing ratios are shown in Fig. 7.7. It should be noted that G' and G'' are scaled by the small particle radius R_s (Fig. 7.7 (a)). For a pure system when $\chi_s = 1$, $G' > G''$, a solid-like response is observed for most of the frequencies. At $0.3 \leq \chi_s \leq 0.5$ the viscous moduli, G'', becomes more predominant than the elastic moduli, G' for the frequencies probed which indicates a liquid-like response of the system. This indicates that the caging effect by neither species dominates at these intermediate mixing ratios promoting mobility of both species. At $\chi_s = 0.01$, the storage moduli is greater than the loss moduli thus indicating a glass-like response in this regime. When storage modulus is scaled as function of the average radius, $\langle R \rangle$, of the binary mixture and represented as a function of χ_s we observe drop in the scaled G' as already seen experimentally (Sentjabrskaja *et al.*, 2013*b*). Here the average radius, $\langle R \rangle$, is

defined as

$$\langle R^3 \rangle = \frac{R_b^3}{\left[1 - \chi_s \left(1 - \frac{1}{\delta^3} \right) \right]} \tag{7.2}$$

This shows softening effect occurring in the binary colloidal mixtures for $\phi = 0.58$ and at intermediate mixing ratio of small particles.
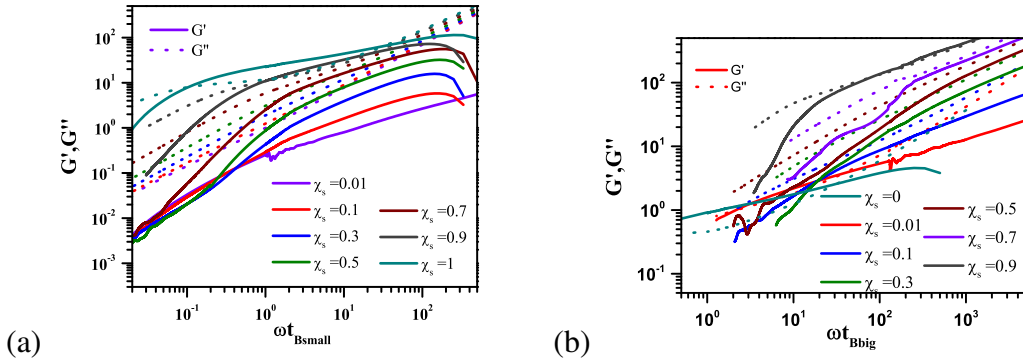
Figure 7.8: Linear viscoelastic response of a binary colloidal mixture with total $\phi = 0.58$ obtained from Generalised Stokes Einstein equation for (a) small particles (b) big particles from the MSD in Fig. 7.2

Fig. 7.8 indicates the linear viscoelastic data for $\phi = 0.58$ extracted for pure small and big species individually by Generalised Stokes Einstein equation using the MSD shown in Fig. 7.2. For small particles in Fig. 7.8 (a), the storage moduli is less than loss moduli for $\chi_s = 0.01$ at all $Pe_{\omega s}$. While in the case of high χ_s ($\chi_s = 0.9$), the storage modulus is greater than the loss modulus for $1 < Pe_{\omega s} < 100$. Additionally, we also observe high $Pe_{\omega s} > 100$ regime from the simulations where the G'' is greater than G'. The absolute values G' and G'' show an increasing trend with mixing ratio for small particles species because the absolute values of the MSD for small species decreases.

The pure species at mixing ratio of $\chi_s = 0$ in Fig. 7.8 (b) indicates the $Pe_{\omega b}$ regime where a glass-like behaviour is observed. In the case of big particles, G' and G'' are extracted for very high $Pe_{\omega b}$ ($Pe_{\omega b} > 10$) regime since t_B for the big particles is 125 times larger than the small species. In general, the fluctuations in the G' and G'' arise from poor fitting of the MSD data with a second order polynomial in order to extract the moduli.
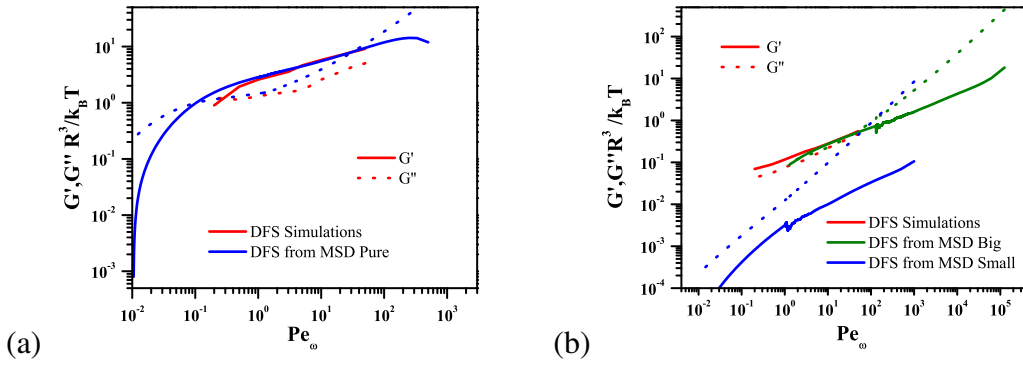
Figure 7.9: (a) Linear viscoelastic response of a pure colloidal glass at $\phi = 0.58$
(b) Linear viscoelastic response of a binary colloidal mixture with total $\phi = 0.58$ at $\chi_s = 0.01$ obtained from Generalised Stokes Einstein relation and oscillatory shear from simulations

In Fig. 7.9 (a) we compare the linear viscoelastic data from oscillatory shear as well and individual species linear viscoelastic response from the MSD. There is a good match between both the elastic and viscous moduli obtained from both the techniques in the case of pure species (Fig. 7.9 (a)). In Fig. 7.9 (b) linear viscoelastic response of the binary glass with viscoelastic response for individual species at $\chi_s = 0.01$ is also compared. The data from oscillatory measurements seem to coincide more with data obtained from the individual big spheres. This indicates that the caging mechanism in this case is driven by big particles and thus contribute to the overall response of the sample. Meanwhile, the small particles exhibit a purely liquid-like response in linear data since the small particles are mobile and travel through the voids formed by the cages of big particles.

Fig. 7.10 (a) at mixing ratio of $\chi_s = 0.5$ depict the individual species and binary mixture show a consistent behaviour where $G'' > G'$. This indicates that the binary colloidal mixture shows as a liquid-like response at this mixing ratio. Here, both species contribute equally to the binary mixture response. In Fig. 7.10 (b) for mixing ratio of $\chi_s = 0.9$, the binary mixture behaves as a glass which is dominated by the caging species of the small particles. Thus, the average response of the binary mixture is very similar to that indicated by the pure small particle glass. While the big species are also caged by the small species the linear response of the individual big species is not clear due to poor

(a)

(b)
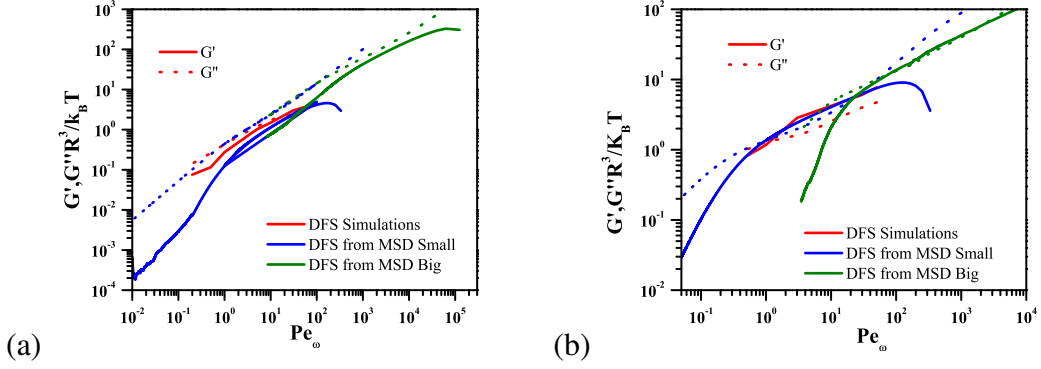
Figure 7.10: Linear viscoelastic response, of a binary colloidal mixture with total $\phi = 0.58$, for individual species from Generalised Stokes Einstein equation and binary mixture oscillatory shear from simulations at (a) $\chi_s = 0.5$ and (b) $\chi_s = 0.9$

statistics at low Pe_ω. In general, the most prominent species drives the linear viscoelastic response and dynamics at rest for the binary mixture.

7.2 Start-up shear

(a)

(b)
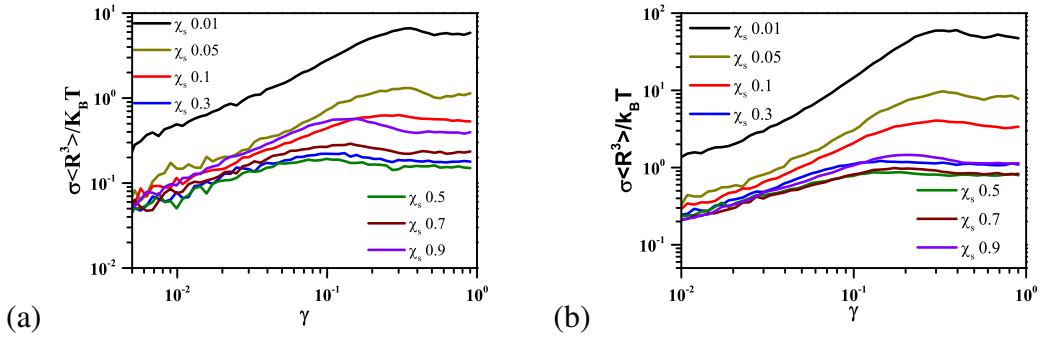
Figure 7.11: Start-up shear for binary colloidal mixture at $\phi = 0.61$ at varying mixing rations of small particles for (a) $Pe_s = 0.1$ and (b) $Pe_s = 1$

In Fig. 7.11 the start-up shear of a binary mixture with volume fraction $\phi = 0.61$ is shown for $Pe_s = 0.1$ and $Pe_s = 1$. The shear stress is scaled as a function of the average radius as defined by Eq. 7.2. For intermediate mixing ratios of small particles a reduction in the steady state stress values can be observed. This is an indication of the softening of the binary mixture. For the lowest ($\chi_s = 0.01$) and highest ($\chi_s = 0.9$) mixing ratios stress overshoot

becomes prominent which disappears for the intermediate mixing ratios. In the intermediate mixing ratios where the stress peak disappears there is a direct transition from elastic to the flow regime.
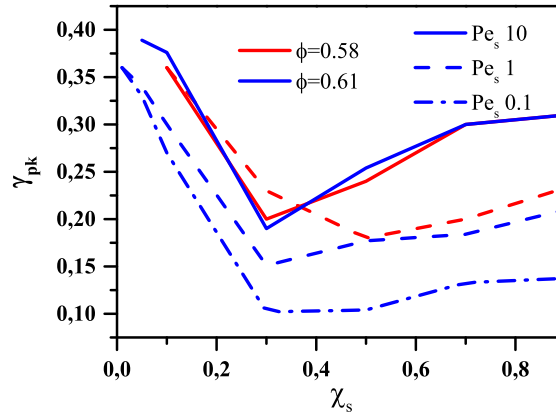
Figure 7.12: The strain at peak of stress overshoot for start-up shear

A non-monotonic response is observed for strain at stress overshoot peak for binary mixtures in Fig. 7.12. The drop of γ_{pk} at intermediate mixing ratios is clear indication for the softening of the binary mixtures. For $\phi = 0.61$ γ_{pk} exhibits a minimum at $\chi_s = 0.3$ although at $\phi = 0.58$ the minimum tends to be a function of the Pe_s. A similar response where the γ_{pk} depicts a minimum at intermediate mixing ratios has also been observed experimentally (Sentjabrskaja *et al.*, 2014). It should be noted that the Pe_s is defined with reference to the small particle thus for all the Pe_s investigated here the big particles experience $Pe > 1$. At $\chi_s \geq 0.7$ and $Pe_s \leq 1$, the Brownian assisted yielding of small particles aids in cage breaks and at $Pe_s > 1$ shear-induced cage breaking by the small species dominates. At $\chi_s < 0.3$, since the cages are dominated by the big particles the cages can deform to a much larger strain before flow occurs leading to an increase in the γ_{pk}.

The intensity of stress overshoot in colloidal glasses indicates the storage of elasticity in the cages (Koumakis *et al.*, 2012*a*, 2016*b*). Thus the intensity of the stress overshoot could lead to the understanding of yielding during start-up shear in binary mixtures as shown in Fig. 7.13. The intensity of the stress overshoot drops to a minimum for the intermediate χ_s values which shows that the stress
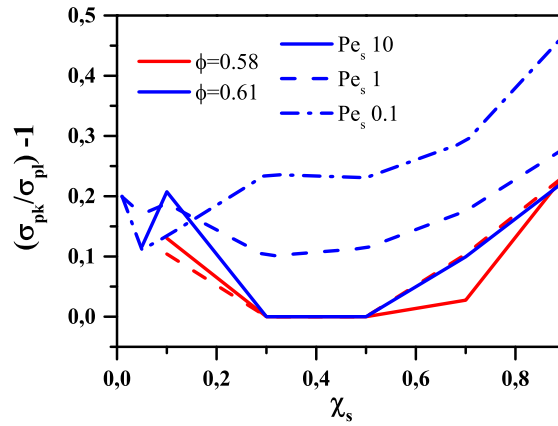
Figure 7.13: Intensity of the stress overshoot comparison for start-up shear

storage efficiency decrease due to cage transition from one species to another. The binary mixtures dominated by small particle cages tends to store more stress than the big particles unlike that seen in the experiments (Sentjabrskaja *et al.*, 2014). The stress intensity peaks in experiments was inversely related to the cage compression. This does not seem valid in these simulations probably due to some depletion effects contributing to the stress intensity overshoot. In experiments it was shown that binary mixtures at low Pe_s exhibit a larger stress overshoot and this is also observed in Fig. 7.13 (Sentjabrskaja *et al.*, 2014).
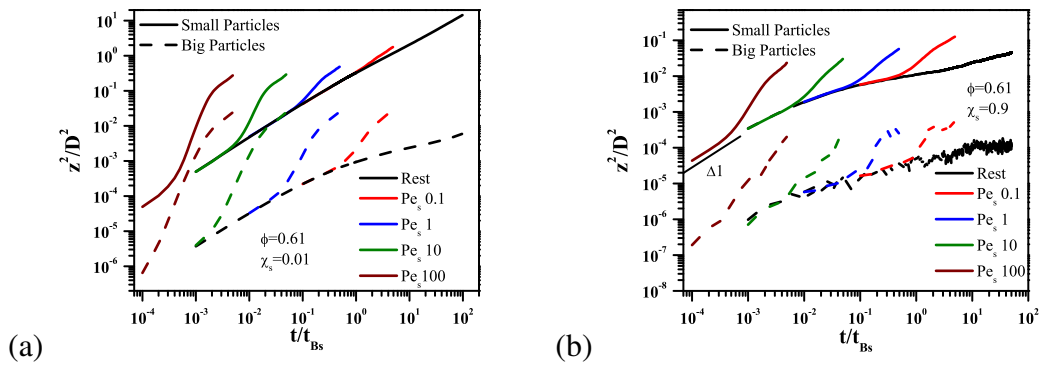
Figure 7.14: Two time mean square displacement for binary colloidal mixture in the vorticity direction at $\phi = 0.61$ for different Pe_s at (a) $\chi_s = 0.01$ and (b) $\chi_s = 0.9$

In Fig. 7.14, the two time MSD of both the small and big particles are followed in the vorticity direction for $\phi = 0.61$ during start-up shear, the dynamics at rest for both small and big species at rest are superimposed. Fig. 7.14 (a) and

(b) compares two extreme cases of caging where the cages are dominated by big species and small species respectively. Fig. 7.14 (a) shows that at $\chi_s = 0.01$ the big particles move into the super-diffusive regime earlier in time than the small particles. At $\chi_s = 0.01$, the big species cages dominate and are first pushed into the super-diffusive regime due to shear. At $Pe_s = 0.1$ the small species does not exhibit super-diffusive regime. As the Pe_s increases, the super-diffusive regime becomes more prominent for the small species. The extent of the super-diffusive regime for the small species depends on Pe_s.

Fig. 7.14 (b) shows the scenario where the caging species is dominated by the small particles. The statistics of the big particles are poor and hence the fluctuating data. Here the caging species of the small particles are pushed into the super-diffusive regime at the same time that the big particles are pushed into this regime at $Pe_s = 0.1$. Thus it can be speculated that caging species drives the dynamics during start-up shear of the binary mixtures. The time delay between the big and small particles for the MSD to deviate from rest existing at $\chi_s = 0.01$ can be attributed to the mobility of the small particles.
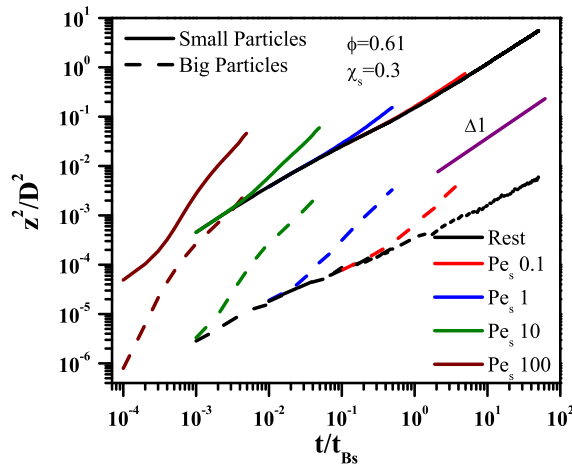
Figure 7.15: Two time mean square displacement for binary colloidal mixture at $\phi = 0.61$ for different Pe_s at $\chi_s = 0.3$

Fig. 7.15 represents the scenario where neither of the species dominates caging. This binary mixture shows different behaviour to binary mixtures in Fig. 7.14. The rest state shows liquid-like dynamics for both the big and small particles. The absence of super-diffusive regime during start-up shear specifi-

cally for the small species, below $Pe_s \leq 10$, is an interesting feature. On the other hand big particles exhibit the super-diffusive response at extremely high Pe. In general, this shows that the super-diffusive dynamics that is present in glasses is absent for transient dynamics of liquid-like systems during start-up shear.

In this chapter, BD simulations was utilized to identify and investigate the phases existing in binary mixtures with size ratio of 0.2 at high volume fractions. The existence two types of glasses are verified. A partially frozen glass where the big particles are frozen and the presence of mobile small particles. The second type of glass in the 'torroncino' glass where the small particles trap the big particles in its matrix. A systematic study by changing the mixing ratio of small particles was performed and the equilibrium properties as well as transient shear characteristics studied. A softening of the high volume fraction glass is observed at intermediate mixing ratios of the small particles. This is attributed to the cage transition from the big to the small particles. Finally the start-up shear dynamics reveal that the caging species present at the specific mixing ratio drives the dynamics in a binary colloidal glass.

CHAPTER 8

CONCLUSION AND PERSPECTIVES

Chapter 4 : Time effects of nearly hard sphere colloidal glasses

Aging effects in nearly hard sphere colloidal glasses manifest in the linear viscoelastic measurements as a weak change in the loss moduli. The colloidal glass shows aging effects, i.e., a rejuvenated colloidal glass with waiting time fall into deeper energy wells. This leads to subtle changes in the loss moduli, G'' in the linear viscoelastic regime. On the other hand transient start-up, stress relaxation and creep experiments show clear manifestations of the aging occurring in the colloidal glass. Since very limited frequencies are probed in the linear viscoelastic regime and aging process affects the long time behaviour of the colloidal glasses it is not being captured.

Comparing non-linear start-up shear and creep during aging we observe that start-up shear is much more energy efficient in fluidizing a colloidal glass than creep. In a start-up shear, a colloidal glass system is fluidized after the elastic regime while during creep at low stresses heterogeneous regions are activated which grow all through the sample until the colloidal glass flows.

Finally, long time creep of high volume fraction colloidal glass shows sudden fluctuations in strain relating to avalanche response, similar to stress drops in the long time stress relaxation. During avalanche processes, colloidal glass exhibit sudden inflection in viscosity with time under stress. Microstructurally, this occurs when the colloidal particles which was jammed suddenly starts to flow.

Based on the above findings one can propose future studies to elucidate open problems. An extension of aging studies could include confocal microscopy and velocimetric studies of colloidal glass to understand the avalanche response

during creep. Moreover efforts in modeling and Stokesian dynamics simulations are required to understand the fundamental driving force for aging in such systems.

Chapter 5 : Transient shear effects of nearly hard sphere colloidal glasses

The transient effects in colloidal glass during shear and after cessation of shear is probed in this chapter. The origin of residual stresses is investigated experimentally and with help of BD simulations. The cage anisotropy in these colloidal glasses does not seem to be the only reason for the retention of the residual stress unlike in soft glasses. Interruption of the flow along the start-up shear curve and following the stress relaxation provides clear indications of sequence of physical processes, an elastic regime followed by a plastic flow regime, occurring during start-up shear. The elastic regime is dominated by the appearance of cage anisotropy in colloidal glass. In the flow regime the cages start to flow with the applied shear rate. Colloidal glass constituting of big particles are prone to shear thickening during steady shear flow. Shear thickening possibly occurs due to jamming of colloidal aggregates which in turn leads to edge effects and instabilities during flow.

Large amplitude oscillatory shear is utilized to understand the non-linear response in concentrated colloidal suspensions and colloidal glasses. Both the suspensions and glasses shows unique features irrespective of particle interaction when examined for both hard sphere and star-like micelles. Below the glass transition, suspensions dissipate stress due to shear thinning, leading to the rise in anharmonicity in the stress with increasing frequency. On the other hand, in colloidal glasses the system dissipates energy by transitioning from viscoelastic solid to a plastic response thus leading to decreasing stress anharmonicity with increasing frequency.

Future studies in direction can be undertaken with the help of Stokesian dynamics to understand how hydrodynamics contribute towards the relaxation of residual stresses. Confocal microscopy complemented by rheology should also help understanding the microscopic dynamics under oscillatory shear for

colloidal suspensions and glasses.

Chapter 6 : Orthogonal Superposition Rheometry of Colloidal glasses under flow

Colloidal glasses are investigated with the help of mechanical superposition of oscillatory flow during steady shear. The activation of relaxation time during shear in hard sphere colloidal glass follows a linear dependence with external shear rate. Moreover, orthogonal frequency superposition of the orthogonal dynamic frequency sweeps was successfully performed. Deviations in superposition at short time was attribute the cage anisotropy. While long time deviations were compared with BD simulations and speculated to be due to the presence of hydrodynamically induced transient clusters. On the other hand, star-like micelles which have a softer potential exhibited a crossover frequency and shear rate relationship with a power law exponent of 0.8. We believe that star-like micelles interpenetrates, also contributing to the relaxation process under shear unlike hard sphere glasses.

Some suggestions for the future studies include, Stokesian dynamics simulations which could be an appropriate tool to understand colloidal glasses under shear and check the validity of orthogonal frequency superposition specifically at long times. MCT or other theoretical framework could also aid in predicting the difference between hard and soft sphere interactions and the dependence of the crossover frequency under shear.

Chapter 7 : Brownian Dynamics simulations of size asymmetric Binary colloidal glasses

Brownian dynamics simulations were employed to investigate the binary glass phases predicted by MCT in large asymmetric mixtures. Two different types of glasses were found to exist in simulations for the asymmetric size ratio investigated, that is a partially frozen glass and a torroncino glass. A partially frozen glass is formed by the caging of big particles with mobile small particles moving

through the interstitial spaces of the trapped big particles. A torroncino glass on the other hand, is related to the caging of the big particles by the large amount of small particles. The microscopic dynamics reveal that the phase transitions occur due to changing mixing ratio of small particles. The caging species is seen to drive the microscopic dynamics under transient start-up shear. Moreover, the simulations tend to corroborate the experimental rheological measurements already existing in literature.

Following the above work we suggest that BD simulation of binary colloidal glasses with higher asymmetry needs to be performed to understand the effects of depletion on the big species. Additionally, binary systems with attractions exhibit immense potential to access a lot of new phases in the phase diagram.

APPENDIX A

Appendix

A.1 Moduli within an oscillatory cycle

Here we try to extract the moduli from theoretical models and experiments during LAOS with an oscillatory cycle. In Fig. A.1 (a) we show a $3D$ mapping of the instantaneous G' and G'' (Koumakis, 2011) for the Giesekus model at Deborah $= 1$. During LAOS, the moduli indicates the system shows viscous flow all throughout the cycle. While R' and R'' (Rogers, 2012) does show an elastic type response within the cycle of LAOS for the same parameters.
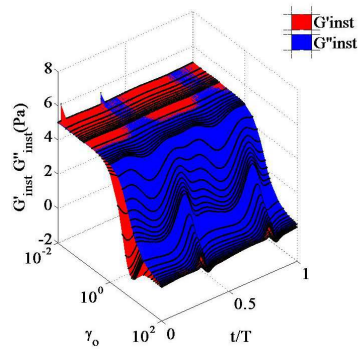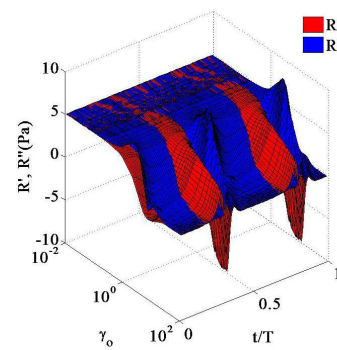
(a)   (b)

Figure A.1: (a) Instantaneous G' and G'' and (b) R' and R'' calculated within a LAOS cycle for Giesekus model at Deborah number 1

A.2   Differential Dynamic Microscopy

Differential dynamic microscopy (DDM) (Cerbino and Trappe, 2008) was performed on hard sphere suspensions and glasses on an already existing optical tweezer set-up. A homemade MATLAB code was developed for post processing the data. The image structure factor for a suspension is shown in Fig. A.2 (a). Interestingly, the colloidal glass (Fig. A.2 (b)) shows a peak for all lag times investigated.

(a)

(b)
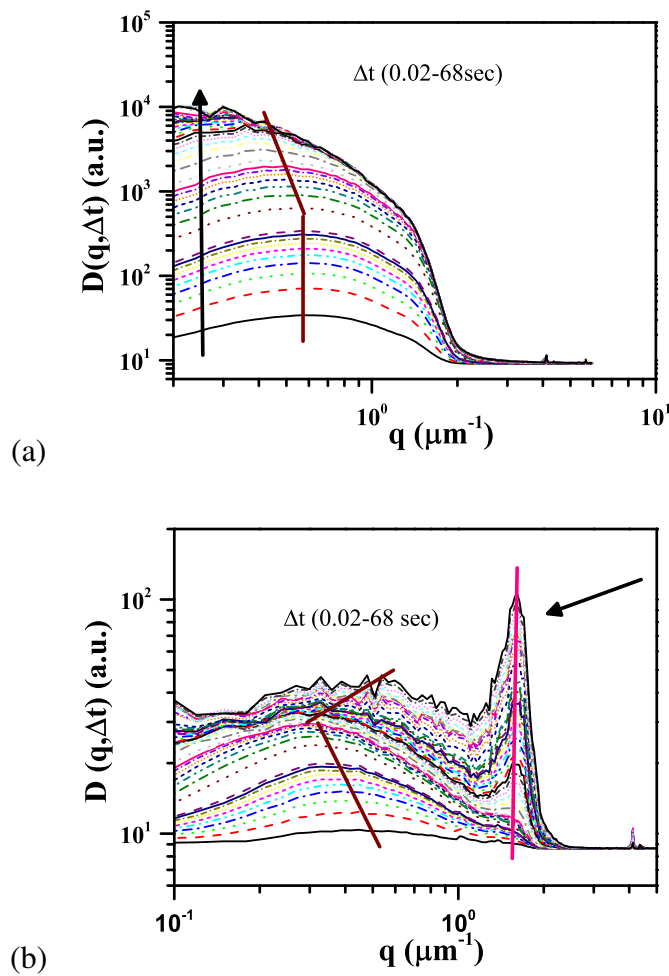
Figure A.2: The image structure function for a colloidal suspension of $R = 350\ nm$ in squalene at (a) $\phi = 0.20$ and (b) $\phi = 0.60$ obtained from DDM

A.3 Non-Linear Response in Rheometers

The non linear stress and strain response of stress controlled rheometers were mapped as function of frequency and strain amplitude for a very viscoelastic colloidal glass sample. This gives information on the contribution of elasticity to the non linear effects on the rheometer.
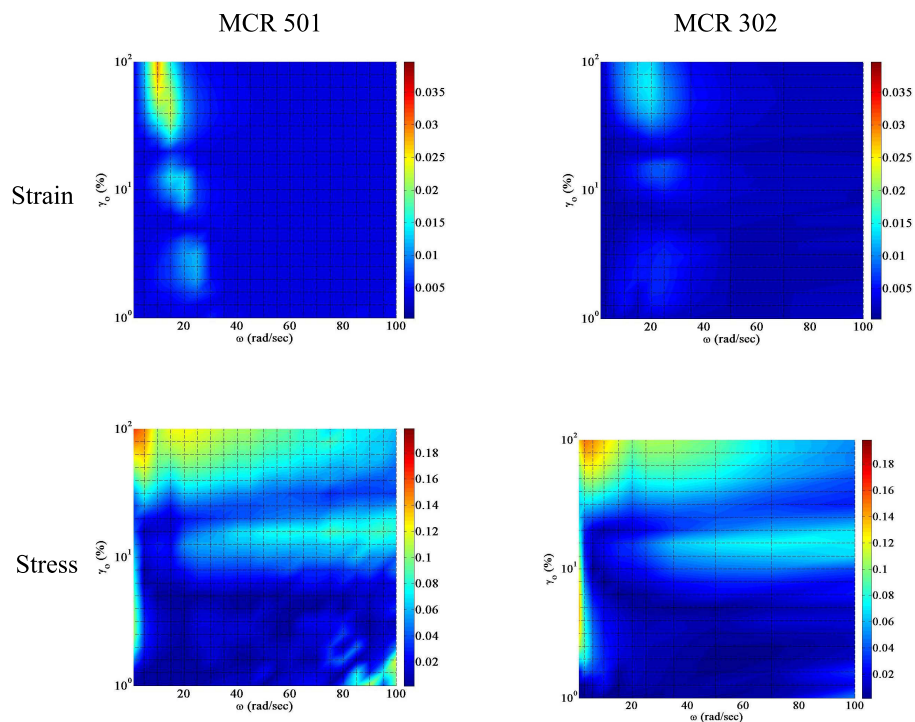
Figure A.3: The stress and strain non linearity mapped during oscillatory measurements mapped for a colloidal suspension $R = 106\ nm$ in squalene at $\phi = 0.61$ in stress controlled rheometer

A.4   Fast time data collection in Rheometer

The fast time data collection capabilities of strain and stress controlled rheome-
ters were tested. This was done by taking out the raw data from the rheometer
and processing it. Although data can be collected in the order of $10 \ ms$ for both
the rheometers, the data from the software can be trusted only above $0.1s$ (Fig.
A.4).

(a)

(b)
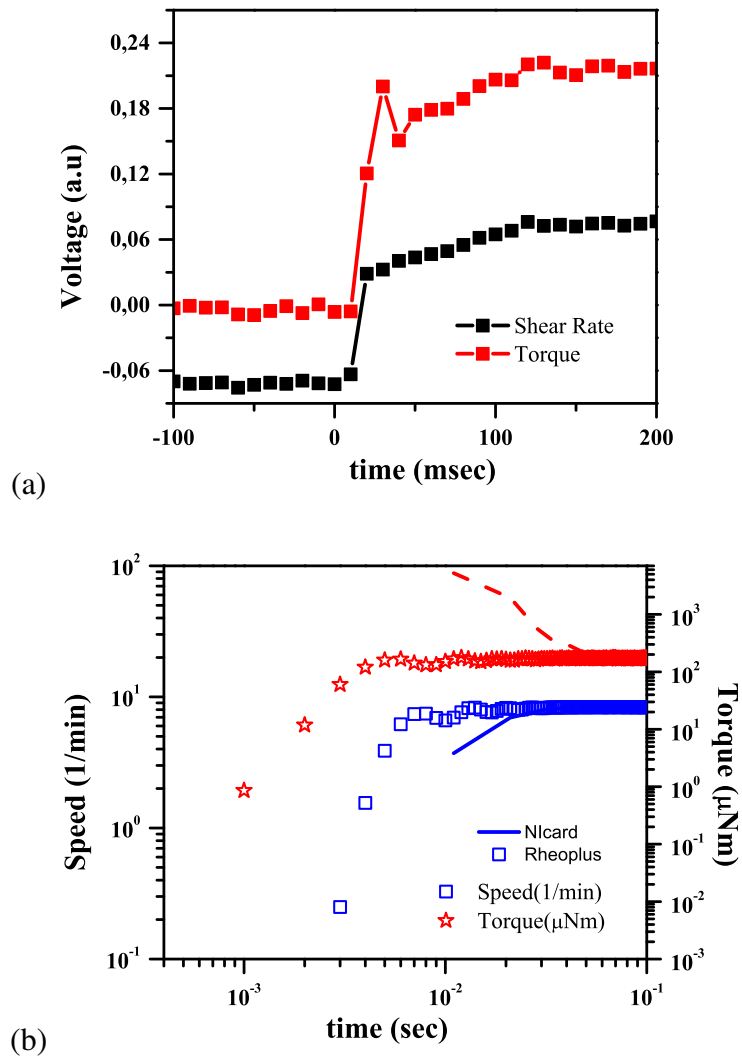
Figure A.4: Fast time data collection for (a) strain controlled at shear reversal of
$5 \ s^{-1}$ for silicone oil $\eta = 1 \ Pas$ and (b) stress controlled rheometer
at transient start-up shear of $50 \ s^{-1}$ for a colloidal suspension at
$\phi = 0.40$

A.5 Very asymmetric size Binary BD simulations

BD simulations was modified and tested to account for extremely low size ratios. The simulations were run in the High processing computer center in University of Crete. A partially frozen glass of big species due to depletion effects becomes prominent at the size ratio $\delta = 0.1$ for binary mixtures shown in Fig. A.5. This will lead to understanding the dynamics of polymers in colloid-polymer mixtures if we assume the polymer to be smallest particles.

$$\phi = 0.58 \qquad\qquad \phi = 0.64$$
$$\chi_s = 0.1 \qquad\qquad \chi_s = 0.1$$
$$\delta = 0.1 \qquad\qquad \delta = 0.1$$
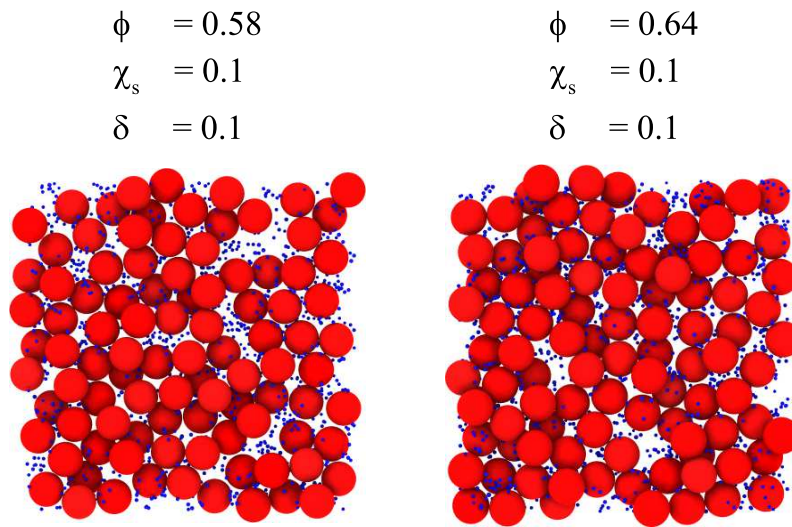
Figure A.5: Images of highly asymmetric binary glasses equilibrated using BD simulations

A.6 Attractive size asymmetric Binary BD simulations

BD simulations were further modified and tested to include Asakura Osawa potential. Fig. A.6 depicts fascinating structures, like the big species acting as anchor points for the small species. Additionally, switching on the attractive potential for a single species is also possible.

$$\phi = 0.44 \quad\quad \phi = 0.44 \quad\quad \phi = 0.61 \quad\quad \phi = 0.61$$
$$\chi_s = 0.1 \quad\quad \chi_s = 0.3 \quad\quad \chi_s = 0.1 \quad\quad \chi_s = 0.3$$
$$\delta = 0.2 \quad\quad \delta = 0.2 \quad\quad \delta = 0.2 \quad\quad \delta = 0.2$$
$$\xi = 0.1 \quad\quad \xi = 0.1 \quad\quad \xi = 0.1 \quad\quad \xi = 0.03$$
$$U_{dep} = -20\,k_BT \quad U_{dep} = -20\,k_BT \quad U_{dep} = -20\,k_BT \quad U_{dep} = -20\,k_BT$$
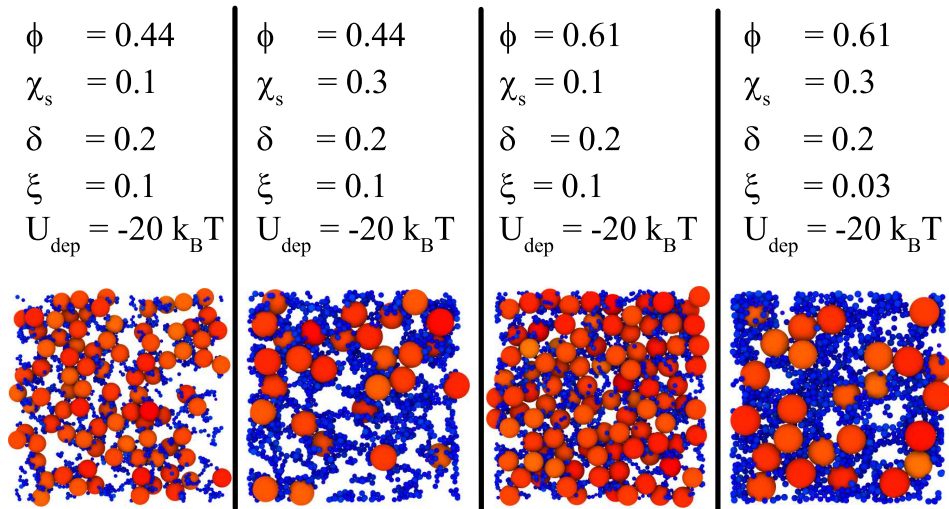
Figure A.6: Images of size asymmetric binary glasses with AO potential attraction from BD simulations

REFERENCES

1. **Aastuen, D. J. W.**, **N. A. Clark**, **L. K. Cotter**, and **B. J. Ackerson** (1986). Nucleation and growth of colloidal crystals. *Phys. Rev. Lett.*, **57**, 1733–1736.

2. **Ackerson, B. J.** (1990). Shear induced order and shear processing of model hard sphere suspensions. *J. Rheol.*, **34**(4), 553–590.

3. **Ackerson, B. J.** and **P. N. Pusey** (1988). Shear-induced order in suspensions of hard spheres. *Phys. Rev. Lett.*, **61**, 1033–1036.

4. **Allen, M. P.** and **D. J. Tildesley**, *Computer simulation of liquids*. Oxford university press, 1989.

5. **Allgaier, J.**, **A. Poppe**, **L. Willner**, and **D. Richter** (1997). Synthesis and characterization of poly[1,4-isoprene-b-(ethylene oxide)] and poly[ethylene-co-propylene-b-(ethylene oxide)] block copolymers. *Macromolecules*, **30**(6), 1582–1586.

6. **Amann, C. P.**, **D. Denisov**, **M. T. Dang**, **B. Struth**, **P. Schall**, and **M. Fuchs** (2015). Shear-induced breaking of cages in colloidal glasses: Scattering experiments and mode coupling theory. *J. Chem. Phys.*, **143**(3).

7. **Angelini, R.**, **E. Zaccarelli**, **F. De Melo Marques**, **M. Sztucki**, **A. Fluerasu**, **G. Ruocco**, and **B. Ruzicka** (2014). Glass-glass transition during aging of a colloidal clay. *Nat. Commun.*, **5**.

8. **Angelini, T. E.**, **E. Hannezo**, **X. Trepat**, **M. Marquez**, **J. J. Fredberg**, and **D. A. Weitz** (2011). Glass-like dynamics of collective cell migration. *Proc. Natl. Acad. Sci. U.S.A.*, **108**(12), 4714–4719.

9. **Angell, C. A.** (1995). Formation of glasses from liquids and biopolymers. *Science*, **267**(5206), 1924–1935.

10. **Angell, C. A.**, **K. L. Ngai**, **G. B. McKenna**, **P. F. McMillan**, and **S. W. Martin** (2000). Relaxation in glass forming liquids and amorphous solids. *J. App. Phys.*, **88**(6), 3113–3157.

11. **Antl, L.**, **J. Goodwin**, **R. Hill**, **R. Ottewill**, **S. Owens**, **S. Papworth**, and **J. Waters** (1986). The preparation of poly(methyl methacrylate) latices in non-aqueous media. *Colloids Surf. ,*, **17**(1), 67 – 78.

12. **Asakura, S.** and **F. Oosawa** (1954). On interaction between two bodies immersed in a solution of macromolecules. *J. Chem. Phys.*, **22**(7), 1255–1256.

13. **Asakura, S.** and **F. Oosawa** (1958). Interaction between particles suspended in solutions of macromolecules. *J. Pol. Sci.*, **33**(126), 183–192.

14. **Bailey, N. P.**, **J. Schiøtz**, **A. Lemaître**, and **K. W. Jacobsen** (2007). Avalanche size scaling in sheared three-dimensional amorphous solid. *Phys. Rev. Lett.*, **98**, 095501.

15. **Baldewa, B.** and **Y. M. Joshi** (2012). Delayed yielding in creep, time-stress superposition and effective time theory for a soft glass. *Soft Matter*, **8**, 789–796.

16. **Ballauff, M.**, **J. M. Brader**, **S. U. Egelhaaf**, **M. Fuchs**, **J. Horbach**, **N. Koumakis**, **M. Krüger**, **M. Laurati**, **K. J. Mutch**, **G. Petekidis**, **M. Siebenbürger**, **T. Voigtmann**, and **J. Zausch** (2013). Residual stresses in glasses. *Phys. Rev. Lett.*, **110**, 215701.

17. **Ballesta, P.**, **R. Besseling**, **L. Isa**, **G. Petekidis**, and **W. C. K. Poon** (2008). Slip and flow of hard-sphere colloidal glasses. *Phys. Rev. Lett.*, **101**, 258301.

18. **Ballesta, P.** and **G. Petekidis** (2016). Creep and aging of hard-sphere glasses under constant stress. *Phys. Rev. E*, **93**, 042613.

19. **Ballesta, P.**, **G. Petekidis**, **L. Isa**, **W. C. K. Poon**, and **R. Besseling** (2012). Wall slip and flow of concentrated hard-sphere colloidal suspensions. *J. Rheol.*, **56**(5), 1005–1037.

20. **Bandyopadhyay, R.**, **P. H. Mohan**, and **Y. M. Joshi** (2010). Stress relaxation in aging soft colloidal glasses. *Soft Matter*, **6**, 1462–1466.

21. **Barnes, H. A.**, **J. F. Hutton**, and **K.Walters**, *An Introduction to Rheology*. Amsterdam:Elsevier, 1989.

22. **Barrat, J.-L.** and **A. Lemaître**, *Dynamical Heterogeneities in Glasses, Colloids and Granular Media*, chapter Heterogeneities in amorphous systems under shear. Oxford Science Publications, 2011.

23. **Barrett, K. E. J.** (1973). Dispersion polymerisation in organic media. *Brit. Polym. J.*, **5**(4), 259–271.

24. **Barrett, K. E. J.** (ed.), *Dispersion polymerization in Organic media*. Wiley London, 1975.

25. **Batchelor, G. K.** (1976). Brownian diffusion of particles with hydrodynamic interaction. *J. Fluid Mech.*, **74**(1), 1–29.

26. **Batchelor, G. K.** (1977). The effect of brownian motion on the bulk stress in a suspension of spherical particles. *J. Fluid Mech.*, **83**(1), 97–117.

27. **Baumgärtel, M.** and **N. Willenbacher** (1996). The relaxation of concentrated polymer solutions. *Rheol. Acta*, **35**(2), 168–185.

28. **Bellour, M.**, **A. Knaebel**, **J. L. Harden**, **F. Lequeux**, and **J.-P. Munch** (2003). Aging processes and scale dependence in soft glassy colloidal suspensions. *Phys. Rev. E*, **67**, 031405.

29. **Berne, B. J.** and **R. Pecora**, *Dynamic light scattering: with applications to chemistry, biology, and physics*. Courier Corporation, 1976.

30. **Berthier, L.**, **G. Biroli**, **J.-P. Bouchaud**, **L. Cipelletti**, **D. E. Masri**, **D. L'Hôte**, **F. Ladieu**, and **M. Pierno** (2005). Direct experimental evidence of a growing length scale accompanying the glass transition. *Science*, **310**(5755), 1797–1800.

31. **Besseling, R.**, **L. Isa**, **P. Ballesta**, **G. Petekidis**, **M. E. Cates**, and **W. C. K. Poon** (2010). Shear banding and flow-concentration coupling in colloidal glasses. *Phys. Rev. Lett.*, **105**, 268301.

32. **Besseling, R.**, **L. Isa**, **E. R. Weeks**, and **W. C. Poon** (2009). Quantitative imaging of colloidal flows. *Adv. Colloid Interface Sci.*, **146**(1-2), 1 – 17.

33. **Besseling, R.**, **E. R. Weeks**, **A. B. Schofield**, and **W. C. K. Poon** (2007). Three-dimensional imaging of colloidal glasses under steady shear. *Phys. Rev. Lett.*, **99**, 028301.

34. **Bocquet, L.**, **A. Colin**, and **A. Ajdari** (2009). Kinetic theory of plastic flow in soft glassy materials. *Phys. Rev. Lett.*, **103**, 036001.

35. **Bouchaud, J.-P.** (1992). Weak ergodicity breaking and aging in disordered systems. *J. Phys. I*, **2**(9), 1705–1713.

36. **Brader, J. M.** (2010). Nonlinear rheology of colloidal dispersions. *J. Phy.: Condens. Matter*, **22**(36), 363101.

37. **Brader, J. M.**, **M. E. Cates**, and **M. Fuchs** (2008). First-principles constitutive equation for suspension rheology. *Phys. Rev. Lett.*, **101**, 138301.

38. **Brader, J. M.**, **M. Siebenbürger**, **M. Ballauff**, **K. Reinheimer**, **M. Wilhelm**, **S. J. Frey**, **F. Weysser**, and **M. Fuchs** (2010). Nonlinear response of dense colloidal suspensions under oscillatory shear: Mode-coupling theory and fourier transform rheology experiments. *Phys. Rev. E*, **82**, 061401.

39. **Brader, J. M.**, **T. Voigtmann**, **M. E. Cates**, and **M. Fuchs** (2007). Dense colloidal suspensions under time-dependent shear. *Phys. Rev. Lett.*, **98**(5), 058301.

40. **Brader, J. M.**, **T. Voigtmann**, **M. Fuchs**, **R. G. Larson**, and **M. E. Cates** (2009). Glass rheology: From mode-coupling theory to a dynamical yield criterion. *Proc. Natl. Acad. Sci. U.S.A.*, **106**(36), 15186–15191.

41. **Brady, J. F.** (2001). Computer simulation of viscous suspensions. *Chem. Eng. Sci.*, **56**(9), 2921 – 2926.

42. **Brady, J. F.** and **G. Bossis** (1988). Stokesian dynamics. *Annu. Rev. Fluid Mech.*, **20**(1), 111–157.

43. **Brambilla, G.**, **D. El Masri**, **M. Pierno**, **L. Berthier**, and **L. Cipelletti** (2010*a*). Brambilla *et al.* reply:. *Phys. Rev. Lett.*, **105**, 199605.

44. **Brambilla, G.**, **D. El Masri**, **M. Pierno**, **L. Berthier**, **L. Cipelletti**, **G. Petekidis**, and **A. Schofield** (2010*b*). Brambilla *et al.* reply:. *Phys. Rev. Lett.*, **104**, 169602.

45. **Brambilla, G.**, **D. El Masri**, **M. Pierno**, **L. Berthier**, **L. Cipelletti**, **G. Petekidis**, and **A. B. Schofield** (2009). Probing the equilibrium dynamics of colloidal hard spheres above the mode-coupling glass transition. *Phys. Rev. Lett.*, **102**, 085703.

46. **Brown, E.** and **H. M. Jaeger** (2014). Shear thickening in concentrated suspensions: phenomenology, mechanisms and relations to jamming. *Rep. Prog. Phys.*, **77**(4), 046602.

47. **Bryant, G.**, **S. R. Williams**, **L. Qian**, **I. K. Snook**, **E. Perez**, and **F. Pincet** (2002). How hard is a colloidal "hard-sphere" interaction? *Phys. Rev. E*, **66**, 060501.

48. **Cates, M. E.**, **M. D. Haw**, and **C. B. Holmes** (2005). Dilatancy, jamming, and the physics of granulation. *J. Phys.: Condens. Matter*, **17**(24), S2517.

49. **Cates, M. E.**, **C. B. Holmes**, **M. Fuchs**, and **O. Henrich** (2003). Schematic mode coupling theories for shear thinning, shear thickening, and jamming. *arXiv preprint cond-mat/0310579*.

50. **Cerbino, R.** and **V. Trappe** (2008). Differential dynamic microscopy: Probing wave vector dependent dynamics with a microscope. *Phys. Rev. Lett.*, **100**, 188102.

51. **Chaudhuri, P.**, **L. Berthier**, **P. I. Hurtado**, and **W. Kob** (2010). When gel and glass meet: A mechanism for multistep relaxation. *Phys. Rev. E*, **81**, 040502.

52. **Chaudhuri, P.**, **L. Berthier**, and **W. Kob** (2007). Universal nature of particle displacements close to glass and jamming transitions. *Phys. Rev. Lett.*, **99**, 060604.

53. **Chen, D.**, **D. Semwogerere**, **J. Sato**, **V. Breedveld**, and **E. R. Weeks** (2010). Microscopic structural relaxation in a sheared supercooled colloidal liquid. *Phys. Rev. E*, **81**, 011403.

54. **Chikkadi, V.** (2011). *Spatial correlations and deformation modes in sheared colloidal glasses*. Ph.D. thesis, Institute of Physics, University of Amsterdam.

55. **Chikkadi, V.**, **D. M. Miedema**, **M. T. Dang**, **B. Nienhuis**, and **P. Schall** (2014). Shear banding of colloidal glasses: Observation of a dynamic first-order transition. *Phys. Rev. Lett.*, **113**, 208301.

56. **Chikkadi, V.**, **G. Wegdam**, **D. Bonn**, **B. Nienhuis**, and **P. Schall** (2011). Long-range strain correlations in sheared colloidal glasses. *Phys. Rev. Lett.*, **107**, 198303.

57. **Christopoulou, C.**, **G. Petekidis**, **B. Erwin**, **M. Cloitre**, and **D. Vlassopoulos** (2009). Ageing and yield behaviour in model soft colloidal glasses. *Phil. Trans. R. Soc. A*, **367**(1909), 5051–5071.

58. **Chung, B.**, **S. Ramakrishnan**, **R. Bandyopadhyay**, **D. Liang**, **C. F. Zukoski**, **J. L. Harden**, and **R. L. Leheny** (2006). Microscopic dynamics of recovery in sheared depletion gels. *Phys. Rev. Lett.*, **96**, 228301.

59. **Cicuta, P.**, **E. J. Stancik**, and **G. G. Fuller** (2003). Shearing or compressing a soft glass in 2d: Time-concentration superposition. *Phys. Rev. Lett.*, **90**, 236101.

60. **Cipelletti, L.**, **H. Bissig**, **V. Trappe**, **P. Ballesta**, and **S. Mazoyer** (2003*a*). Time-resolved correlation: a new tool for studying temporally heterogeneous dynamics. *J. Phys. : Condens Matter*, **15**(1), S257.

61. **Cipelletti, L.** and **L. Ramos** (2005). Slow dynamics in glassy soft matter. *J. Phy.: Condens. Matter*, **17**(6), R253.

62. **Cipelletti, L.**, **L. Ramos**, **S. Manley**, **E. Pitard**, **D. A. Weitz**, **E. E. Pashkovski**, and **M. Johansson** (2003*b*). Universal non-diffusive slow dynamics in aging soft matter. *Farad. Discuss.*, **123**, 237–251.

63. **Cipelletti, L.** and **E. Weeks**, *Dynamical Heterogeneities in Glasses, Colloids and Granular Media*, chapter Glassy dynamics and dynamical heterogeneity in colloid. Oxford Science Publications, 2011.

64. **Cohen, I.**, **B. Davidovitch**, **A. B. Schofield**, **M. P. Brenner**, and **D. A. Weitz** (2006). Slip, yield, and bands in colloidal crystals under oscillatory shear. *Phys. Rev. Lett.*, **97**, 215502.

65. **Conrad, J. C.**, **P. P. Dhillon**, **E. R. Weeks**, **D. R. Reichman**, and **D. A. Weitz** (2006). Contribution of slow clusters to the bulk elasticity near the colloidal glass transition. *Phys. Rev. Lett.*, **97**, 265701.

66. **Courtland, R. E.** and **E. R. Weeks** (2003). Direct visualization of ageing in colloidal glasses. *J. Phy.: Condens. Matter*, **15**(1), S359.

67. **Coussot, P.**, **Q. D. Nguyen**, **H. T. Huynh**, and **D. Bonn** (2002). Avalanche behavior in yield stress fluids. *Phys. Rev. Lett.*, **88**, 175501.

68. **Crocker, J. C.**, **J. A. Matteo**, **A. D. Dinsmore**, and **A. G. Yodh** (1999). Entropic attraction and repulsion in binary colloids probed with a line optical tweezer. *Phys. Rev. Lett.*, **82**, 4352–4355.

69. **Cwalina, C. D.** and **N. J. Wagner** (2014). Material properties of the shear-thickened state in concentrated near hard-sphere colloidal dispersions. *J. Rheol.*, **58**(4), 949–967.

70. **Daga, V. K.** and **N. J. Wagner** (2006). Linear viscoelastic master curves of neat and laponite-filled poly(ethylene oxide)–water solutions. *Rheol. Acta*, **45**(6), 813–824.

71. **de Kruif, C. G.**, **E. M. F. van Iersel**, **A. Vrij**, and **W. B. Russel** (1985). Hard sphere colloidal dispersions: Viscosity as a function of shear rate and volume fraction. *J. Chem. Phys.*, **83**(9), 4717–4725.

72. **de Wijn, A. S.**, **D. M. Miedema**, **B. Nienhuis**, and **P. Schall** (2012). Criticality in dynamic arrest: Correspondence between glasses and traffic. *Phys. Rev. Lett.*, **109**, 228001.

73. **Debenedetti, P. G.** and **F. H. Stillinger** (2001). Supercooled liquids and the glass transition. *Nature*, **410**(6825), 259–267.

74. **D'Haene, P.**, **J. Mewis**, and **G. Fuller** (1993). Scattering dichroism measurements of flow-induced structure of a shear thickening suspension. *J. Colloid Interface Sci.*, **156**(2), 350 – 358.

75. **Donati, C.**, **J. F. Douglas**, **W. Kob**, **S. J. Plimpton**, **P. H. Poole**, and **S. C. Glotzer** (1998). Stringlike cooperative motion in a supercooled liquid. *Phys. Rev. Lett.*, **80**, 2338–2341.

76. **Donati, C.**, **S. C. Glotzer**, **P. H. Poole**, **W. Kob**, and **S. J. Plimpton** (1999). Spatial correlations of mobility and immobility in a glass-forming lennard-jones liquid. *Phys. Rev. E*, **60**, 3107–3119.

77. **Dullaert, K.** and **J. Mewis** (2005). Stress jumps on weakly flocculated dispersions: Steady state and transient results. *J. Colloid Interface Sci.*, **287**(2), 542 – 551.

78. **Dullaert, K.** and **J. Mewis** (2006). A structural kinetics model for thixotropy. *J. Non-Newt. Fluid Mech.*, **139**(1âĂŞ2), 21 – 30.

79. **Dullens, R. P. A.**, **D. G. A. L. Aarts**, and **W. K. Kegel** (2006). Direct measurement of the free energy by optical microscopy. *Proc. Natl. Acad. Sci. U.S.A.*, **103**(3), 529–531.

80. **Duri, A.**, **D. A. Sessoms**, **V. Trappe**, and **L. Cipelletti** (2009). Resolving long-range spatial correlations in jammed colloidal systems using photon correlation imaging. *Phys. Rev. Lett.*, **102**, 085702.

81. **Edgeworth, R.**, **B. J. Dalton**, and **T. Parnell** (1984). The pitch drop experiment. *Euro. J. Phys.*, **5**(4), 198.

82. **Einstein, A.** (1905). Über die von der molekularkinetischen theorie der wärme geforderte bewegung von in ruhenden flüssigkeiten suspendierten teilchen. *Annalen der Physik*, **322**(8), 549–560.

83. **Eisenmann, C.**, **C. Kim**, **J. Mattsson**, and **D. A. Weitz** (2010). Shear melting of a colloidal glass. *Phys. Rev. Lett.*, **104**, 035502.

84. **Ellis, R. J.** and **A. P. Minton** (2003). Cell biology: join the crowd. *Nature*, **425**(6953), 27–28.

85. **Erwin, B. M.**, **M. Cloitre**, **M. Gauthier**, and **D. Vlassopoulos** (2010*a*). Dynamics and rheology of colloidal star polymers. *Soft Matter*, **6**, 2825–2833.

86. **Erwin, B. M.**, **S. A. Rogers**, **M. Cloitre**, and **D. Vlassopoulos** (2010*b*). Examining the validity of strain-rate frequency superposition when measuring the linear viscoelastic properties of soft materials. *J. Rheol.*, **54**(2), 187–195.

87. **Ewoldt, R. H.**, **A. E. Hosoi**, and **G. H. McKinley** (2008). New measures for characterizing nonlinear viscoelasticity in large amplitude oscillatory shear. *J. Rheol.*, **52**(6), 1427–1458.

88. **Fahy, G. M.**, **B. Wowk**, **R. Pagotan**, **A. Chang**, **J. Phan**, **B. Thomson**, and **L. Phan** (2009). Physical and biological aspects of renal vitrification. *Organo-genesis*, **5**(3), 167–175.

89. **Fahy, G. M.**, **B. Wowk**, **J. Wu**, **J. Phan**, **C. Rasch**, **A. Chang**, and **E. Zendejas** (2004). Cryopreservation of organs by vitrification: perspectives and recent advances. *Cryobiology*, **48**(2), 157 – 178. Special issue: Keynote papers from Cryobiomol- 2003.

90. **Falk, M. L.** and **J. S. Langer** (1998). Dynamics of viscoplastic deformation in amorphous solids. *Phys. Rev. E*, **57**, 7192–7205.

91. **Ferry, J. D.**, *Viscoelastic Properties of Polymers*. Wiley, 1980.

92. **Fielding, S. M.**, **P. Sollich**, and **M. E. Cates** (2000). Aging and rheology in soft materials. *J. Rheol.*, **44**(2), 323–369.

93. **Fluerasu, A.**, **A. Moussaïd**, **A. Madsen**, and **A. Schofield** (2007). Slow dynam-ics and aging in colloidal gels studied by x-ray photon correlation spectroscopy. *Phys. Rev. E*, **76**, 010401.

94. **Foss, D. R.** and **J. F. Brady** (2000). Brownian Dynamics simulation of hard-sphere colloidal dispersions. *J. Rheol.*, **44**(3), 629.

95. **Fox, T. G.** and **P. J. Flory** (1948). Viscosity-molecular weight and viscosity-temperature relationships for polystyrene and polyisobutylene1,2. *J. Am. Chem. Soc.*, **70**(7), 2384–2395.

96. **Frith, W.**, **J. Mewis**, and **T. Strivens** (1987). Rheology of concentrated suspen-sions: experimental investigations. *Powder Technol.*, **51**(1), 27 – 34.

97. **Frith, W. J.**, **P. d'Haene**, **R. Buscall**, and **J. Mewis** (1996). Shear thickening in model suspensions of sterically stabilized particles. *J. Rheol.*, **40**(4).

98. **Frith, W. J.**, **T. A. Strivens**, and **J. Mewis** (1990). Dynamic mechanical prop-erties of polymerically stabilized dispersions. *J. Colloid Interface Sci.*, **139**(1), 55 – 62.

99. **Fritschi, S.**, **M. Fuchs**, and **T. Voigtmann** (2014). Mode-coupling analysis of residual stresses in colloidal glasses. *Soft Matter*, **10**, 4822–4832.

100. **Fuchs, M.** and **M. E. Cates** (2002). Theory of nonlinear rheology and yielding of dense colloidal suspensions. *Phys. Rev. Lett.*, **89**, 248304.

101. **Fuchs, M.** and **M. E. Cates** (2003*a*). Non-newtonian viscosity of interacting brownian particles: comparison of theory and data. *J. Phys.:Condens. Matter*, **15**(1), S401.

102. **Fuchs, M.** and **M. E. Cates** (2003*b*). Schematic models for dynamic yielding of sheared colloidal glasses. *Farad. Discuss.*, **123**, 267.

103. **Glotzer, S. C.**, **V. N. Novikov**, and **T. B. Schrøder** (2000). Time-dependent, four-point density correlation function description of dynamical heterogeneity and decoupling in supercooled liquids. *J. Chem. Phys.*, **112**(2), 509–512.

104. **Golde, S.**, **T. Palberg**, and **H. J. Schöpe** (2016). Correlation between dynamical and structural heterogeneities in colloidal hard-sphere suspensions. *Nature Physics*.

105. **Gotze, W.** and **L. Sjogren** (1992). Relaxation processes in supercooled liquids. *Rep. Prog. Phys.*, **55**(3), 241.

106. **Gravish, N.**, **G. Gold**, **A. Zangwill**, **M. A. D. Goodisman**, and **D. I. Goldman** (2015). Glass-like dynamics in confined and congested ant traffic. *Soft Matter*, **11**, 6552–6561.

107. **Gupta, R.**, **B. Baldewa**, and **Y. M. Joshi** (2012). Time temperature superposition in soft glassy materials. *Soft Matter*, **8**, 4171–4176.

108. **Helden, A. V.**, **J. Jansen**, and **A. Vrij** (1981). Preparation and characterization of spherical monodisperse silica dispersions in nonaqueous solvents. *J. Colloid Interface Sci.*, **81**(2), 354 – 368.

109. **Helgeson, M. E.**, **N. J. Wagner**, and **D. Vlassopoulos** (2007). Viscoelasticity and shear melting of colloidal star polymer glasses. *J. Rheol.*, **51**(2), 297–316.

110. **Hermes, M.** and **M. Dijkstra** (2010). Jamming of polydisperse hard spheres: The effect of kinetic arrest. *EPL*, **89**(3), 38005.

111. **Hermes, M.**, **B. M. Guy**, **W. C. K. Poon**, **G. Poy**, **M. E. Cates**, and **M. Wyart** (2016). Unsteady flow and particle migration in dense, non-brownian suspensions. *J. Rheol.*, **60**(5), 905–916.

112. **Heyes, D.** and **J. Melrose** (1993). Brownian dynamics simulations of model hard-sphere suspensions. *J. Non-Newt. Fluid Mech.*, **46**(1), 1 – 28.

113. **Hiltner, P. A.** and **I. M. Krieger** (1969). Diffraction of light by ordered suspensions. *J. Phys. Chem.*, **73**(7), 2386–2389.

114. **Höfling, F.**, **T. Franosch**, and **E. Frey** (2006). Localization transition of the three-dimensional lorentz model and continuum percolation. *Phys. Rev. Lett.*, **96**, 165901.

115. **Horbach, J.**, **W. Kob**, and **K. Binder** (2002). Dynamics of sodium in sodium disilicate: Channel relaxation and sodium diffusion. *Phys. Rev. Lett.*, **88**, 125502.

116. **Hunter, G. L.** and **E. R. Weeks** (2012). The physics of the colloidal glass transition. *Rep. Prog. Phys.*, **75**(6), 066501.

117. **Hyun, K.**, **M. Wilhelm**, **C. O. Klein**, **K. S. Cho**, **J. G. Nam**, **K. H. Ahn**, **S. J. Lee**, **R. H. Ewoldt**, and **G. H. McKinley** (2011). A review of nonlinear oscillatory shear tests: Analysis and application of large amplitude oscillatory shear (laos). *Prog. Polym. Sci.*, **36**(12), 1697 – 1753.

118. **Ianniruberto, G.** and **G. Marrucci** (2014). Convective constraint release (ccr) revisited. *J. Rheol.*, **58**(1), 89–102.

119. **Imhof, A.** and **J. K. G. Dhont** (1995). Experimental phase diagram of a binary colloidal hard-sphere mixture with a large size ratio. *Phys. Rev. Lett.*, **75**, 1662–1665.

120. **Isa, L.**, **R. Besseling**, **A. N. Morozov**, and **W. C. K. Poon** (2009). Velocity oscillations in microfluidic flows of concentrated colloidal suspensions. *Phys. Rev. Lett.*, **102**, 058302.

121. **Isa, L.**, **R. Besseling**, and **W. C. K. Poon** (2007). Shear zones and wall slip in the capillary flow of concentrated colloidal suspensions. *Phys. Rev. Lett.*, **98**, 198305.

122. **Jacob, A. R.**, **A. P. Deshpande**, and **L. Bouteiller** (2014). Large amplitude oscillatory shear of supramolecular materials. *J. Non-Newt. Fluid Mech.*, **206**, 40 – 56.

123. **Jacob, A. R.**, **A. S. Poulos**, **S. Kim**, **J. Vermant**, and **G. Petekidis** (2015). Convective cage release in model colloidal glasses. *Phys. Rev. Lett.*, **115**, 218301.

124. **Joshi, Y. M.** (2014). Dynamics of colloidal glasses and gels. *Annu. Rev. Chem. Biomol. Eng.*, **5**(1), 181–202.

125. **Joshi, Y. M.** (2015). A model for aging under deformation field, residual stresses and strains in soft glassy materials. *Soft Matter*, **11**, 3198–3214.

126. **Joshi, Y. M.** and **G. R. K. Reddy** (2008). Aging in a colloidal glass in creep flow: Time-stress superposition. *Phys. Rev. E*, **77**, 021501.

127. **Kasper, A.**, **E. Bartsch**, and **H. Sillescu** (1998). Self-diffusion in concentrated colloid suspensions studied by digital video microscopy of core-shell tracer particles. *Langmuir*, **14**(18), 5004–5010.

128. **Kaushal, M.** and **Y. M. Joshi** (2014). Linear viscoelasticity of soft glassy materials. *Soft Matter*, **10**, 1891–1894.

129. **Kegel, W. K.** and **A. van Blaaderen** (2000). Direct observation of dynamical heterogeneities in colloidal hard-sphere suspensions. *Science*, **287**(5451), 290–293.

130. **Khalil, N.**, **A. de Candia**, **A. Fierro**, **M. P. Ciamarra**, and **A. Coniglio** (2014). Dynamical arrest: interplay of glass and gel transitions. *Soft Matter*, **10**, 4800–4805.

131. **Kim, S.**, **J. Mewis**, **C. Clasen**, and **J. Vermant** (2013). Superposition rheometry of a wormlike micellar fluid. *Rheol. Acta*, **52**(8-9), 727–740.

132. **Kob, W.**, **J.-L. Barrat**, **F. Sciortino**, and **P. Tartaglia** (2000*a*). Aging in a simple glass former. *J. Phy.: Condens. Matter*, **12**(29), 6385.

133. **Kob, W.**, **C. Donati**, **S. J. Plimpton**, **P. H. Poole**, and **S. C. Glotzer** (1997). Dynamical heterogeneities in a supercooled lennard-jones liquid. *Phys. Rev. Lett.*, **79**, 2827–2830.

134. **Kob, W.**, **F. Sciortino**, and **P. Tartaglia** (2000*b*). Aging as dynamics in configuration space. *EPL*, **49**(5), 590.

135. **Koumakis, N.** (2011). *A study on the effects of interparticle interactions on the dynamics and rheology and aging of colloidal systems out of equilibrium.* Ph.D. thesis, Department of Materials Science and Technology, University of Crete.

136. **Koumakis, N.**, **J. F. Brady**, and **G. Petekidis** (2013). Complex oscillatory yielding of model hard-sphere glasses. *Phys. Rev. Lett.*, **110**, 178301.

137. **Koumakis, N.**, **J. F. Brady**, and **G. Petekidis** (2016*a*). Amorphous and ordered states of concentrated hard spheres under oscillatory shear. *J. Non-Newt. Fluid Mech.*, **233**, 119 – 132. Papers presented at the Rheology Symposium in honor of Prof. R. I. Tanner on the occasion of his 82nd birthday, in Vathi, Samos, Greece.

138. **Koumakis, N.**, **M. Laurati**, **S. U. Egelhaaf**, **J. F. Brady**, and **G. Petekidis** (2012*a*). Yielding of hard-sphere glasses during start-up shear. *Phys. Rev. Lett.*, **108**, 098303.

139. **Koumakis, N.**, **M. Laurati**, **A. R. Jacob**, **K. J. Mutch**, **A. Abdellali**, **A. B. Schofield**, **S. U. Egelhaaf**, **J. F. Brady**, and **G. Petekidis** (2016*b*). Start-up shear of concentrated colloidal hard spheres: Stresses, dynamics, and structure. *J. Rheol.*, **60**(4), 603–623.

140. **Koumakis, N.**, **E. Moghimi**, **R. Besseling**, **W. C. K. Poon**, **J. F. Brady**, and **G. Petekidis** (2015). Tuning colloidal gels by shear. *Soft Matter*, **11**, 4640–4648.

141. **Koumakis, N.**, **A. Pamvouxoglou**, **A. S. Poulos**, and **G. Petekidis** (2012*b*). Direct comparison of the rheology of model hard and soft particle glasses. *Soft Matter*, **8**, 4271.

142. **Koumakis, N.**, **A. B. Schofield**, and **G. Petekidis** (2008). Effects of shear induced crystallization on the rheology and ageing of hard sphere glasses. *Soft Matter*, **4**, 2008–2018.

143. **Kubo, R.** (1966). The fluctuation-dissipation theorem. *Rep. Prog. Phys.*, **29**(1), 255.

144. **Kumar, M. A.**, **R. H. Ewoldt**, and **C. F. Zukoski** (2016). Intrinsic nonlinearities in the mechanics of hard sphere suspensions. *Soft Matter*, **12**, 7655–7662.

145. **Laurati, M.**, **K. J. Mutch**, **N. Koumakis**, **J. Zausch**, **C. P. Amann**, **A. B. Schofield**, **G. Petekidis**, **J. F. Brady**, **J. Horbach**, **M. Fuchs**, and **S. U. Egelhaaf** (2012). Transient dynamics in dense colloidal suspensions under shear: shear rate dependence. *J. Phys.:Condens. Matter*, **24**(46), 464104.

146. **Laurati, M.**, **J. Stellbrink**, **R. Lund**, **L. Willner**, **D. Richter**, and **E. Zaccarelli** (2005). Starlike micelles with starlike interactions: A quantitative evaluation of structure factors and phase diagram. *Phys. Rev. Lett.*, **94**, 195504.

147. **Lačević, N.**, **F. W. Starr**, **T. B. Schrøder**, and **S. C. Glotzer** (2003). Spatially heterogeneous dynamics investigated via a time-dependent four-point density correlation function. *J. Chem. Phys.*, **119**(14), 7372–7387.

148. **Le Grand, A.** and **G. Petekidis** (2008). Effects of particle softness on the rheology and yielding of colloidal glasses. *Rheologica Acta*, **47**(5), 579–590.

149. **Lemaître, A.** and **C. Caroli** (2009). Rate-dependent avalanche size in athermally sheared amorphous solids. *Phys. Rev. Lett.*, **103**, 065501.

150. **Lin, N. Y.**, **C. Ness**, **M. E. Cates**, **J. Sun**, and **I. Cohen** (2016). Tunable shear thickening in suspensions. *Proc. Natl. Acad. Sci. U.S.A.*.

151. **Lin, N. Y. C.**, **S. Goyal**, **X. Cheng**, **R. N. Zia**, **F. A. Escobedo**, and **I. Cohen** (2013). Far-from-equilibrium sheared colloidal liquids: Disentangling relaxation, advection, and shear-induced diffusion. *Phys. Rev. E*, **88**, 062309.

152. **Lin, N. Y. C.**, **B. M. Guy**, **M. Hermes**, **C. Ness**, **J. Sun**, **W. C. K. Poon**, and **I. Cohen** (2015). Hydrodynamic and contact contributions to continuous shear thickening in colloidal suspensions. *Phys. Rev. Lett.*, **115**, 228304.

153. **Lindsay, H. M.** and **P. M. Chaikin** (1982). Elastic properties of colloidal crystals and glasses. *J. Chem. Phys.*, **76**(7), 3774–3781.

154. **Lootens, D.**, **H. Van Damme**, and **P. Hébraud** (2003). Giant stress fluctuations at the jamming transition. *Phys. Rev. Lett.*, **90**, 178301.

155. **Loppinet, B.**, **E. Stiakakis**, **D. Vlassopoulos**, **G. Fytas**, and **J. Roovers** (2001). Reversible thermal gelation in star polymers: an alternative route to jamming of soft matter. *Macromolecules*, **34**(23), 8216–8223.

156. **Lorenzo, G.**, **N. E. Zaritzky**, and **A. N. Califano** (2011). Viscoelastic characterization of fluid and gel like food emulsions stabilized with hydrocolloids. *Procedia Food Sci.*, **1**, 281 – 286.

157. **Lu, Y.**, **X. Lu**, **Z. Qin**, and **J. Shen** (2016). Direct visualization of free-volume-triggered activation of β relaxation in colloidal glass. *Phys. Rev. E*, **94**, 012606.

158. **Lund, R.**, **L. Willner**, **J. Stellbrink**, **P. Lindner**, and **D. Richter** (2006). Logarithmic chain-exchange kinetics of diblock copolymer micelles. *Phys. Rev. Lett.*, **96**, 068302.

159. **Macosko, C. W.**, *Rheology Principles, Measurements and Applications*. New York:VCH, 1994.

160. **Maloney, C. E.** and **A. Lemaître** (2006). Amorphous systems in athermal, quasistatic shear. *Phys. Rev. E*, **74**, 016118.

161. **Marcus, A. H.**, **J. Schofield**, and **S. A. Rice** (1999). Experimental observations of non-gaussian behavior and stringlike cooperative dynamics in concentrated quasi-two-dimensional colloidal liquids. *Phys. Rev. E*, **60**, 5725–5736.

162. **Marrucci, G.** (1996). Dynamics of entanglements: A nonlinear model consistent with the cox-merz rule. *J. Non-Newt. Fluid Mech.*, **62**, 279–289.

163. **Marshall, L.** and **C. F. Zukoski** (1990). Experimental studies on the rheology of hard-sphere suspensions near the glass transition. *J. Phys. Chem.*, **94**(3), 1164–1171.

164. **Martinez, V. A.**, **G. Bryant**, and **W. van Megen** (2008). Slow dynamics and aging of a colloidal hard sphere glass. *Phys. Rev. Lett.*, **101**, 135702.

165. **Martinez, V. A.**, **G. Bryant**, and **W. van Megen** (2010). Aging dynamics of colloidal hard sphere glasses. *J. Chem. Phys.*, **133**(11).

166. **Mason, T. G.** (2000). Estimating the viscoelastic moduli of complex fluids using the generalized stokes-einstein equation. *Rheol. Acta*, **39**(4), 371–378.

167. **Mason, T. G.** and **D. A. Weitz** (1995). Linear viscoelasticity of colloidal hard sphere suspensions near the glass transition. *Phys. Rev. Lett.*, **75**, 2770–2773.

168. **Masri, D. E.**, **G. Brambilla**, **M. Pierno**, **G. Petekidis**, **A. B. Schofield**, **L. Berthier**, and **L. Cipelletti** (2009). Dynamic light scattering measurements in the activated regime of dense colloidal hard spheres. *J. Stat. Mech. Theor. Exp.*, **2009**(07), P07015.

169. **Mayer, C.**, **E. Zaccarelli**, **E. Stiakakis**, **C. Likos**, **F. Sciortino**, **A. Munam**, **M. Gauthier**, **N. Hadjichristidis**, **H. Iatrou**, **P. Tartaglia**, *et al.* (2008). Asymmetric caging in soft colloidal mixtures. *Nat. Mat.*, **7**(10), 780–784.

170. **McKenna, G. B.**, **T. Narita**, and **F. Lequeux** (2009). Soft colloidal matter: A phenomenological comparison of the aging and mechanical responses with those of molecular glasses. *J. Rheol.*, **53**(3), 489–516.

171. **McKenzie, R.** and **D. Vlassopoulos** (2016). Rheological diagnostic tools for state transitions. *J. Rheol.*, **60**(3), 367–378.

172. **Mewis, J.**, **W. J. Frith**, **T. A. Strivens**, and **W. B. Russel** (1989). The rheology of suspensions containing polymerically stabilized particles. *AIChE Journal*, **35**(3), 415–422.

173. **Mewis, J.** and **P. D. Haene** (1993). Prediction of rheological properties in polymer colloids. *Makromol. Chem. Macromol. Symp.*, **68**(1), 213–225.

174. **Mewis, J.** and **G. Schoukens** (1978). Mechanical spectroscopy of colloidal dispersions. *Farad. Discuss. Chem. Soc.*, **65**, 58–64.

175. **Mewis, J.** and **N. J. Wagner** (2009). Thixotropy. *Adv. Colloid Interface Sci.*, **147-148**, 214 – 227. Colloids, polymers and surfactants.Special Issue in honour of Brian Vincent.

176. **Mewis, J.** and **N. J. Wagner**, *Colloidal Suspension Rheology*. Cambridge Series in Chemical Engineering, 2012.

177. **Mézard, M.**, **J. P. Bouchaud**, and **J. Dalibard** (eds.), *Complex Systems*. Springer, Berlin, 2007.

178. **Miyazaki, K.**, **H. M. Wyss**, **D. A. Weitz**, and **D. R. Reichman** (2006). Nonlinear viscoelasticity of metastable complex fluids. *Europhys. Lett.*, **75**(6), 915–921.

179. **Moghimi, E.**, **A. R. Jacob**, **N. Koumakis**, and **G. Petekidis** (under review). Colloidal gels tuned by oscillatory shear.

180. **Moghimi, E.** and **G. Petekidis** (in preparation). Residual stress in colloidal gels.

181. **Mohan, L.**, **R. T. Bonnecaze**, and **M. Cloitre** (2013). Microscopic origin of internal stresses in jammed soft particle suspensions. *Phys. Rev. Lett.*, **111**, 268301.

182. **Mohan, L.**, **M. Cloitre**, and **R. T. Bonnecaze** (2015). Build-up and two-step relaxation of internal stress in jammed suspensions. *J. Rheol.*, **59**(1), 63–84.

183. **Moller, P.**, **A. Fall**, **V. Chikkadi**, **D. Derks**, and **D. Bonn** (2009). An attempt to categorize yield stress fluid behaviour. *Philos. Trans. A:Math. Phys. Eng. Sci.*, **367**(1909), 5139–5155.

184. **Morrison, F. A.**, *Understanding Rheology*. Oxford University Press, 2001.

185. **Murray, C. A.** and **D. H. Van Winkle** (1987). Experimental observation of two-stage melting in a classical two-dimensional screened coulomb system. *Phys. Rev. Lett.*, **58**, 1200–1203.

186. **Mutch, K. J.**, **M. Laurati**, **C. P. Amann**, **M. Fuchs**, and **S. U. Egelhaaf** (2013). Time-dependent flow in arrested states - transient behaviour. *Eur. Phys. J. Spec. Top.*, **222**(11), 2803–2817.

187. **Nägele, G.** and **J. Bergenholtz** (1998). Linear viscoelasticity of colloidal mixtures. *J. Chem. Phys.*, **108**(23), 9893–9904.

188. **Napper, D. H.**, *Polymeric stabilisation of Colloidal Dispersions*. Academic Press London, 1983.

189. **Negi, A. S.** and **C. O. Osuji** (2010). Physical aging and relaxation of residual stresses in a colloidal glass following flow cessation. *J. Rheol.*, **54**(5), 943–958.

190. **O'Connell, P.** and **G. McKenna** (2002). The non-linear viscoelastic response of polycarbonate in torsion: An investigation of time-temperature and time-strain superposition. *Mech. Time Depend. Mat.*, **6**(3), 207–229.

191. **O'Connell, P. A.** and **G. B. McKenna** (1997). Large deformation response of polycarbonate: Time-temperature, time-aging time, and time-strain superposition. *Polym. Eng. Sci.*, **37**(9), 1485–1495.

192. **Ottewill, R.** and **N. S. J. Williams** (1987). Study of particle motion in concentrated dispersions by tracer diffusion. *Nature*, 232–234.

193. **Perera, D. N.** and **P. Harrowell** (1999). Relaxation dynamics and their spatial distribution in a two-dimensional glass-forming mixture. *J. Chem. Phys.*, **111**(12), 5441–5454.

194. **Petekidis, G.**, **A. Moussaid**, and **P. N. Pusey** (2002). Rearrangements in hard-sphere glasses under oscillatory shear strain. *Phys. Rev. E*, **66**(5), 051402.

195. **Petekidis, G.**, **D. Vlassopoulos**, and **P. N. Pusey** (2003). Yielding and flow of colloidal glasses. *Farad. Discuss.*, **123**, 287–302.

196. **Petekidis, G.**, **D. Vlassopoulos**, and **P. N. Pusey** (2004). Yielding and flow of sheared colloidal glasses. *J. Phys.:Condens. Mat.*, **16**, S3955.

197. **Pham, K. N.**, **G. Petekidis**, **D. Vlassopoulos**, **S. U. Egelhaaf**, **W. C. K. Poon**, and **P. N. Pusey** (2008). Yielding behavior of repulsion- and attraction-dominated colloidal glasses. *J. Rheol.*, **52**(2), 649–676.

198. **Pham, K. N.**, **G. Petekidis**, **D. Vlassopoulos**, **S. U. Egelhaaf**, **P. N. Pusey**, and **W. C. K. Poon** (2006). Yielding of colloidal glasses. *EPL*, **75**(4), 624.

199. **Phan, S.-E.**, **W. B. Russel**, **J. Zhu**, and **P. M. Chaikin** (1998). Effects of polydispersity on hard sphere crystals. *J. Chem. Phys.*, **108**(23), 9789–9795.

200. **Poon, W. C. K.**, **E. R. Weeks**, and **C. P. Royall** (2012). On measuring colloidal volume fractions. *Soft Matter*, **8**, 21–30.

201. **Poulos, A. S.**, **F. Renou**, **A. R. Jacob**, **N. Koumakis**, and **G. Petekidis** (2015). Large amplitude oscillatory shear (laos) in model colloidal suspensions and glasses: frequency dependence. *Rheol. Acta*, **54**(8), 715–724.

202. **Poulos, A. S.**, **J. Stellbrink**, and **G. Petekidis** (2013). Flow of concentrated solutions of starlike micelles under large-amplitude oscillatory shear. *Rheol. Acta*, **52**(8), 785–800.

203. **Pusey, P.**, Liquids, freezing and the glass transition. *In* **D. L. J.P. Hansen** and **J. Zinn-Justin** (eds.), *Liquids, Freezing and the Glass Transition, Proceeding Les Houches Summer School*. Elsevier, Amsterdam, 1991.

204. **Pusey, P.** and **W. Van Megen** (1986). Phase behaviour of concentrated suspensions of nearly hard colloidal spheres. *Nature*, **320**(6060), 340–342.

205. **Pusey, P. N.** and **W. van Megen** (1987). Observation of a glass transition in suspensions of spherical colloidal particles. *Phys. Rev. Lett.*, **59**, 2083–2086.

206. **Pusey, P. N.**, **E. Zaccarelli**, **C. Valeriani**, **E. Sanz**, **W. C. K. Poon**, and **M. E. Cates** (2009). Hard spheres: crystallization and glass formation. *Phil. Trans. R. Soc. A*, **367**(1909), 4993–5011.

207. **Rahmani, Y.**, **K. van der Vaart**, **B. van Dam**, **Z. Hu**, **V. Chikkadi**, and **P. Schall** (2012). Dynamic heterogeneity in hard and soft sphere colloidal glasses. *Soft Matter*, **8**, 4264–4270.

208. **Raynaud, L.**, **B. Ernst**, **C. Vergé**, and **J. Mewis** (1996). Rheology of aqueous latices with adsorbed stabilizer layers. *J. Colloid Interface Sci.*, **181**(1), 11 – 19.

209. **Reinhardt, J.**, **F. Weysser**, and **M. Fuchs** (2010). Comment on "probing the equilibrium dynamics of colloidal hard spheres above the mode-coupling glass transition". *Phys. Rev. Lett.*, **105**, 199604.

210. **Renou, F.**, **J. Stellbrink**, and **G. Petekidis** (2010). Yielding processes in a colloidal glass of soft star-like micelles under large amplitude oscillatory shear (laos). *J. Rheol.*, **54**(6), 1219–1242.

211. **Rogers, S. A.** (2012). A sequence of physical processes determined and quantified in laos: An instantaneous local 2d/3d approach. *J. Rheol.*, **56**(5), 1129–1151.

212. **Rogers, S. A.**, **B. M. Erwin**, **D. Vlassopoulos**, and **M. Cloitre** (2011). A sequence of physical processes determined and quantified in laos: Application to a yield stress fluid. *J. Rheol.*, **55**(2), 435–458.

213. **Roovers, J.**, **L. L. Zhou**, **P. M. Toporowski**, **M. van der Zwan**, **H. Iatrou**, and **N. Hadjichristidis** (1993). Regular star polymers with 64 and 128 arms. models for polymeric micelles. *Macromolecules*, **26**(16), 4324–4331.

214. **Rosales-Pelaez, P.**, **P. M. de Hijes**, **E. Sanz**, and **C. Valeriani** (2016). Avalanche mediated devitrification in a glass of pseudo hard-spheres. *J. Stat. Mech. Theor. Exp.*, **2016**(9), 094005.

215. **Royall, C. P.**, **W. C. K. Poon**, and **E. R. Weeks** (2013). In search of colloidal hard spheres. *Soft Matter*, **9**, 17–27.

216. **Rubinstein, M.** and **R. H. Colby**, *Polymer Physics*. Oxford University Press, 2003.

217. **Russel, W. B.**, **D. A. Saville**, and **W. R. Schowalter**, *Colloidal dispersions*. Cambridge university press, 1989.

218. **Saltzman, E. J.**, **G. Yatsenko**, and **K. S. Schweizer** (2008). Anomalous diffusion, structural relaxation and shear thinning in glassy hard sphere fluids. *J. Phy.: Condens. Matter*, **20**(24), 244129.

219. **Sastry, S.**, **T. M. Truskett**, **P. G. Debenedetti**, **S. Torquato**, and **F. H. Stillinger** (1998). Free volume in the hard sphere liquid. *Mol. Phys.*, **95**(2), 289–297.

220. **Schaertl, W.** and **H. Sillescu** (1994). Brownian dynamics of polydisperse colloidal hard spheres: Equilibrium structures and random close packings. *J. Stat. Phys.*, **77**(5), 1007–1025.

221. **Schall, P.**, **D. A. Weitz**, and **F. Spaepen** (2007). Structural rearrangements that govern flow in colloidal glasses. *Science*, **318**(5858), 1895–1899.

222. **Schausberger, A.** and **I. V. Ahrer** (1995). On the time-concentration superposition of the linear viscoelastic properties of plasticized polystyrene melts using the free volume concept. *Macromolecular Chemistry and Physics*, **196**(7), 2161–2172.

223. **Schweizer, K. S.** (2007). Dynamical fluctuation effects in glassy colloidal suspensions. *Curr. Opin. Colloid Interface Sci.*, **12**(6), 297 – 306.

224. **Seiffert, S.** and **J. Sprakel** (2012). Physical chemistry of supramolecular polymer networks. *Chem. Soc. Rev.*, **41**, 909.

225. **Sentjabrskaja, T.**, **E. Babaliari**, **J. Hendricks**, **M. Laurati**, **G. Petekidis**, and **S. U. Egelhaaf** (2013*a*). Yielding of binary colloidal glasses. *Soft Matter*, **9**, 4524–4533.

226. **Sentjabrskaja, T.**, **P. Chaudhuri**, **M. Hermes**, **W. Poon**, **J. Horbach**, **S. Egelhaaf**, and **M. Laurati** (2015). Creep and flow of glasses: strain response linked to the spatial distribution of dynamical heterogeneities. *Sci. Rep.*, **5**, 1884.

227. **Sentjabrskaja, T.**, **D. Guu**, **P. M. Lettinga**, **S. U. Egelhaaf**, and **M. Laurati**, Glasses of dynamically asymmetric binary colloidal mixtures: Quiescent properties and dynamics under shear. *In AIP Conf. Proc.*, volume 1518. 2013*b*.

228. **Sentjabrskaja, T.**, **M. Hermes**, **W. C. K. Poon**, **C. D. Estrada**, **R. Castaneda-Priego**, **S. U. Egelhaaf**, and **M. Laurati** (2014). Transient dynamics during stress overshoots in binary colloidal glasses. *Soft Matter*, **10**, 6546–6555.

229. **Sentjabrskaja, T.**, **E. Zaccarelli**, **C. De Michele**, **F. Sciortino**, **P. Tartaglia**, **T. Voigtmann**, **S. U. Egelhaaf**, and **M. Laurati** (2016). Anomalous dynamics of intruders in a crowded environment of mobile obstacles. *Nature communications*, **7**.

230. **Seto, R.**, **R. Mari**, **J. F. Morris**, and **M. M. Denn** (2013). Discontinuous shear thickening of frictional hard-sphere suspensions. *Phys. Rev. Lett.*, **111**, 218301.

231. **Shamim, N.** and **G. B. McKenna** (2014). Mechanical spectral hole burning in polymer solutions: Comparison with large amplitude oscillatory shear fingerprinting. *J. Rheol.*, **58**(1), 43–62.

232. **Shikata, T.** and **D. S. Pearson** (1994). Viscoelastic behavior of concentrated spherical suspensions. *J. Rheol.*, **38**(3), 601–616.

233. **Siebenbürger, M.**, **M. Ballauff**, and **T. Voigtmann** (2012). Creep in colloidal glasses. *Phys. Rev. Lett.*, **108**, 255701.

234. **Siebenbürger, M.**, **M. Fuchs**, **H. Winter**, and **M. Ballauff** (2009). Viscoelasticity and shear flow of concentrated, noncrystallizing colloidal suspensions: Comparison with mode-coupling theory. *J. Rheol.*, **53**(3), 707–726.

235. **Sierou, A.** and **J. F. Brady** (2001). Accelerated stokesian dynamics simulations. *J. Fluid Mech.*, **448**, 115–146.

236. **Simeonova, N. B.** and **W. K. Kegel** (2004). Gravity-induced aging in glasses of colloidal hard spheres. *Phys. Rev. Lett.*, **93**, 035701.

237. **Simmons, J. M.** (1966). A servo-controlled rheometer for measurement of the dynamic modulus of viscoelastic liquids. *J. Sci. Instrum.*, **43**(12), 887.

238. **Sirota, E. B.**, **H. D. Ou-Yang**, **S. K. Sinha**, **P. M. Chaikin**, **J. D. Axe**, and **Y. Fujii** (1989). Complete phase diagram of a charged colloidal system: A synchro- tron x-ray scattering study. *Phys. Rev. Lett.*, **62**, 1524–1527.

239. **Sollich, P.** (1998). Rheological constitutive equation for a model of soft glassy materials. *Phys. Rev. E*, **58**, 738–759.

240. **Stellbrink, J.**, **G. Rother**, **M. Laurati**, **R. Lund**, **L. Willner**, and **D. Richter** (2004). Poly(ethylene-alt-propylene)-poly(ethylene oxide) diblock copolymer micelles: a colloidal model system with tunable softness. *J. Phy.: Condens. Matter*, **16**(38), S3821.

241. **Stillinger, F. H.** (1995). A topographic view of supercooled liquids and glass formation. *Science*, **267**(5206), 1935–1939.

242. **Strivens, T.** (1976). The shear thickening effect in concentrated dispersion systems. *J. Colloid Interface Sci.*, **57**(3), 476 – 487.

243. **Struik, L. C. E.**, *Physical aging in amorphous polymers and other materials*. Elsevier, 1978.

244. **Tanner, R. I.** (1968). Comparative studies of some simple viscoelastic theories. *Trans. Soc. Rheo.*, **12**(1), 155–182.

245. **Trappe, V.** and **D. A. Weitz** (2000). Scaling of the viscoelasticity of weakly attractive particles. *Phys. Rev. Lett.*, **85**, 449–452.

246. **Truzzolillo, D.**, **D. Marzi**, **J. Marakis**, **B. Capone**, **M. Camargo**, **A. Munam**, **F. Moingeon**, **M. Gauthier**, **C. N. Likos**, and **D. Vlassopoulos** (2013). Glassy states in asymmetric mixtures of soft and hard colloids. *Phys. Rev. Lett.*, **111**, 208301.

247. **Underwood, S. M.**, **J. R. Taylor**, and **W. van Megen** (1994). Sterically stabilized colloidal particles as model hard spheres. *Langmuir*, **10**(10), 3550–3554.

248. **Utz, M.**, **P. G. Debenedetti**, and **F. H. Stillinger** (2000). Atomistic simulation of aging and rejuvenation in glasses. *Phys. Rev. Lett.*, **84**, 1471–1474.

249. **van der Vaart, K.**, **Y. Rahmani**, **R. Zargar**, **Z. Hu**, **D. Bonn**, and **P. Schall** (2013). Rheology of concentrated soft and hard-sphere suspensions. *J. Rheol.*, **57**(4), 1195–1209.

250. **van Megen, W.**, **T. C. Mortensen**, **S. R. Williams**, and **J. Müller** (1998). Measurement of the self-intermediate scattering function of suspensions of hard spherical particles near the glass transition. *Phys. Rev. E*, **58**, 6073–6085.

251. **van Megen, W.** and **S. M. Underwood** (1994). Glass transition in colloidal hard spheres: Measurement and mode-coupling-theory analysis of the coherent intermediate scattering function. *Phys. Rev. E*, **49**, 4206–4220.

252. **van Megen, W.**, **S. M. Underwood**, and **P. N. Pusey** (1991). Nonergodicity parameters of colloidal glasses. *Phys. Rev. Lett.*, **67**, 1586–1589.

253. **van Megen, W.** and **S. R. Williams** (2010). Comment on "probing the equilibrium dynamics of colloidal hard spheres above the mode-coupling glass transition". *Phys. Rev. Lett.*, **104**, 169601.

254. **Vermant, J.**, **P. Moldenaers**, **J. Mewis**, **M. Ellis**, and **R. Garritano** (1997). Orthogonal superposition measurements using a rheometer equipped with a force rebalanced transducer. *Rev. Sci. Instrum.*, **68**(11), 4090–4096.

255. **Vermant, J.**, **L. Walker**, **P. Moldenaers**, and **J. Mewis** (1998). Orthogonal versus parallel superposition measurements. *J. Non-Newt. Fluid Mech.*, **79**(2-3), 173 – 189.

256. **Viasnoff, V.**, **S. Jurine**, and **F. Lequeux** (2003). How are colloidal suspensions that age rejuvenated by strain application? *Farad. Discuss.*, **123**, 253–266.

257. **Voigtmann, T.** (2011). Multiple glasses in asymmetric binary hard spheres. *EPL*, **96**(3), 36006.

258. **Voigtmann, T.** (2014). Nonlinear glassy rheology. *Curr. Opin. Colloid Interface Sci.*, **19**(6), 549–560.

259. **von Kann, S.**, **J. H. Snoeijer**, **D. Lohse**, and **D. van der Meer** (2011). Non-monotonic settling of a sphere in a cornstarch suspension. *Phys. Rev. E*, **84**(6), 060401.

260. **Vrij, A.**, **J. W. Jansen**, **J. K. G. Dhont**, **C. Pathmamanoharan**, **M. M. Kops-Werkhoven**, and **H. M. Fijnaut** (1983). Light scattering of colloidal dispersions in non-polar solvents at finite concentrations. silic spheres as model particles for hard-sphere interactions. *Farad. Discuss. Chem. Soc.*, **76**, 19–35.

261. **Wagner, N. J.** and **W. B. Russel** (1990). Light scattering measurements of a hardâĂŘsphere suspension under shear. *Phys. Fluids A*, **2**(4), 491–502.

262. **Wang, S.**, **E. V. Alekseev**, **J. Ling**, **G. Liu**, **W. Depmeier**, and **T. E. Albrecht-Schmitt** (2010). Polarity and chirality in uranyl borates: Insights into understanding the vitrification of nuclear waste and the development of nonlinear optical materials. *Chem. Mater.*, **22**(6), 2155–2163.

263. **Weeks, E. R.**, **J. C. Crocker**, **A. C. Levitt**, **A. Schofield**, and **D. A. Weitz** (2000). Three-dimensional direct imaging of structural relaxation near the colloidal glass transition. *Science*, **287**(5453), 627–631.

264. **Weeks, E. R.** and **D. Weitz** (2002*a*). Subdiffusion and the cage effect studied near the colloidal glass transition. *Chem. Phys.*, **284**(1-2), 361 – 367.

265. **Weeks, E. R.** and **D. A. Weitz** (2002*b*). Properties of cage rearrangements observed near the colloidal glass transition. *Phys. Rev. Lett.*, **89**, 095704.

266. **Weiss, J.** and **D. Marsan** (2003). Three-dimensional mapping of dislocation avalanches: Clustering and space/time coupling. *Science*, **299**(5603), 89–92.

267. **Wen, Y. H.**, **J. L. Schaefer**, and **L. A. Archer** (2015). Dynamics and rheology of soft colloidal glasses. *ACS Macro Lett.*, **4**(1), 119–123.

268. **Wilhelm, M.**, **D. Maring**, and **H.-W. Spiess** (1998). Fourier-transform rheology. *Rheol. Acta*, **37**(4), 399–405.

269. **Willner, L.**, **O. Jucknischke**, **D. Richter**, **J. Roovers**, **L.-L. Zhou**, **P. M. Toporowski**, **L. J. Fetters**, **J. S. Huang**, **M. Y. Lin**, and **N. Hadjichristidis** (1994). Structural investigation of star polymers in solution by small-angle neutron scattering. *Macromolecules*, **27**(14), 3821–3829.

270. **Wyss, H. M.**, **K. Miyazaki**, **J. Mattsson**, **Z. Hu**, **D. R. Reichman**, and **D. A. Weitz** (2007). Strain-rate frequency superposition: A rheological probe of structural relaxation in soft materials. *Phys. Rev. Lett.*, **98**, 238303.

271. **Yang, J.** and **K. S. Schweizer** (2010). Tunable dynamic fragility and elasticity in dense suspensions of many-arm-star polymer colloids. *EPL*, **90**(6), 66001.

272. **Yang, J.** and **K. S. Schweizer** (2011). Glassy dynamics and mechanical response in dense fluids of soft repulsive spheres. ii. shear modulus, relaxation-elasticity connections, and rheology. *J. Chem. Phys.*, **134**(20), 204909.

273. **Zaccarelli, E.**, **C. Valeriani**, **E. Sanz**, **W. C. K. Poon**, **M. E. Cates**, and **P. N. Pusey** (2009). Crystallization of hard-sphere glasses. *Phys. Rev. Lett.*, **103**, 135704.

274. **Zargar, R.**, **B. Nienhuis**, **P. Schall**, and **D. Bonn** (2013). Direct measurement of the free energy of aging hard sphere colloidal glasses. *Phys. Rev. Lett.*, **110**, 258301.

275. **Zausch, J.** and **J. Horbach** (2009). The build-up and relaxation of stresses in a glass-forming soft-sphere mixture under shear: A computer simulation study. *EPL*, **88**(6), 60001.

276. **Zeegers, J.**, **D. van den Ende**, **C. Blom**, **E. G. Altena**, **G. J. Beukema**, and **J. Mellema** (1995). A sensitive dynamic viscometer for measuring the complex shear modulus in a steady shear flow using the method of orthogonal superposition. *Rheol. Acta*, **34**(6), 606–621.

277. **Zhang, Z.**, **P. J. Yunker**, **P. Habdas**, and **A. G. Yodh** (2011). Cooperative rearrangement regions and dynamical heterogeneities in colloidal glasses with attractive versus repulsive interactions. *Phys. Rev. Lett.*, **107**, 208303.

278. **Zhou, Z.**, **J. V. Hollingsworth**, **S. Hong**, **H. Cheng**, and **C. C. Han** (2014). Yielding behavior in colloidal glasses: Comparison between "hard cage"and "soft cage". *Langmuir*, **30**(20), 5739–5746.

279. **Zhu, J.**, **M. Li**, **R. Rogers**, **W. Meyer**, *et al.* (1997). Crystallization of hard-sphere colloids in microgravity. *Nature*, **387**(6636), 883–885.

LIST OF PAPERS BASED ON THESIS

1. A. S. Poulos, F. Renou, <u>A. R. Jacob</u>, N. Koumakis and G. Petekidis , Large amplitude oscillatory shear in model colloidal suspensions and glasses : Frequency dependence, *Rheologica Acta*, **54**, 715, (2015).

2. <u>A. R. Jacob</u>, A. S. Poulos, S. Kim, J. Vermant and G. Petekidis, Convective cage release in model colloidal glasses, *Physical Review Letters*, **115**, 218301, (2015).

3. N. Koumakis, M. Laurati, <u>A. R. Jacob</u>, K. J. Mutch, A. Abdellali, A. B. Schofield, S. U. Egelhaaf, J. F. Brady and G. Petekidis, Start-up shear of concentrated colloidal hard spheres: Stresses, Dynamics and Structure, *Journal of Rheology*, **60**,603, (2016). **[Cover Issue]**

4. A. S. Poulos, <u>A. R. Jacob</u>, S. Kim, J. Vermant and G. Petekidis, Orthogonal superposition rheometry of a concentrated solution of star like micelles, *In Preparation*.

5. <u>A. R. Jacob</u>, and G. Petekidis, Aging studies of hard sphere colloidal glasses, *In Preparation*.

6. <u>A. R. Jacob</u>, and G. Petekidis, Stress relaxation after flow interruption for hard sphere colloidal glasses during start up shear, *In Preparation*.

7. R. J. E. Andrade, F. J. Galindo-Rosales, L. Campo-Deano, Q. Huang, O. Hassager, <u>A. R. Jacob</u> and G. Petekidis, Structure development in concentrated colloidal suspensions under shear and uniaxial extensional flow, *In Preparation*.

8. T. Sentjabrskaja, J. Hendricks, <u>A. R. Jacob</u>, G. Petekidis, S. U. Egelhaaf and M.Laurati, Application of stress and strain controlled shear on binary colloidal glasses , *In Preparation*.

9. T. Sentjabrskaja, M. Laurati, S. U. Egelhaaf, O. Herbst, J. Horbach, <u>A. R. Jacob</u>, G. Petekidis and T. Voigtmann, Mechanical Properties and Local Dynamics of Asymmetric Colloidal Mixtures, *In Preparation*.